4

THE PETROGRAPHY, PHASE CHEMISTRY AND PETROLOGY OF SOUTH-WEST INDIAN RIDGE BASALTS DREDGED BETWEEN 16 AND 26 DEGREES EAST.

by

CHRISTOPHER CHARLES HAMILTON

DEPARTMENT OF GEOLOGY

UNIVERSITY OF CAPE TOWN

University of Cape Town

DIGITISED

2 0 NOV 2015

AUGUST, 1988.

A thesis submitted in fulfilment of the requirements for the degree of M.Sc. at the University of Cape Town.

The copyright of this thesis vests in the author. No quotation from it or information derived from it is to be published without full acknowledgement of the source. The thesis is to be used for private study or non-commercial research purposes only.

Published by the University of Cape Town (UCT) in terms of the non-exclusive license granted to UCT by the author.

University of Cape Town

FRONTISPIECE

Scanning electron micrographs illustrating the crystal growth of groundmass phases, chiefly plagioclase and pyroxene (augite), in pillow basalt AG22-1-4. A; skeletal or hollow plagioclase (Lofgren, 1974) forms the nucleus of a spherulite comprised of radially intergrown plagioclase and clinopyroxene (Bryan, 1972). B; plagioclase and pyroxene intergrown in lattice-like, reticulate fashion (Bryan, 1972). Small euhedral to subhedral crystals are oxides. C; similar to B at higher magnification. D; Plagioclase (platelets) with intergrown clinopyroxene (rods): phases have common b axes with a and c axes interchanged, indicative of three-dimensional diffusion (and sympathetic solute re-distribution) attendent on dendritic and cellular crystallization (Padden and Keith, 1973; Tiller, 1977). E; an area in D at higher magnification.

****

A

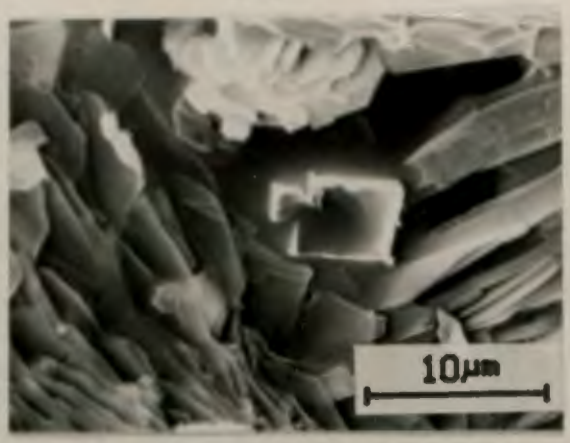

B

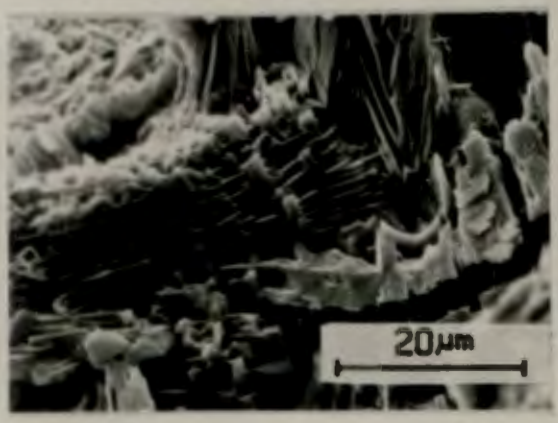

C

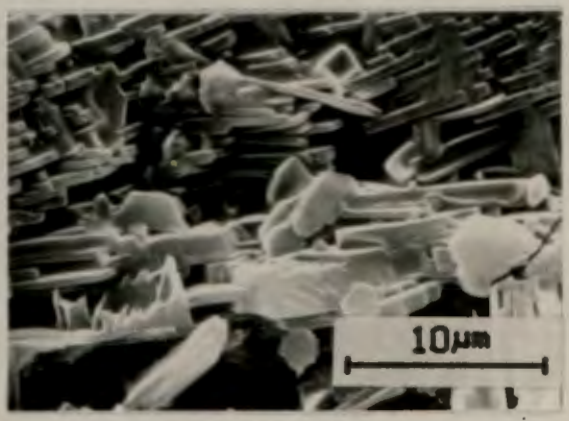

D

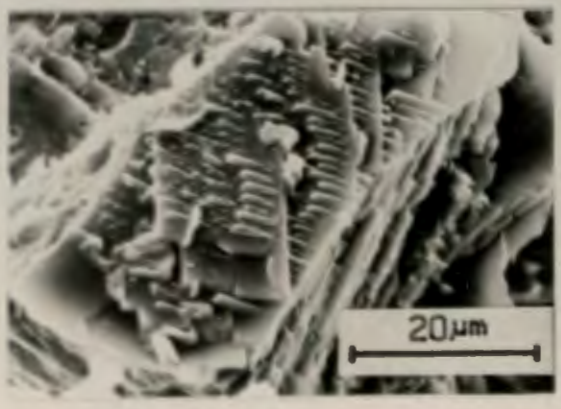

E

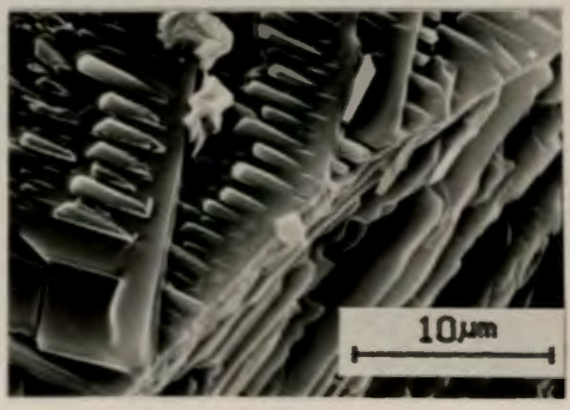

CONTENTS

****

LIST OF TABLES.

LIST OF PLATES.

LIST OF FIGURES.

ACKNOWLEDGEMENTS

First and foremost, thanks are due to Professor A.M. Reid and Dr Anton le Roex for their patience and supervision and for critically reviewing this thesis. An initial debt in particular is owed to Prof Reid for providing the mineralogical inspiration which I believe is known as the "lunar approach" to petrology. The famous lunar rock program (in which Prof. Reid participated) led to important developments in petrology, and MORB petrology is no exception. In this respect and under the guidance of both supervisors, I have been most fortunate. I hope this thesis does them justice.

Without first hand experience in dredging methods and ocean-going geophysics, this thesis project would never have gone beyond an experimental-cum-academic status. For the opportunity of going to sea on two occasions and the experience I obtained, I extend my deepest gratitude to all involved persons. More specifically, thanks go to Anton le Roex, Marshall Otter, Beecher Wooding, Hugh Bergh and American scientists Dr R.L. Fisher, Dr H.J.B. Dick and Dr J.H. Natland for assistance and initial scientific apprenticeship while at sea aboard M.V. Melville in 1984. More recently, I was privileged to participate as a petrologist in the Antarktis IV/4 cruise of the F.S. Polarstern of the Federal Republic of Germany. This cruise

completed the dredging program in this section of the SWIR (see question mark in Figure 1).

For technical and other assistance closer to home, I would like to thank Dick Rickard (electron microprobe), Charles Basson (photomicrographs) and Anton le Roex, Dave Hill and Simon Milner (computing facilities). Anton le Roex kindly provided geochemical data previously obtained on the sample suite. Other people from whom I have benefitted include staff and students of the Geochemistry and Geology Departments. The latter are too numerous to list individually, but I would specifically like to mention Judy Hicks, Jon MacStay, Leon van Heerden and Albert Thamm ("peer support") and Patrick Seias and cohorts (Departmental Assistants). The constant help rendered by Leon van Heerden is thankfully acknowledged.

Special thanks go to Shanaaz Hassiem for her efficient typing and word processing.

The patience and co-operation of my girlfriend, Jillian cannot possibly be overestimated.

Financial support from the CSIR is gratefully acknowledged.

****

DEDICATION

This thesis is dedicated to my family and girlfriend - in partial payment of the debt of gratitude owed to them for their support, patience and understanding.

****

PREFACE

Prior to 1976, knowledge of the submarine lithosphere in the Southern Oceans was limited to studies of ocean island sample suites and a few samples dredged from the South Atlantic (e.g. Dickey et al., 1977). In late 1976, a co-operative U.S.A.-Argentina research cruise took place to the vicinity of the Bouvet Triple Junction (Figure 1) and successfully recovered samples from two major fracture zones transecting the ridge system in this region. Basaltic fragments were made available to the Geochemistry Department of the University of Cape Town and out of this a multi-institutional study arose: the Southern Ocean Lithosphere Project (SOLP).

Participating institutions include the University of Cape Town departments of Geology and Geochemistry, the Bernard Price Institute of Geophysics (Johannesburg), Woods Hole Oceanographic Institute (U.S.A.) and the Massachusetts Institute of Technology (U.S.A.). Among the primary objectives of SOLP are:

(1) The identification, description and analysis of igneous rocks from ridge segments and fracture zones of the South Ocean ridge system and from associated oceanic islands.

(2) Formulating and testing models for the formation of these rocks, for the relationships of rock type to tectonic setting and for the evolution of the Lithosphere in the South Oceans.

(3) Investigating the geographical distribution of the geochemical influence of the Bouvet Mantle Plume on ocean ridge lavas (le Roex et al., 1983, 1985).

A geophysical and dredging cruise forming part of SOLP was made to the Southwest Indian Ridge (SWIR) between 16 and 26°E in October and November of 1981. This cruise (voyage 22 of the S.A. Agulhas) succeeded in recovering basaltic fragments from several localities on two relatively long (>200km) ridge segments. In January 1984, the author undertook the task of investigating the petrography, phase chemistry and petrology of this sample suite. This thesis presents the results of this study to date.

****

ABSTRACT

Basaltic rocks dredged from the Southwest Indian Ridge (SWIR) between 16 and 26°E were investigated by petrographic microscope, electron microprobe and X-ray fluorescence analysis. Basalts are olivine tholeiites with geochemical characteristics similar to normal, depleted mid-ocean ridge basalts (MORB) from the SWIR between 0 and 11° East (le Roex et al., 1983). The suite consists predominantly of aphyric or microporphyritic olivine- and olivine-plagioclase basalts. Several porphyritic lavas are also present.

Microprobe analyses of minerals from representative basalts exhibit a substantial compositional range similar to known MORB mineral chemistry. The observed phases are: plagioclase (An_{84-59}), olivine (Fo_{88-77}), spinel (Cr/Cr+Al=0.27-0.57; $Mg/Mg+Fe^{2+}$=0.78-0.57) and clinopyroxene ($Wo_{39-49}En_{31-44}Fs_{7-19}$). Much of the chemical variation in analysed pyroxene is attributable to metastable partitioning achieved upon quenching (eg. aluminous titansalite through to titaniferous augite).

Investigation of mineral-melt equilibria and the identification of discrete modes of mineral crystallization indicate that the suite has experienced a polybaric crystallization history. Supported by projection of whole rock and glass data in the pseudo-ternary system Diopside-

Olivine-Quartz (Walker et al., 1979), and melt inclusions in plagioclase megacrysts of porphyritic lavas, the postulated pre-eruption history begins at high pressure (>=10kb.), followed by magma ascent (with subsequent resorption and rapid crystal growth) and subsequent fractionation within the oceanic crust.

The inferred petrogenetic model can explain; (1) ranges in mineral chemistry and the origin of megacrysts of plagioclase, high-alumina spinel, olivine and clinopyroxene; (2) different extents of crystal fractionation at individual dredge sites; and (3) distinct geochemical characteristics of lavas from different dredge sites. The observed geochemical diversity indicates that the mantle source beneath this section of the SWIR is heterogeneous at the scale of individual dredges.

Evidence for lateral mantle heterogeneity is provided by between-ridge variations in incompatible inter-element ratios. Firstly, a subset of Dredge 5 lavas (Dredge site on Ridge A) are the least depleted basalts with the following characteristics; Zr/Nb=15-19, Y/Nb=4.1-4.5, Zr/Y=3.7-3.9. As a group, remaining Ridge A basalts have considerably lower Nb contents, with Zr/Nb=26-56, Y/Nb=8-16 and Zr/Y=3.1-3.8. Ridge B basalts are the most depleted with Zr/Nb=45-102, Y/Nb=12-34 and Zr/Y=3.0-3.9. It is suggested that this

relative westward enrichment is related to the influence of the Bouvet mantle plume although this requires detailed isotopic analysis.

****

CHAPTER 1

INTRODUCTION

1.1 General background and previous work

The 65 000 km long mid-ocean ridge system has been the primary focus of attention in studies of submarine basalt for the last 30 years because of the important concepts of sea floor spreading and plate tectonics. Ocean floor basalts represent the volumetrically most significant form of volcanism on earth; lavas are erupted and emplaced along the mid-ocean ridge in response to mantle upwelling and melting, generating new oceanic crust as the lithospheric plates move apart (Basaltic Volcanism Study Project, 1981). By implication, mid-ocean ridge basalt (MORB) should be progressively older away from spreading axes, a prediction confirmed by deep sea drilling results. The rates of spreading (or accretion of new oceanic crust) vary from over 8 cm/yr to less than 1 cm/yr (half spreading rates). Within this framework, global tectonics is described by the lithospheric motion of about 20 plates.

As a result of extensive studies of MORB the world over, two types of basalt with different isotopic and trace element characteristics have been identified. Basalts from topographically "normal" ridge segments have low large-ion

lithophile (LIL) element abundances and are depleted in light rare earth elements (LREE) relative to chondritic (primordial) meteorite compositions. These features and isotopic characteristics (e.g. low $^{87}Sr/^{86}Sr$ and high $^{143}Nd/^{144}Nd$ ratios) require that the mantle source from which MORB is derived has previously experienced a depletion event. Lead isotope systematics suggest that depleted mantle has persisted for at least the last 1.5-2.0 Ga. (Church and Tatsumoto, 1975).

In contrast to the above depleted (or N-type) MORB, ridge basalts from topographic highs and associated with oceanic islands (e.g. Iceland, Azores, Bouvet) have isotopic and trace element characteristics similar to ocean island basalts. These display LIL and LREE enrichment relative to chondritic abundances. This basalt type (enriched or E-type MORB) is more varied than N-type MORB and is often accompanied by transitional tholeiites (T-type MORB) and alkali basalts (e.g. Muir and Tilley, 1966; Aumento et al., 1971; Basaltic Volcanism Study Project, 1981). In terms of petrography, mineralogy and major element chemistry, E-type MORB are considered to be indistinguishable from N-types MORB (Basaltic Volcanism Study Project, 1981). However, N-type basalts show a greater tendency to selective plagioclase enrichment (Bryan, 1983) and pyroxene appears in relatively few basalts and typically at high degrees

Table 1: Summary of geochemical characteristics and proportions of N-type, T-type and P-type MORB from the American-Antarctic Ridge and the Southwest Indian Ridge. Data from Bouvet Island shown for comparison. (From Table 6 of le Roex et al., 1985)

	N-type	T-type	P-type	Bouvet
Southwest Indian Ridge				
Mg no.	67-52	64-44	65-40	43
Zr/Nb	17->64	7.7-11.8	5.8-6.8	6.4
Y/Nb	8->22	1.3-3.0	0.9-1.2	0.9
Zr/Y	1.8-3.6	3.3-7.1	6.1-7.9	7.5
$(La/Sm)_N$	0.5-1.0	1.2-2.0	2.1-26	2.0
$(La/Yb)_N$	0.3-1.1	1.7-4.3	4.8-69	6.8
$^{87}Sr/^{86}Sr$	0.70267-0.70297	0.70291-0.70370	0.70356-0.70364	0.70365-0.70376
$^{143}Nd/^{144}Nd$	0.51312-0.51302	0.51301-0.51284	0.51295-0.51286	0.51282-0.51285
% samples	~ 47	~ 47	6	
American-Antarctic Ridge				
Mg no.	69-35	64-53	61.8	
Zr/Nb	17-78	8.8-15.5	6.3	
Y/Nb	4.6-23	1.9-4.3	0.9	
Zr/Y	2.2-4.2	3.1-4.7	7.1	
$(La/Sm)_N$	0.6-1.0	1.1-1.5	2.4	
$(La/Yb)_N$	0.8-1.1	1.4-2.7	6.6	
$^{87}Sr/^{86}Sr$	0.70263-0.70295	0.70307-0.70334	0.70351	
$^{143}Nd/^{144}Nd$	0.51308-0.51303	0.51296-0.51288	0.51287	
% samples	~ 83	~ 15	~ 2	

fractional crystallization and/or partial melting (e.g. Basaltic Volcanism Study Project, 1981; le Roex and Dick, 1981; le Roex et al., 1982, 1983, 1985). For the most part, geochemical and mineralogical variations observed in MORB suites are quantitatively consistent with control by low pressure crystal fractionation.

It has previously been recognised that not all compositional variations attributed to fractional crystallization can be adequately described by quantitative modelling using observed phenocryst phases (e.g. Claque and Bunch, 1976; Bryan and Moore, 1977; Dungan et al., 1979; Walker et al., 1979; Basaltic Volcanism Study Project, 1981). Substantial amounts of clinopyroxene are often required to account quantitatively for geochemical variations where clinopyroxene is notably absent. The absence of clinopyroxene in the lavas has been attributed either to dissolution as a consequence of magma mixing involving primitive and evolved magmas (Dungan et al., 1978; Dungan and Rhodes, 1978; Rhodes et al., 1979) or clinopyroxene fractionation within the mantle at moderate to high pressure (Kushiro, 1973; Fujii and Kushiro, 1977; Bender et al., 1978; Presnall et al., 1978, 1979). Clinopyroxene may be lost due to gravitative settling and/or resorption as a result of re-equilibration upon magma ascent. Experimental observations are consistent with high pressure clinopyroxene fractionation (e.g. Bence et al., 1979) and low pressure

fractionation of clinopyroxene only at moderate to high degrees of differentiation (Grove and Bryan, 1983).

1.2 Geological setting and sampling

The Southwest Indian Ridge (SWIR), marking the present day spreading locus between the African and Antarctic plates, extends eastwards over 5 000 km from the Bouvet triple junction past the Prince Edward Islands to the Central Indian Ocean triple junction (Figure 1). Figure 1 depicts the regional setting of the SWIR, relative to the Bouvet triple junction, and the locations of successful rock dredges obtained under the auspices of SOLP. These cruises are tabulated in Table 2 which includes for the sake of completion the 1974 cruise-115 of the R/V Chain (Dickey et al., 1977).

The SWIR is an extremely slow-spreading ridge (<1cm/yr. half spreading rate; Sclater et al., 1976,1978), characterised toward the western end by several short ridge segments transected by long, transform faults. Between 16 and 26°E, the SWIR has a relatively simple and therefore unique morphology: two long ridge segments, each over 250 km. in length, are present, offset approximately 20 km. by a short transform fault at about 20°20'E. Figure 2 is a more detailed map illustrating the bathymetry of the ridge system between 16 and 26°E and the locations of dredges studied in this thesis.

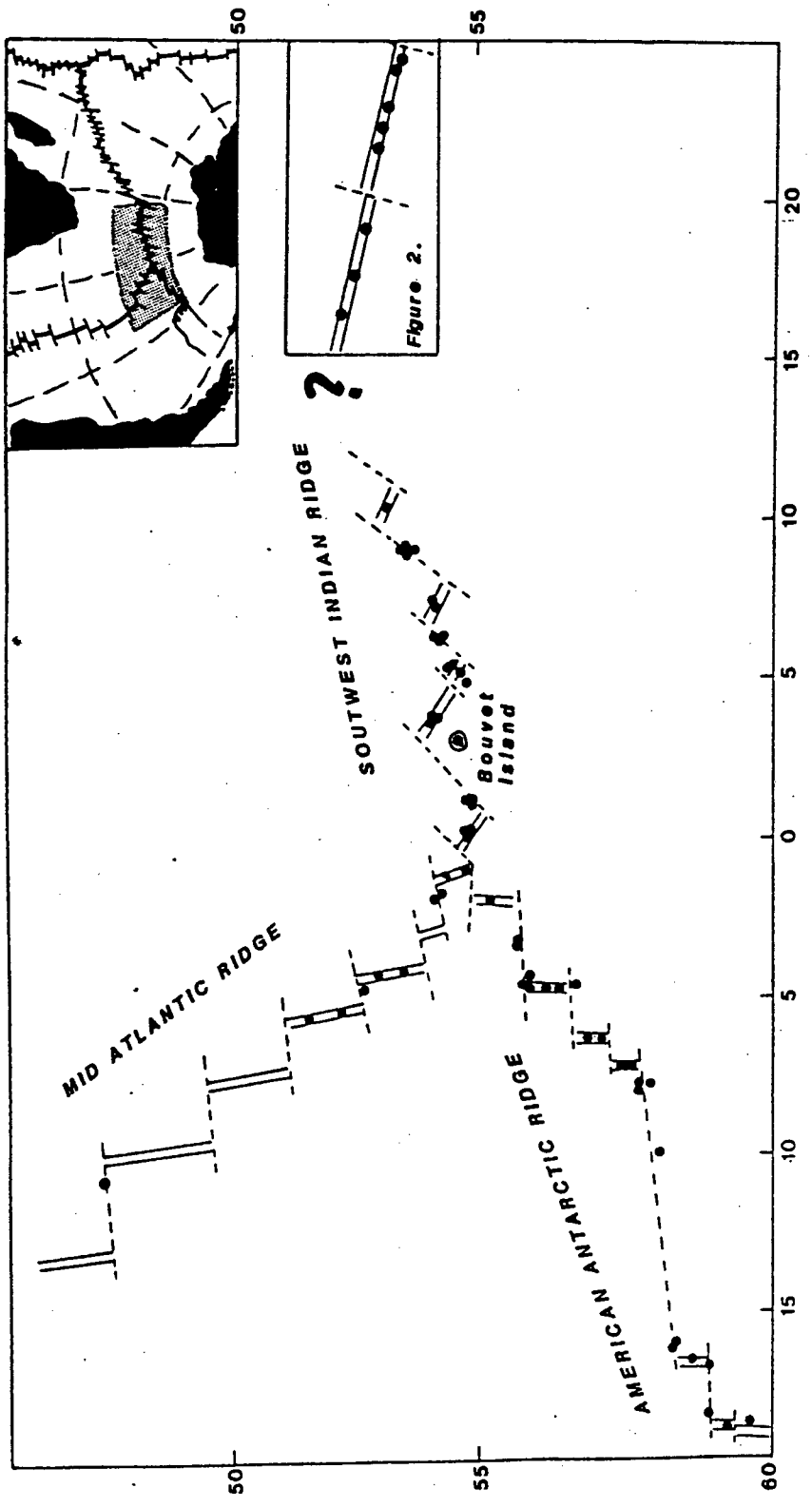

Figure 1: Sketch map of the Southern Ocean ridge system in the vicinity of Bouvet Triple Junction. Circles represent locations of dredge stations to date. Shaded portion depicts the study area of this thesis. Adapted from le Roex et al. (1983; 1985) The question mark indicates ridge morphology unresolved at time of publication.

CRUISE DESTINATION	SHIP	DATES
1. CHAIN 115; Bouvet Triple Junction (2°W-6°E)	R.V. Chain	Jan-Feb, 1974
2. ISLAS ORCADAS 11-76; AAR-SWIR (4°W-11°E)	R.V. Islas Orcadas	November, 1976
3. ATLANTIS II-107; SWIR (1°W-10°E)	R.V. Atlantis II	Mar-Apr, 1980
4. VULCAN LEG5; AAR (4°-18°W)	R.V. Melville	Dec '80-Jan '81
5. AGULHAS 22; SWIR (15°-25°E)	M.V. S.A. Agulhas	Oct-Nov, 1981
6. AGULHAS 32; M.A.R. (54°-47°S)	M.V. S.A. Agulhas	Sept-Oct, 1983

Table 2: Geophysical and dredging cruises performed in the Southern Ocean. Cruises 1 to 6 are sources of dredge localities in Figure 1. References: (1) Dickey et al., 1977; (2) le Roex, 1980; (3) le Roex et al., 1983; (4) le Roex et al, 1985; (5) le Roex, unpublished data; (6) le Roex et al., (1987). Abbreviations are : AAR = American-Antarctic Ridge, MAR = Mid-Atlantic Ridge, SWIR = Southwest Indian Ridge.

The two ridge segments (hereafter referred to as Ridge A and Ridge B, designating the western and eastern segments respectively) trend in a direction of 108°. Ridge A is at least 250km long and may continue further westward to coincide with the ridge segment at 52°S 15°E mapped by Norton (1976). Ridge B is about 300km long, transected at its eastern end by a transform fault known as the Du Toit Fracture Zone (Fisher et al., 1982).

The rift valley depression delineating the ridge segments is between 3500 and 4500 metres deep and flanking crestal mountains shoal to a depth of between 2000 and 2800 metres. The central valley is about 30km wide on average.

Dredges were conducted on the ridge axis once the central valley and its associated magnetic signature were clearly defined by bathymetric echosounding and magnetometer signals. Co-ordinates of locations were established by satellite navigation.

Eight out of fourteen dredge attempts were successful in recovering samples (see Table 3 for locations and contents) and preliminary hand specimen description and curation were completed on board ship. Sample numbers have the prefix AG22 followed by two numbers designating dredge station and sample number respectively (for example, sample number AG22-1-2 is sample 2 from Dredge 1).

1.3 The scope of this study

This thesis aims to document the compositional variation of the Agulhas 22 basalt suite. The objectives of the project are:

(1) To establish and document the within- and between-ridge variation in terms of petrography, phase chemistry and whole rock chemistry.

(2) To interpret compositional variations and discuss some of the probable physico-chemical controls on their origin.

1.4 Sample selection and analytical methods

Immediately following the cruise, major element analyses of natural glasses from eruptive surfaces of 68 pillow basalts were obtained by Dr A.P. le Roex and M.L. Otter. Samples were analysed by electron microprobe with a defocussed electron beam (~30 microns diameter), 15 kV accelerating voltage and 1500 nanoamperes beam current on a Cambridge Microscan Model 5 microanalyser. On line reduction followed the method of Bence and Albee (1968) using correction factors of Albee and Ray (1970).

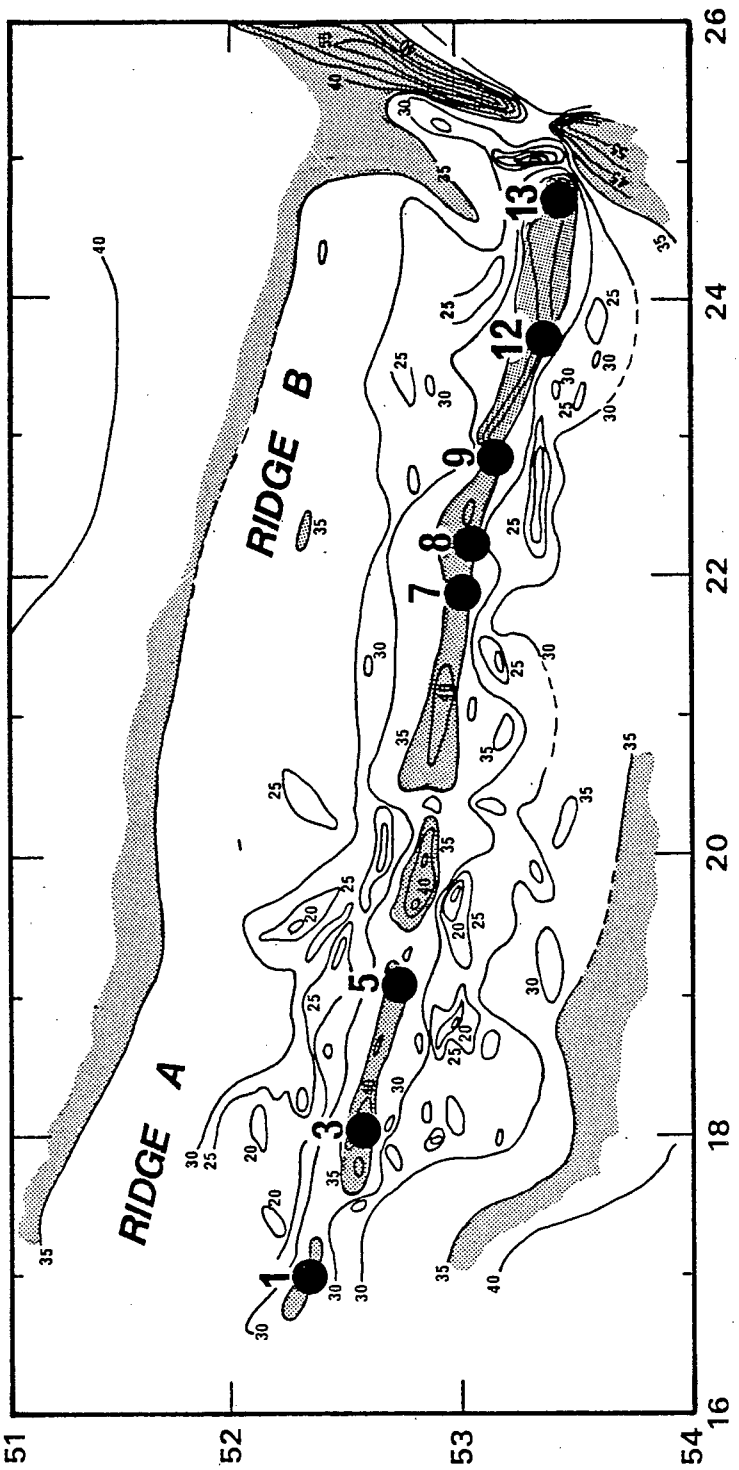

Figure 2: Detailed bathymetry of the SWIR between 16 and 26°E. Solid dots represent successful dredge hauls. Adapted from an unpublished map by Dr. H. Bergh; ships tracks omitted for clarity.

Table 3: Locations and contents of successful dredge hauls obtained on cruise 22 of the S.A. Agulhas

DREDGE NO.	LOCATION	(DEPTH)	DESCRIPTION
	15-20°E: Ridge A		
1	52°17'S/16°54'E Median valley north wall	(3700 m)	32(11.8 kg) fresh aphyric pillow basalt fragments.
3	57°36.5S/18°02.4'E Median valley, bottom of south wall.	(4200 m)	30 (10.1 kg) lightly weathered aphyric pillow basalt fragments. 5 fragments of moderately weathered plagioclase porphyritic basalt. Plus 110 kg. small uncut samples.
5	54°15.6'S/19°05.8'E Median valley, south wall	(3500-3700 m)	80 (59 kg) lightly plagioclase porphyritic and olivine-plagioclase porphyritic pillow basalt fragments. 1 (4 kg) lightly weathered sparsely plagioclase porphyritic diabase fragment. 5 (4.1 kg) sparsely plagioclase porphyritic vesicular pillow basalt fragments. Plus 80 kg small uncut samples.
	20-25°E: Ridge B		
7	53°01.4'S/21°50'E Median valley, south wall.	(3300 m)	2 (1 kg) moderately weathered aphyric basalt fragments.
8	53°06.3'S/22°11.8'E Median valley, south wall.	(3690 m)	15 (17 kg) lightly weathered sparsely plagioclase porphyritic pillow basalt fragments. 9 (9 kg) plagioclase porphyritic (10-20% plagioclase) pillow basalt fragments. Plus 25 kg unsampled fragments.
9	53°09.5'S/22°19.8'E Median valley, south wall.	(3850 m)	5 (6 kg) lightly weathered aphyric pillow basalt fragments.
12	53°23.6'S/23°11.5'E Median valley, south wall.	(3650 m)	19 (24 kg) moderate to lightly weathered plagioclase (10-40%)-olivine (0-1%) porphyritic pillow basalt fragments. 15 (6.8kg) moderate to lightly weathered moderately plagioclase (3-10%) porphyritic pillow basalt fragments. 35 (8.5 kg) lightly weathered aphyric pillow basalt fragments. 2 (5.5 kg) lightly weathered dia-base fragments. 1 (0.2 kg) pumice bomb. Plus 85kg small uncut samples.
13	53°21.5'S/24°45.5'E Median valley, south wall.	(3850 m)	36 (27 kg) lightly weathered aphyric and sparsely plagioclase porphyritic pillow basalt fragments. Plus 80 kg small uncut, glassy pillow basalt fragments.

Glass and petrographic data were combined to select samples for whole rock X-ray fluorescence (XRF) analysis. To aid sample selection of aphyric lavas, preliminary XRF analyses for Ni, Zr, Nb, Y, Rb and Sr were made on 23mm diameter discs cut from aphyric rock slabs, 0.5 to 1.0cm thick. To minimize effects of particle size and phenocryst distribution on absolute compositions, samples were selected for detailed preparation and were chosen on the basis of Zr/Nb, Zr/Y and Y/Nb ratios (known to be indicators of magma types and/or source region characteristics, e.g. Schilling et al., 1983; Erlank and Kable, 1976; le Roex et al., 1983) as well as Ni/Zr ratios (an indicator of degree of differentiation).

Major elements, with the exception of Na, were analysed on discs prepared by the lithium tetraborate fusion method of Norrish and Hutton (1969). Trace elements and Na were analysed by XRF on pressed powder briquettes, prepared using the method of Baird (1961). Major elements, Ba and Sc were analysed by a Siemens SRS-1 X-ray spectrometer and remaining trace elements were analysed on a Phillips PW1400 XRF spectrometer. Routine operating conditions are given by Duncan et al. (1984).

The whole rock XRF data, 34 selected polished sections and the entire Agulhas 22 basalt collection (~300 samples) were made available to the author at the beginning of this project. An extensive petrographic study was carried out

which, together with the XRF data, served to identify within-dredge variation in terms of distinct petrographic and/or chemical basalt groups (lithologies), from which samples were selected for detailed petrographic and phase-chemistry investigation.

Electron microprobe analyses obtained by the author were made with a Cameca Camebax electron microprobe with an on-line data reduction program using a ZAF correction procedure. Operating conditions routinely employed were 15kV accelerating voltage and 40nA beam current. Ten second counting times were routinely used and a focussed beam with a diameter of 2 microns was used for the majority of analyses. For analysing feldspars the beam was defocussed (10-20 microns diameter) and for natural glasses, an even larger spot size (20-50 microns diameter) was used. To improve Ni determinations in olivine, an accelerating voltage of 25kV and 50 second counting time were used. Details of standards, counting errors and a full analysis directory are given in Appendix 1.

****

CHAPTER 2

PETROGRAPHY

2.1 General Introduction

The Agulhas 22 basalt suite consists largely of subangular rock fragments with glassy margins (70% of recovered samples have a glassy surface). Glass is commonly restricted to a single rounded surface which may show flow structures (e.g. sample AG22-13-36 resembles a ropey or pahoehoe lava). On this basis, the sample suite is considered to be dominantly extrusive, samples being either pillow basalt fragments or pieces of submarine sheet flows (Ballard et al., 1979; Natland, 1980).

Basalts are classified according to the scheme of Bryan (1983), a classification based on the presence of crystalline phases recognisable in samples. For example, an olivine basalt is one in which olivine is the only silicate phenocryst phase present. The petrographic groupings, consistent with phase equilibrium experiments on oceanic basalts are:

olivine basalts (± spinel)

olivine-plagioclase basalts

olivine-plagioclase-pyroxene basalts

Definitions of types of crystals as "microlites", "microphenocrysts" and "phenocrysts" follow the nomenclature of Bryan (1979) with the term "megacryst" used in preference to "xenocryst" since it is non-genetic. Note that grain size alone is not necessarily distinctive and a combination of physical properties (Table 4) are used as criteria for classification.

Nomenclature and textural terms are adopted from the Basaltic Volcanism Study Project, (1981) and McKenzie et al. (1981) and closely follow the Deep Sea Drilling Project (DSDP) convention. Crystal morphologies are described using the terminology of Bryan (1972), Lofgren (1974) and Donaldson (1976). Textural variations observed are typical of ocean floor basalts described elsewhere (e.g. Bryan, 1972, 1983; Natland, 1978, 1980; Kirkpatrick, 1979; Basaltic Volcanism Study Project, 1981).

With increasing distance away from the glassy surface, groundmass textures vary from totally glassy (holohyaline) through to holocrystalline. This gradational variation, typically present in all samples has two important consequences: firstly, glass selvedges provide an easy and efficient method of basalt classification and secondly, coarse-grained interiors may be petrographically indistinct from intrusive basalts. In this respect, samples originally classified as diabase (or dolerite, ie. of intrusive origin;

Table 4: Characteristics of different crystal types observed in oceanic pillow basalts, according to Bryan (1979)

Crystal type	Typical size	Characteristics
Megacryst	>0.5mm	Large, subhedral to anhedral, commonly showing evidence of corrosion and/or reverse zoning.
Phenocryst	≥0.5mm	Generally smaller than megacrysts, subhedral to euhedral; little or no evidence of corrosion.
Microphenocryst	<0.5mm	Generally smaller than phenocrysts of the same phase, euhedral with a tendancy toward skeletal forms.
Microlite	<250um	Generally smaller than microphenocrysts of the same phase, commonly tiny skeletal crytals. e.g. "Belt buckle"-plagioclase and "lantern" - olivine (Bryan, 1972).

shipboard classification) could represent interiors of sheet flows although diabase textures are generally more interlocking and medium to coarse grained relative to flow interiors. In view of similar mineral and whole rock chemistry this distinction is carried no further except in descriptive terms.

Textural variations within pillow basalts allow the recognition of three broad textural zones with gradational boundaries (Bryan, 1972). From the glassy margin inward these are:

(i) A glassy zone (Zone 1 of Bryan, 1972) generally less than 1cm wide, either completely glassy or vitrophyric. Olivine and/or plagioclase generally occur as microphenocrysts in this zone. Skeletal (dendritic) and acicular microlites of these phases may be present, generally increasing in abundance toward zone 2.

(ii) A spherulitic or variolitic zone (zone 2) is characterised by a dense intergrowth of spherulites, generally 3 to 4cm thick. Spherulites are brown in colour and increase in diameter away from the glassy zone. At the interface between zones 1 and 2, spherulites appear fuzzy and indistinct with acicular crystallites radiating from a common nucleus which may be distinguishable microphenocrysts or microlites of olivine and plagioclase. Further inward, spherulites adopt a sheaf or bow-tie morphology in which acicular intergrowths of plagioclase and clinopyroxene are recognisable. Intergrowths occur in fan-shaped to axiolitic morphology (Lofgren, 1974); plumose and reticulate intergrowths (Bryan, 1972) are common in these

paragenetically late crystallization products (see frontispiece). Titanomagnetite, and rarely ilmenite, occur as skeletal to anhedral grains in this zone.

(iii) A holocrystalline (interior) zone (zone 3) is marked by a general uniformity in groundmass texture. Bow-tie spherulites typically give way to recognisable microlitic plagioclase with interstitial, coarser grained, plagioclase-pyroxene fan-shaped intergrowths. In more slowly cooled portions, pyroxene may be granular and an ophitic or subophitic texture may predominate. Generally, the texture is intersertal, groundmass textures exhibiting an open bow-tie habit.

In addition to the within-sample textural variation described above, a gradational, between-sample, variation is also present. More specifically, aphyric basalts exhibit a regular texture (spherulitic to fan-spherulitic) whereas porphyritic basalts typically are hyalo-ophitic (or hyalopilitic) to intersertal.

Factors known to affect texture include dimensions and morphology of eruptive units, nucleation and cooling rates, nucleation density, flow and settling rates of crystals, and intrinsic variables such as viscosity and composition (Basaltic Volcanism Study Project, 1981). The three

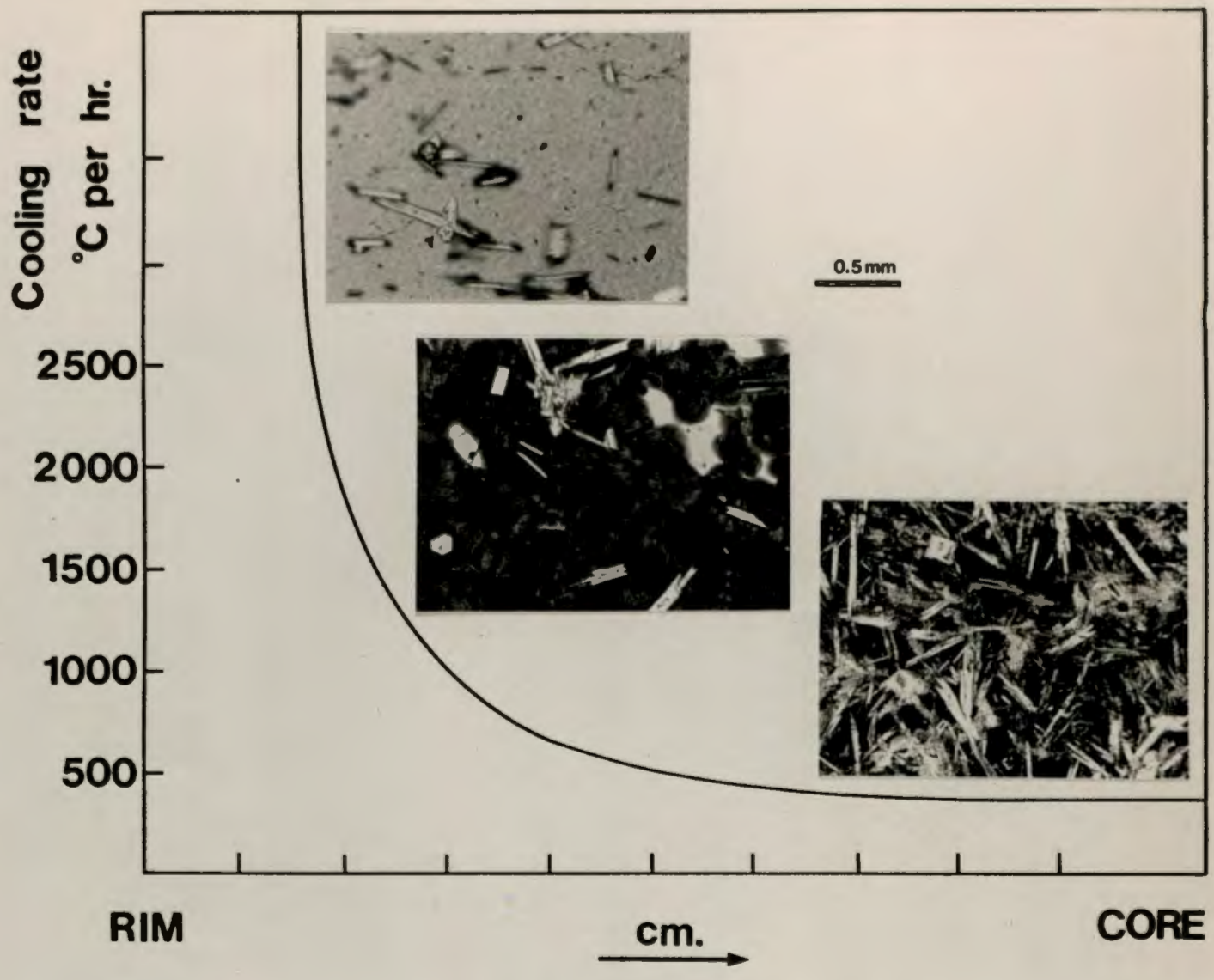

Figure 3 Textural variation in a pillow basalt as a function of cooling rate. Curve depicts the instantaneous cross-sectional cooling rate profile as a function of radial position for a spherical magma body (25 cm. diameter) at the 1000°C isotherm (cooled from 1140°C, surface temperature of 0°C and assuming a thermal diffusivity of 0.01 $cm.^2$/second; after Schiffman and Lofgren, 1982; based on conductive cooling model of Jaeger, 1967). Note that core cooling rates are always in excess of 200°C/hr.; they would be even higher for smaller pillows. Photomicrographs of olivine-plagioclase basalt AG22-1-13: (a) glassy zone, (b) spherulitic zone (1 cm. from cut surface) and (c) interior zone (4 cm. from cut surface).

textural zones described above occur as a function of decreasing cooling rate experienced by basalt magma with increased distance from the eruptive surface (e.g. Muir and Tilley, 1966; Bryan, 1972; Brandeis et al., 1984). Figure 3 is a schematic diagram illustrating the undercooling (or quenching) as a function of distance from the surface of a spherical body (e.g. an individual pillow). The term undercooling is defined as the negative temperature differential, $-\Delta T$, between the equilibrium liquidus temperature and the actual temperature at which crystallization occurs. Hence, extreme values of $-\Delta T$ $_{arrest}$ crystallization (the melt becomes a glass) while low $-\Delta T$ permits crystallization to proceed more normally. In this respect, samples have been compared by studying equivalent positions in textural zones in each of the chosen fragments (cf. Photomicrographs, Figure 3).

2.2 Petrography of Individual Dredge Hauls

In this section, detailed petrographic descriptions of selected samples together with mineral compositions are presented for individual dredge locations. Table 5 summarizes the petrographic characteristics of 34 studied samples.

2.2.1 Ridge A; Dredge 1

Samples are fresh, glass encrusted pillow basalt or lava

SAMPLE NUMBER	HAND SPECIMEN DESCRIPTION LITHOLOGY	(GRAIN SIZE)	WEATHERING	GLASS	THIN SECTION CHARACTERISTICS PHENOCRYSTS OLIVINE	PLAGIOCLASE	SPINEL	CPX	MICROPHENOCRYSTS OLIVINE	PLAGIOCLASE	SPINEL	MATRIX (+GLASS)	ACCESSORY OPAQUES Fe-Ti OXIDES	SULPHIDES	SECONDARY PHASES	VESICLES	TEXTURE OF GROUNDMASS	CLASSIFICATION AFTER BRYAN(1983)
AG22-1-1	APHYRIC	(A)	L	✓	-	-	-	-	3%	1%	tr	96%	Mt	Py,Po	Li	tr	FAN SPHERULITIC	OL-PLAG BASALT
AG22-1-4	APHYRIC	(A)	L	✓	-	-	-	-	5%	10%	tr	85%	Mt	Py,Po	Li	tr	FAN SPHERULITIC	OL-PLAG BASALT
AG22-1-13	APHYRIC	(A)	L	✓	-	-	-	-	5%	10%	tr	85%	Mt	Py,Po	Li	tr	FAN SPHERULITIC	OL-PLAG BASALT
AG22-3-2	APHYRIC	(A)	L	✓	-	-	-	-	5%	-	-	95%	Mt	Py,Po	Pa,Sm,Li	tr	FAN SPHERULITIC	OL BASALT
AG22-3-4	APHYRIC	(A)	L	✓	-	-	-	-	5%	-	tr	95%	Mt	Py,Po	Sm,Li	tr	FAN SPHERULITIC	OL BASALT
AG22-3-6	APHYRIC	(A)	L	✓	-	-	-	-	5%	-	-	95%	Mt	Py,Po	Sm,Li	tr	FAN SPHERULITIC	OL BASALT
AG22-3-8	APHYRIC	(A)	L	✓	-	-	-	-	5%	-	-	95%	Mt	Py,Po	Sm,Li	tr	INTERSERTAL	OL BASALT
AG22-3-20	APHYRIC	(F)	L	-	-	<1%	-	-	5%	50%	tr	45%	Mt,Ilm	Py,Po,Cp	Sm,Li	tr	INTERGRANULAR	OL-PLAG BASALT
AG22-3-23	APHYRIC	(A)	L/M	-	-	-	-	-	5%	-	-	95%	Mt	Py,Po	Sm,Li,Chl	tr	FAN SPHERULITIC	OL BASALT
AG22-3-29	APHYRIC	(A)	M/H	-	-	-	-	-	5%	-	-	95%	Mt	Py,Po	Sm,Li	tr	VARIOLITIC	OL BASALT
AG22-3-34	APHYRIC	(M)	M	-	-	<1%	-	-	5%	50%	-	45%	Mt,Ilm	Py,Po,Cp	Sm,Li	tr	INTERGRANULAR	OL-PLAG BASALT
AG22-5-8	APHYRIC	(A)	L/M	✓	-	-	-	-	4%	-	tr	96%	Mt	Py,Po,Cp,Pn	Sm,Li	tr	FAN SPHERULITIC	OL BASALT
AG22-5-9	APHYRIC	(A)	M	✓	<1%	-	-	-	4%	-	-	96%	Mt	Py,Po,Cp,Pn	Sm,Li	tr	VARIOLITIC	OL BASALT
AG22-5-10	APHYRIC	(A)	L	✓	-	-	-	-	4%	-	-	96%	Mt	Py,Po	Sm,Li	tr	FAN SPHERULITIC	OL BASALT
AG22-5-14	APHYRIC	(A)	L	✓	-	<1%	-	-	5%	1%		94%	Mt	Py,Po	Sm,Li	<1%	INTERSERTAL	OL-PLAG BASALT
AG22-7-1	APHYRIC	(A)	L	✓	-	-	-	-	5%	2%	1%	92%	Mt	Py,Po	Li	tr	FAN SPHERULITIC	OL-PLAG BASALT
AG22-8-1	S.P.	(A)	L	-	-	3%	-	-	5%	15%	-	50%	Mt	Py,Po	Sm,Li	tr	INTERSERTAL	OL-PLAG BASALT
AG22-8-2	S.P.	(A)	L	-	-	3%	-	-	5%	15%	-	40%	Mt,Ilm	Py,Po,Cp	Sm,Li	tr	INTERGRANULAR	OL-PLAG BASALT
AG22-8-9	S.P.	(A)	L	✓	-	3%	-	-	5%	55%	-	50%	Mt	Py	Sm,Li	tr	INTERSERTAL	OL-PLAG BASALT
AG22-8-11	S.P.	(A)	L	✓	-	2%	-	-	5%	45%	-	50%	Mt	Py,Po,Cp	Sm,Li	<2%		OL-PLAG BASALT
AG22-8-15	S.P.	(A)	L	✓	-	1%	-	-	5%	45%	-	50%	Mt	Py	Sm,Li	<2%	TO	OL-PLAG BASALT
AG22-8-16	PORPHYRITIC	(A)	L	✓	<1%	7%	tr*	-	5%	7%	-	80%	Mt	Py	Sm,Li	tr		OL-PLAG BASALT
AG22-8-19	PORPHYRITIC	(A)	L	✓	1%	7%	tr	-	5%	7%	-	80%	Mt	Py,Po	Sm,Li	tr	HYALOPILITIC	OL-PLAG BASALT
AG22-8-24	PORPHYRITIC	(A)	L	✓	1%	20%	tr	-	5%	20%	-	55%	Mt	Py,Po,Cp	Sm,Li	tr		OL-PLAG BASALT
AG22-9-1	APHYRIC	(A)	L/M	✓	-	-	-	-	7%	8%	<1%	85%	Mt	Py	Li	tr	INTERSERTAL	OL-PLAG BASALT
AG22-9-2	APHYRIC	(A)	L/M	-	-	-	-	-	7%	8%	<1%	85%	Mt	Py	Li	tr	INTERSERTAL	OL-PLAG BASALT
AG22-12-1	PORPHYRITIC	(A)	L/M	✓	1%	40%	tr	tr	5%	10%	-	45%	Mt	Py	Li	tr	INTERSERTAL	OL-PLAG-CPX BASALT
AG22-12-4	PORPHYRITIC	(A)	L/M	✓	1%	30%	tr	-	5%	10%	-	45%	Mt	Py,Po	Li	tr	TO	OL-PLAG BASALT
AG22-12-20	PORPHYRITIC	(A)	L/M	✓	1%	10%	tr	-	10%	15%	-	65%	Mt	Py,Po	Li	tr	HYALOPILITIC	OL-PLAG BASALT
AG22-12-35	APHYRIC	(A)	L	✓	-	-	-	-	5%	-	tr	95%	Mt	Py	-	tr	FIN DENDRIC	OL BASALT
AG22-13-1	APHYRIC	(A)	L	✓	-	-	-	-	2%	-	-	98%	Mt	Py	Li	tr	FAN SPHERULITIC	OL BASALT
AG22-13-14	APHYRIC	(A)	L	✓	-	-	-	-	5%	-	-	80%	Mt	Py,Po	Li	1%	INTERSERTAL	OL-PLAG BASALT
AG22-13-25	APHYRIC	(A)	L	✓	-	-	-	-	2%	-	-	98%	Mt	Py	Li	tr	FAN SPHERULITIC	OL BASALT
AG22-13-32	APHYRIC	(A)	L	✓	-	-	-	-	2%	-	-	98%	Mt	Py	Li	tr	FAN SPHERULITIC	OL BASALT

LITHOLOGY
SP = sparsely porphyritic
A = aphanitic
F = fine grained
M = medium grained

WEATHERING
L = light discolouring at edges
M = moderately discoloured
H = highly discoloured

MINERALS
CPX = clinopyroxene
* = includes high-alumina spinel megacryst.

MODES
tr = trace

OPAQUE PHASES
Mt = titanomagnetite
Ilm = ilmenite
Py = pyrite
Po = pyrrhotite
Cp = chalcopyrite
Pn = pentlandite

SECONDARY PHASES
Li = limonite+hydroxides
Sm = smectite clays
Pa = palagonite
Chl = chlorite

CLASSIFICATION SCHEME
OL = olivine
PLAG = plagioclase
CPX = clinopyroxene

Table 5: Petrographic characteristics of 34 selected basalts of the Agulhas 22 basalt suite, modes estimated visually

fragments. All fragments are very fine grained (aphanitic) and aphyric. Samples selected for detailed study (AG22-1-1, AG22-1-4; AG22-1-13) have microphenocrysts of olivine and plagioclase (size 0.2mm) plus spinel set in an arborescent hypocrystalline matrix. Euhedral olivine (Fo_{85-87}) and plagioclase (An_{67-74}) are closely associated, commonly forming glomeroporphyritic clusters up to 3mm in size. Chrome-spinel microphenocrysts (average size, 20 microns) occur as inclusions in olivine as well as discreet crystals in the matrix. The matrix comprises interlocking plagioclase and pyroxene and interstitial skeletal titanomagnetite (<2 microns in size) as well as subordinate sulphide (pyrite and pyrrhotite) spherules and blebs (2-5 microns).* Several vesicles in glassy zones are adorned with sulphide spherules (Plate 1). Minor limonite staining occurs in the matrix; other secondary phases are absent.

2.2.2 Ridge A; Dredge 3

Dredge 3 recovered variably altered angular to subangular basalt fragments, relatively few of which have quench glass. Fragments are mostly aphanitic and despite the rare occurrence of plagioclase phenocrysts (<2mm in length), all are classified as aphyric. Several samples are fine to

*Interstitial opaque phases (Fe-Ti oxides, sulphides) occur in most samples from 5 microns size down to the limit of visibility in the microscope. They are not discussed further here; see Table 5 for details.

medium grained and were initially designated (shipboard classification) as diabase (or dolerite). Many samples (especially the coarser samples) are fairly extensively altered with secondary chlorite replacing groundmass minerals and showing up as distinct colour banding on fracture surfaces. The green discoloration penetrates 2 to 5cm into the samples, leaving cores grey in colour and presumably relatively unaltered.

Detailed investigation of eight samples (Table 5) shows that they are olivine basalts with well developed quench textures. Microphenocrysts (average size 0.25mm) of olivine (Fo_{83-85}) occur in a hyalocrystalline matrix with rare red-brown chrome spinel octahedra. Plagioclase microlites are absent from quench glass and rare laths (An_{62-66}) occur intergrown with olivine microlites elsewhere in the samples. Dendritic to euhedral olivine crystallites (Fo_{80-82}) are common in the quench glass and in coarser textural zones where they occur intergrown with more sodic plagioclase microlites (An_{58-62}).

Secondary phases include green to yellow smectites which commonly line vesicles walls and replace ferromagnesian groundmass phases (Plate 1). Quench glasses are also visibly discoloured and altered. Fresh glass is typically clear yellow-brown (e.g. AG22-3-6) while altered glasses

PLATE 1.

A. Fresh, quench glass with sparse plagioclase spherulites and dendritic (spinifex) olivine. Sample AG22-3-6.

B. Altered glass (palagonite), Sample AG22-3-2. Note fringes of palagonite bordering perlitic cracks.

C. Decorated vesicle and olivine microlite (to left) with dendritic overgrowth.Sulphide spherules (specks adhering to vesicle walls) are too small to analyse by microprobe. Sample AG22-12-4.

D. Altered 'lantern-and-chain' olivine microlites in a cryptocrystalline groundmass; variolitic basalt AG22-3-29.

E. Olivine basalt with spherulitic texture and segregation vesicles. Note how several vesicles are further lined with smectite (green to orange clays) and/or Fe-Mn hydroxides. Note also the olivine microphenocrysts and how they border vesicles. Sample AG22-3-23.

F. Spherulites in Textural Zone 2, sample AG22-5-10. Note the arrangement of olivine microphenocrysts in a semi-circular crystal-ring structure.

G. Plagioclase megacryst in sample AG22-3-34 with fringe of skeletal quench plagioclase. Numbers indicate compositions in Mole % anorthite. Compare with detail in Figure H.

H. Same megacryst as in G, under crossed nicols. Note the zoning pattern; anhedral, calcic core with oscillatory zoned mantle region. Mantle begins with inclusion-rich zone and is reverse zoned. See how the crystal outline truncates the zoning pattern, providing evidence for resorption.

PLATE 1

A

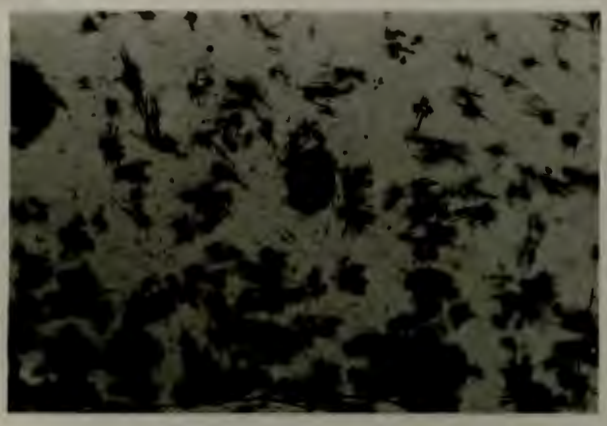

1.0 mm

B

0.85 mm

C

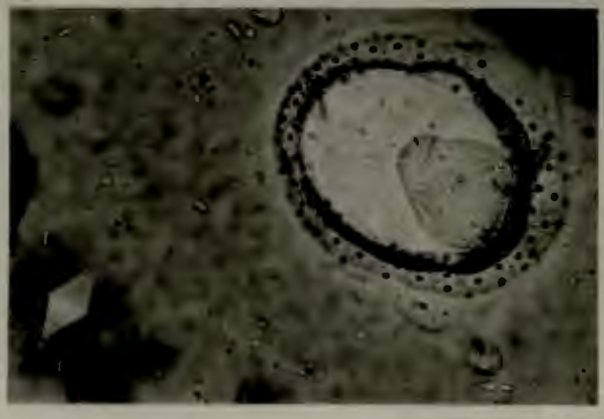

0.1 mm

D

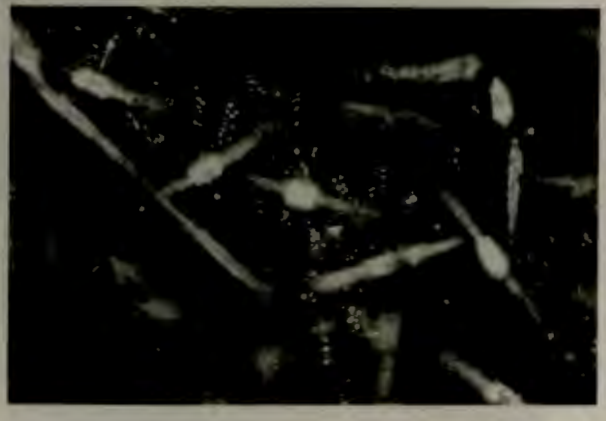

0.13 mm

E

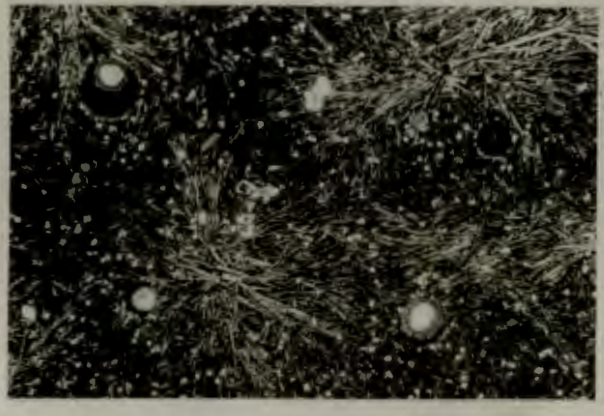

2.5 mm

F

0.85 mm

G

1.3 mm

H

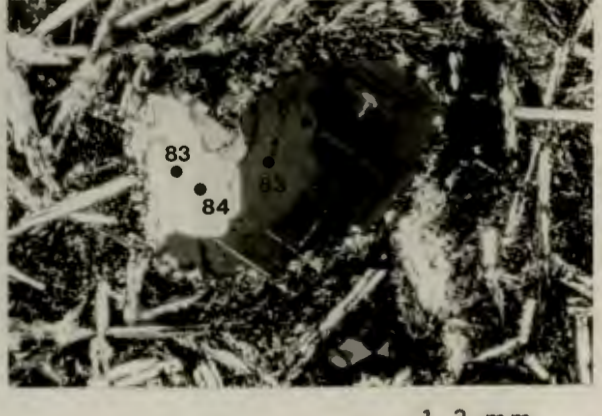

1.3 mm

range from dusty olive-brown (AG22-3-8) to dull orange-brown (e.g. AG22-3-2). In sample AG22-3-2, glass is altered to a murky amorphous palagonite and further to an anisotropic fibrous palagonite along perlitic fractures (Plate 1).

Several samples, particularly AG22-3-23 and AG22-3-29, are extensively altered and have vesicles which are filled to various extents with dark microcrystalline mesostasis. Such segregation vesicles (0.5-1.0mm diameter) have been described by several authors (e.g. Smith 1967; Jones, 1969; Bideau et al., 1977; Sato, 1978; Shibata et al., 1979; Walker et al., 1980; Bideau and Hekinian, 1984). Secondary infilling may occur in the form of yellow to orange smectites and/or brown botryoidal ferromanganese phase(s) (e.g. Plate 1).

Surrounding many vesicles in several samples (e.g. AG22-3-23) are many olivine microlites arranged in circular ring-structures generally only one crystal wide. Sample AG22-3-29 shows a classic variolitic texture with plagioclase spherulites surrounded by dark red-brown haloes of secondary oxide phases. Spectacular skeletal "lantern chain" olivine microlites are also altered (Plate 1).

Coarse grained samples (AG22-3-20, AG22-3-34) have euhedral olivine (Fo_{79-83}) microphenocrysts commonly intergrown with

plagioclase (An_{63-68}) and set in an intergranular matrix of skeletal plagioclase (An_{54-64}) and granular to skeletal pyroxene of varied composition (Wo_{39-49}, En_{34-44}, Fs_{13-24}). Interstitial titanomagnetite and ilmenite form subhedral grains up to 200 microns in size. Sulphides are pyrite and pyrrhotite (up to 10 microns) and rare pyrrhotite spherules contain tiny flecks of chalcopyrite.

Sample AG22-3-34 contains a rounded plagioclase glomerocryst comprising at least two megacrysts less than 1mm in size each. Crystals are normally zoned (An_{84} -An_{81}) with skeletal overgrowths of a more sodic composition (An_{66-65}) similar to groundmass or microphenocryst plagioclase. The external form of these crystals transects the zoning pattern suggesting that the megacryst has suffered resorption (Plate 1).

2.2.3 Ridge A; Dredge 5

The basalts from Dredge 5 include variably altered glass bearing pillow basalt, glass free massive basalt and several vesicular basalt fragments (30% vesicles by volume). The vesicular basalts (5 samples) were not studied in detail. Samples are aphanitic and in spite of rare olivine and/or plagioclase phenocrysts (typically 1 to 3 per 20 cm. diameter sample where present, 1-3mm in size) they are classified as aphyric. Although glass is normally fresh, samples are typically

discoloured with green-brown colour banding. Sample AG22-5-9 has a clayey surface beneath which a distinct variolitic texture is evident.

Thin sections were made of 4 samples, three of which are olivine basalts (AG22-5-8, AG22-5-9, AG22-5-10) and the fourth, an olivine-plagioclase basalt (AG22-5-14). The olivine basalts are olivine microporphyritic with skeletal to euhedral olivine (Fo_{84-86}) and quench microlites (Fo_{81}) set in a hyalocrystalline matrix. Rare red-brown euhedral spinels occur and skeletal groundmass plagioclase (<0.2mm long) is characteristically acicular (An_{68-70}). A single plagioclase megacryst (1mm in length) in sample AG22-5-8 is normally zoned (An_{84-81}) with a rounded morphology. In sample AG22-5-9, 1 to 5mm large olivine phenocrysts (Fo_{88}) are normally zoned to compositions of the microphenocrysts (Fo_{85}). In addition to typical sulphide phases, pyrrhotite spherules (AG22-5-8) may also contain a highly reflective phase,probably pentlandite (eg. Czamanske and Moore, 1977).

The olivine-plagioclase basalt (AG22-5-14) has a similar texture to olivine basalts but olivine microlites are rare. Olivine (Fo_{83}) and plagioclase (An_{61-64}) microphenocrysts are set in an arborescent, hyalocrystalline matrix.

An interesting petrographic feature occurs in the olivine basalts of Dredge 5 (e.g. AG22-5-10, see Plate 1). These

are semi-circular rings of microphenocrysts, 1 to 2mm in diameter, having the same groundmass material within and without; i.e. they are not nucleated around vesicles as in sample AG22-3-23, for example. These structures are associated with plagioclase spherulites which are typically orientated in trains parallel to the quench glass surface. In a detailed investigation of similar structures in pillow basalts from the Oceanographer Fracture Zone on the Mid-Atlantic Ridge at 35°N, Walker et al. (1980) identified "crystal-ring microstructures", typically only one crystal wide with equant microphenocrysts orientated such that the smooth crystal faces are presented toward the inner perimeter of the structure. Walker et al. (1980) suggest that "mechanical disruption of the partially solidified inner surface of the pillow lava skin produces a dispersion of cool globules in the pillow interior" and crystals adhere to these "tacky" globules to form the crystal-ring structures. The apparent association between crystal ring structures and spherulites suggest that spherulites act as "globules" to which crystals become attached.

2.2.4 Ridge B; Dredge 7

The two samples recovered in this dredge are fragments of glass-encrusted microporphyritic basalt. Detailed investigation of sample AG22-7-1 shows olivine (Fo_{87-86}) and plagioclase (An_{66-68}) microphenocrysts (0.3mm average size)

set in a hyalocrystalline matrix. Chrome spinel occurs poikilitically enclosed within olivine and free in the matrix. Olivine and plagioclase occur in glomeroporphyritic clusters in both bowtie fashion and with plagioclase often poikilitically enclosed in subhedral olivine. Quench microlites (0.05mm) of olivine (skeletal to euhedral) are present.

2.2.5 Ridge B; Dredge 8

Basalts recovered at this station include two broad groups: sparsely plagioclase porphyritic ($\leq$ 2% phenocrysts) samples and olivine-plagioclase porphyritic (10-20% phenocrysts, <1% olivine) fragments. Two thirds of all samples have quench glass and samples are only lightly weathered with minor ferromanganese coating on surfaces. Five sparsely porphyritic samples (Table 5) and three porphyritic samples were studied in detail.

All samples are olivine-plagioclase basalts with olivine (Fo_{84-81}) and plagioclase microphenocrysts (average size 0.3mm) set in a groundmass ranging from hyaline to holocrystalline. Chrome spinel$\pm$ is present in two samples (AG22-8-11 and AG22-8-16) as discrete "free floating" microphenocrysts in the matrix. Generally, microphenocryst contents correlate with phenocryst/megacryst content: a higher proportion is present in porphyritic basalts than in

sparsely porphyritic basalts. Phenocrysts recognised in hand specimens are divided into megacrysts and phenocrysts on the basis of crystal morphologies and zoning patterns.

For example, olivine phenocrysts (Fo_{86}) are present in samples AG22-8-16 and AG22-8-24. Crystals are rounded in form, compositionally homogeneous, and occur in plagioclase-olivine glomerocrysts (e.g. AG22-8-24) and/or as discrete crystals ($\leq$ 1mm in size). Discrete phenocrysts occasionally show evidence of cuspate anhedral outlines indicating a history of resorption (Thornber and Huebner, 1985).

Plagioclase crystals are divided into phenocrysts and megacrysts, the latter being further subdivided into two distinct types. Phenocrysts are tabular (aspect ratio, or length to width ratio $\geq$ 4), subhedral to euhedral crystals typically 1 to 4 mm in size. They are normally zoned (An_{70-66}). Phenocrysts occur both as discrete crystals and as glomerocrysts in which crystals are juxtaposed along (010) faces; i.e. in synneusis arrangement (Vance, 1969).

Type 1 megacrysts are subhedral to rounded crystals of Ca-Bytownite composition (An_{84-80}) and are normally zoned. Average crystal size is 1 to 2mm and they typically form large glomerocrysts. Discrete crystals up to 4mm long

PLATE 2.

A. Pillow lava with intersertal texture, Sample AG22-8-1. Compare the grain size with Sample AG22-8-2 (Micrograph B).

B. Intersertal to sub-ophitic texture, Sample AG22-8-2. Note how fine grained the sample is relative to Sample AG22-8-1.

C. Photomicrographs of megacrysts in pillow lava AG22-12-1; olivine at left and plagioclase at right. Note similar morphology of plagioclase to megacryst depicted in Plate 1, Figs. G and H (AG22-3-34).

D. Olivine megacryst (see micrograph C) in AG22-12-1, showing kink banding indicative of shock history. Crossed nicols.

E. High-alumina spinel inclusion in plagioclase megacryst, porphyritic pillow lava AG22-8-16.

F. Clinopyroxene megacryst with subhedral to skeletal outline; AG22-12-1. Partially embayed outline and inclusions provide evidence for resorption prior to growth of outer, inclusion-free rims (skeletal in upper portion).

G. Cryptocrystalline groundmass; AG22-12-35. The abundant dendritic/feathery phase is pyroxene; euhedral olivine microlite at upper right.

H. Quench glass, pillow lava AG22-12-35; compare with photomicrograph G.

PLATE 2

A

0.5 mm

B

0.5 mm

C

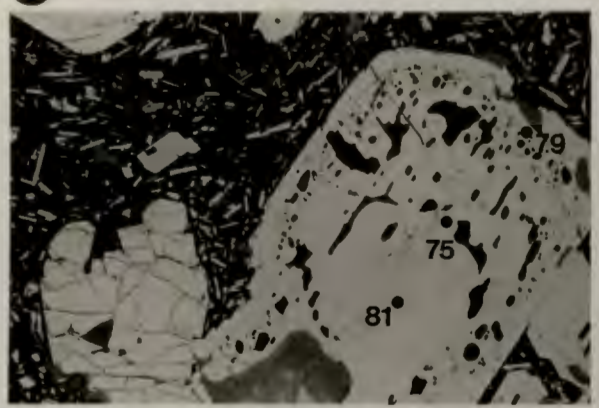

2.5 mm

D

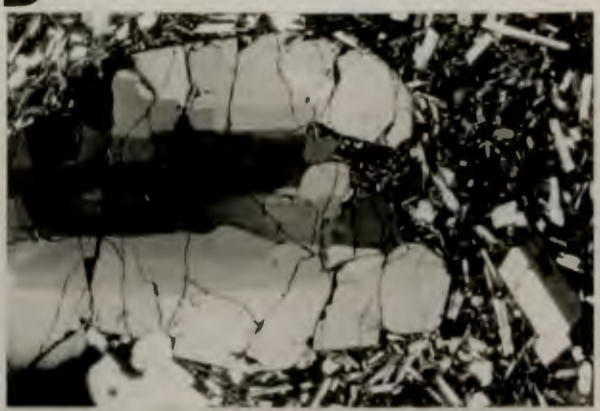

1.3 mm

E

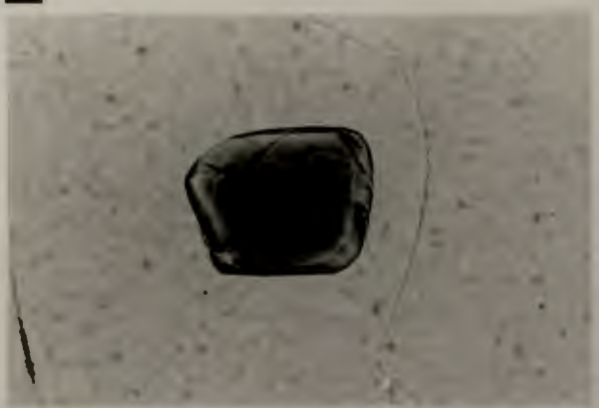

0.1 mm

F

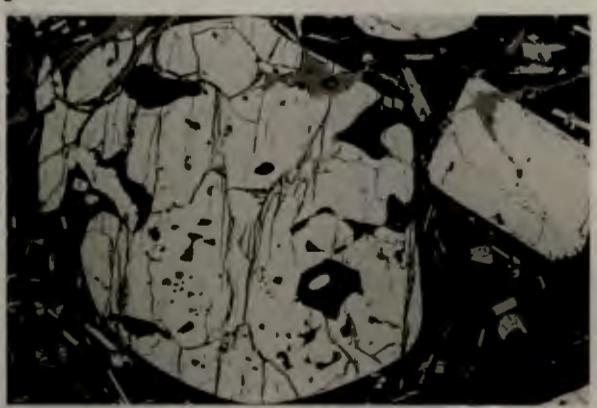

1.3 mm

G

0.8 mm

H

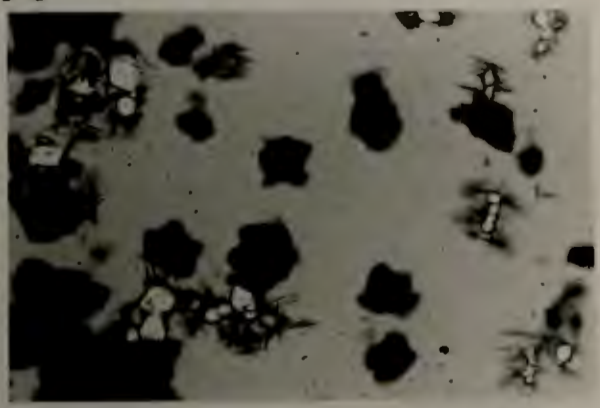

1.0 mm

may poikilitically enclose smaller plagioclase crystals. In one sample (AG22-8-16), an amber coloured high alumina spinel is included in a plagioclase megacryst (Plate 2). Large chrome spinel crystals are commonly associated with plagioclase megacrysts. Melt inclusions occur in many crystals, typically arranged along specific crystallographic planes. These inclusions are common in type 1 megacrysts and are described in detail in the following chapter.

Type 2 plagioclase megacrysts are characterised by reverse zoning in crystals of Na-Bytownite composition (An_{75-79}). They typically show a complex internal morphology and euhedral outline. Any combination of the following features may be present in these megacrysts: a homogeneous rounded or subhedral region, usually the core; patchily zoned, inclusion rich regions; regions of oscillatory zoning; a more calcic region around the oscillatory zoned region, usually euhedral; and a thin skeletal rim of quench plagioclase.

The groundmass of Dredge 8 samples ranges from aphanitic-hyalocrystalline to fine grained intersertal. In contrast to pillow basalt AG22-8-1, the groundmass of sample AG22-8-2 is even finer grained but more crystalline (Plate 2; Figs A and B), and has a greater proportion of ilmenite than AG22-8-1, compatible with the interpretation that sample

AG22-8-2 is more evolved and probably of intrusive affinity. Secondary phases in Dredge 8 basalts include orange to green smectites, occasionally found in vesicles and a red-orange Fe-hydroxide phase replacing groundmass oxide and ferromagnesian phases.

2.2.6 Ridge B; Dredge 9

The three samples recovered in this dredge are all fragments of glass rich microporphyritic pillow lava. Two samples were studied in detail (AG22-9-1; AG22-9-2); fragments have microphenocrysts of olivine (Fo_{88-87}) and plagioclase (An_{69-71}) set in a hyalocrystalline matrix. Chrome spinel microphenocrysts (10 microns in size) occur in poikilitic relationship to olivine or free in the matrix. Spinels compare with other spinels in the Agulhas 22 sample suite and have a similar chemistry to those reported elsewhere from the Southwest Indian Ridge (e.g. le Roex et al., 1983). Secondary phases are absent from the sections studied.

2.2.7 Ridge B; Dredge 12

Dredge 12 yielded pillow basalt fragments with fresh quench glass. Samples include porphyritic basalts (5-40% phenocrysts) and aphyric basalts. Four samples were investigated in detail. Sample AG22-12-35 is aphyric, totally devoid of phenocrysts or microphenocrysts (Plate 2), with skeletal quench olivine microlites (Fo_{86-85}) embedded

in a unique quench textured groundmass of olivine and clinopyroxene dendrites (Plate 2). Rare plagioclase spherulites comprise skeletal plagioclase microlites (An_{60-64}) barely large enough for microprobe analysis.

Plagioclase porphyritic samples include sparsely to moderately porphyritic olivine-plagioclase basalt (AG22-12-20), highly porphyritic olivine-plagioclase basalt (AG22-12-4) and a highly porphyritic olivine-plagioclase-pyroxene basalt (AG22-12-1). Pyroxene bearing basalt AG22-12-1 has the highest modal proportion (40%) of plagioclase phenocrysts/megacrysts.

Skeletal to euhedral olivine microphenocrysts (Fo_{85-83}) and plagioclase microphenocrysts (An_{69-60}) occur in a matrix ranging from hyalopilitic to spherulitic. Equant microlites of olivine (Fo_{82-81}) are common as well as skeletal rims with this composition upon microphenocrysts, phenocrysts and megacrysts.

Olivine phenocrysts (Fo_{86-84}), about 0.5mm in size on average, are normally zoned, and larger crystals (megacrysts; up to 1mm in size) may be more magnesian (e.g. Fo_{87-85}; sample AG22-12-4). Several olivine megacrysts are present in AG22-12-1, characterised by planar fractures and patchy extinction (mosaicism) similar to olivine microfabrics in shocked terrestrial and lunar olivine (e.g.

Stoffler, 1972). Megacrysts frequently exhibit irregular rounded outlines with periodically and regularly arranged cusps smaller than 10 microns in size, indicating a period of resorption (Thornber and Huebner, 1985).

Plagioclase megacrysts and phenocrysts fall into the same textural and compositional categories as Dredge 8 plagioclase crystals. Phenocrysts (1-6mm in size) are untwinned to simply twinned euhedral crystals (An_{66-63}). Large yellow-amber spinel phenocrysts are typically associated with olivine megacrysts and poikilitic type 1 plagioclase megacrysts.

Inclusion rich areas in plagioclase megacrysts are more sodic than elsewhere in a given crystal, and have a relatively constant composition (An_{79}). In samples AG22-12-1 and AG22-12-20, a few megacrysts occur with a spectacular graphic morphology (Plate 3-F). It is unclear whether this morphology is a primary growth feature or the result of resorption. However, the composition of these crystals (An_{79}) corresponds to the "inclusion" phase described above, suggesting that the texture is primary, and probably indicative of rapid (skeletal) growth.

The single clinopyroxene phenocryst (megacryst) present in sample AG22-12-1 is subhedral (2 mm. in size) with a

PLATE 3.

A. Glomeroporphyritic plagioclase in pillow lava AG22-8-16. Large crystal is a type 1 plagioclase megacryst with inclusion of high-alumina spinel (sp; see Plate 2,E). Note the large, elongate inclusions and parallel arrangement of crystals.

B. Same as A, crossed nicols.

C. Type 2 plagioclase megacrysts in pillow lava AG22-12-4. These are characterised by inclusions in core regions, oscillatory zoning and euhedral habit.

D. Same as C above, crossed nicols.

E. Glomeroporphyritic plagioclase phenocrysts with associated large chrome-spinel phenocrysts; Sample AG22-8-24.

F. Highly skeletal (type 1) plagioclase megacryst sectioned close to (001); pillow lava AG22-12-1. The complex internal morphology suggests an origin due to skeletal growth and melt inclusion capture upon very rapid growth.

G: Edge of type 1 plagioclase megacryst, AG22-8-24. Note the band of vapour-rich melt inclusions parallel to the crystal growth zone.

H. Detail of vapour-rich melt inclusions, AG22-8-24. The spherical vapour bubbles range from about $1/3^{rd}$ to $1/6^{th}$ of the size of inclusions. Note devitrified melt inclusion (to left).

PLATE 3

A

2.5 mm

B

2.5 mm

C

2.5 mm

D

2.5 mm

E

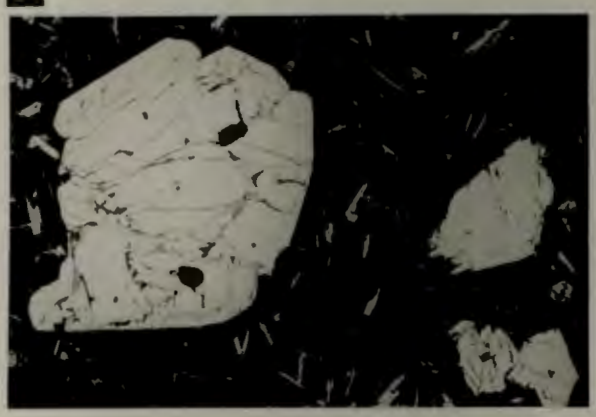

1.9 mm

F

1.0 mm

G

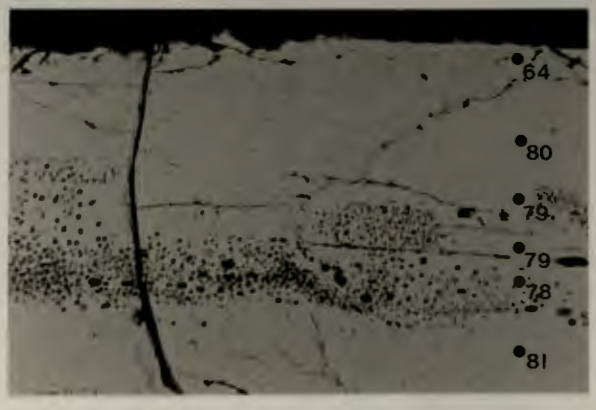

1.3 mm

H

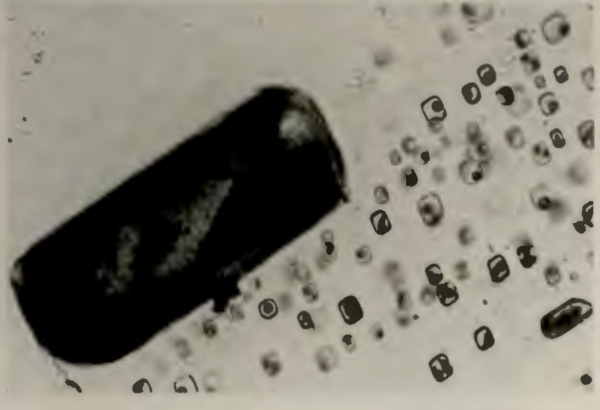

0.1 mm

slightly skeletal habit (Plate 2-F). It is reverse zoned ($Wo_{41}En_{49}Fs_{10}$ - $Wo_{42}En_{51}Fs_{7}$) and includes an olivine microphenocryst (Fo_{84}) at the rim. Alteration of groundmass phases is minor with hydrous phases mainly restricted to areas bordering vesicles.

2.2.8 Ridge B; Dredge 13

Basaltic rocks of Dredge 13 are fragments of aphyric pillow basalt with lustrous black glass on quench surfaces. Rare plagioclase phenocrysts occur in several samples. Five samples were studied in detail and two petrographically distinct lithologies are identifiable: olivine basalts (4 samples) and an olivine-plagioclase basalt (AG22-13-14). Olivine basalts (AG22-13-1, AG22-13-24, AG22-13-25, AG22-13-32) have euhedral olivine (Fo_{88-86}) microphenocrysts set in a hyaline to fan-spherulitic groundmass rich in skeletal quench olivine (Fo_{80-78}) microlites and microlitic plagioclase (An_{69-64}) laths. Olivine-plagioclase basalt AG22-13-14 is olivine and plagioclase microporphyritic (~5 vol. per cent olivine, ~15 vol. per cent plagioclase) with skeletal to euhedral olivine (Fo_{85}) and plagioclase (An_{69-64}) microphenocrysts. Microphenocrysts are typically 0.3mm in size and predominantly occur intergrown in bowtie fashion. A euhedral, reverse zoned plagioclase megacryst (An_{74-77}), 1mm in size, was observed in thin section.

****

CHAPTER 3

MINERALOGY

3.1 General Statement

Many aspects of magmatic processes can be understood only through the study of mineral paragenesis and element partitioning among coexisting phases in rock samples. Detailed information on mineral compositions is necessary for the testing of fractionation models, both with respect to melting and crystallization (Bryan et al., 1969; O'Hara, 1977; Hanson and Langmuir, 1978). Mineral chemistry, zoning and growth forms provide important clues to the changing composition of coexisting liquids as well as to physical conditions such as supercooling (Lofgren, 1971; Lasaga, 1982). Representive mineral analyses from the identified basalt types described in Chapter 2 are given in Tables 6 to 9. The complete data set is listed on microfiche (Appendix 1). The aim of this chapter is to demonstrate that mineral compositions are important indicators of their parental magma compositions, and that minerals, especially plagioclase, may be useful recorders of magmatic behaviour.

Uniform variations in mineral chemistry, and in particular uniform minor element variations are often interpreted as evidence for consanguinity of a suite of lavas; that is, whether lavas are related by fractional crystallization from a common parental magma (e.g. Bryan et al., 1979; O'Donnel

and Presnall, 1980). Should more than one parental magma be involved, one might expect displaced or discontinuous mineral compositional variations (e.g. Bougalt and Hekinian, 1974; le Roex et al., 1981, le Roex, 1985).

Since the majority of the Agulhas 22 basalts are aphyric with microphenocrysts (typically <5%) rarely exceeding 0.5mm in size, the whole rock chemistry of these samples should be representative of liquid compositions. Porphyritic lavas present a problem due to the possibility of phenocryst accumulation and re-distribution (e.g. Staudigel and Bryan, 1981). Nonetheless, with an awareness of such problems, a study of mineral-liquid elemental exchange (e.g. Mg-Fe exchange between olivine and co-existing liquid; Roeder and Emslie, 1970) has been conducted to assess mineral and co-existing glass (and/or whole rock chemistry) relationships.

3.2 Olivine

Representative olivine analyses are presented in Table 6 and the range in compositions depicted in Figure 4. Olivine microphenocrysts (Fo_{88-80}) are ubiquitous and are virtually unzoned (core to rim variation is within microprobe precision; 0.4 mole % forsterite). Where present, quench microlites (Fo_{84-81}) are more Fe-rich than microphenocrysts, commonly by 1 to 4 mole per cent fayalite. Olivine to

Table 6 : Representative olivine analyses; counting time on Ni = 50 seconds. Abbreviations as follows: meg. = megacryst; ph. = phenocryst; ml. = microlite; c. = core; r. = rim. Cation proportions based on 4 oxygens. n.d. = below limit of detection.

	AG22-1-4 mp		AG22-1-13 mp		AG22-3-2 mp	AG22-3-4 mp		AG22-3-8 mp	AG22-3-20 mp		AG22-5-8 mp	
	c	r	c	r		c	r		c	r	c	r
SiO_2	40,38	38,53	39,74	40,17	39,39	40,11	38,47	39,24	40,02	39,99	39,57	39,38
Cr_2O_3	0,05	0,05	0,09	0,09	n.d	n.d	n.d	n.d	0,05	n.d	0,05	n.d
FeO	12,76	13,63	11,79	12,26	14,95	14,39	15,75	15,68	14,31	14,86	13,50	14,60
MnO	0,22	0,19	0,18	0,19	0,23	0,20	0,21	0,27	0,19	0,24	0,19	0,21
MgO	46,92	46,15	46,84	46,40	44,24	45,51	43,99	44,26	45,45	45,23	46,41	45,85
CaO	0,30	0,33	0,28	0,31	0,31	0,29	0,42	0,31	0,27	0,30	0,33	0,30
NiO	0,24	0,23	0,25	0,23	0,19	0,20	0,17	0,17	0,18	0,17	0,24	0,22
TOTAL	100,87	99,11	99,17	99,65	99,30	100,70	99,04	99,92	100,46	100,78	100,29	100,56
Si	0,996	0,975	0,993	1,000	0,997	0,997	0,982	0,991	0,998	0,996	0,986	0,984
Cr	0,001	0,001	0,002	0,002	-	-	-	-	0,001	-	0,001	-
Fe	0,263	0,289	0,246	0,255	0,316	0,299	0,337	0,331	0,298	0,309	0,281	0,305
Mn	0,005	0,004	0.004	0,004	0,005	0,004	0,005	0,006	0,004	0,005	0,004	0,005
Mg	1,725	1,724	1,744	1,722	1,669	1,687	1,674	1,666	1,689	1,679	1,723	1,707
Ca	0,008	0,009	0,008	0,008	0,008	0,008	0,011	0,008	0,007	0,008	0,009	0,008
Ni	0,005	0,005	0,005	0,005	0,004	0,004	0,004	0,004	0,004	0,003	0,005	0,004
% Fo	86,8	85,8	87,2	86,7	83,7	84,6	83,0	83,0	84,7	84,1	85,6	84,5

	AG22-5-10 mp		AG22-5-14 mp		AG22-7-1 mp		AG22-8-2 mp	AG22-8-9 mp		AG22-8-16 mp		AG22-8-24 ml
	c	r	c	r	c	r		c	r	c	r	
SiO_2	39,43	38,89	39,33	37,69	39,69	39,51	39,46	39,53	39,15	39,81	39,67	38,31
Cr_2O_3	n.d	n.d	n.d	n.d	n.d	n.d	0,05	0,06	n.d	0,06	n.d	n.d
FeO	13,86	14,08	15,18	16,17	12,26	13,04	16,80	15,29	16,09	16,05	16,75	17,23
MnO	0,22	0,20	0,21	0,35	0,22	0,24	0,25	0,28	0,26	0,22	0,24	0,34
MgO	46,08	45,80	44,94	44,74	46,39	45,93	43,88	44,89	44,86	44,07	43,50	42,94
CaO	0,34	0,29	0,30	0,30	0,27	0,30	0,28	0,28	0,28	0,31	0,30	0,29
NiO	0,23	0,22	0,15	0,14	0,16	0,15	0,12	0,14	0,13	0,12	0,10	0,09
TOTAL	100,15	99,48	100,09	99,40	99,00	99,16	100,86	100,40	100,78	100,64	100,56	99,10
Si	0,986	0,981	0,989	0,963	0,995	0,993	0,992	0,991	0,982	0,999	0,999	0,985
Cr	-	-	-	-	-	-	0,001	0,001	-	0,001	-	-
Fe	0,290	0,297	0,319	0,346	0,257	0,274	0,353	0,321	0,338	0,337	0,353	0,370
Mn	0,005	0,004	0,005	0,008	0,005	0,005	0,005	0,005	0,006	0,005	0,005	0,007
Mg	1,717	1,722	1,684	1,704	1,733	1,720	1,644	1,678	1,678	1,648	1,633	1,644
Ca	0,009	0,008	0,008	0,008	0,007	0,008	0,008	0,008	0,008	0,008	0,008	0,008
Ni	0,005	0,005	0,003	0,003	0,003	0,003	0,002	0,003	0,003	0,002	0,002	0,002
% Fo	85,2	84,9	83,8	82,7	86,7	86,9	82,0	83,6	82,9	82,7	81,9	81,6

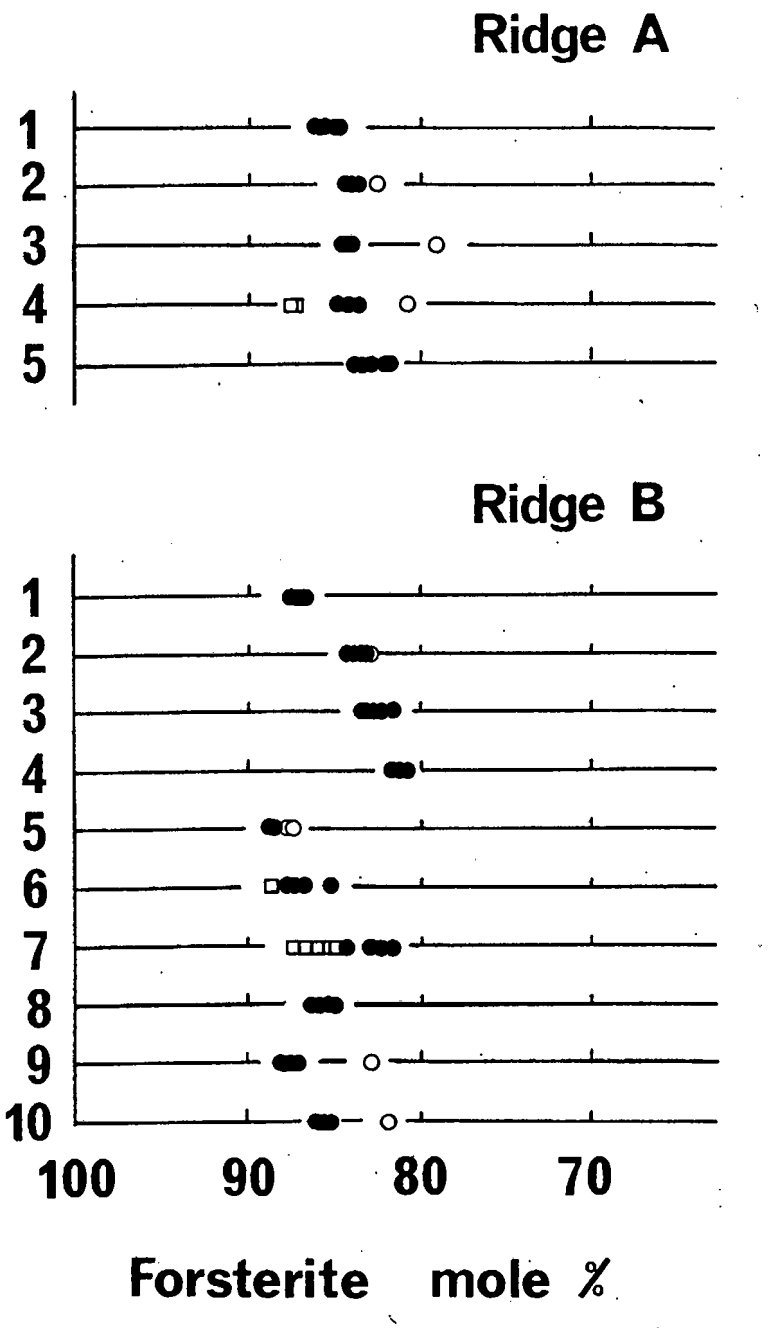

Figure 4: Olivine compositions in selected Agulhas 22 lavas. Squares are phenocrysts and megacrysts; filled circles are microphenocrysts; open circles are microlites. Samples as follows:

	Ridge A		Ridge B		
1	AG22-1-1	1	AG22-7-1	7	AG22-12-4
2	AG22-3-4	2	AG22-8-9	8	AG22-12-35
3	AG22-3-20	3	AG22-8-16	9	AG22-13-1
4	AG22-5-9	4	AG22-8-2	10	AG22-13-14
5	AG22-5-14	5	AG22-9-1		
		6	AG22-12-1		

olivine variation within a single thin section is significant, especially with respect to phenocrysts and megacrysts of porphyritic samples. Phenocrysts (Fo_{87-83}) and megacrysts (Fo_{88-86}) (Figure 4) are normally zoned (maximum zoning observed was 3 mole % forsterite). There is significant between-dredge overlap in compositions; the increase in fayalite contents, and the ranges present, within individual dredges generally correspond with chemical differentiation trends of whole rocks described in Chapter 4.

The distribution of magnesium and ferrous iron between olivine and co-existing liquids can be used to assess whether olivine crystals are in equilibrium with host rocks in which they occur. This distribution is represented by the equation:

$$^1/_2(Mg_2SiO_4)_{olivine} + {}^1/_2(Fe_2SiO_4)_{liquid} = {}^1/_2(Mg_2SiO_4)_{liquid} + {}^1/_2(Fe_2SiO_4)_{olivine} \quad \ldots(1)$$

The equilibrium partition coefficient (or distribution coefficient, K_d) for this reaction can be written as:

$$K_D = \frac{(X^{ol}_{FeO}) \,/\, (X^{liq}_{FeO})}{(X^{ol}_{MgO}) \,/\, (X^{liq}_{MgO})} \quad \ldots\ldots(2)$$

where X^{ol}_{FeO} = mole fraction of FeO in olivine etc.

Roeder and Emslie (1970) experimentally investigated this partitioning for a range in basaltic composition, temperature (1150-1300°C) and oxygen fugacity ($10^{-0.68}$ to 10^{-12} atmospheres) at one atmosphere total pressure. They determined that the value of K_D (equation 2) was essentially constant (0.30 $\pm$ 0.03) and independent of oxygen fugacity and temperature. Although a number of authors have predicted a slightly higher average of 0.33 (Cawthorne et al., 1974; Thompson, 1975; O'Hara, 1977) subsequent experimental studies have confirmed the value of 0.3 $\pm$ 0.03 over a wide variety of compositions (Roeder, 1974; Longhi et al. 1978). Longhi et al. (1978) also observed a small but significant compositional effect on the FeO-MgO distribution, which they attributed to variations in silica concentration. Moreover, Longhi et al. (1978) noticed a pressure effect above 5 kbar.

Despite the observation that K_D is most certainly affected by variables such as pressure (Longhi et al., 1978; Bender et al., 1978), for the purpose of this study, values of between 0.27 and 0.33 are regarded as representing equilibrium conditions. It is also noted that olivine microphenocrysts predominantly crystallize in erupting magmas at pressures within the oceanic crust (Fisk, 1986).

On the assumption that the most Fe-rich olivine should be in equilibrium with the host glass, the FeO content of the

quench glass may be determined using equation 2 above. This is important since the electron microprobe is unable to distinguish between ferrous (Fe^{2+}) and ferric (Fe^{3+}) iron, and all iron is assumed to be ferrous. Thus, the procedure outlined above allows the estimation of the Fe_2O_3/FeO ratio of glasses. The average calculated Fe_2O_3/FeO ratio is 0.17 $\pm$ 0.06, similar to that proposed by Brooks (1976) for ocean floor basalts (ie. $Fe_2O_3/FeO=0.15$).

The partitioning of Mg and Fe between olivine core compositions and the corresponding whole rock compositions (assuming $Fe_2O_3/FeO=0.15$ for whole rock data) is shown in Figure 5, together with olivine microlite-glass partitioning. Microphenocryst core compositions closely approximate equilibrium distribution. A complete listing of olivine equilibria data is given in Appendix 2, Table A-5. Several phenocrysts and even a few megacrysts satisfy equilibrium partitioning. Compositions too magnesian to have equilibrated with coexisting quench glasses include several megacrysts (specifically in evolved porphyritic basalts) and glomerocryst olivine (Fo_{88}) in sample AG22-5-9. The latter composition implies crystallization from a host magma with $Mg^{\#}$ ~0.70, and megacryst compositions (Fo_{86}) suggest derivation from a liquid with $Mg^{\#}$ ~0.65. The maximum calculated $Mg^{\#}$ (0.70) is within the range inferred for primary mantle derived magmas (Rhodes et al., 1979; Pallister and Gregory, 1983).

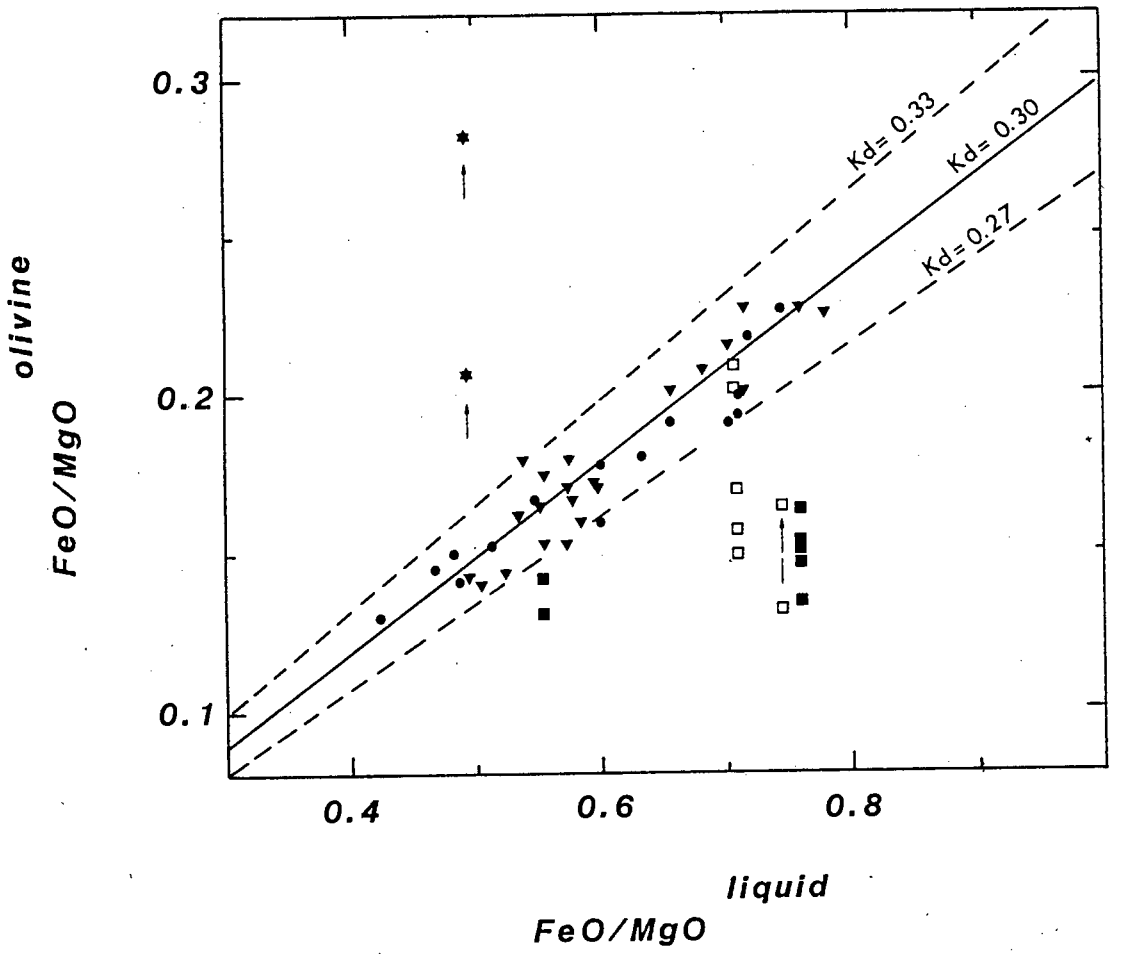

Figure 5: FeO/MgO (mole ratio) of olivine versus FeO/MgO of proposed coexisting liquids. Triangles are Fe-rich olivine vs. quench glass; circles are Mg-rich olivine vs. whole rock; squares are phenocryst and megacryst olivine vs. whole rock (filled symbols),- or glass (open symbols), where whole rock data are unavailable and/or rock shows evidence for crystal accumulation. Arrows indicate zoning and illustrate crystallization of Fe-rich olivine from differentiated interstitial groundmass in sample AG22-13-1 (stars).

The experimental studies of Roeder and Emslie (1970) and Roeder (1974) showed that a linear relationship exists between the logarithm of the olivine-liquid equilibrium distribution coefficients and reciprocal temperature. Hence, temperatures of olivine crystallization may be obtained by the equation:

$$\log K_D = 171/T-0.63 \qquad .....(3)$$

(equation 3 of Roeder and Emslie, 1970), with T in (degrees) Kelvin.

Similar equations reflecting the dependence of K_D on temperature have been obtained and refined by a number of workers for individual oxide species (e.g. Roeder and Emslie, 1970; Roeder, 1974; Leeman and Scheidegger, 1977; Longhi et al., 1978; Fisk et al., 1980; Ford et al., 1983). For comparison with other sample suites, and to avoid differences in the oxidation state of Fe in basaltic liquids, the following equation of Roeder (1974) is commonly used:

$$\log K_{Mg} = 3480/T-1.7 \qquad .....(4)$$

where $K_{Mg} = X^{ol}_{Mg}/X^{liq}_{Mg}$ and X^{A}_{Mg} denotes the mole fraction

of Mg in phase A. It is noted that temperatures are only approximate since geothermometers are not precisely defined for specific gross liquid compositions; geothermometers should ideally be derived from a particular set of experimental data for specific bulk compositions (e.g. Leeman and Scheidegger, 1977; Fisk et al., 1980). In this study, the FeO/MgO thermometer of Roeder and Emslie (1970) as modified by Nathan and van Kirk (1978) and the MgO thermometer of Roeder (1974) have been employed (see appendix 2). The former method is used to predict the equilibrium phase composition and the temperature of appearance and effectively is a further refinement of information from published silicate systems and rock melting experiments available prior to 1978. Equations are complex (e.g. Nathan and Van Kirk, 1978; Ford et al., 1983; cf their equation 3 and Table 2) and take into account empirical component activities and the effect of additional components.

Liquidus temperatures based on whole rock compositions range from 1251°C (aphyric sample AG22-9-1) to 1198°C. This entire range is similar to that inferred from the whole rock composition range on the olivine saturation surface of Roeder and Emslie (Figure 6).

The most Fe rich olivine compositions (including microlite

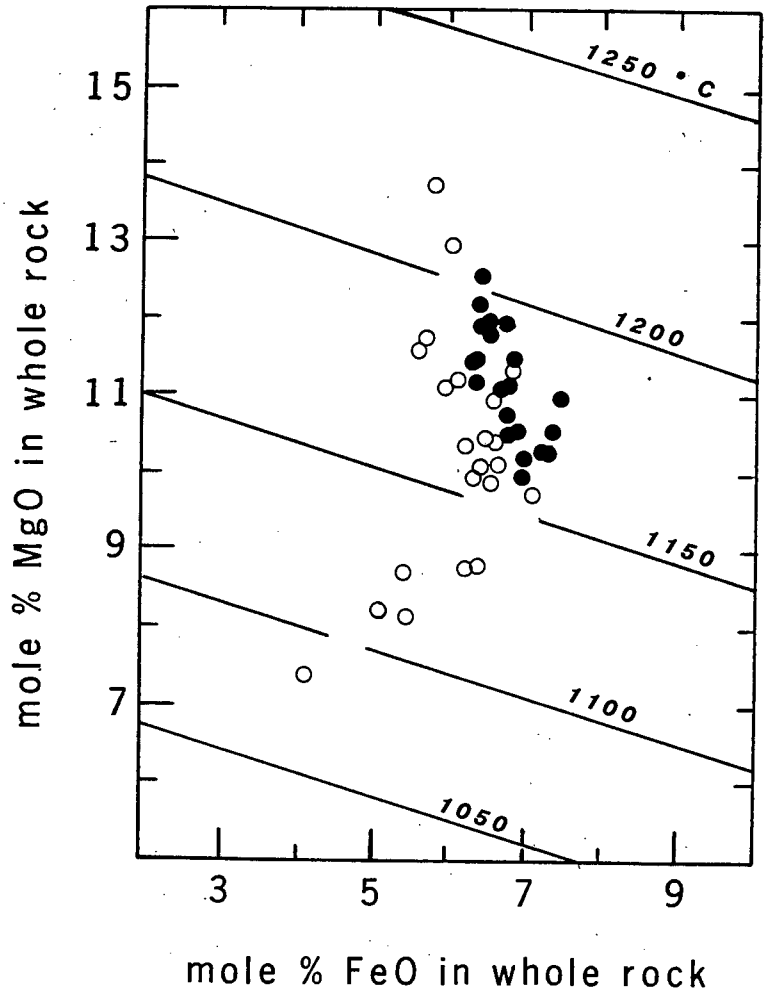

Figure 6: Mole % FeO vs MgO of Agulhas 22 whole rock data. Isotherms from Roeder and Emslie (1970). Filled circles=Ridge A, open circles=Ridge B.

compositions) and coexisting glass compositions have been used to determine quench olivine crystallization temperatures by the MgO thermometer of Roeder (1974). Temperatures obtained are thus considered to represent extrusion temperatures (e.g. Schilling and Sigurdsson, 1979). Calculated temperatures show a relatively restricted range from 1166°C (AG22-1-1) to 1103°C (AG22-5-9) which are significantly lower than liquidus temperatures. By contrast, crystallization temperatures of most magnesian olivines determined to be in equilibrium with whole rocks range from 1151°C (AG22-7-1) to 1119°C (AG22-8-2). These are well within the range of eruption temperatures.

Minor element concentrations in olivine vary systematically with respect to forsterite content. CaO and MnO contents increase with decreasing forsterite content and average concentrations (CaO = 0.1-0.4wt%; MnO = 0.1-0.3wt%) are typical of volcanic olivine compositions (Simkin and Smith, 1970).

High CaO contents in olivine microlites (up to 0.9wt%) are probably erroneous, resulting from fluorescence of matrix material, since detectable Al_2O_3 (1.5 wt%) is present and poor summations occur. Ni contents decrease systematically with decreasing forsterite content. In Figure 7, the decrease in NiO is plotted as a function of decreasing forsterite content. With the exception of megacryst

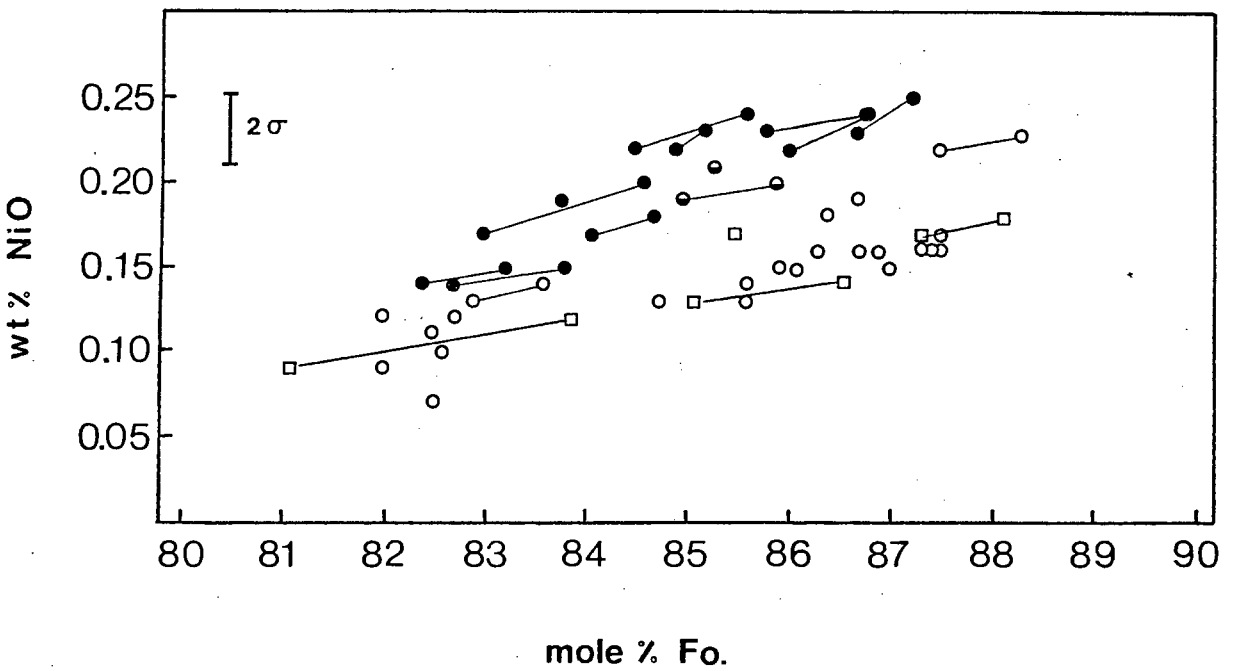

Figure 7 : Nickel versus forsterite content for selected Agulhas 22 basalt olivines. Ridge A olivines (filled circles) have a higher Ni content at a given forsterite content than Ridge B basalt olivine (open circles). Circles represent both microphenocrysts and microlites while squares represent phenocrysts and megacrysts. Tie-lines represent core to rim variation. Half-filled symbols represent microphenocrysts in pillow lava AG22-12-35. (Compare similar displacement in glass data; Figure 22.)

olivine, Ridge A olivines have significantly higher NiO at a given forsterite content than Ridge B olivines. The general trend of Ni variation with decreasing Fo. content is continuous from megacrysts to microphenocrysts suggesting that the former olivines are products of higher temperature crystallization from common parental magmas.

Shock fabrics in certain olivines argue in favour of a xenocryst origin. Although microprobe analyses (ie. Ni zoning characteristics - based on 50 second counting times) revealed no supporting chemical evidence (eg. Nabalek and Langmuir, 1986), these specific olivines are considered to be xenocrysts. These should be investigated further.

3.3 Plagioclase

Representative plagioclase analyses are presented in Table 7 and individual analyses are depicted in Figure 8. The full range of analysed plagioclase extends from calcic bytownite through to intermediate labradorite. K_2O contents are very low (corresponding to less than 0.6 mole % orthoclase component) and in this respect resembles typical MORB plagioclase (Bryan, 1972). In general, higher K_2O contents correlate with higher albite contents.

Plagioclase microphenocrysts range in composition from An_{75} to An_{59}. The entire range may be found in a single thin

Table 7 : Representative plagioclase analyses. Abbreviations as in Table 6. Symbols in parentheses as follows:

I = type I plagioclase megacryst; II = type II plagioclase megacryst; i. = inner (eg. inner portion of mantle zone); o. = outer; rim(1) = (001) sector; rim(2) = (hk0) sector.

	AG22-1-1 mp		AG22-3-2 mp		AG22-3-4 mp		ml	ml	AG22-3-34 mp		meg; rounded core
	c	r	c	r	c	r			c	r	
SiO_2	51,46	50,77	52,68	52,42	50,98	51,28	53,15	54,81	53,86	53,21	48,12
Al_2O_3	29,99	30,91	28,35	28,69	30,96	30,34	29,0	27,93	28,65	29,33	32,65
FeO*	0,38	0,41	1,12	0,95	0,50	0,64	0,97	0,84	0,79	0,68	0,27
MgO	0,27	0,24	0,42	0,37	0,25	0,21	0,30	0,25	0,27	0,26	0,19
CaO	13,98	14,49	11,90	12,30	13,34	13,29	12,34	10,99	12,34	12,98	16,82
Na_2O	3,31	3,08	4,73	4,53	3,71	4,09	4,56	5,21	4,34	4,17	1,90
K_2O	n.d	n.d	n.d	0,05	n.d	0,05	0,05	0,06	n.d	0,05	n.d
TOTAL	99,37	99,90	99,20	99,30	99,74	99,90	100,38	100,09	100,23	100,66	99,95
Si	,354	2,316	2,416	2,403	2,325	2,340	2,409	2,478	2,436	2,402	2,208
Al	1,617	1,661	1,533	1,550	1,664	1,632	1,550	1,488	1,527	1,560	1,766
Fe	0,015	0,016	0,043	0,036	0,019	0,025	0,027	0,032	0,030	0,026	0,010
Mg	0,018	0,016	0,029	0,025	0,017	0,015	0,020	0,017	0,018	0,017	0,013
Ca	0,685	0,708	0,585	0,604	0,652	0,650	0,599	0,532	0,598	0,628	0,827
Na	0,293	0,272	0,420	0,403	0,328	0,362	0,401	0,457	0,380	0,365	0,169
K	-	-	-	0,003	-	0,003	0,003	0,003	-	0,003	-
Ab	30,0	27,9	41,7	40,0	33,4	35,6	40,0	46,0	38,8	36,7	17,0
Or	-	-	-	-	-	-	-	0,3	-	0,3	-
An	70,0	72,1	58,2	60,0	66,6	64,4	60,0	53,7	61,2	63,0	83,0

	Inclusion rich	r	AG22-5-8 meg c	AG22-5-8 meg r	AG22-5-8 mp c	AG22-5-8 mp r	AG22-5-14 mp c	AG22-5-14 mp r	AG22-7-1 mp c	AG22-7-1 mp r(1)	AG22-7-1 mp r(2)
SiO_2	49,06	48,95	47,79	47,95	51,58	51,68	52,50	52,84	42,62	52,77	52,00
Al_2O_3	32,41	32,84	33,30	32,83	30,76	29,26	29,72	28,49	29,70	29,59	30,03
FeO*	0,33	0,27	0,25	0,30	0,65	1,43	0,85	1,11	0,57	0,67	0,83
MgO	0,20	0,21	0,18	0,20	0,27	0,89	0,27	0,43	0,27	0,28	0,27
CaO	16,13	16,57	16,95	16,27	14,17	13,55	13,04	12,43	13,69	13,75	13,67
Na_2O	2,36	2,13	1,76	2,13	3,49	3,58	4,35	4,48	3,84	3,65	3,74
K_2O	n.d	n.d	n.d	n.d	n.d	n.d	0,06	0,07	n.d	n.d	n.d
TOTAL	100,49	100,98	100,22	99,67	100,92	100,39	100,79	99,85	100,68	00,71	100,54
Si	2,235	2,221	2,187	2,205	2,330	2,354	2,375	2,411	2,378	2,383	2,357
Al	1,741	1,756	1,796	1,779	1,638	1,571	1,584	1,532	1,582	1,575	1,605
Fe	0,013	0,010	0,009	0,012	0,025	0,055	0,032	0,042	0,021	0,025	0,032
Mg	0,014	0,015	0,012	0,014	0,018	0,060	0,018	0,029	0,018	0,019	0,018
Ca	0,787	0,806	0,831	0,801	0,686	0,661	0,632	0,608	0,663	0,665	0,664
Na	0,209	0,187	0,156	0,189	0,306	0,316	0,381	0,396	0,337	0,320	0,329
K	-	-	-	-	-	-	0,002	0,004	-	-	-
Ab	21,0	18,8	16,0	19,1	30,9	32,5	37,5	39,3	33,9	32,6	33,2
Or	-	-	-	-	-	-	0,2	0,4	-	-	-
An	79,0	81,2	84,0	80,9	69,1	67,5	62,3	60,3	66,1	67,4	66,8

Table 7. (continued)

	AG22-8-2						AG22-8-16			
	mp		phen		meg(I)		mp		phen	
	c	r	c	r	c	r	c	r	c	r
SiO_2	53,93	53,80	53,22	53,64	49,08	48,88	53,53	53,63	51,39	52,49
Al_2O_3	28,30	28,45	28,33	28,79	31,22	30,82	28,66	29,67	30,72	30,12
FeO*	0,58	0,68	0,45	0,43	0,33	0,46	0,56	0,52	0,48	0,26
MgO	0,21	0,22	0,19	0,20	0,19	0,18	0,21	0,20	0,19	0,27
CaO	12,43	12,96	13,73	13,60	16,49	16,31	12,41	12,68	14,35	13,73
Na_2O	4,65	4,43	3,96	4,05	2,25	2,37	4,28	4,17	3,44	3,78
K_2O	0,05	0,05	n.d	0,05	n.d	n.d	0,05	0,04	n.d	0,04
TOTAL	100,15	100,59	99,88	100,71	99,58	99,01	99,69	100,90	100,56	100,68
Si	2,444	2,431	2,423	2,420	2,260	2,265	2,433	2,409	2,329	2,369
Al	1,512	1,515	1,520	1,531	1,694	1,683	1,535	1,571	1,641	1,602
Fe	0,022	0,026	0,017	0,016	0,013	0,018	0,021	0,020	0,018	0,010
Mg	0,014	0,015	0,013	0,013	0,013	0,012	0,014	0,013	0,013	0,018
Ca	0,604	0,628	0,670	0,657	0,813	0,810	0,605	0,610	0,697	0,664
Na	0,408	0,388	0,349	0,350	0,201	0,213	0,377	0,363	0,302	0,330
K	0,003	0,003	-	0,003	-	-	0,003	0,002	-	0,002
Ab	40,2	38,1	34,3	34,7	19,9	20,8	38,3	37,2	30,4	33,2
Or	0,3	0,3	-	0,03	-	-	0,03	0,2	-	0,2
An	59,5	61,6	65,7	65,0	80,1	79,2	61,4	62,6	69,6	66,6

	composite megacryst				AG22-9-1		AG22-12-4				
					mp		mp			phen	
	core(c)	core(r)	mantle(i)	mantle(o)	c	r	c	r(1)	r(2)	c	r
SiO_2	47,63	48,77	49,86	48,90	51,97	51,56	53,53	53,30	53,51	51,92	52,87
Al_2O_3	32,98	32,52	31,56	32,61	29,67	29,98	28,70	28,80	28,45	30,34	29,07
FeO*	0,28	0,26	0,28	0,42	0,49	0,42	0,82	0,62	0,54	0,378	0,50
MgO	0,18	0,20	0,22	0,18	0,27	0,26	0,39	0,23	0,24	0,18	0,22
CaO	17,19	16,79	15,55	16,38	14,33	14,60	12,93	12,76	12,20	13,64	12,90
Na_2O	1,72	2,02	2,75	2,34	3,49	3,32	4,03	4,14	4,50	3,70	4,16
K_2O	n.d	n.d	n.d	n.d	n.d	n.d	0,04	0,04	0,05	n.d	0,05
TOTAL	99,98	100,56	100,21	100,83	100,21	100,14	100,43	99,90	99,49	100,14	99,76
Si	2,188	2,223	2,274	2,224	2,363	2,347	2,422	2,421	2,438	2,356	2,406
Al	1,786	1,747	1,696	1,748	1,590	1,608	1,530	1,543	1,527	1,623	1,560
Fe	0,011	0,010	0,011	0,016	0,019	0,016	0,031	0,024	0,021	0,014	0,019
Mg	0,012	0,013	0,015	0,012	0,019	0,017	0,026	0,016	0,016	0,012	0,014
Ca	0,846	0,820	0,760	0,798	0,698	0,712	0,627	0,621	0,596	0,663	0,629
Na	0,154	0,179	0,243	0,206	0,308	0,293	0,353	0,364	0,398	0,325	0,367
K	-	-	-	-	-	-	0,002	0,002	0,003	-	0,003
Ab	15,4	17,9	24,3	20,7	30,6	29,1	36,0	36,9	39,9	32,8	36,7
Or	-	-	-	-	-	-	0,2	0,2	0,3	-	0,3
An	84,6	82,1	75,7	79,3	69,4	70,9	63,8	62,9	59,8	67,2	63,0

Table 7. (continued)

	Composite meg(I)				AG22-12-4 meg(II)		AG22-12-35 mp	
	core		mantle					
	c	r	r(i)	r(o)	c	r	c	r
SiO_2	48,44	48,50	51,80	50,33	50,69	49,95	52,52	52,62
Al_2O_3	32,16	32,24	30,53	31,50	30,61	31,14	29,29	28,92
FeO*	0,25	0,37	0,35	0,35	0,35	0,38	0,85	0,77
MgO	0,16	0,19	0,23	0,18	0,22	0,21	0,29	0,31
CaO	16,00	15,69	14,23	15,11	14,96	15,50	13,05	12,25
Na_2O	2,17	2,35	3,35	2,90	2,92	2,68	4,25	4,49
K_2O	n.d	n.d	n.d	n.d	n.d	n.d	n.d	0,07
TOTAL	99,19	99,33	100,48	100,60	99,75	99,87	100,20	99,42
Si	2,234	2,234	2,345	2,292	2,318	2,286	2,387	2,406
Al	1,748	1,750	1,629	1,684	1,649	1,680	1,566	1,558
Fe	0,010	0,014	0,013	0,013	0,013	0,015	0,032	0,029
Mg	0,011	0,013	0,016	0,012	0,015	0,014	0,020	0,021
Ca	0,791	0,774	0,690	0,731	0,733	0,760	0,636	0,600
Na	0,194	0,209	0,294	0,255	0,259	0,238	0,375	0,400
K	–	–	–	–	–	–	–	0,004
Ab	19,7	21,4	29,9	25,7	26,1	23,8	37,0	39,7
Or	–	–	–	–	–	–	–	0,4
An	80,3	78,6	70,1	74,3	73,9	76,2	63,0	59,9

	AG22-13-1 mp		AG22-13-14 mp		ph	
	c	r	c	r	c	r
SiO_2	50,86	51,80	53,23	52,84	49,70	50,18
Al_2O_3	30,33	29,16	29,20	29,55	31,75	31,61
FeO*	0,53	0,82	0,59	0,34	0,37	0,49
MgO	0,31	0,36	0,29	0,22	0,20	0,20
CaO	13,68	12,90	13,14	13,25	15,55	14,96
Na_2O	3,63	4,07	3,98	3,87	2,57	2,87
K_2O	n.d	n.d	n.d	0,04	0,04	n.d
TOTAL	99,35	99,15	100,42	100,10	100,18	100,32
Si	2,332	2,379	2,407	2,395	2,268	2,284
Al	1,639	1,578	1,556	1,578	1,707	1,696
Fe	0,020	0,032	0,022	0,013	0,014	0,019
Mg	0,021	0,025	0,019	0,015	0,013	0,014
Ca	0,672	0,635	0,636	0,643	0,760	0,729
Na	0,323	0,362	0,349	0,340	0,227	0,254
K	–	–	–	0,002	0,003	–
Ab	32,5	36,2	35,5	34,5	23,2	25,9
Or	–	–	–	0,2	–	–
An	67,5	63,6	64,5	65,3	76,8	74,1

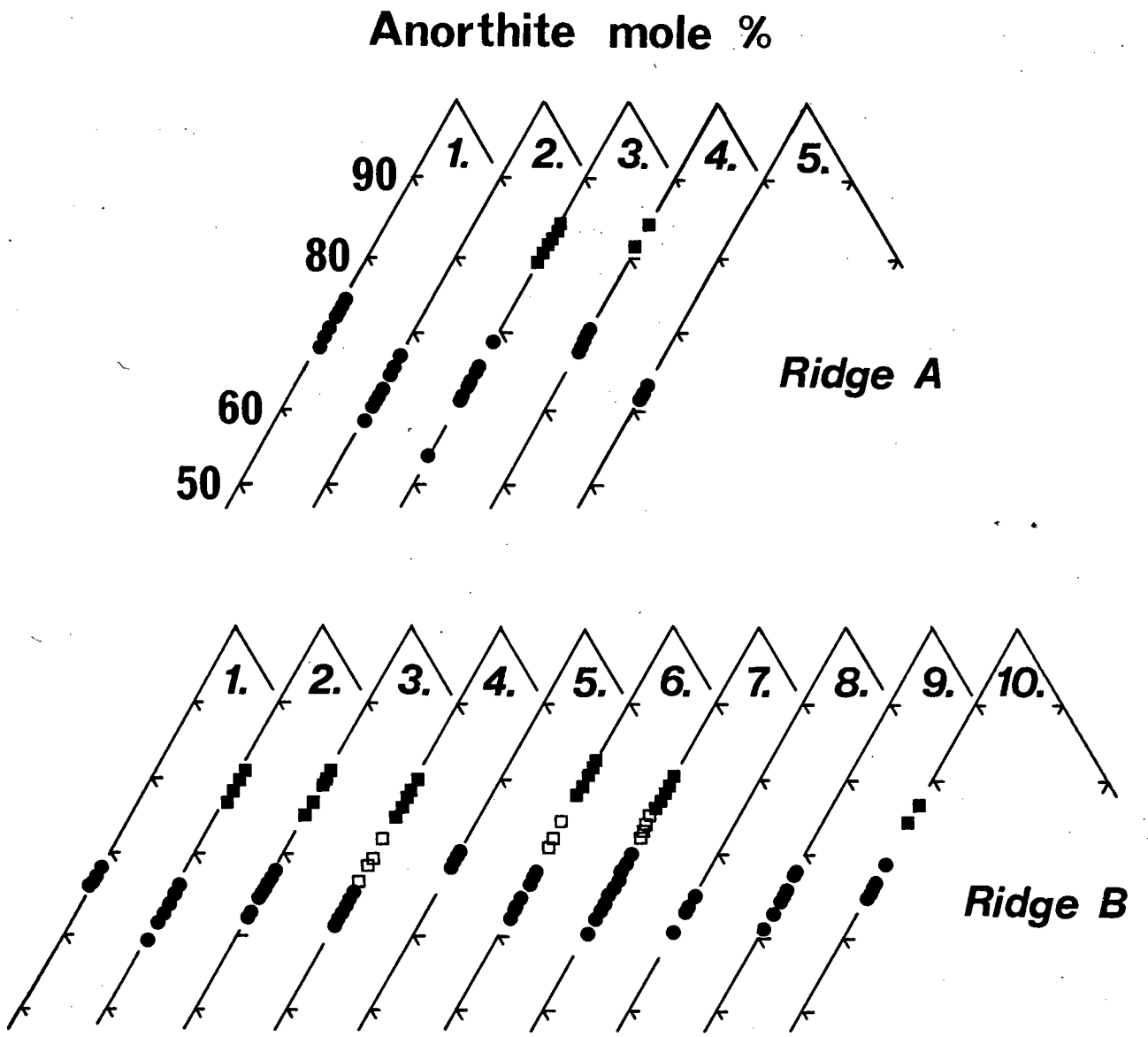

Figure 8: Plagioclase compositions in selected Agulhas 22 lavas. Filled squares = Type 1 megacrysts; open squares = Type 2 megacrysts; filled circles = phenocrysts, microphenocrysts and microlites. Samples as follows:

	Ridge A		Ridge B		
1	AG22-1-1	1	AG22-7-1	6	AG22-12-1
2	AG22-3-4	2	AG22-8-2	7	AG22-12-4
3	AG22-3-34	3	AG22-8-9	8	AG22-12-35
4	AG22-5-5	4	AG22-8-16	9	AG22-13-1
5	AG22-5-14	5	AG22-9-1	10	AG22-13-14

section and microphenocrysts are frequently reverse and sector zoned. Bryan (1972, 1974) described this sector zoning in detail. Phenocryst compositions correspond to most calcic microphenocryst compositions. Phenocrysts are normally zoned to unzoned, suggesting equilibration with host liquids. Megacryst compositional ranges are bimodal: type 1 megacrysts generally fall into the calcic bytownite range, while type 2 megacrysts are sodic bytownite. Type 1 megacrysts are unzoned to normally zoned and frequently contain melt inclusions in more sodic growth zones (An_{79}). Such megacrysts are rounded and resorbed and evidently out of equilibrium with host basalts.

Type 2 megacrysts are characterized by inclusion rich cores and reverse zoning (Plate 3D). Reverse zoning is accompanied by a complex morphological change; typically from a patchily zoned sodic core (An_{74}) through to an oscillatory zoned mantle (An_{77}) and an unzoned rim (An_{78}). This reverse zoning and morphologic change is indicative of a progressively decreasing growth rate (e.g. Vance, 1969; Lofgren, 1974; Allegre et al., 1981; Provost, 1985). Most crystals have a skeletal outermost rim with a composition similar to quench microphenocrysts.

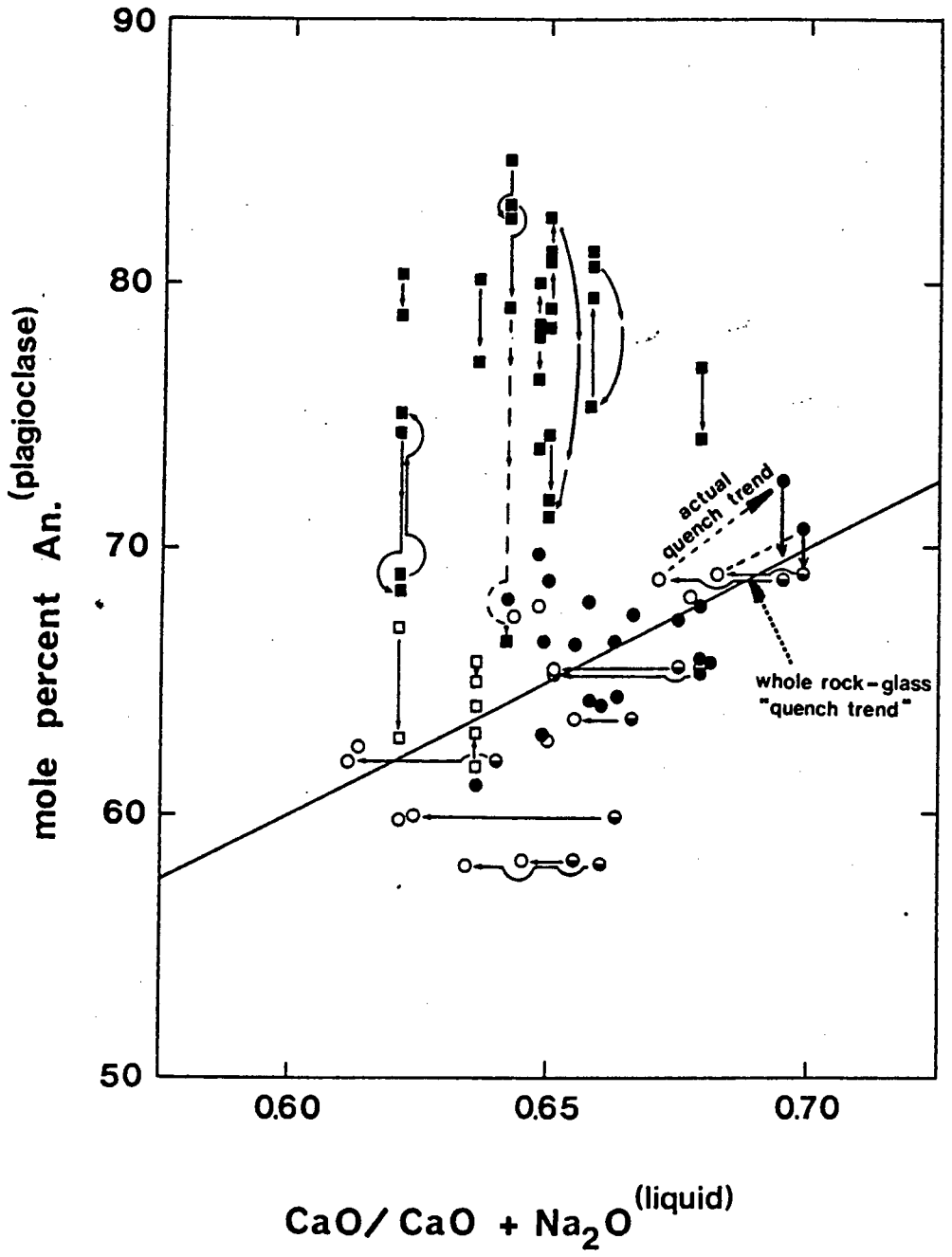

Figure 9: Plagioclase anorthite content versus Ca/Ca+Na mole ratio of corresponding whole rock and/or quench glass. (Quench glass used for porphyritic lavas). Vertical arrows indicate zoning trends in phenocryst (open squares) and megacryst (filled squares) plagioclase. Horizontal arrows represent microphenocryst "quench" trends; microphenocryst plagioclases are, in general, in chemical equilibrium with quench glasses (open circles) - they typically display reverse zoning towards equilibrium with whole rock compositions (filled circles).* Solid line depicts plagioclase compositions in equilibrium with host lavas as determined by the method of Nathan and van Kirk (1978).

---

* Half-filled circles represent apparent whole rock-microphenocryst equilibria.

From Figure 9 it is evident that several microphenocryst compositions are too albitic to have equilibrated with whole rock compositions. However, these microphenocrysts evidently satisfy (near) equilibrium partitioning with coexisting quench glasses (Figure 9). This observation coupled with reverse and sector zoning relationships indicate that microphenocryst compositions are controlled by quenching. Several phenocryst compositions are evidently equilibrium phases, while megacryst plagioclase is too anorthitic to have equilibrated with whole rock compositions, implying crystallization from more primitive calcic melts ($CaO/CaO+Na_2O \leq 0.80$ or up to 70% normative An/An+Ab).

Plagioclase microphenocrysts afford the opportunity of calculating eruption temperatures to compare with those determined by olivine microphenocrysts. The plagioclase geothermometer of Kudo and Weill (1970) as refined by Mathez (1973) is used for this purpose. The plagioclase-melt equilibrium is given by the reaction:

$$\underset{\text{liquid}}{Na + Si} + \underset{\text{anorthite}}{CaAl_2Si_2O_8} \rightleftharpoons \underset{\text{liquid}}{Ca + Al} + \underset{\text{albite}}{NaAlSi_3O_8} \quad ....(6)$$

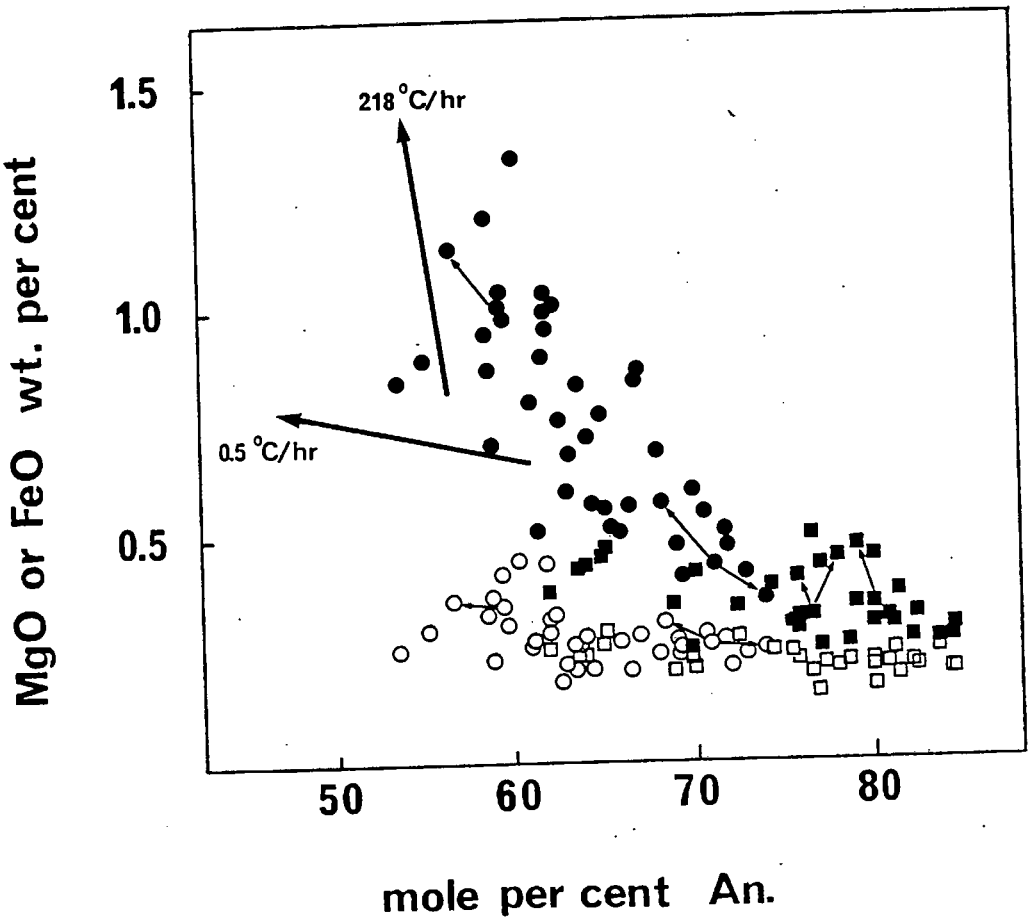

Figure 10: FeO (closed symbols) and MgO (open symbols) in Agulhas 22 basalt plagioclase. Large vectors represent experimental cooling trends of Schiffman and Lofgren (1982). Squares = phenocrysts and megacrysts; circles = microphenocrysts. Several tie-lines indicate within crystal variation (eg. reverse and sector zoned microphenocrysts).

(equation 1 of Mathez, 1973). Assuming ideal behaviour, the calculated reciprocal temperature equation (equation 7a of Mathez, 1973) is

$$\ln \lambda/\sigma \times 10^4 \times \Phi/T = 11.76 \times 10^{-3} \times T - 19.01 \quad ....(7)$$

The input data are: $\lambda = X_{Na}X_{Si}/X_{Ca}X_{Al}$, $\Phi = X_{Ca} + X_{Al} - X_{Si} - X_{Na}$ and $\sigma = (X_{Ab}/X_{An})/(\alpha_{Ab}/\alpha_{An})$; where X_A = atomic fraction of element A in the melt, X_{Ab}/X_{An} the plagioclase composition and α_{Ab}/α_{An} is an activity correction coefficient (Figure 3 of Mathez, 1973). An added restriction is that $X_{Na}+X_{Si}+X_{Ca}+X_{Al} = 1$.

Estimated temperatures of crystallization, based on assuming equilibration of most sodic microphenocryst rim compositions and quench glass compositions range from 1200°C to 1162°C (See Appendix 2, Table A-7). These are significantly higher than those determined by olivine equilibria. These temperatures correspond to plagioclase liquidus temperatures determined on whole rock compositions by the method of Nathan and Van Kirk (1978).

Calculations performed by the method of Nathan and van Kirk (1978) were determined by computer; a program (XTALS) modified by Professor A. R. Duncan of the Geochemistry

Figure 11: Substitutional relationships in Agulhas 22 basalt plagioclase. Units are cations per 8 oxygens. Solid lines depict theoretical relationships for ideal albite-anorthite mixtures. Several data points are omitted for clarity.

(a) Ca vs Al. Linear regression analysis of all data yields the equation (with correlation coefficient, R = 0.83):

$$Ca = 0.758Al - 0.742$$

(b) Ca vs Si. Note the near perfect substitution but higher Ca contents relative to ideal plagioclase. Linear regression analysis of all data yields (R = 0.893):

$$Ca = -0.905Si + 2.6066$$

(c) Ca vs Al+2Fe+2Mg. Note the large scatter of data. Linear regression analysis of all data (R = 0.667) yields:

$$Ca = 0.841(Al+2Fe+2Mg) - 0.941$$

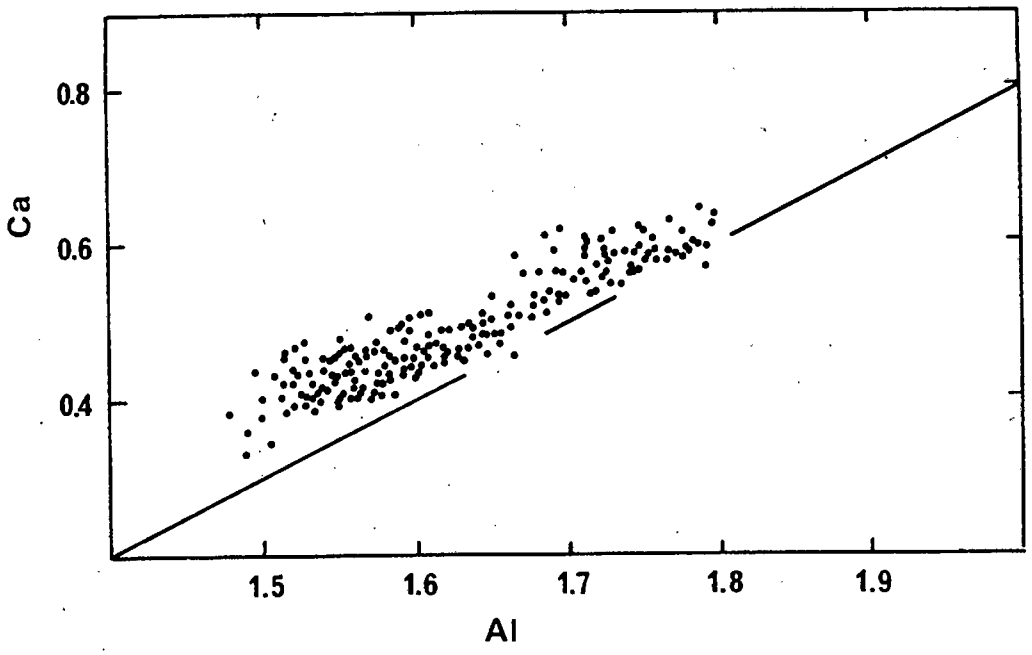
0.8
0.6
0.4
Ca
1.5
1.6
1.7
1.8
1.9
Al

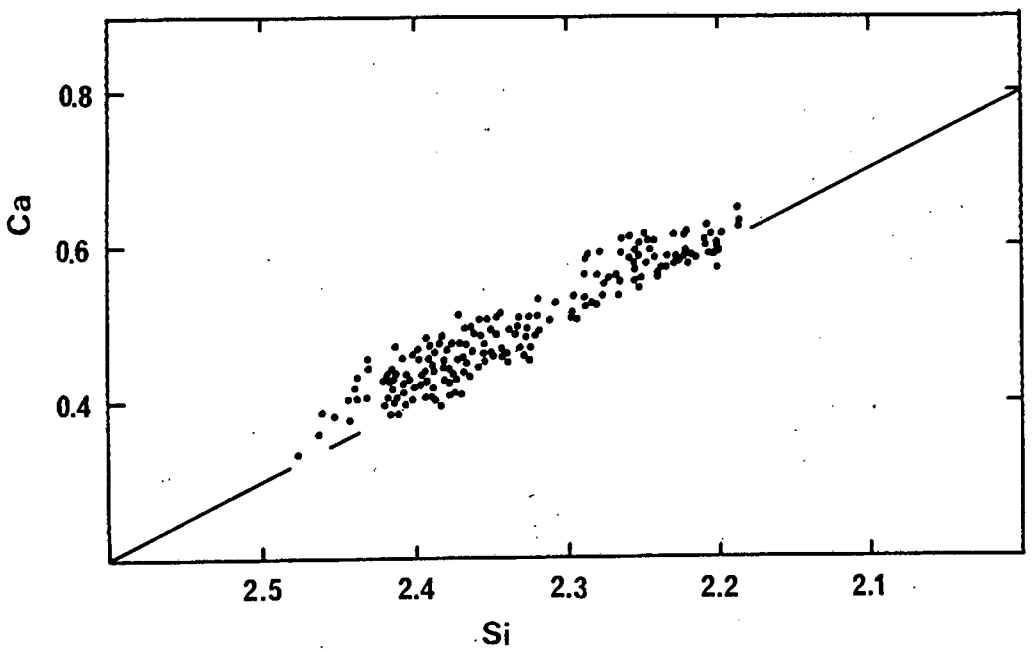
0.8
0.6
0.4
Ca
2.5
2.4
2.3
2.2
2.1
Si

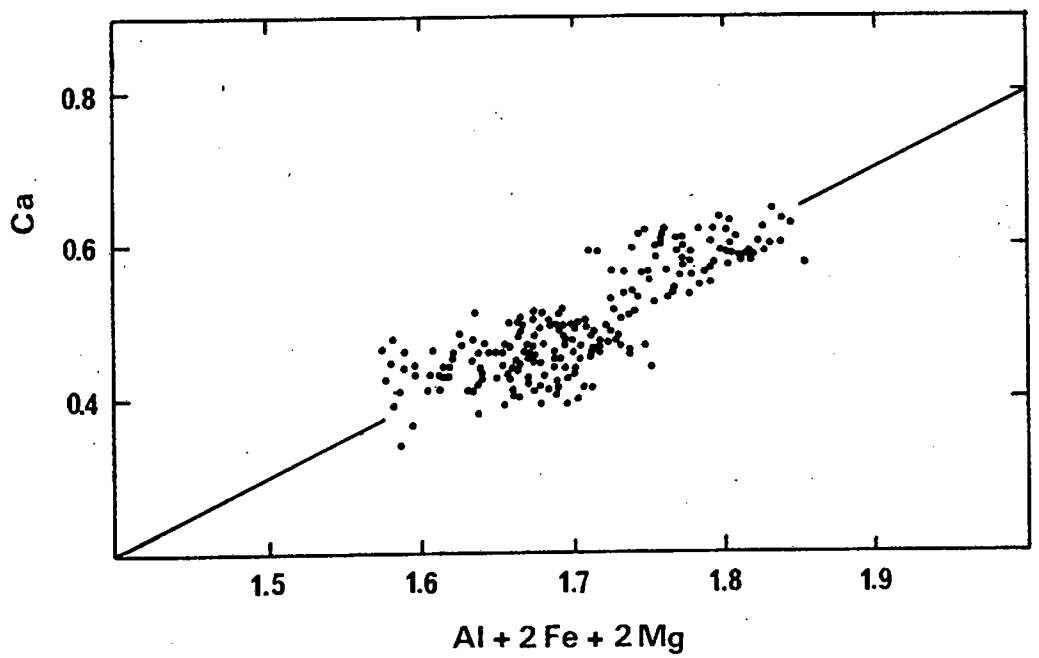
0.8
0.6
0.4
Ca
1.5
1.6
1.7
1.8
1.9
Al + 2 Fe + 2 Mg

Department for the HP1000* was employed. The high temperatures are explained for the most part by the ease of plagioclase nucleation in silicate melts (e.g. Gibb, 1974), and in part perhaps due to the fact that up to 10 mole % of Ca is present in the $Ca(Fe,Mg)Si_3O_8$ molecule rather than in anorthite (see later). Several authors have also noted higher temperatures obtained by plagioclase thermometry relative to olivine thermometry (e.g. Frey et al., 1974).

Minor elements in plagioclase include Fe and Mg. FeO (0.2-1.6 wt %) and MgO (0.1-0.5 wt %) contents are plotted versus anorthite content in Figure 10. This diagram illustrates three important points:

(1) MgO contents are always lower than FeO contents.

(2) Both FeO and MgO increase with increasing albite content.

(3) At a given anorthite content, minimum FeO and MgO contents are apparently lower in phenocrysts and megacrysts than in microphenocrysts and microlites.

---

* Hewlett Packard model 1000 Computer

These features may be qualitatively explained by the kinetic effects of cooling rate experienced by crystals (and host liquids) and the greater ease of iron-magnesium substitution in sea floor basalt plagioclase with increasing albite content (Bryan, 1974). The effect of rapid cooling on crystal growth is to increase the proportion of impurities in a crystal which would otherwise be expelled by diffusion (e.g. Leung, 1974; Grove and Bence, 1977; Coish and Taylor, 1979; Kirkpatrick, 1983).

Schiffman and Lofgren (1982) have experimentally investigated the effects of cooling rate on the mineral chemistry of a Columbia River basalt. Trends in iron-magnesium distribution in natural and experimentally grown plagioclase (Schiffman and Lofgren, 1982) are shown in Figure 10 along with the Agulhas 22 basalt plagioclase data.

At known cooling rates, Schiffman and Lofgren determined that plagioclases crystallized with systematically higher FeO and MgO contents as cooling rate increased. By direct analogy, Agulhas 22 basalt plagioclase compositions imply that megacrysts and phenocrysts probably experienced slow cooling rates (corresponding to the 0.5°C/hr vector; Figure 10) while microphenocrysts and microlites grew at extremely rapid rates (cf 218°C/hr vector; Figure 10). Crystal morphologies of the latter

crystal types have been experimentally reproduced by Lofgren (1974) at a cooling rate of 250°C/hr while chain and feather olivine microlites observed in several Agulhas 22 basalts evidently attest to cooling rates of greater than 200°C/hr (Donaldson, 1976). Furthermore, relatively high Fe contents in type 2 megacrysts imply that, relative to type 1 megacrysts, these crystals grew at greater cooling rates.

The iron-magnesium substitution in MORB plagioclase is best explained in terms of divalent Fe and Mg substituting for Al in a formula unit of the type $Ca(Fe,Mg)Si_3O_8$ (Bryan, 1972). This substitution is favoured by decreasing temperature (Bryan, 1974) and thus it is expected that the molecule behaves thermodynamically similarly to albite (see point 2 above). Similar conclusions regarding the charge balance and occupancy have been reached by Crawford (1973) and Wenk and Wilde (1973) in view of stoichiometric arguments. The approach of Bryan (1972) is adopted here in order to investigate Fe and Mg site occupancy in Agulhas 22 basalt plagioclase.

Charge balance in plagioclase feldspars is of the type $R^{2+}(R^{3+})_2Si_2O_8$ in the anorthite end member and $R^{+}(R^{3+})Si_3O_8$ (or $R^{2+}R^{2+}Si_3O_8$) in the albite end member. If

all the Ca is combined in formula units of an anorthite molecule, the expressions

$$Ca = Al - 1 \quad \text{and} \quad Ca = -1.0Si + 3.0$$

will be fulfilled. Theoretically, Fe and/or Mg can substitute for Ca in this molecule to give:

$$Ca + Fe + Mg = Al - 1.0 \quad \text{and} \quad Ca + Fe + Mg = 1.0Si + 3.0$$

Similarly, in an albite molecule, Fe and Mg may substitute for Al, giving:

$$Ca = (Al+2Fe+2Mg)-1 \quad \text{and} \quad Ca = -1.0(Si-Fe-Mg)+3$$

Figures 11 a, b and c show virtually analogous findings to Bryan (1972). An apparent excess of Ca is present over that expected in a pure anorthite (solid lines), increasing with decreasing Ca content (Figures a and b). The "excess" Ca is thus best explained in terms of a $Ca(Fe,Mg)Si_3O_8$ molecule. Moreover, Figure 11c, displays near (perfect) ideal distribution (Ca vs [Al+2Fe+2Mg]) implying Fe-Mg substitution for Al. The observed scatter may be a function of significant Fe^{3+} which may substitute directly for Al (Bryan, 1972).

Miura (1984) has investigated possible plagioclase

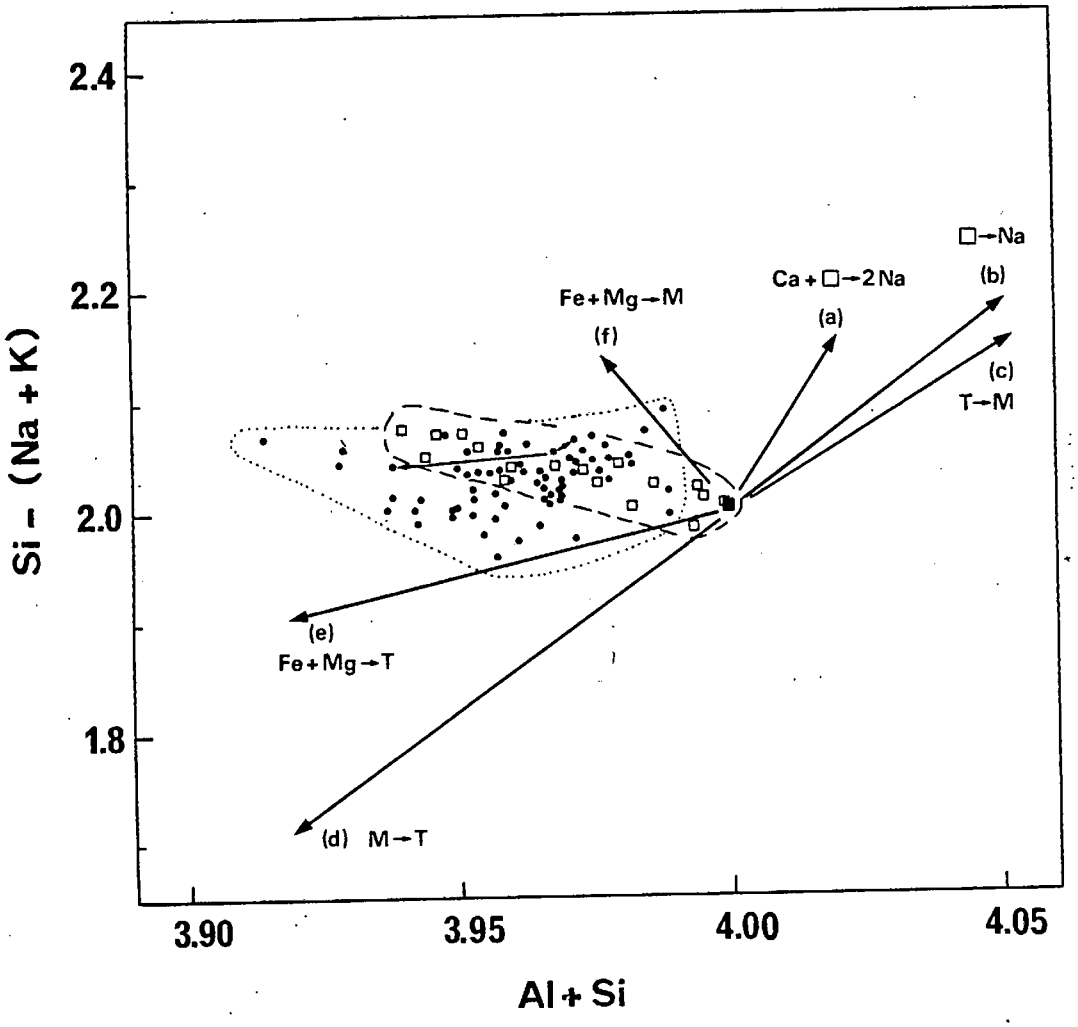

Figure 12: Variation of Si - (Na+K) and Al+Si in Agulhas 22 basalt plagioclase. Squares represent phenocrysts and megacrysts, circles are microphenocrysts. Several analyses are omitted for clarity but the distribution of points is not affected (see fields outlined). Substitutional vectors radiating from ideal plagioclase feldspar (filled square) are from Miura (1984) where T = tetrahedral site, M = octahedral site and □ = vacancy. Small arrows indicate sector zoned microphenocryst, sample AG22-1-4. Substitution in reverse zoned sector, [(001); rapid growth direction], mimics vector e while normal zoned sector (010) mimics vector c.

substitution in some detail. By computer simulation, various substitutions have been identified and are evident as substitutional vectors in a plot of Si-(Na+K) vs Al+Si (Figure 12). The Agulhas 22 plagioclase data indicate that Fe and Mg apparently occupy both the tetrahedral and octahedral cation sites and by implication that the scatter in Figure 11c is in part due to Fe^{3+} substitution for Al. Plagioclase megacrysts define a trend between vectors 'e'and 'f' of Miura (1984) while microphenocryst plagioclase exhibits a greater scatter indicating a greater involvement of vector 'e' presumably due to quenching.

Because of the obvious kinetic control on Fe/Mg partitioning in plagioclase and the different crystallo-chemical properties of the two cation sites it is not considered possible to attach much (if any) significance to Fe/Mg ratios of plagioclase in an attempt to characterise host magmas from which they crystallized (e.g. Kuo and Kirkpatrick, 1982).

3.4 Spinel

Spinel is present in 9 of 15 petrographically distinct basalts. Representative analyses are given in Table 8 and individual analyses are plotted in Figure 13. Reported

Table 8 : Representative oxide analyses; Agulhas 22 basalts. Abbreviations as in Table 6. Cation proportions based on 4 oxygens; 3 for ilmenite. Cr# = 100Cr/Cr+Al; Mg# = 100Mg/Mg+Fe .

	AG22-1-1	AG22-1-4 in plag		AG22-3-4	AG22-7-1 in ol		AG22-8-16 mp	
		c	r		c	r	c	r
TiO_2	1,08	0,47	0,63	1,40	1,02	1,02	1,14	1,18
Al_2O_3	26,71	27,99	28,82	26,44	25,18	25,37	24,23	24,14
Cr_2O_3	34,82	33,19	32,19	34,75	35,30	36,22	36,25	35,64
Fe_2O_3	8,20	8,49	9,19	7,59	9,32	8,59	8,70	8,78
FeO	13,55	13,01	13,47	14,71	13,00	13,48	16,17	16,06
MnO	0,16	0,15	0,22	0,18	0,20	0,16	0,28	0,18
MgO	15,23	15,92	15,67	14,54	15,27	15,06	13,29	13,22
CnO	n.d	n.d	n.d	0,17	0,05	0,19	0,05	0,12
TOTAL	99,71	99,24	100,84	99,79	99,35	100,10	100,12	99,33
Ti	0,023	0,010	0,014	0,032	0,023	0,023	0,026	0,027
Al	0,943	1,038	0,989	0,938	0,897	0,899	0,872	0,875
Cr	0,825	0,755	0,781	0,827	0,844	0,861	0,875	0,867
Fe^{3+}	0,185	0,186	0,201	0,172	0,212	0,194	0,200	0,203
Fe^{2+}	0,339	0,317	0,328	0,370	0,329	0,339	0,413	0,413
Mn	0,004	0,004	0,005	0,005	0,005	0,004	0,007	0,005
Mg	0,680	0,690	0,680	0,652	0,688	0,674	0,605	0,606
Ca	-	-	-	0,005	0,002	0,006	0,002	0,004
Cr#	46,7	42,1	44,1	46,9	48,5	48,9	50,1	49,8
Mg#	66,7	68,6	67,5	63,8	67,7	66,6	59,4	59,5

	meg in plag		AG22-9-1 mp		AG22-12-1 mp in plag		AG22-12-4 ph		AG22-3-20 ilm	mt
	c	r	c	r	c	r	c	r		
TiO_2	0,26	0,26	0,65	0,62	0,50	0,57	0,69	1,07	47,84	22,49
Al_2O_3	41,71	41,86	28,69	28,45	32,79	33,43	28,37	218,03	0,19	1,47
Cr_2O_3	23,42	23,20	34,98	34,87	32,65	31,50	33,51	33,08	n.d.	n.d
Fe_2O_3	3,58	3,66	6,89	7,01	5,45	5,86	8,48	8,73	12,05	24,16
FeO	11,08	11,31	12,08	11,99	10,64	11,36	12,42	13,98	36,44	50,41
MnO	0,14	0,14	0,18	0,21	0,18	0,13	0,25	0,27	0,42	0,83
MgO	18,81	8,67	16,13	16,05	17,44	17,16	15,31	14,28	3,36	0,75
CaO	n.d	0,06	n.d	n.d	n.d	0,05	n.d	0,08	0,14	0,14
TOTAL	99,02	99,17	99,62	99,22	99,67	100,07	99,05	99,53	100,46	100,26
Ti	0,005	0,005	0,014	0,014	0,011	0,012	0,015	0,024	0,885	0,626
Al	1,366	1,369	1,000	0,996	1,115	1,132	1,001	0,992	0,006	0,064
Cr	0,514	0,509	0,818	0,819	0,745	0,716	0,793	0,785	-	-
Fe^{3+}	0,074	0,077	0,153	0,157	0,118	0,127	0,191	0,198	0,223	0,673
Fe^{2+}	0,257	0,263	0,299	0,298	0,257	0,273	0,311	0,351	0,750	1,562
Mn	0,003	0,003	0,005	0,005	0,004	0,003	0,006	0,007	0,009	0,026
Mg	0,778	0,772	0,711	0,711	0,750	0,735	0,682	0,639	0,123	0,041
Ca	-	0,002	-	-	-	0,002	-	0,003	0,004	0,006
Cr#	27,4	27,1	45,0	45,1	40,1	38,7	44,2	44,2	(Ilm)87,2	(Us)65,0
Mg#	75,2	74,6	70,4	70,5	74,5	72,9	68,7	64,5	(Hm)12,8	(Mt)35,0

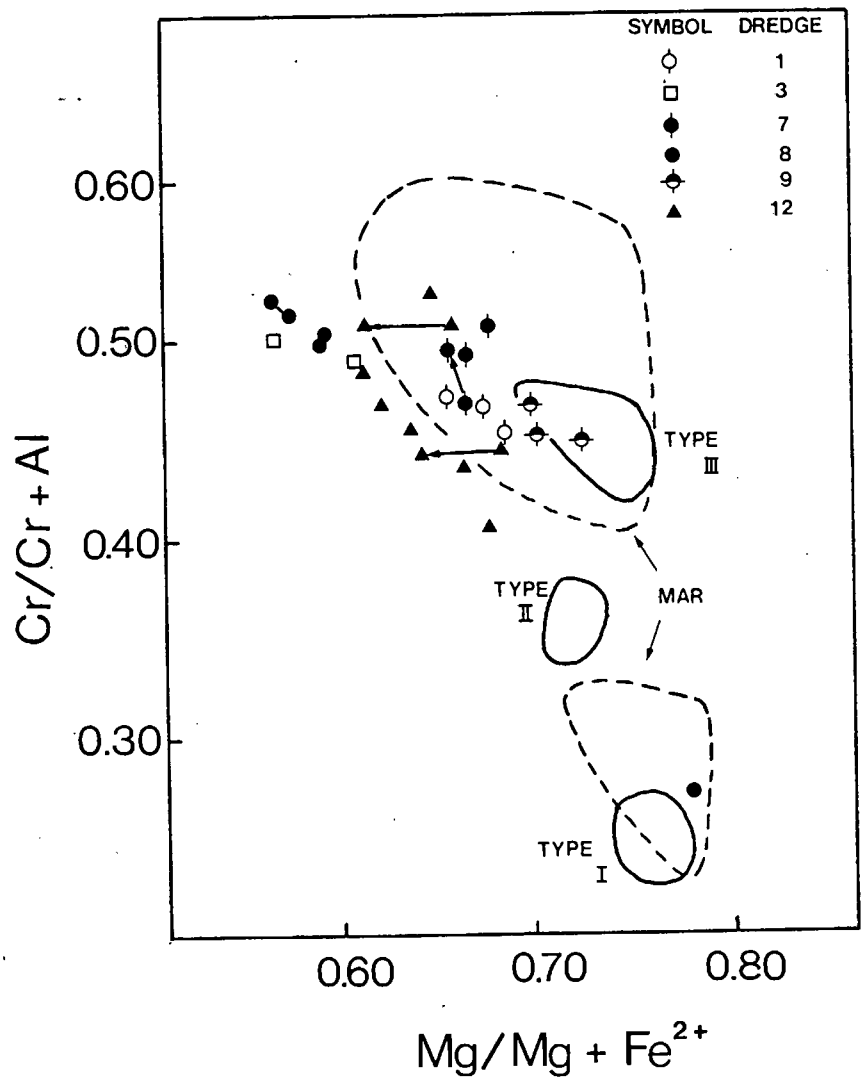

Figure 13: Cr/(Cr+Al) versus Mg/(Mg+Fe^{2+}) of selected spinels (chosen to reflect the maximum variation in compositions) in Agulhas 22 basalts. Fields represent Mid-Atlantic Ridge Spinels (Sigurdsson and Schilling, 1976;- dashed outline) and three identified spinel types in FAMOUS basalt 527-1-1 (Fisk and Bence, 1978; continuous outline). See text for discussion. Note zoning trends (arrows) and an approximately linear relationship shown by Dredge 8 and 12 spinels (slope $\simeq$ unity).

Fe_2O_3 contents were calculated assuming perfect stoichiometry (Finger, 1972). Compositions are comparable with spinels from other abyssal basalts. Following the terminology of Sigurdsson and Schilling (1976) two spinel types are present. Chrome spinels (Cr/Cr+Al = 0.40 - 0.52), frequently associated with olivine microphenocrysts and phenocrysts as well as plagioclase megacrysts, are compositionally similar to typical MORB spinel (Sigurdsson and Schilling, 1976; Sigurdsson, 1977; Fisk and Bence, 1978; Dick and Bullen, 1984). Several spinels, particularly those from porphyritic basalts, are slightly less magnesian than typical chrome spinels and appear to define a linear trend (with slope of unity) in Mg/Mg+Fe - Cr/Cr+Al space (Figure 13). The single high-aluminia spinel (included in megacryst plagioclase, sample AG22-8-16) has a composition (Cr/Cr+Al = 0.27; Mg/Mg+Fe = 0.78) corresponding to high alumina spinels from high alumina picrites from the Mid-Atlantic ridge (Sigurdsson and Schilling, 1976; Fisk and Bence, 1978).

Zoning is rare but two types have been recognised, correlating with the following occurrences: (1) spinels included in olivine, and (2) spinels associated with plagioclase and/or discrete isolated crystals. Zoned spinels in olivine have constant Cr/Cr+Al ratios while Mg/Mg+Fe ratios decrease from core to rim (Figure 13). Zoning of spinels in plagioclase involves an increase in

Cr/Cr+Al from core to rim while Mg/Mg+Fe decreases, or remains constant. High alumina spinel is unzoned.

The decrease in Mg/Mg+Fe in olivine related spinels is consistent with spinel cores having crystallized prior to olivine (they are poikilitically included) and rim crystallization upon crystallization of olivine. Such Mg/Mg+Fe fractionation by spinel has been identified by various workers (Graham et al., 1978; Dick and Bullen, 1984) and is consistent with paragenic relations in MORB (i.e. spinel followed by olivine crystallization). In particular, Dick and Bullen (1984) describe spinels of these compositions as "quench" spinels crystallized at the ocean floor. This implies therefore that rim compositions are probably in equilibrium with magmatic liquid compositions, a contention supported by somewhat similar spinel and whole rock Mg/Mg+Fe ratios (i.e. $Mg^{*}_{spinel}/Mg^{*}_{whole\ rock} \simeq 1$ - see also Irvine; 1965, 1967). Zoning involving increasing Cr/Cr+Al is compatible with fractionation of plagioclase. As plagioclase crystallizes, the Al content of the residual melt at the plagioclase crystal-melt interface would be expected to decrease and hence Cr/Cr+Al should increase. Alternately, increasing Cr/Cr+Al may reflect a bulk compositional increase favoured by decreasing fO_2 with

differentiation (Hill and Roeder, 1974). Mg/Mg+Fe ratios should remain unaffected or, in the presence of concomitant olivine crystallization, decrease.

The origin of high alumina spinel has been proposed as due to high pressure crystallization (Green et al., 1972; Sigurdsson and Schilling, 1976; Fisk and Bence, 1978; Dick and Bullen, 1984). Experimental evidence from lunar basalt studies (Green et al., 1972) indicates that increasing pressure increases Al content of spinels and hence should lower the Cr/Cr+Al ratio. Fisk and Bence (1980) were able to synthesize type II and III spinels (Figure 13) in experiments on FAMOUS basalt 527-1-1, but not high alumina (type I) spinels. They concluded that the former spinels crystallized at lower pressures (crustal) and inferred that pressure was the critical factor governing the formation of high alumina spinel (Fisk and Bence, 1980).

Despite the absence of unequivocal experimental evidence, the effect of increasing pressure does favour the smaller partial molar volume of the Al-spinel (e.g. Robie and Waldbaum, 1968; Dickey and Yoder, 1972; Thy, 1983). Moreover, high pressure can also be expected to increase

3.5 Clinopyroxene

Selected clinopyroxene analyses are presented in Table 9 and individual analyses are depicted in Figure 14. The megacryst pyroxene (sample AG22-12-1) is reverse zoned (Wo_{41} En_{49} Fs_{10} - Wo_{42} En_{51} Fs_{7}) and compositionally similar to early crystallized Ca-rich pyroxene (augite) from tholeiitic magmas (McBirney and Noyes, 1979) and MORB (Grove and Bryan, 1983). Analysed groundmass pyroxene compositions are highly variable, even within a single grain. This variability (10 mole % range in Wo and En; 13 mole % range in Fs) corresponds to a range from salite-ferrosalite to ferroaugite (Deer, Howie and Zussman, 1978). Despite the apparent scatter in Figure 14, two trends are present in groundmass pyroxene. Most conspicuous is a significant decrease in wollastonite (Ca) component from cores to rims of several grains at a constant Mg/Mg+Fe ratio. The other trend is one of iron enrichment paralleling that of iron enrichment in tholeiitic magmas (Muir and Tilley, 1964).

Groundmass pyroxene compositions correspond to pyroxenes known to be of alkaline affinity (Le Bas, 1962). In particular, they are titaniferous pyroxenes (TiO_2 =1.4-4.6 wt %) with a high proportion of non-quadrilateral components (e.g. Al_2O_3 = 2.3-7.6 wt %; Na_2O= 0.5-0.9 wt %) but with low Cr_2O_3 (<0.2 wt %) contents. In contrast, megacryst pyroxene has higher Cr_2O_3 (0.5-1%) and lower Al_2O_3 (2.6-

Table 9: Representative clinopyroxene analyses
meg = single pyroxene megacryst (AG22-12-1);
ml = skeletal microlites (coarse-grained Dredge 3 basalts).
Cation proportions based on 6 oxygens.

	AG22-12-1 meg		AG22-3-20 ml		AG22-3-34 ml	
	c	r	r	c	r	c
SiO_2	51,52	52,34	49,91	43,98	45,52	46,12
TiO_2	0,78	0,37	1,83	4,55	4,23	3,34
Al_2O_3	3,26	2,57	2,26	6,92	5,88	6,84
Cr_2O_3	0,47	0,88	n.d	0,38	0,30	0,12
FeO*	6,30	4,53	10,80	9,64	9,68	7,25
MnO	0,22	0,16	0,27	0,14	0,10	0,08
MgO	16,97	18,09	14,57	11,15	11,71	12,85
CaO	19,73	20,35	20,20	22,05	21,56	22,34
Na_2O	0,36	0,35	0,54	0,88	0,86	0,85
TOTAL	99,61	99,63	100,42	99,60	99,85	99,79
Si	1,899	1,917	1,875	1,682	1,731	1,734
Ti	0,011	0,010	0,052	0,131	0,121	0,095
Al	0,142	0,111	0,100	0,313	0,263	0,303
Cr	0,014	0,025	-	0,012	0,009	0,004
Fe	0,194	0,139	0,339	0,309	0,308	0,228
Mn	0,007	0,005	0,009	0,004	0,003	0,003
Mg	0,932	0,987	0,816	0,637	0,664	0,720
Ca	0,779	0,798	0,813	0,905	0,879	0,900
Na	0,026	0,025	0,039	0,065	0,063	0,062
Wo	40,7	41,4	41,1	48,8	47,4	48,6
En	48,7	51,2	41,3	34,3	35,8	38,9
Fs	10,6	7,4	17,6	16,9	16,8	12,5

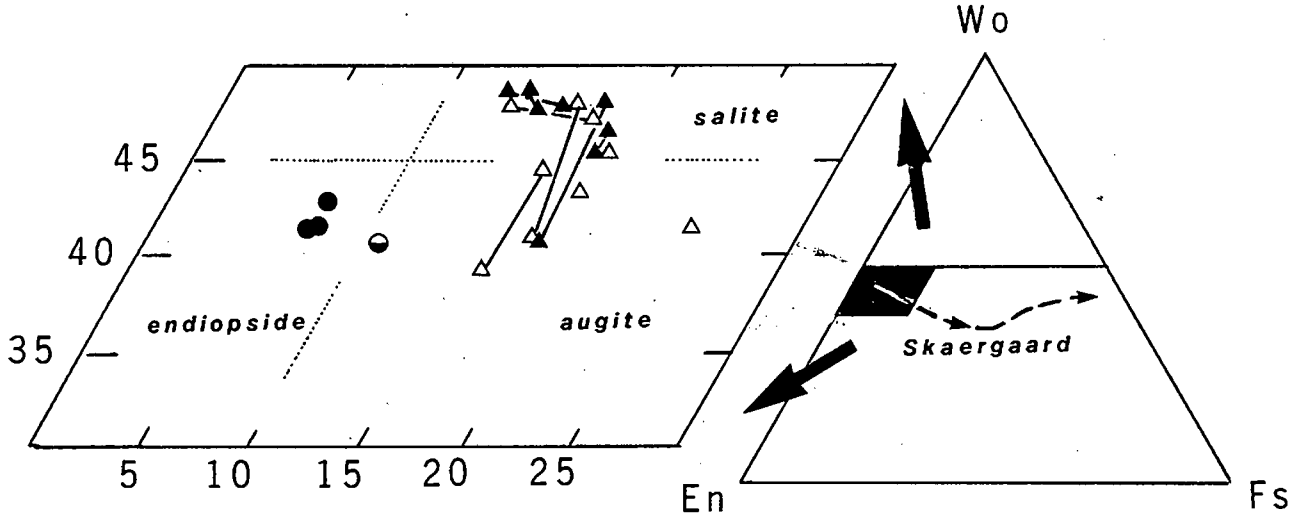

Figure 14: Pyroxene Ca-Fe-Mg end-member compositional variation in Agulhas 22 basalts. Filled circles = megacryst rims; half filled circle = megacryst core; filled triangles = AG22-3-34 groundmass pyroxene; open triangles = AG22-3-20 groundmass pyroxene. Skaegaard pyroxene trend from McBirney and Noyes (1979). Large arrows refer to enlarged view of shaded portion in right hand diagram.

3.5%), TiO_2 (0.4-0.8%) and Na_2O (0.4%) contents than groundmass pyroxene.

Al_2O_3 in individual grains shows a strong negative correlation with SiO_2 (Figure 15a) suggesting that the majority of Al is located in tetrahedral sites. Ti is positively correlated with Al (Figure 15b) and Ti substitution for Al is about five time greater in groundmass pyroxene than in phenocryst (megacryst) pyroxene. Components other than quadrilateral components substitute in megacryst pyroxene in the form of a Ca-Tschermak molecule, whereas in groundmass pyroxene it is as a titanpyroxene molecule (Figure 16).

Groundmass pyroxene compositions are similar to those found in North Atlantic pillow basalts (Coish and Taylor, 1979). Variations are ascribed to the effect of rapid cooling on crystallized pyroxene (Coish and Taylor, 1979). Experimental evidence (Grove and Bence, 1977) indicates that cooling rate strongly affects the substitution of TiO_2, Al_2O_3 and Cr_2O_3 in pyroxene; increasing cooling rate favours increased substitution of TiO_2 and Al_2O_3 but decreasing Cr_2O_3. Groundmass pyroxene compositions therefore, represent a record of metastable crystal/liquid partitioning consequent on rapid crystallization (Deer et al., 1978) rather than reflecting crystallization from different host liquids (LeBas, 1962; cf Figure 15a). The metastable partitioning is best explained in terms of variations in

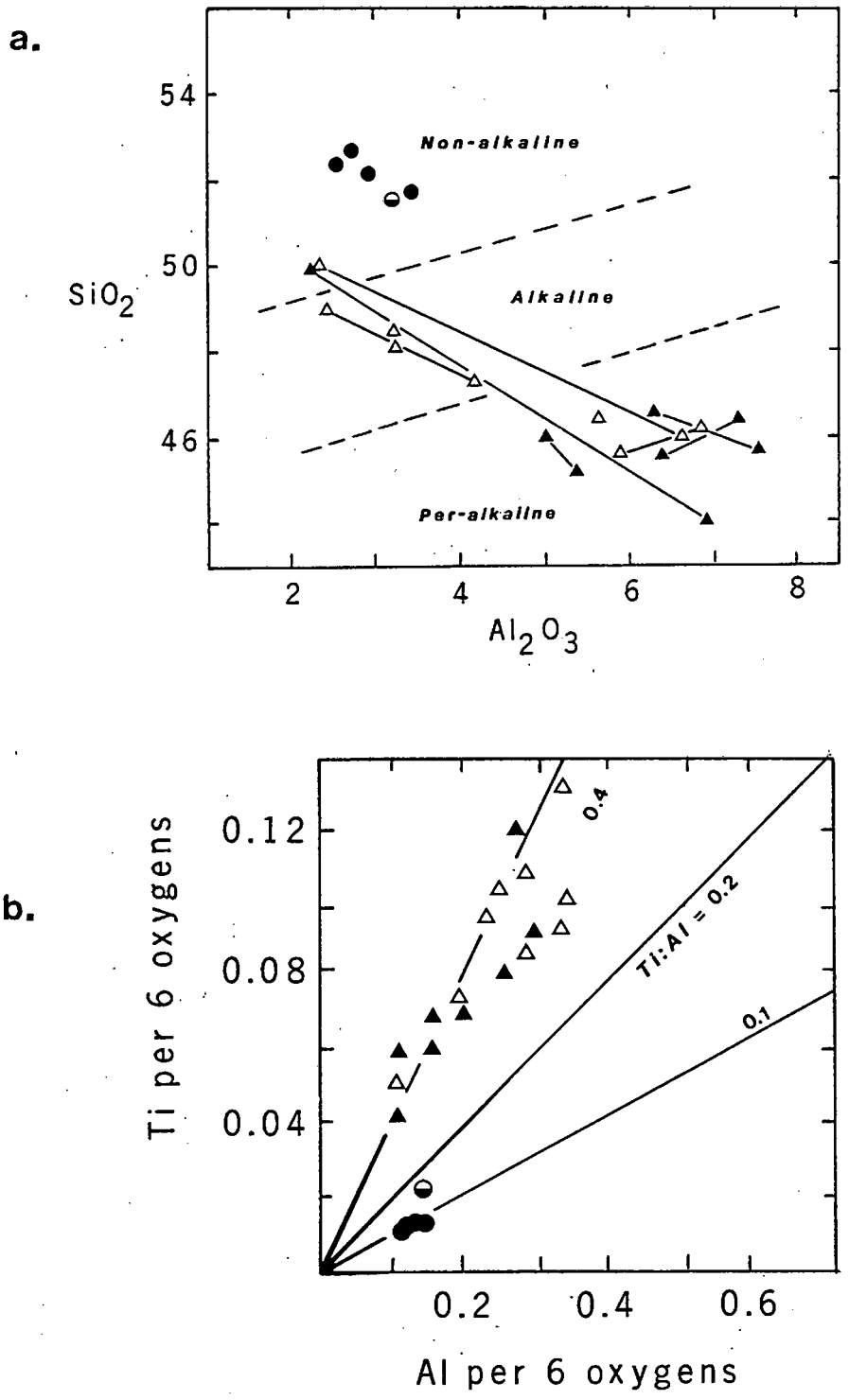

Figure 15: Variation of Si, Ti and Al in analysed Agulhas 22 pyroxenes. (a) SiO_2 vs Al_2O_3; fields of alkaline and other magmas taken from le Bas (1962), (b) Ti vs Al (atomic) in pyroxenes. Note the different Ti/Al ratios. Symbols as in Figure 14.

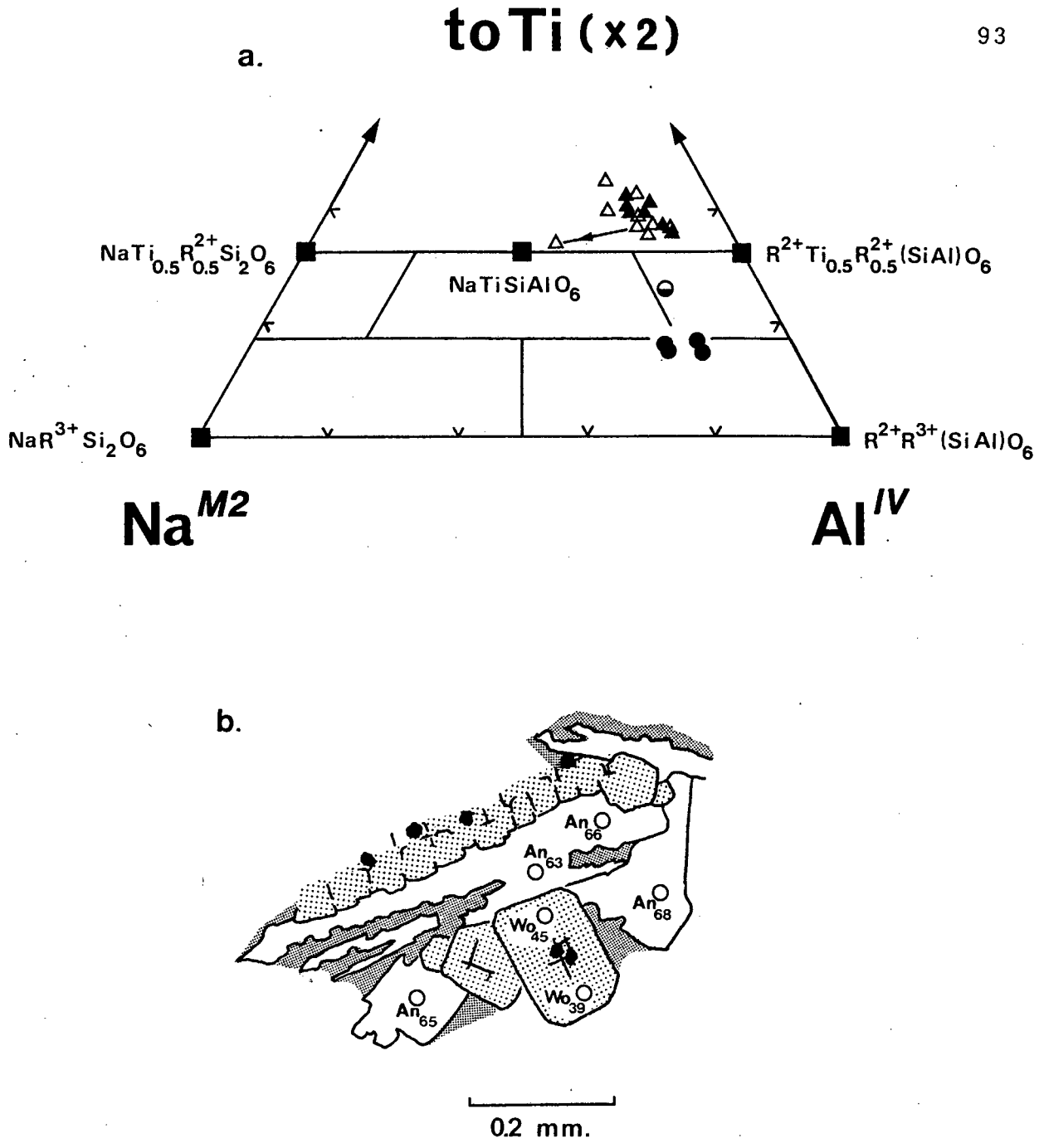

Figure 16: (a) Variation of "others" components (Papike et al., 1974) in analysed Agulhas 22 basalt pyroxenes. Tie-line represents within-grain variation in a single groundmass pyroxene, basalt AG22-3-20. Symbols as in Figure 14.

(b) Schematic representation of intergrown groundmass plagioclase and clinopyroxene, basalt AG22-3-20 (see tie-line in Figure (a)). Compositions given as percentage Ca- end-member; pyroxene of composition Wo_{39} is offset towards Na^{M2} in Figure (a).

silica activity (eg. Carmichael et al., 1970) and the delay in nucleation of plagioclase (Gibb, 1974; Lofgren, 1980). Direct evidence for the latter process is present in the form of reverse zoning in Agulhas 22 basalt groundmass plagioclase and the apparent interaction of plagioclase and pyroxene in basalt AG22-3-20 (Figure 16).

Carmichael et al. (1970) have shown that variations in silica activity can account for pyroxene and plagioclase compositions according to the equilibria:

$$CaAl_2SiO_6 + SiO_2 \rightleftharpoons CaAl_2Si_2O_8$$

PYX MELT PLAG

A delay in the nucleation of plagioclase (Gibb, 1974) would be expected to shift the reaction in the favour of the formation of Ca-Tschermak pyroxene molecule. In this regard Rong-Shu and MacKenzie (1981) note that supercooling and the failure of plagioclase to nucleate results in pyroxene compositions which "may depart appreciably from the equilibrium composition".

The Fe/Mg exchange between pyroxenes and whole rock or coexisting glass compositions (assuming an Fe_2O_3/FeO ratio of 0.15 for these host liquids) is depicted in Figure 17. Groundmass compositions are evidently too Fe-rich to have equilibrated with whole rock compositions, an observation supporting metastable crystal/liquid equilibria attendant

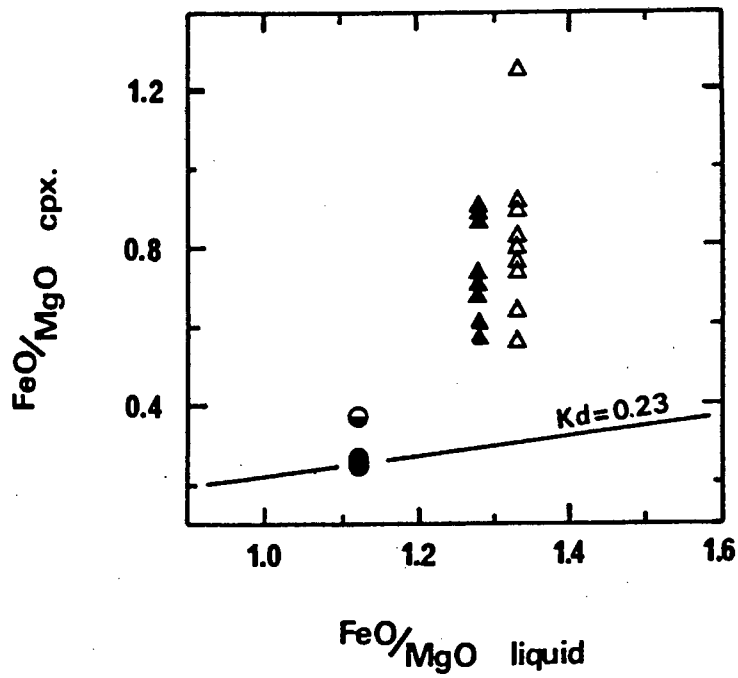

Figure 17: FeO/MgO (molar ratio) of analysed pyroxenes versus FeO/MgO of co-existing whole-rock (AG22-3-20 and AG22-3-34; no glass) and glass (AG22-12-1; no whole rock analysis available) compositions. Symbols as in Figure 14.

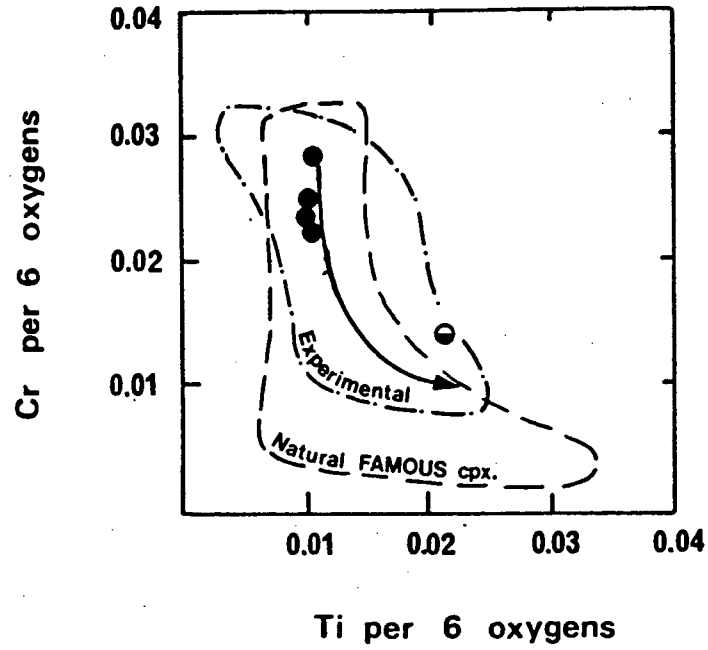

Figure 18: Cr vs Ti in Agulhas 22 megacryst pyroxene. Symbols as in Figure 14. Fields of experimental and natural pyroxenes of FAMOUS area low-pressure pyroxene (Grove and Bryan, 1983) shown for comparison. Arrow depicts trend of early to late crystallizing clinopyroxene (cpx).

upon supercooling. Megacryst pyroxene, however, displays an equilibrium partitioning coefficient for Fe/Mg exchange between rim compositions and quench glass; i.e. K_D=0.23, the accepted equilibrium value (Bryan, 1979; Grove and Bryan, 1983). In Figure 18, the similarity of the rim composition and early formed low pressure pyroxenes of Grove and Bryan (1983) is illustrated.

A value of 0.33 is determined for the Fe/Mg distribution between the megacryst core composition and quench glass. Although the whole rock composition is unknown, this K_D would presumably be similar to or less than that between the megacryst core and the whole rock composition (this is because glasses generally have similar or higher FeO/MgO ratios than corresponding whole rock compositions; see Chapter 5). Nevertheless, the high K_D relative to rim compositions implies that the core composition crystallized from a liquid with a higher FeO/MgO ratio or alternatively, that core crystallization occurred at elevated pressure, since it is known that the $K_{D(Fe/Mg)}$ between high Ca pyroxene and basaltic liquid increases with pressure (Bence and Bender, 1978). More specifically, experimental work on primitive FAMOUS basalt 527-1-1 (Bence and Bender, 1978) has established that $K_{D(Fe/Mg)}$ is 0.35 at 10Kb and 1280°C and 0.34 at 15Kb and 1340°C.

mole % giekelite component. End member compositions are calculated by the method of Stormer (1983). The procedure (Stormer, 1983; page 390) is outlined below:

(1) Determine cation molar proportions for both spinel (Ti-Mt) and rhombohedral (Ilm) phase.

(2) Normalize the spinel formula unit to 3 cation sites and rhombohedral formula to 2 cation sites.

(3) Determine the sum of cationic charges per formula unit, subtract 8 for spinel and 6 for rhombohedral phase. Remaining value represents charge deficiency (or excess).

(4) Eliminate this value by converting Fe^{2+} to Fe^{3+} or vice versa. If unable to, it cannot represent a stoichiometric oxide phase.

(5) Determine the mole fraction of Fe^{2+} relative to the sum of all divalent cations, and of Fe^{3+} to all trivalent cations.

(6) Calculate $X^{\text{spinel phase}}_{\text{ulvospinel}}$ and $X^{\text{rhombohedral phase}}_{\text{ilmenite}}$ by the equations a and b below:

$$X_{USP} = 1 - X_{Fe_3O_4} = 0.5 n_{Fe^{3+},F}(x_{Fe^{2+},S2+})(x_{Fe^{3+},S3+}) \quad ..(a)$$

$$X_{ILM} = 1 - 0.5 n_{Fe^{3+},F} \quad .....(b)$$

where

$n_{Fe^{3+},F}$ = total number of Fe^{3+} ions per formula unit

$x_{Fe^{2+},S2+}$ = mole fraction of Fe^{2+} to the sum of divalent cations

$X_{Fe3+,S3+}$ = mole fraction of Fe_{3+} to the sum of trivalent cations

(7) Determine the temperature (T) and oxygen fugacity (fO_2) using X_{USP} and X_{ILM} with chosen relationship.

The coexisting oxide phases in sample AG22-3-20, when projected on the T-fO_2 grid of Buddington and Lindsley (1964; their Figure 5) give a temperature of last equilibration of 1100°C at an oxygen fugacity of 10^{-9} atmospheres. Despite the uncertainty of ±50°C (Buddington and Lindsley, 1964), this temperature is consistent with quench temperatures determined by olivine and plagioclase thermometry and corresponds to typical temperatures obtained by ocean floor basalt oxide geothermometry (Haggerty, 1976). Following the calculation procedure of Powell and Powell (1977) a crystallization temperature of 1111°C and fO_2 of $10^{-8.1}$ atm. is indicated.

****

CHAPTER 4

RESIDUAL GLASS AND MELT INCLUSIONS

4.1 Natural glasses; Introduction

Natural glasses in the form of residual quenched rinds of pillow basalts as well as trapped melt inclusions are potentially useful recorders of magmatic evolution. For example, glass compositions have been used to show the importance of low pressure (e.g. Melson et al., 1976; Walker et al.,1979) as well as high pressure (e.g. Bender et al., 1984) fractionation. Melt inclusion data have been cited as evidence for primitive and/or primary magmatic precursor melts (Watson, 1976; Donaldson and Brown, 1977; le Roex et al., 1981) as well as magma mixing (Dungan and Rhodes, 1978; Natland et al., 1983; Price et al., 1986). Of critical significance is the need to establish the relationships between residual melts and host whole rocks and/or crystals.

4.2 Major element chemistry of glasses

Previous studies on quench glass compositions have emphasized the importance of glasses as representing true liquid compositions unaffected by mechanical phenocryst addition (e.g. Melson et al., 1976; Natland and Melson, 1980; Bender et al., 1984). Melson et al. (1976) and other workers have established that many MORB glasses are relatively homogeneous at electron microprobe precision and

Sample	SiO_2	TiO_2	Al_2O_3	FeO	MnO	MgO	CaO	Na_2O	K_2O	P_2O_5	Total
AG22-1-4	49.59	1.46	15.76	9.09	0.20	8.36	11.43	3.01	0.10	n.d.	99.00
AG22-1-13	50.26	1.58	15.92	9.33	0.16	8.00	11.45	3.09	0.12	0.16	99.96
AG22-3-4	50.44	1.78	15.37	10.30	0.17	7.20	10.80	3.28	0.18	0.16	99.68
AG22-3-8	50.47	1.99	14.93	10.67	0.19	7.74	10.60	3.47	0.12	n.d.	100.21
AG22-5-8	49.30	1.44	16.80	9.38	0.19	8.09	11.15	3.42	0.12	n.d.	99.89
AG22-5-10	49.52	1.52	15.75	10.03	0.19	8.37	10.64	3.31	0.17	0.20	99.74
AG22-5-14	49.93	2.00	15.18	10.54	0.13	7.30	10.55	3.71	0.27	0.19	99.82
AG22-7-1	50.56	1.60	16.36	9.02	0.17	7.65	11.27	3.20	0.11	n.d.	100.07
AG22-8-9	50.82	1.97	14.78	10.29	0.22	7.29	10.90	3.61	0.17	0.17	100.22
AG22-8-24	50.21	2.35	14.99	10.91	0.18	6.92	10.31	3.52	0.19	0.25	99.58
AG22-9-1	50.66	1.33	16.75	8.57	0.14	8.10	11.91	3.06	0.07	n.d.	100.59
AG22-12-1	50.60	1.55	16.10	8.76	0.16	7.85	11.29	3.36	0.13	n.d.	99.80
AG22-12-4	50.66	2.08	14.61	10.32	0.20	6.84	10.88	3.67	0.13	0.22	99.61
AG22-12-35	50.18	1.38	15.48	9.60	0.20	8.10	10.57	3.53	0.12	0.17	99.80
AG22-13-14	50.75	1.30	15.63	9.15	0.16	7.90	11.63	3.44	0.11	n.d.	100.20
AG22-13-1	50.37	1.35	16.96	8.21	0.14	8.21	10.90	3.17	0.12	n.d.	99.53
Average	50.27	1.70	15.71	9.64	0.18	7.75	11.02	3.37	0.14	0.16	[1.24] 99.94
Average - Ridge A	49.93	1.68	15.67	9.91	0.18	7.87	10.95	3.33	0.15	-	[1.26] 99.67
Average - Ridge B	50.33	1.71	15.74	9.42	0.17	7.65	11.07	3.40	0.13	-	[1.23] 99.82
Average MORB	50.54 ±1.78	1.62 ±0.50	15.27 ±1.13	10.69 ±1.67		7.29 ±1.54	11.16 ±1.54	2.69 ±0.77	0.16 ±0.23		[1.47] 99.42
Average 22-25°N	50.72 ±0.29	1.61 ±0.23	15.46 ±0.49	10.00 ±0.81		7.34 ±0.51	11.23 ±0.61	2.97 ±0.19	0.13 ±0.04		[1.36] 99.46
Cayman Trough		1.70						3.50	0.25		[1.1-1.2] FeO^t/MgO

Analyses of 16 samples of this study (average of +/- 5 points per sample) and chosen to be representative of major composition groups (considering also 68 analyses - le Roex, unpublished data - performed on Cambridge microprobe). Average MORB from Melson et al., (1976), Average 22-25°N, MAR from Bryan et al. (1981), Cayman Trough (Caribbean Plate) data from Thompson et al. (1979).

Table 10. : Representative analyses of pillow basalt glasses.

	AG22-1-4 MiP Ol-pl	AG22-1-13 MiP Ol-pl	AG22-3-4 MiP Ol-pl	AG22-3-8 MiP Ol-pl	AG22-5-8 MiP Ol	AG22-5-10 MiP Ol	AG22-5-14 MiP Ol	AG22-7-1 MiP Ol-pl
Q	-	-	-	-	-	-	-	-
Or	0.60	0.71	1.08	0.71	0.71	1.02	1.61	0.65
Ab	25.90	26.19	27.98	29.28	26.66	28.24	29.96	27.10
An	29.25	29.22	26.69	24.80	30.14	27.63	23.69	29.96
Ne	-	-	-	-	1.26	-	0.92	-
Di	23.08	22.51	22.36	22.57	20.58	20.85	23.57	21.17
Hy	3.10	5.83	7.11	5.26	-	0.47	-	6.90
Ol	13.62	10.87	9.54	11.71	16.24	17.07	14.26	9.57
Mt	1.77	1.79	1.99	2.04	1.80	1.94	2.04	1.73
Ilm	2.79	3.00	3.39	3.78	2.74	2.93	3.81	3.04

	AG22-8-9 SPP Ol-pl	AG22-8-24 OPP Ol-pl	AG22-9-1 MiP Ol-pl	AG22-12-1 OPP Ol-pl-cpx	AG22-12-4 OPP Ol-pl	AG22-12-35 MiP Ol	AG22-13-1 MiP Ol	AG22-13-14 MiP Ol-pl
Q	-	-	-	-	-	-	-	-
Or	1.00	1.13	0.41	0.77	0.77	0.71	0.72	0.65
Ab	30.40	30.00	25.64	28.53	31.27	29.97	27.09	29.07
An	23.62	24.54	31.71	28.47	28.00	26.04	31.73	26.88
Ne	-	-	-	-	-	-	-	-
Di	24.72	22.10	21.74	22.52	25.69	21.62	18.52	25.04
Hy	3.11	5.60	6.33	3.30	2.42	1.86	6.53	0.54
Ol	11.52	10.20	10.13	11.89	10.98	14.55	11.36	13.72
Mt	2.00	2.11	1.63	1.68	2.03	1.88	1.59	1.75
Ilm	3.73	4.48	2.52	2.95	3.96	3.48	2.57	2.57

MiP = microporphyritic, SPP = sparsely plagioclase porphyritic, OPP = olivine-plagioclase porphyritic, Ol = olivine, pl = plagioclase, cpx = clinopyroxene.

Table 11. : Normative mineralogy of glasses. (Table 10). Calculated assuming $FeO/Fe_2O_3 = 0.15$.

The average K_2O content of Agulhas 22 basalt glass is similar to average normal MORB of comparable FeO*/MgO from the MAR at 22°N (Bryan et al., 1981). In terms of TiO_2 and Na_2O (Figure 20,a) Agulhas 22 glasses are transitional between Atlantic MORB from 22°N and glasses from the slow spreading Mid-Cayman rise (Thompson et al., 1980). In a plot of TiO_2 versus FeO*/MgO ratio (Fig 20,b) the Agulhas 22 basalts plot within the field of known SWIR basalts (le Roex et al., 1982; 1983) and compared with <u>average</u> SWIR basalts they have slightly higher TiO_2 and Na_2O contents at a given FeO*/MgO ratio.

Oxide versus MgO variation diagrams for Agulhas 22 basalt glasses are presented in Figure 21. Despite significant scatter in oxide concentrations at a given MgO content (owing to chemical variation between geographic sites) the data describe broadly coherent evolutionary trends similar to chemical variations observed in MORB from the Atlantic, Pacific and Indian Oceans (Flower, 1980). These include increasing FeO, TiO_2, Na_2O, K_2O and P_2O_5 and decreasing CaO and Al_2O_3 contents as MgO decreases.*

Although there is a significant overlap in oxide abundances, there is a suggestion of a between-ridge variation, namely lower average SiO_2 and higher FeO contents in Ridge A glasses relative to Ridge B glasses. In Figure 22, the Fe-Mg

---

* However, scatter in K_2O is probably due to alteration, while low-pressure al $\pm$ plag fractionation is accountable for scatter in CaO (Francis, 1986).

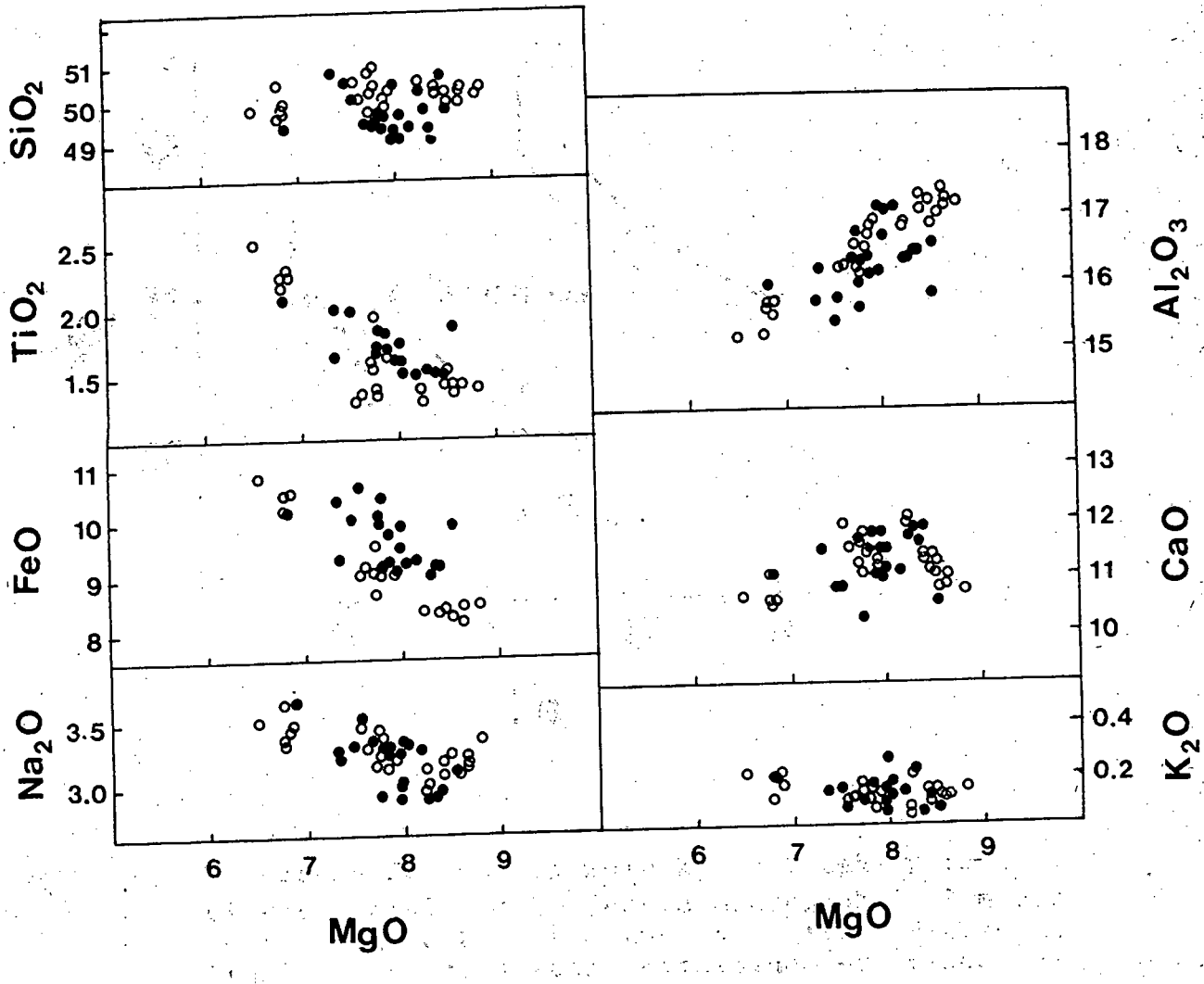

Figure 21: Oxide versus MgO variation diagrams for Agulhas 22 basalt glasses. Filled circles are Ridge A glasses, open circles are Ridge B glasses.

variation is illustrated in terms of cation mole percent values.

The two distinct trends in Figure 22, corresponding to Ridge A and Ridge B basalt (sample AG22-12-35 is an exception), show a similar displacement to that found in East Pacific Rise (EPR) basalts by Bender et al. (1984). In an analogous model to that proposed for the EPR basalts, the distinct trends in Agulhas 22 basalt glass could reflect different liquid lines of descent from parental magmas derived by different degrees of partial melting or from compositionally distinct source regions. This aspect is discussed further in a later section.

Major element compositional variation in MORB glasses define apparent cotectics in the normative plagioclase-olivine-pyroxene ternary (Miyashiro et al., 1970; Shido et al., 1971; Bryan and Dick, 1982). Bryan and Dick (1982) have shown that genetically related two-phase and three-phase saturated basalts project on to common pseudo-cotectics in this ternary normative system. They concluded that parallel but offset trends in this system represent compositional shifts in liquid lines of descent as a function of upper mantle heterogeneity.

The Agulhas 22 glass data are plotted in this normative ternary (Figure 23) and it is immediately apparent that

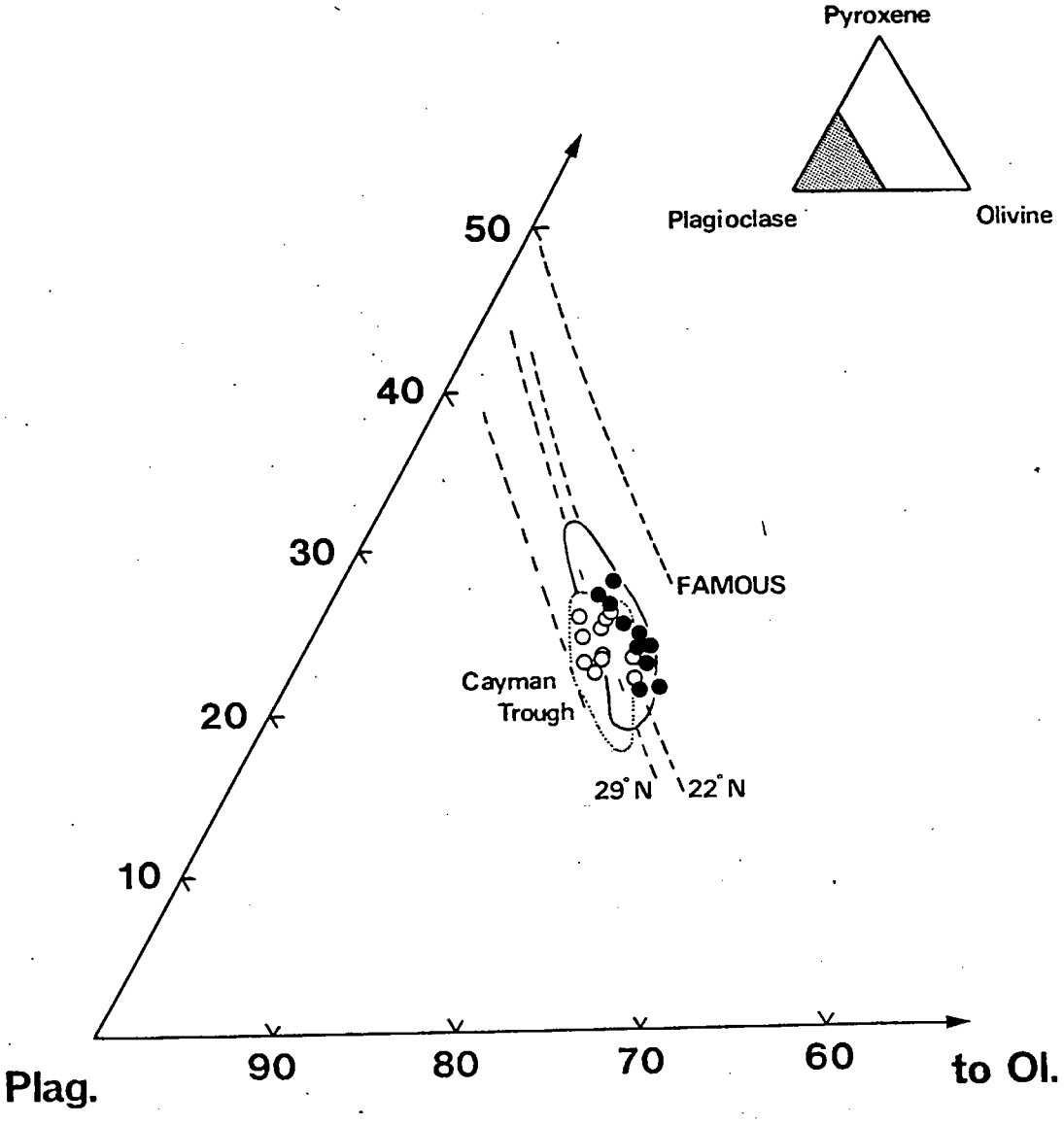

Figure 23: Normative plagioclase - pyroxene - olivine compositions of Ridge A and B basalt glass. On average, Ridge B glasses have a higher normative plagioclase content than Ridge A glasses. Symbols as in Figure 21. Fields include all glass analyses (le Roex, unpublished data) for Ridge A (solid line) and B (dotted line) lavas.

average glass compositions are significantly different for the two ridge segments. In spite of considerable overlap of samples, this average difference is comparable to the difference observed in basalts from the MAR at 22 and 29°N (Bryan and Dick, 1982). More specifically, Ridge B glasses are offset to higher normative plagioclase contents relative to Ridge A basalt glass.

To obtain a qualitative evaluation of phases involved in producing the glass fractionation trends, use has been made of a plot of CaO/Al_2O_3 (weight ratio) versus Mg* (Bence et al., 1979). The Mg* ($Mg/Mg+Fe^{2+}$ ratio) is employed as an index of olivine or pyroxene fractionation while the CaO/Al_2O_3 ratio reflects pyroxene or plagioclase fractionation. Plagioclase crystallization (CaO/Al_2O_3 ~ 0.5) will increase the ratio in the residual melt whereas high Ca pyroxene (CaO/Al_2O_3 ~ 7) crystallization will dramatically decrease the ratio. Olivine crystallization will leave it unchanged.

As a group, the glasses show a relatively large scatter in Figure 24 and CaO/Al_2O_3 ratios are generally higher than in corresponding whole rocks. The latter observation, together with increases in CaO/Al_2O_3 ratios with decreasing Mg* in glasses of specific dredges (e.g. Dredge 3, 5 and 13) is consistent with control by olivine and plagioclase

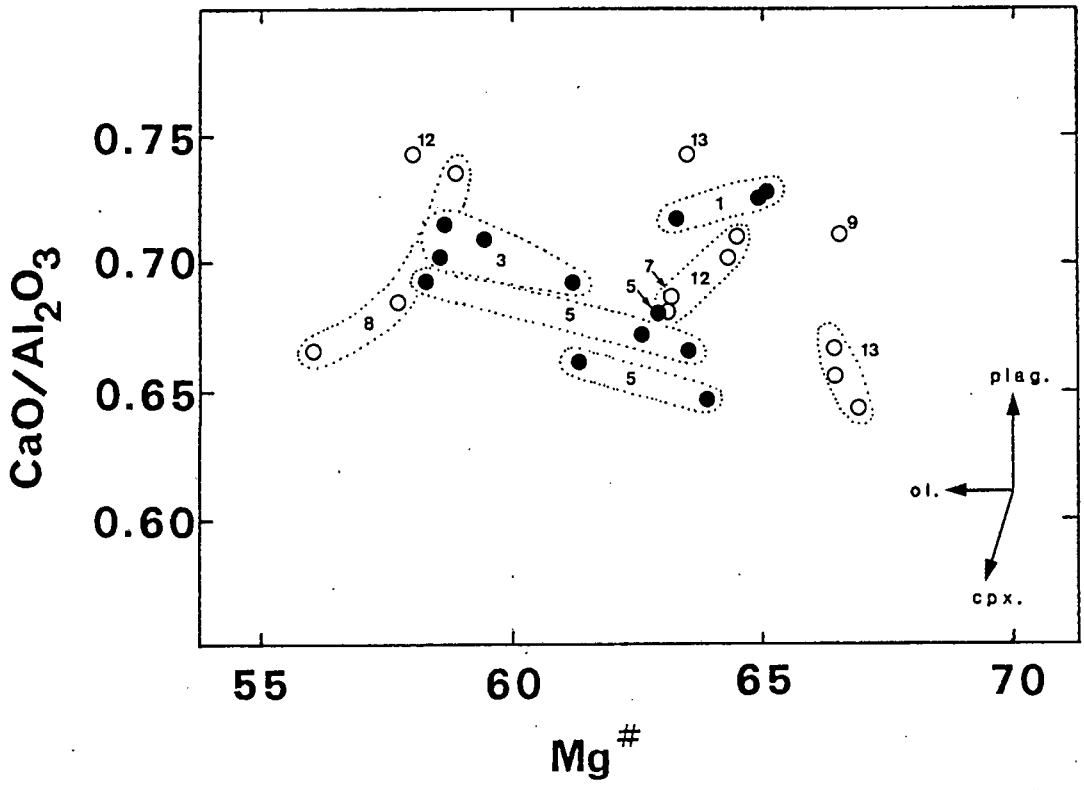

Figure 24: CaO/Al_2O_3 (wt % ratio) versus $Mg^{\#}$ for Agulhas 22 glasses (this study). Symbols as in Figure 21. Dotted lines enclose fields of basalts with similar trace element characteristics; note the coherent trends consistent with fractional crystallization.

fractionation. In contrast, decreasing CaO/Al_2O_3 ratios with decreasing Mg^* (e.g. Dredge 1, 8 and 12) suggest control by clinopyroxene fractionation (see also whole rock data). The coherent trends in glass data for individual Dredge hauls suggest an origin due to fractional crystallization.

4.3 Melt Inclusions; an introduction

Examination of the nature and significance of melt inclusions may yield important information on physico-chemical conditions of a fractionating magma (Roedder, 1976). In particular, it has successfully been demonstrated that such inclusions in liquidus minerals may provide important constraints on magma compositions at the time of melt entrapment (e.g. Anderson and Wright, 1972; Anderson, 1976; Watson, 1976; Donaldson and Brown, 1977; Dungan and Rhodes, 1978; le Roex et al., 1981). Melt inclusions in Agulhas 22 basalts occur in most mineral phases but only sufficiently large enough to analyse by microprobe in plagioclase crystals in the plagioclase porphyritic basalts of Dredges 8 and 12.

Melt inclusions in plagioclase megacrysts range from small oval micro-inclusions (<0.3mm) to large irregularly shaped inclusions up to 2mm long. Inclusions can be subdivided into two categories based on shape, size and distribution, although there is some gradation between categories.

Type 1 inclusions vary from oval to subspherical micro-inclusions (30-300 microns) to large (2mm) individual inclusions. In small inclusions, melts are glassy with a higher refractive index than host plagioclase, whereas larger ones are frequently occupied by a devitrified dark-brown melt (Plate 3,H). Spherical vapour bubbles (diameter roughly 1/6th of inclusion) occur in most inclusions and daughter crystals are rare (minute unidentifiable transparent to yellow-brown daughter crystals have been observed). Micro-inclusions are restricted to highly calcic type 1 megacrysts, and it is this association that is characteristic.

Irregular (type 2) inclusions vary from isolated oval shaped forms to larger bleb-like and rod-like interleading forms typically orientated along growth zones (Plate 3,A). Lengths range from 100 microns to 1.0mm, and included material ranges from glassy to devitrified with fringes of post-entrapment crystallization products extending inward from inclusion walls. Type 2 inclusions occur in both type 1 and type 2 plagioclase megacrysts but are more numerous in the latter. Interleading, channel-like inclusions are most common and conspicuous in plagioclase of composition An_{79}, which can display spectacular skeletal morphology in sections cut parallel to (110); eg. Plate 3,F. In type 2 plagioclase megacrysts exhibiting patchy zoning, inclusions frequently occur in negative crystal form.

4.4 Melt Inclusion Chemistry

Representative melt inclusion analyses are presented in Table 13. Analyses were obtained using a relatively broad beam ($\geq$ 5um diameter). Where large enough, inclusions were analysed at their centres and near inclusion walls. Contamination by excitation of host plagioclase was generally only noted among inclusions similar in size to the beam size (e.g. analyses 1-5, Table 12).

The chemical variation is illustrated in Figure 25. The usefulness of the CaO/Al_2O_3 ratio versus $Mg^{\#}$ has been discussed in an earlier section and the whole rock variation in Ridge B lavas is shown for comparison. Interaction of inclusions and host plagioclase should be reflected in varying CaO/Al_2O_3 at a constant $Mg^{\#}$; for example micro-inclusions mentioned above have lower CaO/Al_2O_3 than large inclusions, attributable to fluorescence of host plagioclase.

The TiO_2-$Mg^{\#}$ diagram (Figure 25,a) is most often employed in melt inclusion studies because: (a) post-entrapment crystallization should not markedly affect $Mg^{\#}$, and (b) TiO_2 is relatively incompatible and should be an indicator of post-entrapment crystallization (e.g. Dungan and Rhodes, 1978; Clocchiatti and Massare, 1985). Minimum TiO_2 contents of melt inclusions (Figure 25,a), at a given $Mg^{\#}$, are relatively uniform. Moreover, they are also similar

Table 12 : Representative analyses of melt inclusions in plagioclase megacrysts; Dredge 8 and 12 porphyritic lavas.
$Mg\#$ calculated assuming $Fe_2O_3/FeO = 0.15$.

	1	2	3	4	5	6	7	8	9	10
SiO_2	47,79	47,22	47,61	50,30	50,17	50,93	49,75	50,21	49,72	50,25
TiO_2	1,42	1,34	1,06	1,11	1,21	1,86	1,20	1,56	1,58	1,41
Al_2O_3	16,01	16,71	16,27	16,24	16,40	15,15	16,74	15,31	15,28	16,51
FeO*	10,69	10,82	10,98	8,10	8,19	9,81	8,36	9,99	9,47	8,59
MnO	0,18	0,14	0,18	0,12	0,15	0,27	0,15	0,13	0,13	0,13
MgO	12,64	12,37	12,29	9,07	9,40	8,42	9,11	8,47	9,15	8,52
CaO	10,64	10,80	10,10	10,94	10,81	10,72	11,28	10,83	10,82	11,07
Na_2O	1,36	1,35	1,36	1,14	3,22	3,48	2,98	3,63	3,52	3,01
K_2O	0,12	0,14	0,22	0,11	0,13	0,13	0,12	0,12	0,12	n.d
TOTAL	100,93	100,90	100,07	99,13	99,68	100,78	99,69	100,25	99,79	99,48
Mg#	0,706	0,698	0,693	0,694	0,699	0,634	0,688	0,631	0,662	0,667

Analyses 1 to 3; Type 1 megacryst (An_{81}); AG22-8-16
4; Type 1 megacryst (An_{79}); AG22-12-1
5; Type 1 megacryst (An_{80-78}); AG22-12-2
6; Type 2 megacryst (An_{72-75}); AG22-8-1
7; Type 2 megacryst (An_{74-77}); AG22-12-1
8 to 9; Type 2 megacryst (An_{70-76}); AG22-12-4
10; Type 2 megacryst (An_{76-78}); AG22-12-20

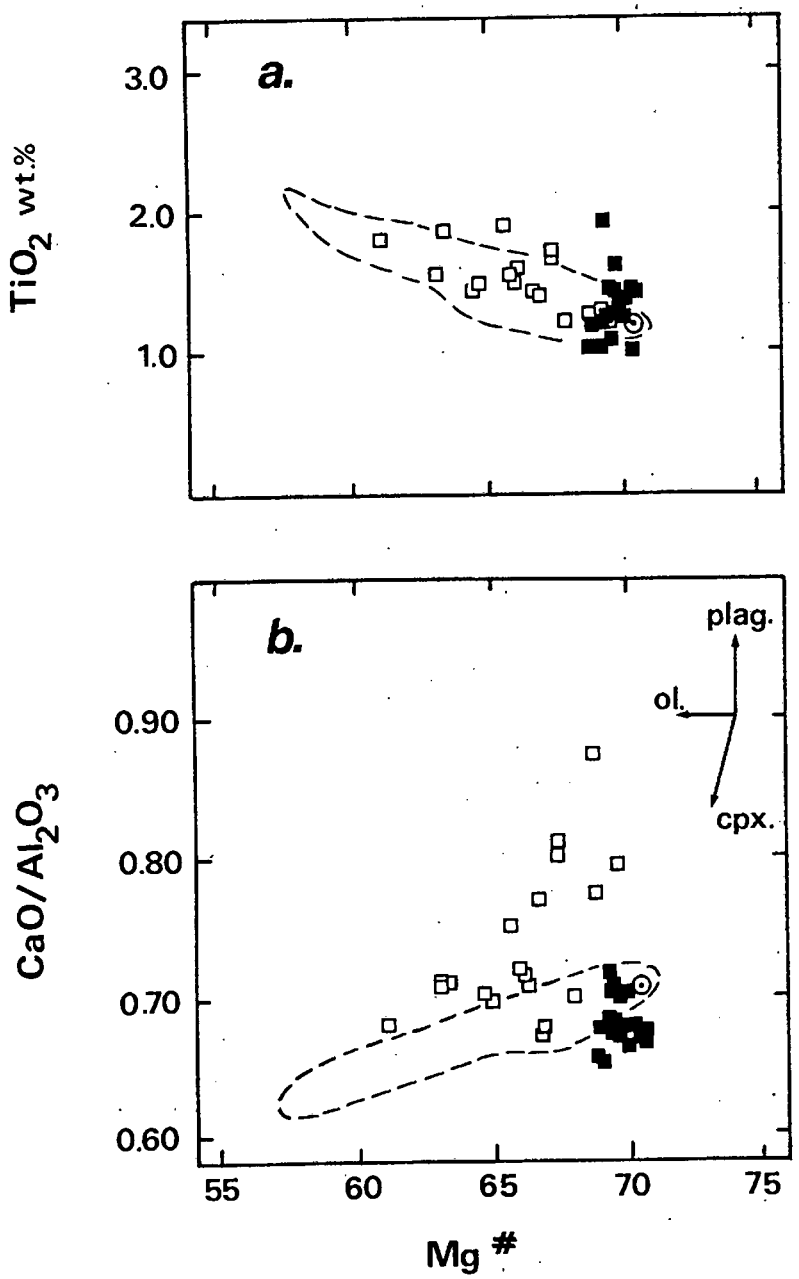

Figure 25: Variation of CaO/Al_2O_3 and TiO_2 with Mg* of melt inclusions in plagioclase megacrysts. Filled squares represent type 1 inclusions, open squares are type 2 inclusions. The circle represents lavaAG22-9-2. Field of Ridge B whole rocks for comparison.

to whole rock TiO_2 contents which define a well constrained linear relationship. Several high TiO_2 contents reflect the importance of post-entrapment crystallization in governing melt inclusion chemistry. This is supported by petrographic evidence (Plate 3) and correspondingly elevated CaO/Al_2O_3 values.

In addition to the above observations, it is evident that inclusions nearer the centre of several plagioclase crystals have apparently suffered more post-entrapment crystallizatioin than those successively further away (i.e. they have higher CaO/Al_2O_3 ratios and TiO_2 contents). This supports the contention that the inclusions originated due to growth under supersaturated conditions if primary crystallization was rapid, as skeletal morphologies suggest (Plate 3). Alternatively, if growth was slow, the post-entrapment crystallization may be purely a function of time. In view of known crystal growth rates (e.g. as low as 0.3mm/yr; Kirkpatrick, 1977) this may be possible.

As can be seen in Figure 25, melt inclusion chemistry correlates with crystal composition; inclusions in labradorite plagioclase display a range in $Mg^{\#}$ similar to that observed in whole rock compositions while inclusions in bytownitic plagioclase have a restricted $Mg^{\#}$, converging on, or similar to, the composition of most primitive lava

AG22-9-2. TiO_2 contents and CaO/Al_2O_3 ratios of AG22-9-2 and the inferred primitive inclusion composition are also similar. This supports the view that the melt inclusions are cogenetic, that is, they share a common parentage and hence that crystals are liquidus products of a higher temperature stage of crystallization (e.g. Fisk et al., 1982).

In conclusion, although somewhat modified by post-entrapment crystallization, melt inclusions provide evidence for two broad episodes of crystallization. The first involved entrapment of a magma similar in composition to primitive lava AG22-9-2 in bytownitic plagioclase. The second event is indicated by inclusion of a relatively more evolved, and evolving magma in zoned labradoritic plagioclase.

****

CHAPTER 5

WHOLE ROCK GEOCHEMISTRY

5.1 Introduction

The aim of this chapter is to present the Agulhas 22 geochemical data with the view to determining the petrogenesis of the lavas. The data is presented in terms of within-sample and between-sample variations and within- and between-dredge variations. Variations are then evaluated in terms of fractional crystallization.

Major, minor and trace element data (le Roex, unpublished data) are presented in Tables 15 to 19. Error estimates are given in Appendix 1.

5.2 Alteration

The majority of Agulhas 22 basalts show varied evidence of alteration with Fe-hydroxides and secondary clay minerals (especially Dredge 3 and 5 samples). Observed L.O.I. - loss on ignition at 1000°C: H_2O+CO_2 and other volatile components - values (0.38-1.47 wt%) demonstrate that analysed basalts may be moderately altered (average LOI = 0.82 wt %).

Sea floor alteration is known to be a complex phenomenon involving for the most part a decrease in the contents of

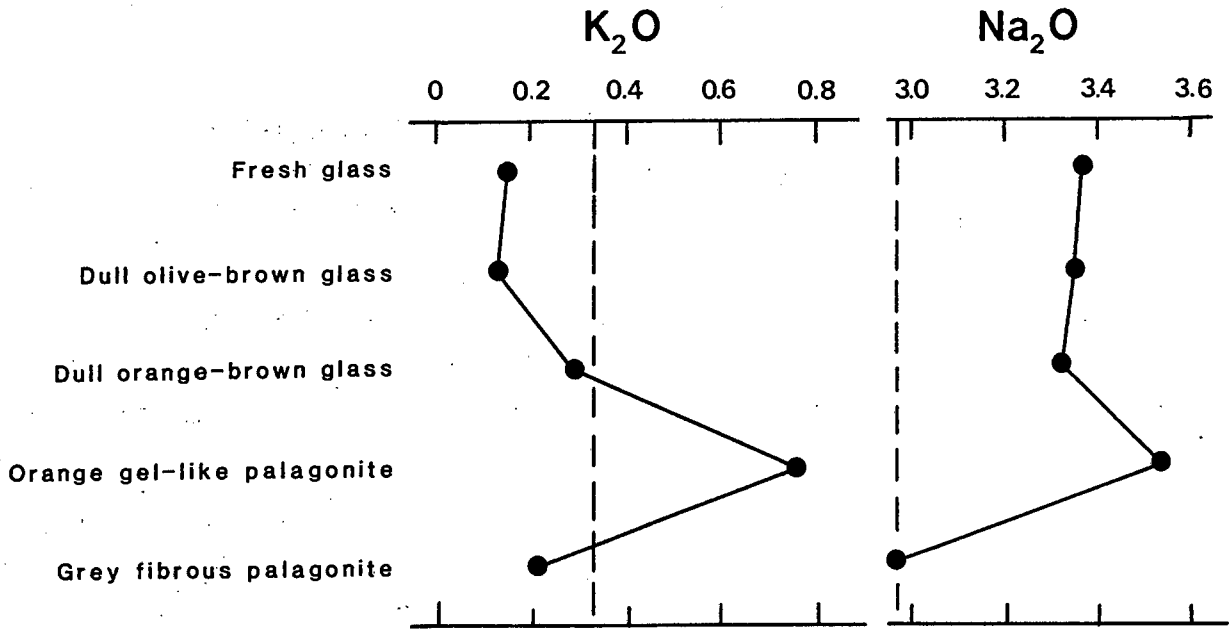

Figure 26: A graphical profile illustrating the chemical change involving alkalis (wt. %) accompanying alteration of glass to palagonite in lava AG22-3-2. Note that the values of analysis 3 (Table 13) have been plotted directly without normalization. Dotted lines represent whole rock composition.

	1.	2.	3.	4.	5.
SiO_2	50.25	48.95	47.52	49.87	49.62
TiO_2	1.90	1.74	1.66	1.63	1.89
Al_2O_3	15.55	16.13	15.72	16.57	15.07
FeO	10.59	9.85	9.64	10.12	10.49
NiO	0.15	0.16	0.12	0.12	0.18
MgO	7.51	7.59	7.35	7.81	7.32
CaO	10.66	11.23	10.39	11.18	10.48
Na_2O	3.35	3.32	3.53	2.97	2.98
K_2O	0.15	0.29	0.76	0.21	0.20
Total	100.03	99.25	96.69	100.47	100.01*

Table 13: Compositions of quench glass and whole rock of lava AG22-3-2. Numbers represent fresh (1) to altered (2,3,4) glasses and whole rock composition (5). (* includes 0.83% LOI, 0.48% H_2O). Note the overall increase in alkalis to orange gel-palagonite (analysis 3, Figure 26), particularly K_2O. Characteristics are consistent with low-temperature sea-water alteration by percolation along radial cooling cracks observed by Scott and Hajash (1976).

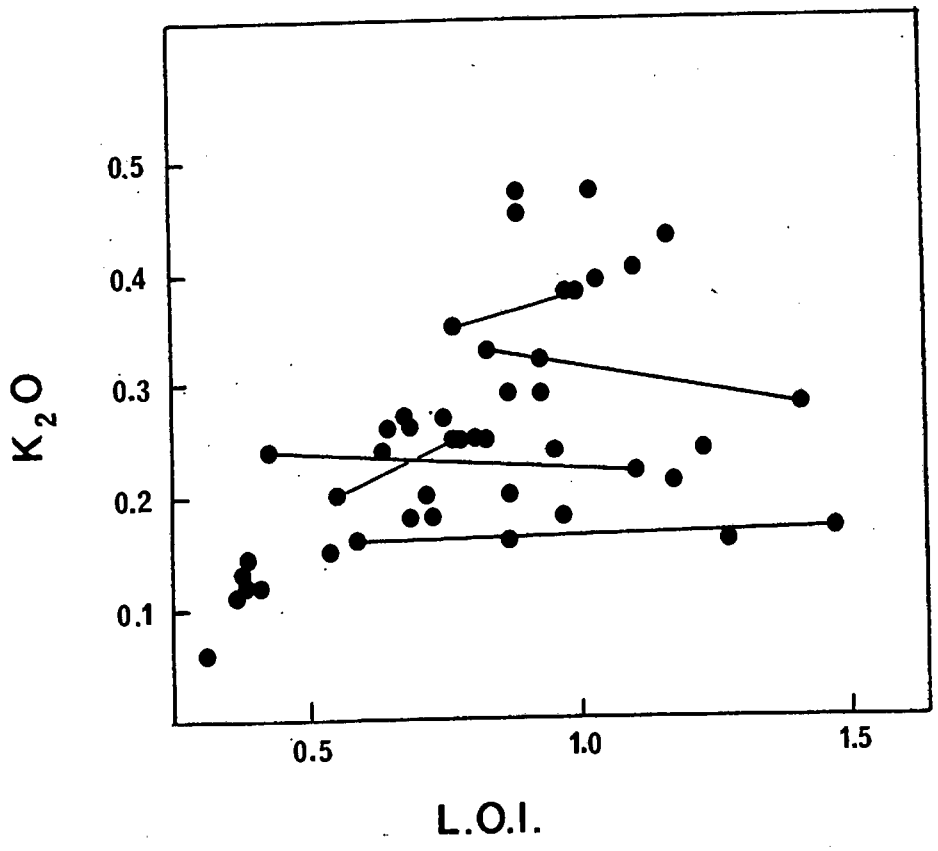

Figure 27: K_2O versus percentage weight loss on ignition (LOI) for Agulhas 22 basalts. Note the general positive correlation but varied behaviour described by tie-lines joining chemically similar samples identified by less mobile elements and trace element abundances.

SiO_2, CaO, MgO and Ni and an increase in L.O.I., K, Rb and total iron (Miyashiro et al., 1970; Hart, 1969; 1970; Hart et al., 1974). A plot of K_2O versus LOI (Figure 27) for Agulhas 22 basalts demonstrates that K_2O behaves in a very unpredictable fashion, consistent with the mobile nature of this element (Hart, 1969; 1970).

Relative to fresh glass, palagonitized glass of sample AG22-3-2 is enriched in K_2O by a factor of 5 (see Table 13 and Figure 26), explicable in terms of the effect of seawater exchange (ie. added by percolating seawaters; Scott and Hajash, 1976).

Other elements known to be affected to varying degrees by alteration processes include Rb, Ba, Sr, Cu and Co (Hart et al., 1974; Humphris et al., 1978; Staudigel et al., 1981). Hart (1969; 1970) established that Rb is generally enriched 2.5 times faster than K during seawater alteration. In Figure 31, it is evident that there is a substantial scatter in Rb contents in Agulhas 22 basalts which is in accord with the above observation.

For this reason Rb and K are avoided in subsequent sections and emphasis is placed instead on less mobile elements and specifically elements which are considered to be immobile in ocean floor basalt alteration (e.g. Ti, P, Zr, Nb, Y, Cr, V and Zn; Hart et al., 1974; Erlank and Kable 1976; Humphris

and Thompson, 1978; Staudigel et al., 1981; Alt and Honnorez, 1984).

5.3 Within-sample variation

Relationships between glass and corresponding whole rock compositions may be visualized in MgO-variation diagrams (Figure 28) in which glass-whole rock pairs are indicated by tie-lines. Also shown are vectors representing trends expected by addition (or removal) of indicated proportions (volume per cent) of plagioclase, pyroxene and/or olivine to an arbitrarily chosen composition (Staudigel and Bryan, 1981).

Three types of tie-lines are present. Type 1 tie-lines parallel the olivine vector leading to an MgO depletion in quench glass relative to whole rock. Type 2 tie-lines parallel the plagioclase vector leading to an MgO depletion in whole rock relative to quench glass. Type 3 tie-lines require a combination of plagioclase and a mafic phase leading to an MgO depletion in quench glass relative to whole rock. Staudigel and Bryan (1981) recognised the former two types of tie-line relationships in basalts from IPOD sites 417 and 418 in the North Atlantic. These authors emphasized the importance of phenocryst redistribution (especially plagioclase; type 2 tie-lines) in controlling whole rock compositions.

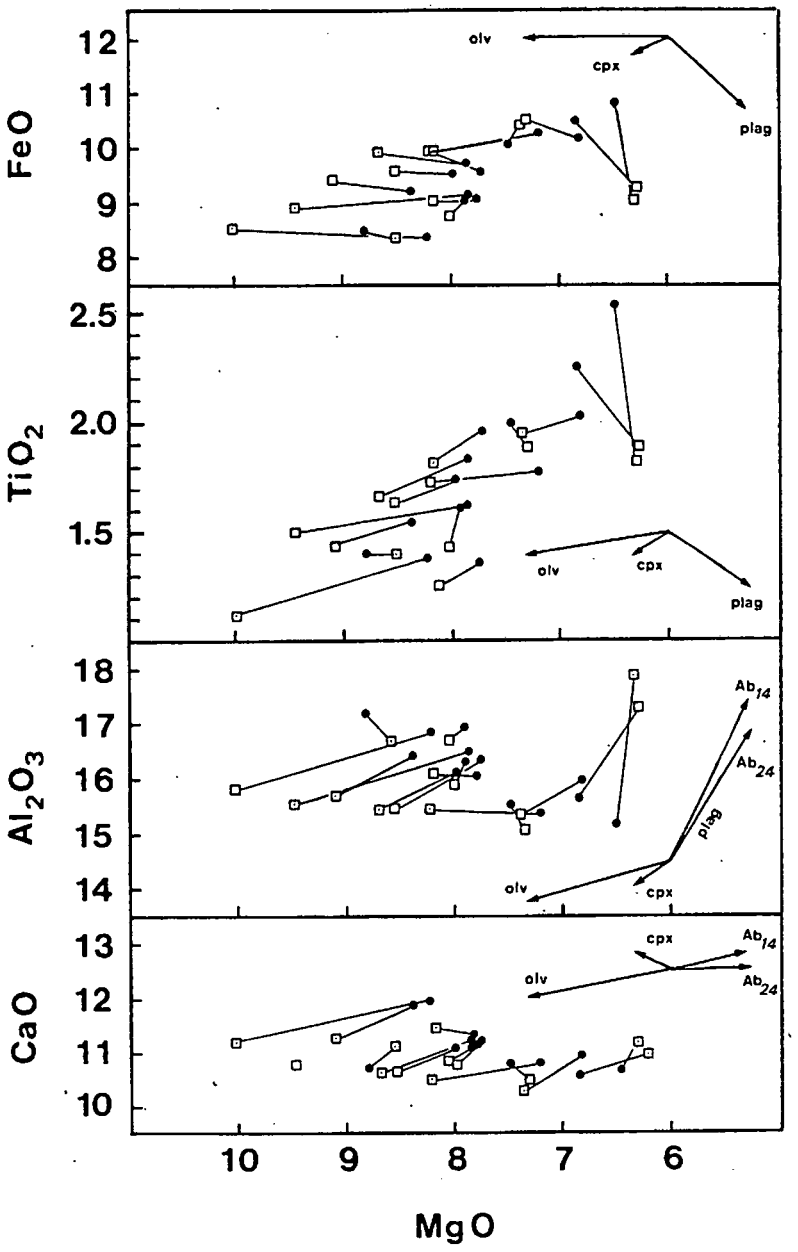

Figure 28: Selected MgO-oxide variation diagrams to illustrate glass (circles) versus whole rock (squares) relationships in Agulhas 22 basalts. Vectors represent addition of 3 volume % olivine (olv), pyroxene (cpx) and plagioclase (plag, Ab) to an arbitrary composition (Staudigel and Bryan, 1981).

Similar relationships are relevant to Agulhas 22 porphyritic lavas. Glass-whole rock relationships in aphyric and sparsely porphyritic lavas are consistent with observed microphenocryst phases and modes (see Figure 28 and Table 5).

For reasons outlined above, glass compositions have been used in preference to whole rock compositions in many studies (e.g. Natland and Melson, 1980; Bender et al., 1984). Nevertheless, since Dredge 7 and 9 lavas are aphyric (microporphyritic) it is not unreasonable to expect that whole rock compositions may represent liquid compositions. In fact, in terms of $Mg^{\#}$ and MgO abundances, these whole rock compositions are similar to several known primitive quench glass and MORB compositions recovered from the Atlantic Ocean to date (e.g. Table 14). This is significant since the latter compositions are considered by many petrologists to represent primary (or near primary) magmas formed by direct melting of the suboceanic mantle (e.g. Presnall et al., 1979; Basaltic Volcanism Study Project, 1981).

In this respect, and as argued in Chapter 6 later, samples AG22-7-2 and AG22-9-1 are even more primitive than primitive basalts documented by Bryan et al (1979) which they believe are primary magmas formed near 9 kb (eg. Presnall et al, 1979).

TABLE 14: Some primitive compositions of selected basalt and basalt glasses from the literature.

	1	2	3	4
SiO_2	50.30	50.40	49.10	49.40
TiO_2	0.73	0.70	0.62	0.81
Al_2O_3	16.60	15.60	16.50	15.64
FeO*	7.99	7.10	8.78	7.44
MnO	0.12	0.20	0.15	0.15
MgO	10.20	9.10	10.30	10.01
CaO	13.20	13.60	12.40	12.93
Na_2O	2.00	2.00	1.92	1.95
K_2O	0.01	0.30	0.07	0.17
	101.15	99.00	99.84	98.50
Mg#	72.10	72.20	69.90	73.10
Ni, ppm	200		232	249

1. Quench glass, South Atlantic: Frey et al. (1974): Sample 3-18-7-1.
2. Melt inclusion reconstruction, Bouvet Triple Junction: Watson (1976).
3. "Primitive" glass, FAMOUS area (Langmuir et al., 1977; table 1, 527-1-1).
4. Aphyric basalt, 45°N MAR (Dungan and Rhodes, 1978: Chain 43-4-23).

5.4 Within-dredge variation

In this section, the compositional variations in analysed basalt samples is given. Distinct glass and whole rock groups are recognised on the basis of chemical equivalence, analogous to the procedure of Melson et al. (1976). Oxide differences in major element analyses are compared to analytical error (tolerance of 2 sigma) and, in whole rock analyses, grouping is aided by absolute and relative abundances of trace elements (Tables 15 to 19).

5.4.1 Ridge A

Dredge 1

Major element analyses of natural glasses from eight randomly selected samples establish that glasses exhibit a restricted range in composition. Relative to average MORB glass (Melson et al., 1976) the $Mg^{\#}$ (100 X $Mg/Mg+Fe^{2+}$ assuming $Fe_2O_3/FeO=0.15$; Brooks, 1976) indicates that compositions are fairly evolved ($Mg^{\#}$=65-63) with relatively high TiO_2 (1.5-1.6 wt%), Al_2O_3 (16.1-16.5 wt%) and Na_2O (2.9-3.1 wt%) and low K_2O (0.06-0.22 wt%) contents.

Whole rock chemical analysis of AG22-1-1 establishes that this pillow lava is an olivine normative tholeiite with a relatively primitive composition (e.g. $Mg^{\#}$=66; MgO=9.1 wt%;

Table 15: Whole-rock analyses (wt. %) of selected basalts of Dredge 1 and 3. Fe_2O_3 and Mg# calculated assuming Fe_2O_3/FeO = 0.15. Trace elements in ppm. Mineral norms calculated with Fe_2O_3 = 0.15, normalized volatile free. AP = aphyric; PP = plagioclase porphyritic; SP = sparsely porphyritic; OPP = olivine plagioclase porphyritic.

	A622-1-1 AP	A622-3-2 AP	A622-3-4 AP	A622-3-20 AP	A622-3-23 AP	A622-3-29 AP	A622-3-34 AP
SiO_2	49.32	49.62	49.19	49.47	49.07	48.72	49.00
TiO_2	1.43	1.89	1.73	1.74	1.74	1.91	1.81
Al_2O_3	15.70	15.07	15.43	15.28	15.34	14.98	15.56
Fe_2O_3	1.25	1.39	1.31	1.30	1.43	1.40	1.32
FeO	8.30	9.24	8.76	8.66	9.53	9.30	8.82
MnO	0.16	0.18	0.18	0.17	0.17	0.19	0.16
MgO	9.10	7.32	8.23	7.69	7.90	7.45	7.52
CaO	11.26	10.48	10.49	10.66	10.40	10.42	10.73
Na_2O	2.73	2.98	3.06	3.19	3.13	3.03	3.30
K_2O	0.12	0.33	0.35	0.39	0.38	0.28	0.21
P_2O_5	0.14	0.20	0.19	0.19	0.18	0.21	0.19
L.O.I	0.39	0.83	0.77	1.03	0.99	1.41	1.17
H_2O	0.19	0.48	0.39	0.53	0.38	0.79	0.64
Total	100.09	100.01	100.08	100.30	100.64	100.09	100.43
Zr	98	145	130	132	128	146	137
Nb	2.3	2.6	3.6	3.1	3.5	4.5	3.0
Y	32	41	35	36	38	41	40
Rb	1.7	5.0	3.9	6.5	9.2	4.8	3.4
Ba	14.2	13.3	14.9	16.5	15.0	19.0	9.6
Sr	129	154	164	166	142	160	146
Co	51	49	51	46	52	49	47
Cr	394	223	320	272	255	246	255
Ni	188	121	170	131	161	137	120
V	240	283	250	255	255	279	258
Zn	72	85	81	79	85	86	77
Cu	65	58	58	56	65	58	60
Sc	39	42	37	39	39	40	38
Zr/Nb	43	56	36	43	37	32	46
Zr/Y	3.1	3.5	3.7	3.7	3.4	3.6	3.4
Y/Nb	14.0	15.8	9.7	11.6	10.9	9.1	13.3
Ti/Zr	88	79	81	80	82	79	80
Ti/P	14.2	13.1	12.6	12.7	13.4	12.6	13.2
Zr/Ba	6.9	10.9	10.0	8.0	8.5	7.6	14.2
Mg#	66.1	58.5	62.6	61.3	59.6	58.8	60.3
Qz	-	-	-	-	-	-	-
Or	0.72	1.97	2.09	2.33	2.26	1.69	1.26
Ab	23.21	25.55	26.17	27.34	26.68	26.19	28.31
An	30.38	27.12	27.63	26.56	26.88	27.02	27.40
Ne	-	-	-	-	-	-	-
Di	20.15	19.83	19.32	21.00	19.55	19.95	20.66
Hy	8.69	12.39	6.20	4.98	4.38	8.82	3.04
Ol	11.98	6.99	12.90	12.10	14.41	10.06	13.45
Mt	1.82	2.04	1.92	1.91	2.09	2.07	1.94
Ilm	2.73	3.64	3.32	3.35	3.33	3.71	3.49
Ap	0.33	0.48	0.45	0.45	0.43	0.51	0.46

Ni=188 ppm; Cr=394 ppm), comparable to published analyses of primitive MORB (Table 14). Primary magmas to MORB are expected to have $Mg^{\#}$=68-73 (Ito, 1973; Green et al., 1979), Ni>200 ppm (Hart and Davis, 1978; Sato, 1977), and Cr>400 ppm (Sun et al., 1979).

Zr (98 ppm), Nb (2.3 ppm) and Y (32 ppm) abundances are within the range typical for MORB (e.g. Kable, 1972; Erlank and Kable, 1976; le Roex et al., 1983, 1985). Relative abundances of these incompatible elements (e.g. Zr/Nb=43; Zr/Y=3.1; Y/Nb=14) indicate the sample to be typical N-type MORB. The sample has a Ti/Zr ratio of 88, very close to average Indian Ocean basalt (av. Ti/Zr=90; Frey et al., 1980) and SWIR basalt between 0 and 11°E (av. Ti/Zr=87; le Roex et al., 1983).

Dredge 3

Analysed quench glasses exhibit a wider range in composition and a more evolved nature than Dredge 1 glass (e.g. $Mg^{\#}$=61-58; MgO=8.5-7.5 wt%; TiO_2=1.8-2.0 wt%). Relative to Dredge 1 glass they have lower Al_2O_3 (15.6-16.0 wt%) and CaO (10.2-11.1 wt%) and higher Na_2O (2.9-3.5 wt%) contents. K_2O contents are low (0.06-0.15 wt%).

Major and trace element XRF analyses of six selected samples (two pillow basalts, four without glass) are presented in

Table 15. Samples are olivine normative (7-14% olivine in the norm) with a similar range in composition to the quench glasses (e.g. $Mg^{\#}$=62-59; MgO=8.2-7.3 wt%; TiO_2=1.7-1.9 wt%).

Relatively high LOI values (0.77-1.41 wt%) demonstrate the moderately altered nature of the samples. The range in ferromagnesian trace element abundances (e.g. Ni=170-120 ppm; Cr=320-246 ppm) similarly demonstrate the moderately evolved nature and chemical variation of the basalts.

Incompatible trace element abundances (e.g. Zr=130-146 ppm; Nb=2.6-4.5 ppm; Y=35-41 ppm) also demonstrate this range in composition. Incompatible element ratios (e.g. Zr/Nb=32-56; Y/Nb=9-16; Zr/Y=3.4-3.7) are within the range of N-type MORB ratios from the SWIR (le Roex et al., 1983) and similar to those characteristics of Dredge 1 basalts. Ti/Zr ratios (80 $\pm$ 2) are significantly lower than chondritic and north Atlantic averages (Ti/Zr=100-110; Sun et al., 1979), and more closely resemble those of the American-Antarctic Ridge (AAR) basalts between 4 and 18°W (av. Ti/Zr=83 $\pm$ 11; le Roex et al., 1985).

The relatively coherent trends in oxide and trace element abundances suggest that the samples may be related by fractional crystallization. A fractional crystallization model attempting to relate basalt AG22-3-2 to AG22-3-4 is given in Chapter 6. Despite the broadly coherent trends,

differences in Zr/Nb ratios cannot be reproduced by simple olivine and plagioclase fractionation (Zr and Nb are incompatible in these phases; see Chapter 6), suggesting that these differences are perhaps due to partial melting and/or source region characteristics (le Roex et al., 1987).

Dredge 5

Microprobe analyses of quench glasses establish that samples from Dredge 5 (Table 16) are olivine normative with a similar but wider range in composition to Dredge 3 glasses (e.g. $Mg^{\#}$=64-58; MgO=8.2-6.8 wt%; TiO_2=1.5-2.1 wt%). On the basis of K_2O and TiO_2 contents however, two broad chemical glass types are identified (eg. Table 10). Type I glasses (the majority of glasses) have, for the same range in $Mg^{\#}$, lower K_2O (0.05-0.18 wt%) and TiO_2 (1.5-1.8 wt%) contents than Type II (2 samples) glasses which have K_2O=0.20-0.26 wt% and TiO_2=1.7-2.1 wt%. CaO and Al_2O_3 contents are generally lower than Dredge 1 glasses but in most primitive samples (e.g. AG22-5-1, AG22-5-6), Al_2O_3 contents are high (Al_2O_3=17.1 wt%) relative to samples from other dredges with similar $Mg^{\#}$ (e.g. Al_2O_3=16.1 wt% & $Mg^{\#}$=66 in AG22-1-8; Al_2O_3=15.8 wt% & $Mg^{\#}$=66 in AG22-3-4).

Major and trace element XRF analyses of bulk rock samples similarly reflect the within-dredge variation described by glass compositions. $Mg^{\#}$ ranges from 66-59, Ni=189-113 ppm and TiO_2=1.4-2.0 wt%. Samples are olivine tholeiites (9-16

TABLE 16: Whole rock analyses of Dredge 5 basalts. Fe_2O_3 and Mg# calculated assuming $Fe_2O_3/FeO = 0.15$. Abbreviations as in Table 15.

	A622-5-2 AP	A622-5-7 AP	A622-5-14 AP	A622-5-15 AP	A622-5-18 AP	A622-5-31 AP	A622-5-38 AP	A622-5-46 AP	A622-5-48 AP	A622-5-51 AP	A622-5-59 AP	A622-5-65 AP	A622-5-66 AP	A622-5-68 AP
SiO_2	49.70	50.03	49.44	49.34	49.44	49.57	49.37	49.14	49.33	49.49	48.94	49.75	49.37	49.08
TiO_2	1.58	1.60	1.96	1.58	1.59	1.67	1.64	1.43	1.77	1.66	1.50	1.69	1.96	1.62
Al_2O_3	15.82	15.91	15.32	15.87	15.79	15.45	15.46	16.50	15.37	15.75	15.70	15.53	15.32	15.32
Fe_2O_3	1.23	1.24	1.38	1.29	1.25	1.31	1.27	1.24	1.32	1.31	1.24	1.31	1.33	1.25
FeO	8.18	8.25	9.19	8.61	8.30	8.73	8.44	8.28	8.83	8.74	8.28	8.72	8.89	8.34
MnO	0.18	0.17	0.17	0.16	0.16	0.16	0.16	0.15	0.17	0.16	0.17	0.16	0.16	0.16
MgO	8.31	8.14	7.36	7.98	8.14	8.68	8.54	8.35	7.24	8.05	8.81	7.55	7.14	8.61
CaO	10.99	11.04	10.28	10.74	11.01	10.61	10.64	10.99	10.55	10.73	10.64	10.72	10.38	10.56
Na_2O	3.10	3.06	3.19	3.06	2.99	3.04	3.16	3.16	3.19	3.14	3.19	3.42	3.40	3.01
K_2O	0.24	0.26	0.47	0.29	0.26	0.27	0.45	0.20	0.16	0.24	0.18	0.22	0.46	0.38
P_2O_5	0.17	0.18	0.23	0.16	0.17	0.18	0.21	0.15	0.18	0.17	0.15	0.17	0.23	0.21
L.O.I	0.64	0.69	0.89	0.87	0.65	0.68	0.89	0.87	1.27	0.43	0.97	1.10	1.16	0.97
H_2O	0.23	0.27	0.34	0.36	0.23	0.25	0.34	0.40	0.71	0.31	0.37	0.36	0.40	0.37
Total	100.37	100.84	100.22	100.31	100.48	100.48	100.57	100.86	100.09	100.18	100.14	100.70	100.20	99.88
Zr	115	117	146	116	115	127	128	103	133	123	113	125	147	128
Nb	4.0	4.5	9.8	3.2	3.6	2.8	7.6	2.9	2.5	3.1	<1.4	<1.4	9.6	7.7
Y	34	34	40	33	33	34	34	30	38	35	32	37	39	33
Rb	1.6	2.7	6.8	3.8	3.5	2.7	6.4	2.2	3.1	4.5	3.3	4.4	7.1	6.1
Ba	17.2	17.3	41	10.4	15.0	14.4	34	10.7	8.0	12.3	4.8	7.6	41	36
Sr	146	148	182	156	148	168	191	164	151	157	148	150	185	192
Co	49	48	46	51	48	51	50	51	48	48	50	47	48	50
Cr	322	322	188	280	321	340	350	306	239	266	354	237	186	353
Ni	144	143	115	152	148	172	181	155	115	144	189	113	118	178
V	241	244	270	232	244	242	239	205	262	241	229	247	265	238
Zn	72	74	84	75	72	76	76	70	80	77	70	76	82	76
Cu	55	58	50	63	58	62	57	67	61	61	60	62	53	58
Sc	38	38	40	39	38	39	36	36	40	39	36	35	37	38
Zr/Nb	29	26	14.9	36	32	45	18.8	36	53	40	>81	>89	15.3	16.6
Zr/Y	3.4	3.4	3.7	3.5	3.5	3.7	3.8	3.4	3.5	3.5	3.5	3.4	3.8	3.9
Y/Nb	8.5	7.6	4.1	10.3	9.1	12.1	4.5	10.3	15.2	11.3	>23	>26	4.1	4.3
Ti/Zr	83	83	81	83	84	80	78	84	81	82	80	82	81	77
Ti/P	12.9	12.3	11.8	13.7	13.0	12.9	10.8	13.2	16.4	13.6	13.6	13.8	11.8	10.7
Zr/Ba	6.6	6.8	3.6	11.2	7.7	8.9	3.7	9.6	16.6	10.0	23.5	28.4	3.7	3.5
Mg#	64.4	63.7	58.8	62.3	63.6	63.9	64.3	64.2	59.4	62.1	65.5	60.7	58.9	64.8
Qz	-	-	-	-	-	-	-	-	-	-	-	-	-	-
Or	1.42	1.54	2.81	1.73	1.54	1.60	2.68	1.19	0.96	1.42	1.08	1.31	2.75	2.28
Ab	26.37	25.93	27.27	26.13	25.40	25.81	26.92	26.85	27.51	26.72	27.32	29.16	29.17	25.85
An	28.68	28.94	26.36	28.98	29.01	27.80	26.85	30.37	27.67	28.33	28.33	26.58	25.53	27.57
Ne	-	-	-	-	-	-	-	-	-	-	-	-	-	-
Di	20.31	20.10	19.34	19.35	20.10	19.37	20.24	19.02	20.01	19.62	19.57	21.14	20.56	19.65
Hy	5.52	7.33	6.84	6.06	8.57	6.90	2.30	1.49	9.11	5.66	2.17	3.12	3.01	5.66
Ol	12.50	10.91	11.07	12.46	10.13	13.01	15.54	16.20	8.93	12.76	16.48	13.15	12.72	13.53
Mt	1.79	1.80	2.02	1.89	1.82	1.91	1.85	1.81	1.95	1.91	1.82	1.91	1.95	1.84
Ilm	3.02	3.04	3.76	3.03	3.03	3.18	3.14	2.73	3.43	3.17	2.88	3.23	3.77	3.12
Ap	0.41	0.43	0.55	0.38	0.41	0.43	0.50	0.36	0.43	0.41	0.36	0.41	0.55	0.50

wt.% olivine in the norm) which, on the basis of incompatible element abundances, can be separated into the two types indicated by glass chemistry. Type I basalts have relatively low incompatible minor element (e.g. TiO_2=1.43-1.77 wt%; P_2O_5=0.15-0.18 wt%; K_2O=0.16-0.29 wt%) abundances and incompatible trace element abundances (e.g. Zr=103-133 ppm; Nb=2.5-4.5 ppm; Rb=1.6-4.5 ppm; Ba=4.8-17.3) with Ti/Zr ratios (80-84) similar to AAR basalts from 4-18°W (le Roex et al., 1985) and Dredge 3 basalts.

Type II basalts have, for the same range in $Mg^{\#}$, higher incompatible minor element contents (e.g. TiO_2=1.62-1.96 wt%; P_2O_5=0.21-0.23 wt%; K_2O=0.38-0.47 wt%) as well as incompatible trace elements abundances (e.g. Zr=128-147 ppm; Nb=7.6-9.8 ppm; Rb=6.1-7.1 ppm; Ba=34-41 ppm Sr=182-192 ppm). Selected incompatible element ratios (Zr/Nb=14.9-18.8; Zr/Y=3.7-3.9; Y/Nb=4.1-4.5) reflect the more enriched, or less depleted, character of type II basalts which are nonetheless within the range of N-type MORB from the Southern Ocean (le Roex et al., 1983, 1985). Zr/Nb ratios are apparently intermediate between average T-type and N-type MORB from the AAR (le Roex et al., 1985) with an average (16.4) close to chondritic (16; e.g. Mason, 1972; Sun et al., 1979). The more mobile incompatible elements (e.g. Rb, Sr, Ba; Hart, 1971) show a greater scatter in type I basalts, suggesting that some of this variation may be attributed to alteration effects.

The relatively coherent variations within type I basalts suggests a relationship via fractional crystallization. Nevertheless, differences do exist between basalts that are considered impossible to achieve by simple fractional crystallization (see Chapter 6). Such differences (eg. incompatible inter-element ratios), are considered to reflect differences in partial melting or source region characteristics. To a first approximation, type I basalts are thought to reflect derivation from a depleted, N-type MORB source similar to SWIR MORB between 0 and 11° E (le Roex et al., 1987). In contrast, type II basalts appear to reflect (distinct) source characteristics of a less depleted mantle.

5.4.2 Ridge B

Dredge 7

Major element microprobe analyses of quench glasses from two selected samples establish that they are chemically similar and, moreover, similar in composition to most primitive glasses from Ridge A dredge hauls (e.g. $Mg^{\#}$=63; MgO=7.8 wt%; TiO_2=1.6 wt%). Bulk rock analysis of AG22-7-1 (Table 17) indicates that it is more primitive than the corresponding quench glass and samples previously described (e.g. $Mg^{\#}$=68; MgO=9.47 wt%; TiO_2=1.5 wt%, Ni=214 ppm; Cr=405 ppm).

Table 17: Whole-rock analyses of selected Dredge 7, 8 and 9 basalts. Details as in Table 15.

	A622-7-1 AP	A622-8-1 SP	A622-8-2 SP	A622-8-9 SP	A622-8-11 SP	A622-8-15 SP	A622-8-19 PP	A622-8-24 PP	A622-9-2 AP
SiO_2	50.25	49.89	49.81	49.63	49.71	49.85	49.38	49.45	49.86
TiO_2	1.50	1.75	2.14	1.73	1.76	1.76	1.89	1.83	1.19
Al_2O_3	15.58	16.12	15.48	16.02	15.95	16.10	17.27	17.87	15.85
Fe_2O_3	1.18	1.25	1.35	1.27	1.26	1.27	1.23	1.19	1.13
FeO	7.86	8.32	9.00	8.45	8.39	8.48	8.18	7.96	7.55
MnO	0.15	0.16	0.17	0.16	0.15	0.17	0.16	0.14	0.15
MgO	9.47	7.52	6.95	7.24	7.10	7.49	6.29	6.31	10.02
CaO	10.75	10.69	10.31	10.63	10.68	10.70	10.91	11.14	11.15
Na_2O	2.81	3.15	3.26	3.06	3.14	2.97	3.03	2.88	2.66
K_2O	0.12	0.25	0.47	0.32	0.40	0.22	0.29	0.24	0.06
P_2O_5	0.15	0.19	0.26	0.19	0.20	0.20	0.23	0.22	0.11
L.O.I	0.41	0.83	1.02	0.93	1.10	0.75	0.93	0.95	0.31
H_2O	0.06	0.21	0.25	0.40	0.45	0.27	0.31	0.31	0.08
Total	100.29	100.33	100.47	100.03	100.29	100.23	100.10	100.49	100.12
Zr	115	139	181	137	139	140	161	155	81
Nb	1.4	2.5	2.8	2.2	2.4	2.5	3.6	1.9	<1.4
Y	32	38	47	37	37	39	42	41	27
Rb	<1.3	1.3	5.8	4.5	6.6	2.2	2.0	1.9	<1.3
Ba	7.4	6.8	9.5	6.9	6.4	7.2	7.3	6.5	<2
Sr	141	160	155	159	166	159	164	168	123
Co	51	46	47	45	43	46	41	40	52
Cr	405	264	243	263	261	268	231	237	551
Ni	214	117	106	111	106	115	99	93	243
V	236	247	280	252	247	259	253	250	206
Zn	71	78	87	79	78	79	78	81	65
Cu	55	49	45	50	51	49	41	39	63
Sc	38	35	35	37	36	37	33	32	36
Zr/Nb	82	56	65	62	58	56	45	82	>75
Zr/Y	3.6	3.7	3.9	3.7	3.8	3.6	3.8	3.8	3.0
Y/Nb	23	15.2	16.8	16.8	15.4	15.6	11.7	22	>44
Ti/Zr	79	76	72	77	7	76	71	72	80
Ti/P	13.9	12.8	11.4	12.6	12.2	12.2	11.4	11.5	12.7
Zr/Ba	10.6	20	19.5	19.8	22	19.4	22	23.8	32.3
Mg#	68.2	61.7	57.9	60.4	60.1	61.1	57.8	58.6	61.9
Q	-	-	-	-	-	-	-	-	-
Or	0.71	1.49	2.80	1.91	2.39	1.31	1.73	1.43	0.35
Ab	23.82	26.85	27.81	26.23	26.91	25.33	25.94	24.56	22.57
An	29.60	29.32	26.43	29.42	28.61	30.18	33.04	35.40	31.22
Ne	-	-	-	-	-	-	-	-	-
Di	18.47	18.54	19.16	18.57	19.37	17.94	16.52	15.40	19.00
Hy	13.34	9.13	8.39	10.05	8.08	12.72	10.65	12.59	11.16
Ol	9.14	9.05	8.75	8.17	8.93	6.82	6.15	4.87	11.54
Mt	1.71	1.83	1.97	1.87	1.85	1.86	1.80	1.74	1.64
Ilm	2.85	3.35	4.10	3.33	3.38	3.37	3.63	3.50	2.27
Ap	0.36	0.45	0.62	0.46	0.48	0.48	0.55	0.53	0.26

In terms of trace element abundances, sample AG22-7-1 is similar to Ridge A basalts but with a low (close to detection limit by XRF) Nb content (1.4 ppm). The high Zr/Nb ratio (82), Y/Nb ratio (32) and comparatively low Zr/Y ratio (3.6) reflect a "depleted" character similar to N-type MORB from the Southern Ocean (le Roex et al., 1983, 1985). The Ti/Zr ratio (79) is close to the average Ridge A value (av. Ti/Zr=81 $\pm$ 2).

Although it is apparent that the Zr/Nb ratio is significantly higher than average Ridge A basalt (av. Zr/Nb ~ 40, excluding Type II basalts from Dredge 5), caution should be exercised when comparing Zr/Nb ratios at very low Nb contents. Analytical errors in Nb under these circumstances can result in a large apparent range in Zr/Nb ratio (see Table below).

Sample	Reported Zr/Nb	Maximum* Zr/Nb	Minimum** Zr/Nb	Range
AG22-1-1	43	53	36	17
AG22-3-2	56	67	48	19
AG22-3-4	36	41	32	9
AG22-5-46	36	42	31	11
AG22-5-48	53	65	45	20
AG22-7-1	82	121	62	59

(* Reported (+1 sigma error); ** Reported (-1 sigma error)

Dredge 8

Glasses of Dredge 8 are the most evolved thus far described (e.g. $Mg^{\#}$=59-55; MgO=7.29-6.5 wt%; TiO_2=2.0-2.5 wt%). Bulk rock analyses (Table 17) indicate that lavas are moderately evolved (e.g. $Mg^{\#}$=62-58; MgO=7.5-6.3 wt%; TiO2=1.7-2.1 wt.%, Ni=117-93 ppm; Cr=264-231 ppm); porphyritic basalts with high Al_2O_3 (17.3-17.9 wt%) reflect the importance of plagioclase accumulation (see Section 5.3). Aphyric sample AG22-8-2 has a similar $Mg^{\#}$ to porphyritic samples AG22-8-19 & -24 (Table 17) but higher TiO_2 and ferromagnesian trace element abundances. Incompatible element ratios are similar.

Incompatible element abundances in Dredge 8 basalts also show a range in composition (e.g. Zr=137-181 ppm; Nb=2.2-3.6 ppm; Y=37-47 ppm) while interelement ratios (e.g. Zr/Nb=45-82; Zr/Y=3.6-3.9; Y/Nb=15-22) reflect a N-type MORB character (e.g. le Roex et al., 1983, 1985). Ti/Zr ratios (71-77) are low but nonetheless fall within the range of known SWIR basalt (Ti/Zr=87 ± 16; le Roex et al., 1983).

The relatively coherent geochemical characteristics of Dredge 8 basalts suggest that they may be related to a common parental magma by crystal fractionation/accumulation. The low Nb contents (close to the limit of detection) render

comparison of interelement ratios (involving Nb) suspect; a systematic decrease in Ti/Zr ratios from aphyric basalts to porphyritic basalts could be achieved by fractional crystallization involving clinopyroxene. Supporting evidence for such a hypothesis is noted in decreasing CaO/Al_2O_3 ratios with decreasing $Mg^{\#}$ (eg. see Figure 24).

Dredge 9

Dredge 9 quench glass analyses (3 of 5 recovered samples) are chemically similar and they are the most primitive glasses thus far described (e.g. $Mg^{\#}$=66-67; TiO_2=1.3-1.4 wt%; FeO=8.4 wt%; see Table 17).

Bulk rock analysis of AG22-9-2 indicates the lava to be less evolved than the quench glass (e.g. $Mg^{\#}$=70; MgO=10.0 wt%; TiO_2=1.2 wt%). The sample has very high compatible trace element abundances (e.g. Ni=243 ppm; Cr=551 ppm) and low incompatible trace element abundances (e.g. Zr=81 ppm; Y=27 ppm; Nb, Rb and Ba are below detection limits). High MgO, Ni and Cr contents are within the range expected for a primary magma (e.g. Ni>200 ppm; Sato, 1977; Hart and Davis, 1978). Incompatible element ratios (e.g. Zr/Y=3.0; Ti/Zr=89) indicate this sample to be similar to the N-type MORB of Dredge 1. This lava is the most primitive in the entire Agulhas 22 suite.

Dredge 12

Consideration of quench glass analyses yields three distinct glass compositions apparently related to three petrographically distinct lavas (Tables 10 and 18). Glass from sample AG22-12-4, a porphyritic olivine-plagioclase basalt, is the most evolved (e.g. $Mg^{\#}$=58; MgO=6.8 wt%; TiO_2=2.2 wt%) while aphyric basalt AG22-12-35 and the remaining samples have similar $Mg^{\#}$ (~65) but differ in TiO_2 and Al_2O_3 contents (Table 10). In particular, aphyric basalt AG22-12-35 has higher TiO_2 (2.0 wt%) and lower Al_2O_3 (16.2 wt%) contents than sparsely porphyritic samples and porphyritic olivine-plagioclase-clinopyroxene basalt AG-22-12-1 (TiO_2=1.6 wt%; Al_2O_3=16.5-16.9 wt%).

Bulk rock analyses of selected samples similarly reflect the presence of three apparently distinct basalt compositions. Plagioclase porphyritic basalts have high Al_2O_3 contents (17.9-22.0 wt%) and display a concomitant decrease in other major, and trace element, abundances reflecting dilution by plagioclase accumulation. Sparsely porphyritic basalts display a range in composition (e.g. $Mg^{\#}$=65-61; MgO=8.0-7.1 wt%; TiO_2=1.4-1.7 wt%) demonstrated also by trace element abundances (e.g. Zr=108-132 ppm; Y=30-37 ppm; Ni=151-120 ppm; Cr=336-262 ppm). Relatively restricted ranges of Nb, Ba and Sr (Ba=3.9-5.7 ppm; Sr=151-157 ppm; Nb=1.3-1.6 ppm) occur and Rb values are low (2.5 ppm to below detection

Table 18: Whole rock analyses of selected Dredge 12 basalts. Details as in Table 15.

	A622-12-3 PP	A622-12-11 PP	A622-12-13 PP	A622-12-23 SP	A622-12-24 SP	A622-12-26 SP	A622-12-27 PP	A622-12-31 SP	A622-12-35 AP	A622-12-42 AP	A622-12-63 AP
SiO_2	49.75	49.92	49.33	49.54	49.76	49.76	49.92	49.75	49.85	49.90	49.19
TiO_2	1.28	1.56	1.00	1.67	1.62	1.43	1.38	1.74	1.81	1.76	1.80
Al_2O_3	19.40	18.66	22.03	16.91	16.88	16.71	17.91	16.55	15.45	16.04	15.31
Fe_2O_3	0.98	1.05	0.79	1.22	1.20	1.16	1.04	1.24	1.31	1.29	1.25
FeO	6.52	7.02	5.30	8.12	8.02	7.70	6.90	8.25	8.74	8.63	8.34
MnO	0.13	0.12	0.09	0.15	0.15	0.15	0.12	0.16	0.16	0.19	0.15
MgO	5.94	5.92	5.38	7.14	7.49	8.04	6.24	7.25	8.19	7.54	7.82
CaO	11.91	11.42	12.53	10.82	11.04	11.10	11.60	10.75	10.44	10.63	10.33
Na_2O	3.01	3.46	2.86	3.12	2.94	2.92	3.10	3.12	2.93	2.89	3.38
K_2O	0.20	0.25	0.16	0.25	0.18	0.18	0.24	0.25	0.16	0.20	0.17
P_2O_5	0.14	0.18	0.11	0.21	0.17	0.15	0.14	0.19	0.20	0.20	0.20
L.O.I	0.72	0.81	0.87	0.78	0.69	0.73	1.23	0.77	0.59	0.56	1.47
H_2O	0.22	0.22	0.38	0.23	0.17	0.24	0.60	0.38	0.21	0.18	0.73
Total	100.20	100.59	100.83	100.16	100.31	100.27	100.42	100.40	100.04	100.01	100.14
Zr	97	124	77	132	122	108	102	134	146	140	145
Nb	<1.3	2.2	<1.3	1.3	1.6	1.4	<1.3	1.5	<1.3	1.9	2.2
Y	28	34	21	37	36	30	29	37	39	38	39
Rb	2.9	5.2	3.5	2.5	<1.3	<1.3	3.7	1.8	<1.3	1.9	1.8
Ba	3.0	8.7	<2	3.9	5.7	4.5	5.4	4.9	7.3	7.6	7.1
Sr	180	186	200	157	151	152	171	155	153	158	161
Co	35	38	30	43	44	45	37	44	49	45	47
Cr	247	206	260	262	298	336	284	263	335	279	306
Ni	76	73	86	121	120	151	87	126	159	122	151
V	194	216	150	237	242	218	214	244	266	257	248
Zn	59	64	46	74	76	70	62	76	80	80	77
Cu	41	41	42	47	48	52	54	48	54	50	54
Sc	31	30	26	34	35	35	34	34	39	37	32
Zr/Nb	>150	56	>67	102	76	77	>95	89	>122	74	66
Zr/Y	3.5	3.6	3.7	3.6	3.4	3.6	3.5	3.6	3.7	3.7	3.7
Y/Nb	>46	15.5	18.4	34	23	21	>27	25	>32	20	17.7
Ti/Zr	80	76	79	77	80	80	82	79	75	76	75
Ti/P	12.7	12.0	12.6	11.0	13.2	13.2	13.7	12.7	12.6	12.2	12.5
Zr/Ba	32	14.2	>100	34	21	24	18.8	27	20	18.4	20
Mg#	61.9	60.0	64.4	61.0	62.5	65.0	61.7	61.0	62.5	60.9	62.6
Q	-	-	-	-	-	-	-	-	-	-	-
Or	1.19	1.48	0.95	1.49	1.07	1.07	1.44	1.49	0.95	1.19	1.03
Ab	25.66	29.40	24.30	26.63	25.01	24.89	26.60	26.60	24.98	24.64	29.20
An	39.13	34.80	47.00	31.67	32.51	32.18	34.74	30.64	28.75	30.43	26.65
Ne	-	-	-	-	-	-	-	-	-	-	-
Di	15.88	17.07	11.95	17.20	17.46	18.10	18.51	17.81	18.00	17.45	19.81
Hy	7.05	1.90	5.08	8.09	10.84	9.54	7.68	9.10	14.30	14.89	5.30
Ol	6.90	10.41	7.41	9.45	7.87	9.45	6.52	8.77	7.17	5.68	12.20
Mt	1.43	1.53	1.15	1.78	1.75	1.69	1.53	1.81	1.91	1.88	1.85
Ilm	2.45	2.98	1.91	3.20	3.09	2.73	2.66	3.33	3.46	3.37	3.49
Ap	0.33	0.43	0.26	0.50	0.41	0.36	0.34	0.45	0.48	0.48	0.48

limit). The depleted nature of these basalts is reflected in high Zr/Nb ratios (77-102) and Y/Nb ratios (21-34), and low Zr/Y ratios (3.4-3.6) similar to characteristics of N-type MORB described by le Roex et al. (1983) from the SWIR. Aphyric basalts exhibit a more restricted compositional range (e.g. $Mg^{\#}$=63-61; MgO=8.2-7.5 wt%; TiO_2=1.8 wt%; Zr=140-146 ppm; Y=38-39 ppm) than sparsely porphyritic basalts, with higher Ba (7.1-7.6 ppm) contents. Incompatible element ratios (e.g. Zr/Nb=66-74; Zr/Y=3.7; Y/Nb=18-20; Ti/Zr=75-76) are similar to those found in the sparsely porphyritic lavas.

Since the Nb contents of Dredge 12 basalts are close to the limit of detection, it is not possible to establish with certainty whether all samples are genetically related. However, the broadly coherent variations in major and trace element abundances suggest an origin due to fractional crystallization (a scheme relating basalts AG22-12-23 and AG22-12-26 is presented in Chapter 6).

Dredge 13

Quench glass and bulk rock analyses of selected samples indicate the presence of two chemically distinct lavas (Tables 10 and 19). Quench glasses of the olivine basalts are relatively primitive (e.g. $Mg^{\#}$=67; MgO=8.2-8.9 wt%; TiO_2=1.4-1.5 wt%) and in this respect resemble Dredge 9

Table 19: Whole rock analyses and norms of selected Dredge 13 basalts. Details as in Table 15.

	A622-13-1 AP	A622-13-14 AP	A622-13-24 AP	A622-13-25 AP
SiO_2	50.30	50.52	50.06	50.29
TiO_2	1.41	1.25	1.40	1.41
Al_2O_3	16.67	16.08	16.59	16.69
Fe_2O_3	1.09	1.20	1.12	1.11
FeO	7.26	7.97	7.48	7.42
MnO	0.14	0.16	0.14	0.15
MgO	8.45	8.17	8.54	8.57
CaO	11.05	11.44	10.99	11.05
Na_2O	3.06	2.99	2.95	2.93
K_2O	0.15	0.11	0.14	0.13
P_2O_5	0.15	0.11	0.16	0.15
L.O.I	0.54	0.37	0.39	0.38
H_2O	0.15	0.11	0.10	0.10
Total	100.42	100.48	100.06	100.38
Zr	108	78	108	109
Nb	2.2	<1.4	1.5	1.5
Y	30	27	29	30
Rb	1.3	<1.3	1.3	<1.3
Ba	6.0	2.2	4.1	5.0
Sr	164	146	165	165
Co	47	47	47	47
Cr	337	375	340	338
Ni	161	105	165	162
V	218	207	220	221
Zn	65	68	66	66
Co	53	69	56	56
Sc	35	39	35	36
Zr/Nb	49	>38	72	73
Zr/Y	3.6	2.9	3.7	3.6
Y/Nb	13.6	>32	19.3	20
Ti/Zr	79	97	79	78
Ti/P	13.0	15.8	12.1	13.0
Zr/Ba	22	36	26	22
Mg#	67.5	64.6	67.0	67.3
Q	-	-	-	-
Or	0.89	0.65	0.83	0.77
Ab	25.96	25.30	25.07	24.82
An	31.39	30.13	31.75	22.94
Ne	-	-	-	-
Di	18.29	21.07	17.78	17.70
Hy	8.91	9.19	10.26	11.04
Ol	9.95	9.30	9.63	9.00
Mt	1.58	1.74	1.63	1.61
Ilm	2.69	2.37	2.67	2.68
Ap	0.36	0.26	0.38	0.36

glasses. However, they have unusually high Al_2O_3 (16.7-17.4 wt%) contents relative to known primitive MORB glasses (e.g. Melson et al., 1976; see also Table 14). Coupled with low CaO (10.7-11.3 wt%) contents, these lavas have low CaO/Al_2O_3 ratios (average CaO/Al_2O_3 wt% ratio ~0.64). Following the classification of Kuno (1960) these glasses may be classified as high alumina basalt. Quench glass of olivine-plagioclase basalt (AG22-13-14) appears to be slightly more evolved than the olivine basalt glass in terms of $Mg^{\#}$ (65-63), MgO (7.6-7.9 wt%) and FeO (8.9-9.2 wt%). However, AG22-13-14 has a lower TiO_2 content (1.3 wt%) and a higher CaO/Al_2O_3 ratio (~0.72 average).

Bulk rock analyses serve to distinguish the two basalt types more clearly. Three selected olivine-basalts are fairly primitive (e.g. $Mg^{\#}$=67; MgO=8.5 wt%; TiO_2=1.4 wt%; Ni=161-165 ppm; Cr=337-340 ppm) with moderate incompatible trace element abundances (e.g. Zr=108-109 ppm; Nb=1.5-2.2 ppm; Y=29-30; Rb$\leq$1.3; Ba=4.1-6.0 ppm; Sr=164-165 ppm). Selected inter-element ratios (e.g. Zr/Nb=49-73; Zr/Y=3.6-3.7; Y/Nb=14-20; Ti/Zr=78-79) indicate that they are similar to N-type MORB from this ridge segment.

The olivine-plagioclase basalt AG22-13-14 has an $Mg^{\#}$ of 65 and a similar MgO content (8.2 wt%) to the olivine basalts. In terms of Ni abundances, AG22-13-14 appears to be more evolved than the olivine basalts. However, relative to the

latter, the TiO_2 content is somewhat lower (1.2 wt% TiO_2) and the Cr content is higher (375 ppm).

Selected incompatible element ratios (e.g. Zr/Nb >38, Nb < 1.4;; Zr/Y=2.9; Y/Nb≥13) indicate that the sample possesses N-type MORB characteristics (le Roex et al., 1983, 1985). The Ti/Zr ratio (97) of this sample is the highest in the Agulhas 22 suite and is similar to chondritic and North Atlantic averages (Ti/Zr=100-110; Sun et al., 1979).

The geochemical characteristics of analysed Dredge 13 lavas suggest that the within-dredge variation cannot be achieved by a simple fractional crystallization relationship. Rather, it is evident that two distinct parental magmas are required, providing evidence for distinct source region characteristics on a local scale.

5.5 Between-Dredge and Between-Ridge variation.

5.5.1 Major elements

Major element concentrations are plotted on conventional MgO-variation diagrams (Figure 29) to illustrate between-ridge chemical variations. From these diagrams it is apparent that (a) the lavas exhibit a wide range in composition (MgO=10 to 5 wt.%); (b) that most oxides show broadly coherent variations with decreasing MgO and (c),

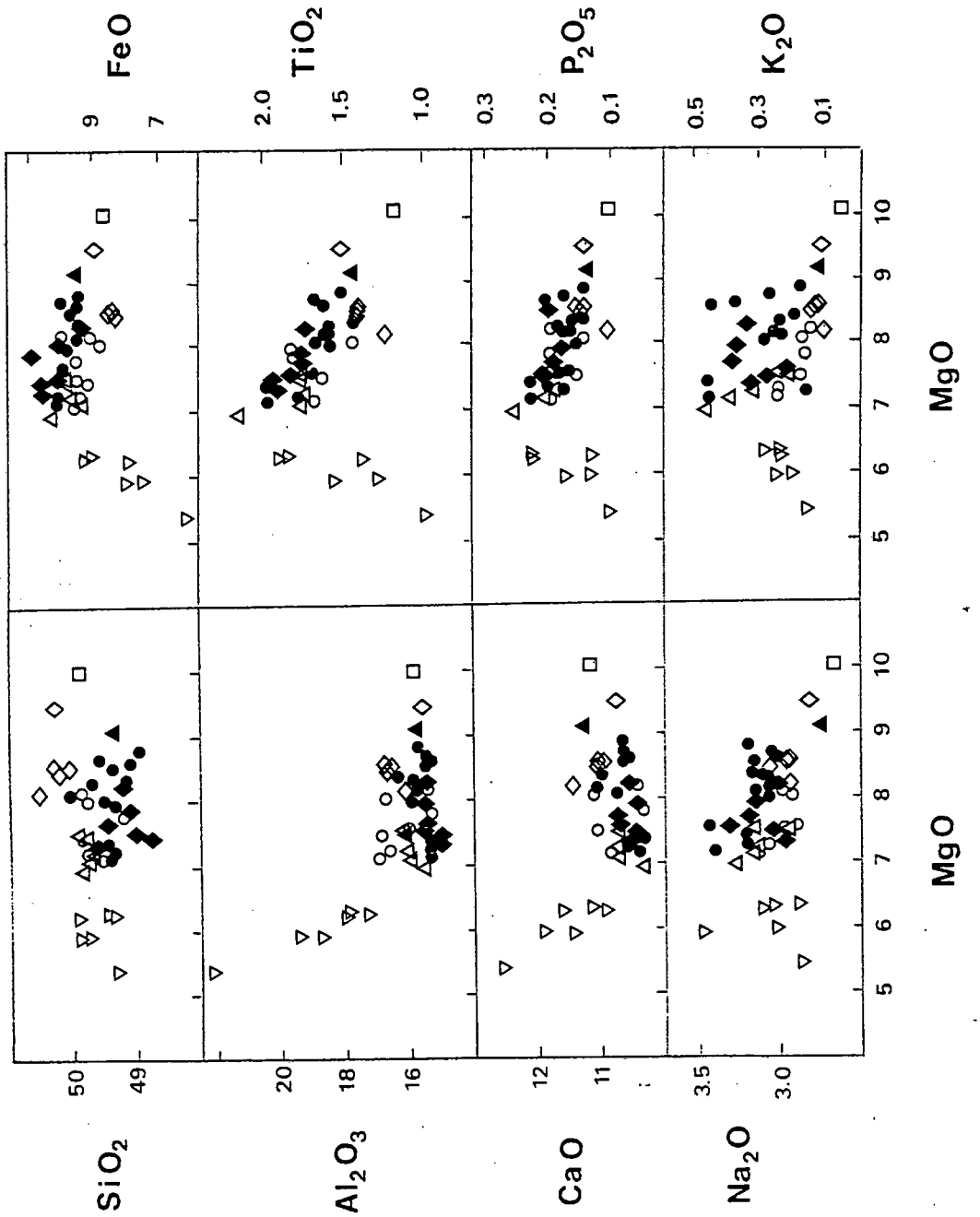

Figure 29: Oxide versus MgO variation diagrams for Agulhas 22 basalts. Symbols as follows;

▲ - Dredge 1
◆ - Dredge 3
● - Dredge 5
◇ - Dredge 7
△ - Dredge 8
□ - Dredge 9
○ - Dredge 12
◇ - Dredge 13

▽ - Porphyritic basalts

that the plagioclase phyric basalts show distinct trends consistent with plagioclase accumulation. The observed trends are broadly consistent with crystal-liquid differentiation processes operating on more than one parental magma. The decrease in CaO and Al_2O_3, and increase in K_2O, TiO_2 and P_2O_5 with decreasing MgO in the aphyric and sparsely porphyritic lavas are consistent with simultaneous crystallization of olivine and plagioclase. These aspects are discussed further in Chapter 6.

Figure 30 shows a uniform increase in TiO_2 content with increasing FeO^*/MgO in aphyric lavas, while the porphyritic lavas are displaced from the main trend to lower TiO_2 contents; reflecting dilution of TiO_2 by addition of plagioclase phenocrysts (see high Al_2O_3 contents). Ridge B lavas show a greater range in FeO^*/MgO than Ridge A lavas. Aphyric basalt AG22-13-14 has a low TiO_2 content relative to the other Ridge B samples with a similar FeO^*/MgO ratio, suggesting that this sample has experienced a somewhat different petrogenetic history.

The incompatible elements Ti and P show a good positive correlation (Figure 31) which suggests that the mantle source is relatively homogeneous with respect to TiO_2 and P_2O_5 (eg. le Roex and Dick, 1981) since all samples evidently cannot be related by simple fractional crystallization.

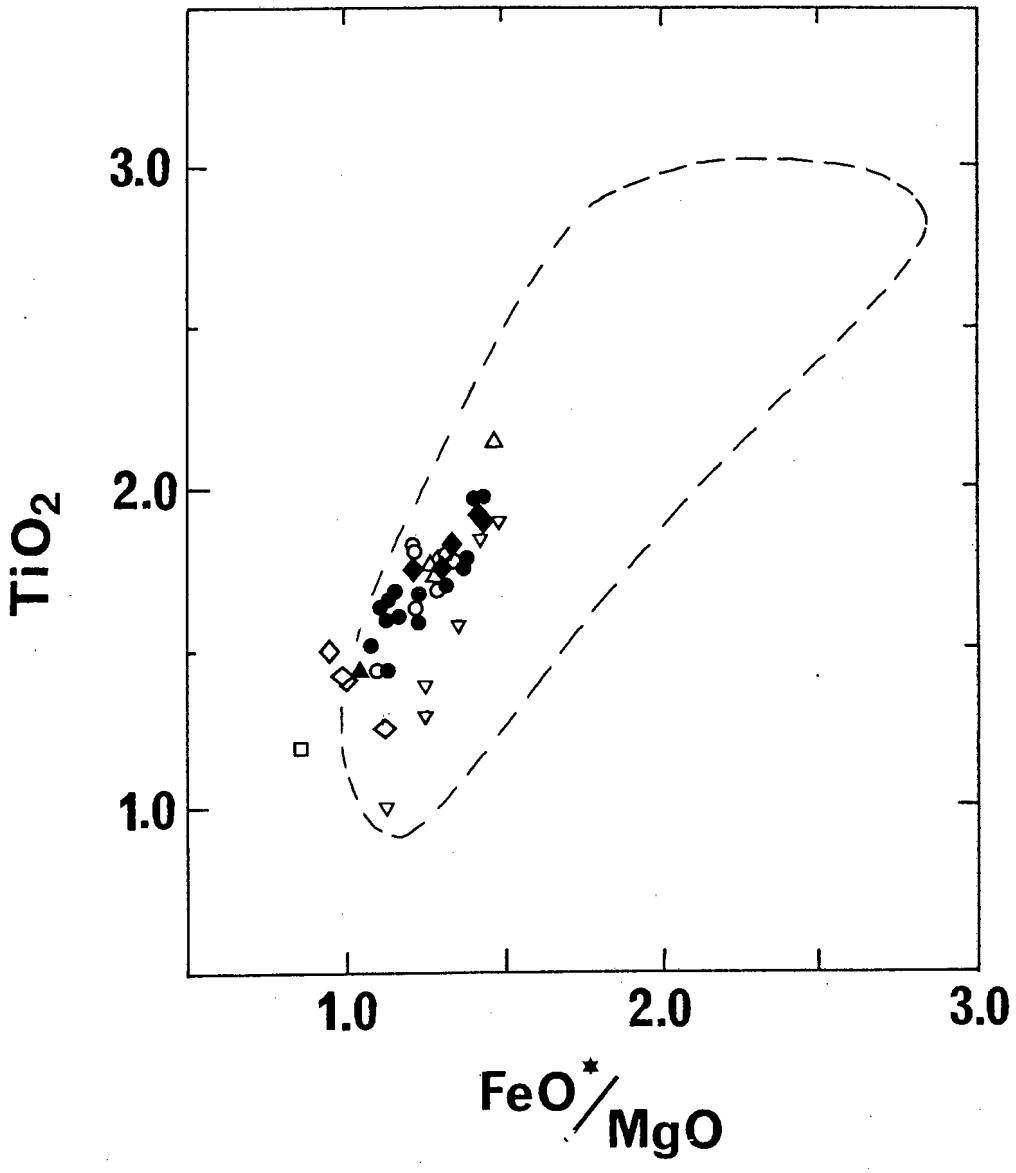

Figure 30: TiO_2 versus FeO^*/MgO ratio for Agulhas 22 lavas. Symbols as in Figure 29. Field of Southwest Indian Ridge MORB (le Roex et al., 1983; 1985) shown for comparison.

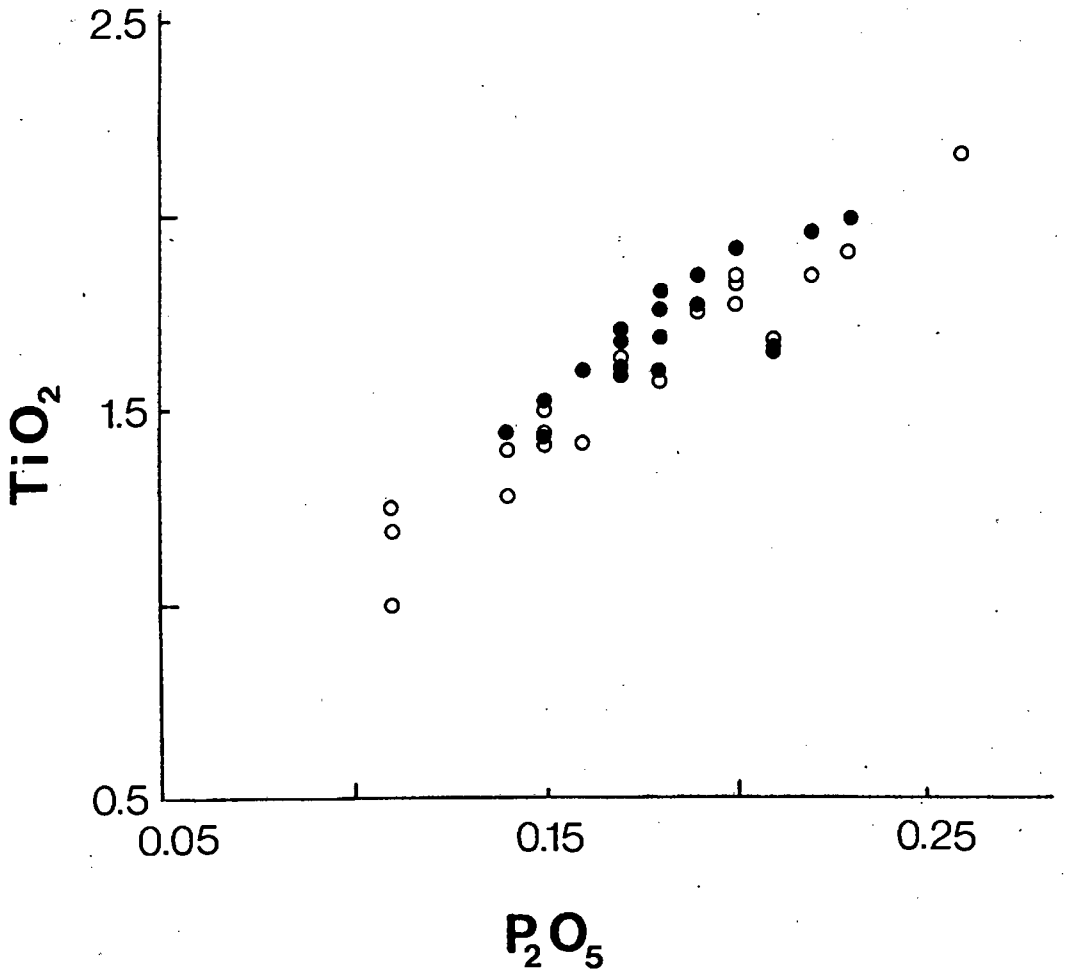

Figure 31: TiO_2 versus P_2O_5 in Agulhas 22 basalts. Symbols as in Figure 21.

5.5.2 Trace elements

The Agulhas 22 trace element data are plotted in Figure 32 using Zr as an index of differentiation. The incompatible elements Y and Ba (to a lesser extent) increase with increasing Zr whereas the compatible trace elements Ni and Cr decrease. V correlates positively with Zr and Sc remains constant. These variations are broadly consistent with crystal-liquid fractionation. Porphyritic lavas (particularly Dredge 12) tend to obscure the compatible trace element trends. These lavas have low transition element contents, consistent with the hypothesis that they have experienced plagioclase accumulation and consequent dilution of transition element concentrations.

Compatible trace elements are relatively sensitive indicators of crystal fractionation (Basaltic Volcanism Study Project, 1981). A strong negative correlation between highly compatible elements and increasing Zr content reflects the importance of olivine (Ni), spinel (Cr) and perhaps pyroxene(Cr) crystallization. It is important to note the displacement of Ridge A lavas toward higher Ni contents relative to Ridge B lavas. This displacement supports the variation in Ni contents of analysed olivine from the respective ridge segments (Figure 7).

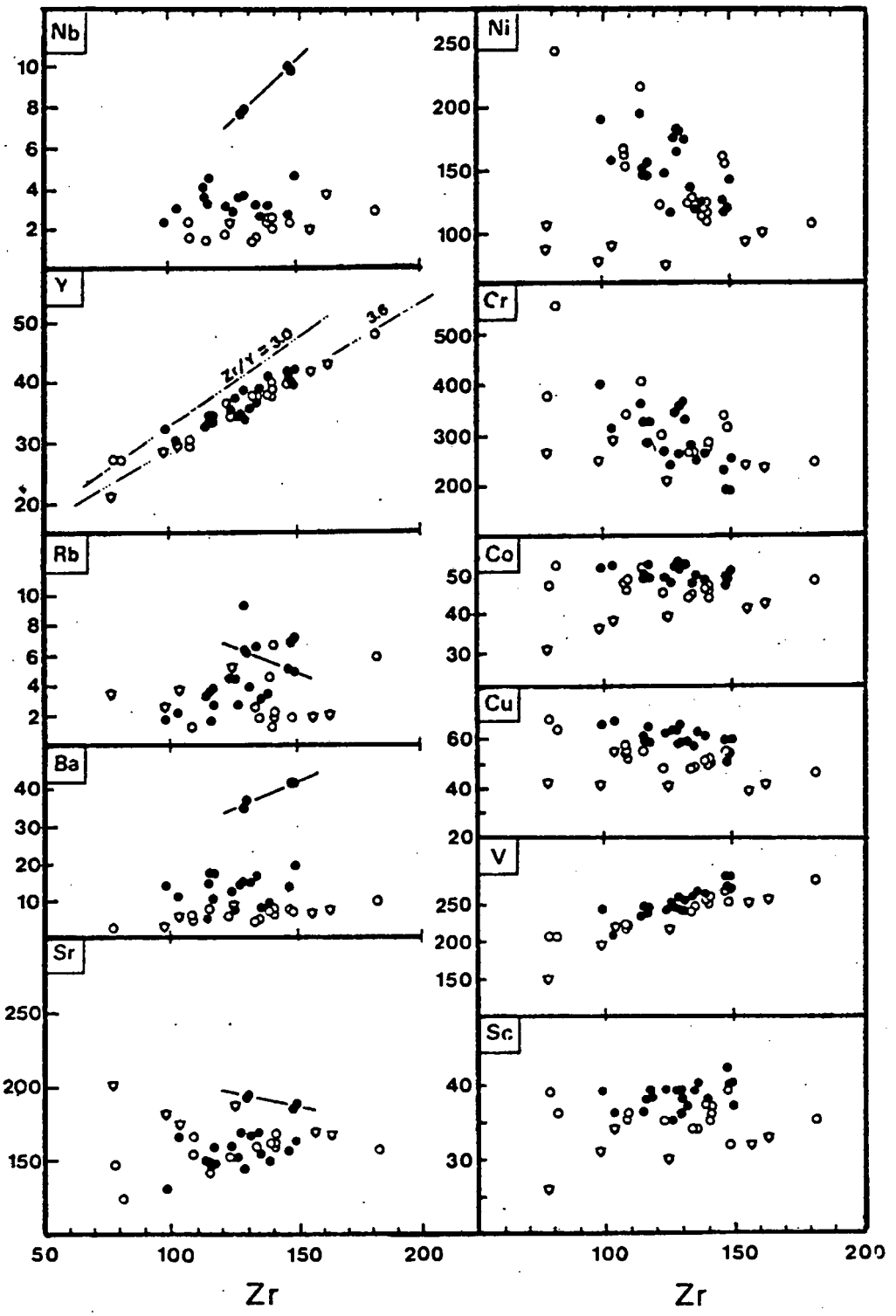

Figure 32: Trace element versus Zr abundances for Agulhas 22 basalts. Symbols as in Figure 21. Solid line depicts the variation in "less depleted" Dredge 5 basalts. ⊙ = Porphyritic basalts. Note fine-scale differences in Zr/Y ratios (c.f. two sub-parallel trends with Zr/Y = 3.0 and 3.6); see text for discussion.

Cu and Co show a slight decrease with increasing Zr. V increases with increasing Zr content despite the evidence presented earlier for clinopyroxene fractionation (V is relatively compatible in clinopyroxene, and should thus decrease with increasing Zr). Nevertheless, this observation does not necessarily refute the involvement of clinopyroxene in crystal fractionation. Moreover, Frey et al. (1974) concluded that since Sc and V correlated with TiO_2 (implying bulk K_D's of less than unity), high pressure pyroxene fractionation was either relatively unimportant in MORB genesis or alternatively, that olivine and plagioclase fractionation overshadows the effect of pyroxene removal. In Figure 33 it is evident that V correlates positively with TiO_2 while Sc remains relatively constant (albeit with a broad scatter), implying a K_D of close to unity. The within-dredge scatter in Sc content correlates with variation shown in an earlier section to be largely a function of olivine and plagioclase crystallization.

Transition element abundance variations are therefore qualitatively in accord with crystal fractionation of the phenocrysts observed in the Agulhas 22 basalt suite. Higher Cu, Co and Sc contents in Ridge A basalts relative to Ridge B basalts (Figure 32) preclude a between ridge relationship by a simple crystal fractionation process. Although Sr displays a considerable scatter which is perhaps attributable to alteration (Hart et al., 1974), it is

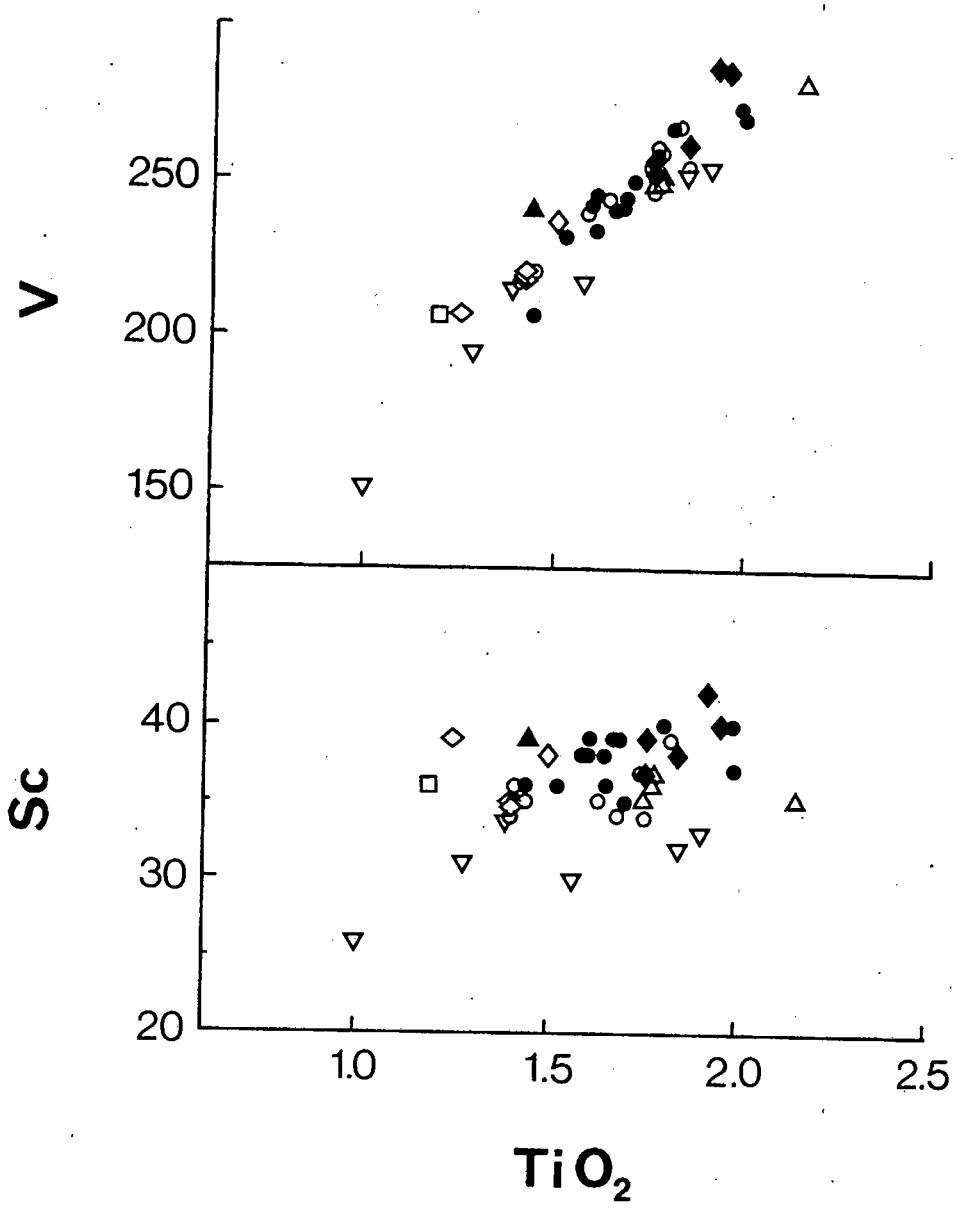

Figure 33: Sc and V contents versus TiO_2 in Agulhas 22 basalts. Symbols as in Figure 29.

evident that less depleted Dredge 5 basalts have higher Sr contents than remaining basalts. Decreasing Sr contents within this distinct subset of basalts is consistent with the compatible nature of Sr in plagioclase.

Incompatible trace element abundances (Zr, Nb, Y, Ba) increase with increasing differentiation and relative abundances serve to distinguish distinct magma types. Within dredge Zr/Y, Zr/Nb and Zr/Ba ratios however, are relatively constant. Less depleted Dredge 5 samples have distinctly higher Nb and Ba contents for the same range in Zr as remaining Dredge 5 and other basalts. Similarly, although a considerable overlap in Zr/Y ratio exists, the entire range in Zr/Y ratio (3.0-3.9) is considered too great to have resulted from crystal fractionation. More specifically, fine scale differences appear to define two subparallel groups of data, one corresponding to a Zr/Y ratio of ± 3.0 (AG22-1-1, AG22-9-2, AG22-13-14) and another with a Zr/Y ratio of ± 3.6 (the remaining Dredge 13 lavas and other samples straddle this trend).

Notwithstanding the presence of the two groups defined by Zr/Y ratios, the within-ridge and between ridge variation in selected incompatible element ratios (including Ti/Zr) precludes a simple relationship by fractional crystallization between basalts from different sites. For example, sample AG22-13-14 has a higher Ti/Zr ratio (97)

than samples AG22-1-1 and AG22-9-2 (Ti/Zr ~88). Similarly, Dredge 3 lavas have a slightly higher Ti/Zr ratio (average Ti/Zr=80) than Dredge 9 lavas (average Ti/Zr=75).

In addition to the within-ridge variation described above, coherent trends defined by Zr/Nb and Zr/Ba ratios indicate that Ridge B basalts are more depleted in Nb and Ba contents relative to Ridge A basalts. The within- and between-ridge variation is depicted in Figure 34 as a function of geographic location; individual magma types can be recognised by distinct inter-element ratios.

The contrasting Zr/Nb and Zr/Ba ratios are taken as evidence for distinct source region characteristics (eg. le Roex et al., 1983,1985,1987), whereas other differences (including the apparent between-ridge major element decoupling and Ni abundances of olivines) are qualitatively consistent with an origin due to partial melting. For example, with reference to Figure 22 (inset), partial melting of a peridotite mantle yields a trend of decreasing Mg at constant Fe, whereas fractional crystallization yields a trend of decreasing Mg and increasing Fe. Parallel but offset trends of the latter type may therefore reflect crystallization of parental magmas derived by differing degrees of partial melting (Basaltic Volcanism Study Project, 1981). Differences in Ni contents of olivine are consistent with the fact that the partition coefficient for

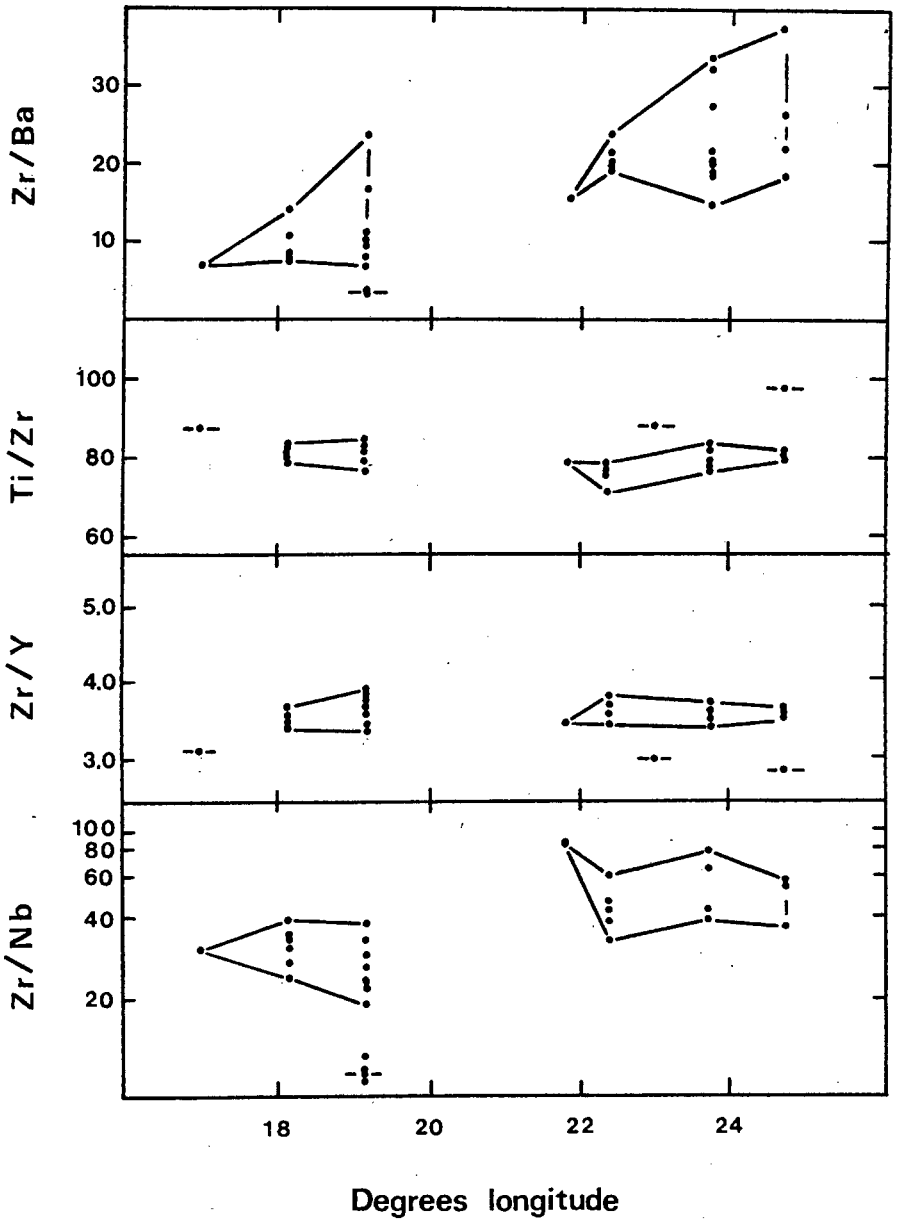

Figure 34: Selected inter-element ratios of Agulhas 22 basalts plotted as a function of geographic location.

Ni in olivine is strongly dependant on the MgO content of the host liquid (Hart and Davis, 1978).

5.6 The SWIR between 16 and 26°E: Regional Comparison

It is instructive to compare and contrast the Agulhas 22 basalt geochemistry with the geochemistry of MORB from the Circum-Antarctic Ridge System. In particular, it is important to investigate chemical characteristics within the framework of the petrogenetic model(s) postulated to account for upper mantle heterogeneity and enrichment related to the Bouvet Mantle Plume (e.g. le Roex et al., 1983; 1985; 1987).

It has been noted that the Agulhas 22 MORB compare with normal MORB dredged between 0 and 11°E (le Roex et al., 1983). Similar fine scale geochemical variations (e.g. Ti/Zr, Zr/Y and Zr/Nb ratios) to those found in the Agulhas 22 basalt suite have been noted in SWIR basalts and basalts from the Southern MAR (le Roex et al., 1983, 1987). Since it is now well established that incompatible element ratios (e.g. Ti/Zr, Zr/Y) are important indicators of source region characteristics (le Roex et al., 1987 and references therein) the preferred model postulated to account for the geochemical variations in Southern Ocean MORB (le Roex et al., 1983; 1985; 1987) is one in which the upper mantle is heterogeneous on a local scale. In this respect, the mantle beneath the SWIR between 16 and 26°E appears to be no

different: the Agulhas 22 lavas indicate that the upper mantle in this area is heterogeneous on the scale of individual dredges.

Relative to average SWIR MORB, the Agulhas 22 basalts have higher TiO_2, Al_2O_3 and Na_2O contents. In this respect, it is perhaps important to recall that Thompson et al. (1979) reported on basalts with relatively high TiO_2 and Na_2O contents from the very slowly spreading Mid-Cayman Rise. These authors suggested that these basalts represented products of high pressure crystal fractionation, and proposed that the observed enrichments were a consequence of a favourable tectonic setting. Relative to the present study, an analogous model for the high Na_2O contents is proposed (see Chapter 6) although it is recognised that partial melting may also affect Na_2O contents (eg. Sun et al, 1979).

With due consideration to sampling constraints, it is important to note the conspicuous absence of transitional (T-tpe) MORB in the Agulhas 22 suite (Figure 35). This fact and the progressive eastward incompatible element depletion indicated by Y/Nb, Zr/Ba and Zr/Nb ratios, is taken as evidence for the decreasing westward influence of an enriched MORB component in SWIR basalts between 16 and 26°E. It is perhaps important to emphasize that even the "less depleted" Dredge 5 basalts share characteristics of

average normal MORB dredged between 0 and 11°E (le Roex et al., 1983).

The model preferred here is analogous to the model proposed by le Roex et al. (1985) for the decreasing westward influence of the Bouvet Mantle Plume in MORB from the American-Antarctic Ridge, although isotopic data are required to substantiate this.

****

CHAPTER 6

PETROGENESIS

6.1 Normative Mineralogy; Comparison with Experimental Investigations on MORB.

Current understanding of processes involved in MORB genesis (i.e. origins, crystallization and melting) has benefitted much from experimental investigations (e.g. Bender et al., 1978; Walker et al., 1979; Fisk et al., 1980; Stolper, 1980; Takahashi and Kushiro, 1983). Assuming that experimental conditions and experimentally determined phase relationships correspond with those in natural basalt suites, comparison of natural basalt data and experimental results may yield important constraints on MORB genesis.

For example, it has been shown that the array of basalt compositions from the Oceanographer Fracture Zone at 35°N on the Mid-Atlantic Ridge can be generated by extensive fractional crystallization of plagioclase + olivine and plagioclase + olivine + clinopyroxene from more primitive MORB under anhydrous conditions at low (<1kb) pressure (Walker et al., 1979). Experimental results (Walker et al., 1979) indicate that residual liquids move along the plagioclase-saturated liquidus in the diopside-olivine-silica ternary (Figure 35).

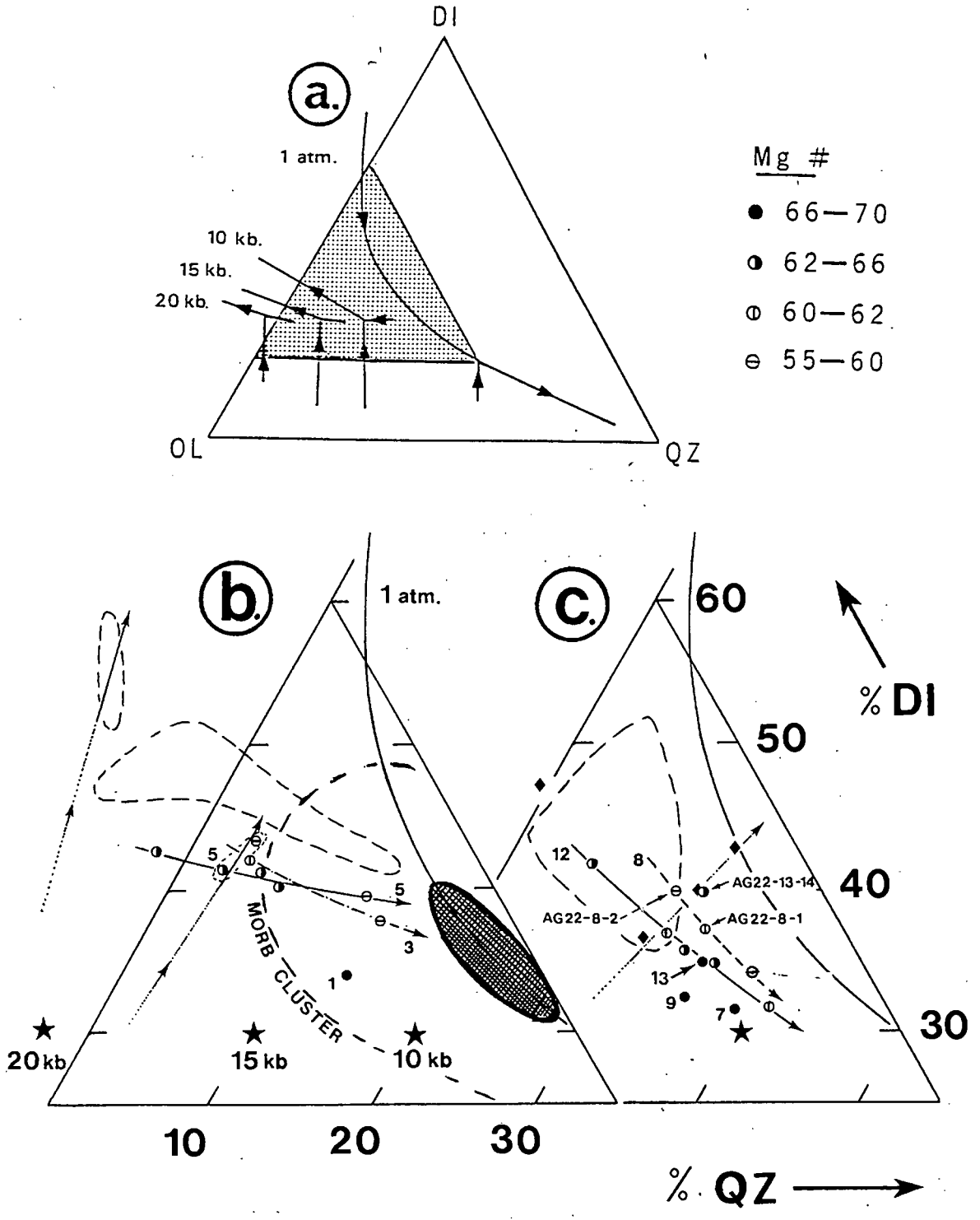

Figure 35: Agulhas 22 basalts plotted in the pseudoternary diopside (Di) - olivine (Ol) - quartz (QZ) after Walker et al. (1979). (a) Cotectics determined by Stolper (1980); (b) Ridge A basalts; (c) Ridge B basalts. MORB cluster from Stolper (1980). Dotted fields represent fields of glass data. Numbers refer to Dredge stations and specific samples are discussed in the text. Diamonds are Dredge 12 porphyritic lavas. Hachured ellipse defines a field of 2 sigma (95%) confidence, illustrating the plotting uncertainty, involving all oxides, about an arbitrarily chosen point (Presnall and Hoover, 1984). Dotted lines (arrowed) are chords from the OL-apex representing low-pressure olivine +/- plagioclase fractionation.

High pressure fractionation has received a great deal of attention in MORB petrogenesis (eg. Bender et al., 1978,1984; Bryan, 1979; Thompson et al., 1980; Flower, 1980, 1981; Fisk et al., 1980; Elthon et al., 1982). It has been shown by these workers that high pressure crystallization leads to the enhancement of clinopyroxene fractionation at the expense of plagioclase. This would cause Ti and Fe to increase less for a given decrease in Mg content than at the (low pressure) 1 atmosphere saturation surface (Bender et al., 1978, 1984). This observation is relevant to Figure 28.

To evaluate the petrogenesis of AG22 basalts, glass and whole rock compositions have been plotted on the diopside-olivine-silica portion of the plagioclase-olivine-diopside-silica tetrahedron (Figure 35; after Walker et al., 1979). Also shown in this diagram are experimentally determined cotectics at various pressures (Walker et al., 1979; Stolper, 1980).

Facts to emerge from Figure 35 include:

(1) Whole rock and glass compositions all plot within the low-pressure olivine (+/- plagioclase) phase field.

(2) Compositions plot within the low silica - high olivine portion of the MORB cluster. In particular, magnesian compositions (Mg > 66) plot close to the 10 kb.

cotectic of Stolper (1980); ie. they correspond to liquids expected at pressures near 9 kb.

(3) Relative to whole rock compositions, glasses correspond to more evolved liquids and more importantly, show an overprinting of low pressure evolution. The offset of glass data toward lower normative silica is an artifact of the projection scheme (see later).

(4) Fractionation trends involving decreasing Mg# among lavas of individual dredges are predominantly down and to the right in Figure 35, consistent with cotectic olivine + clinopyroxene + plagioclase fractionation at pressures of greater than 1kb. In contrast, Dredge 12 glass and porphyritic basalt data, as well as "less enriched" basalts of Dredge 5, define trends of olivine +/- plagioclase fractionation toward the 1 atmosphere three-phase saturated cotectic.

(5) In contrast to the "normal" fractionation trends discussed in 4 above, the most evolved Dredge 8 lava (AG22-8-2; Mg = 58; TiO_2 = 2.1 wt. %) plots away from the quartz apex and the (presumably parental) least evolved Dredge 8 lava (AG22-8-1; Mg = 62; TiO_2 = 1.8 wt. %). Fractionation in this sense is compatible with high pressure (>10kb) crystal fractionation (Stolper, 1980).

The offset of the Agulhas 22 data relative to the majority of MORB reflects the characteristically high Na_2O contents of the sample suite. (In the projection algorithm, increasing Na_2O leads to less SiO_2 available for QZ (Walker et al., 1979). In addition, the sense of variation in projected data in this pseudoternary is sensitive to analytical uncertainty (Presnall et al., 1979; Presnall and Hoover, 1984) particularly in Na_2O, CaO and SiO_2 (see Figure 35). This would explain the apparent exaggeration of Ridge A basalt trends and data which appear to be undersaturated in Figure 35 but which do not contain normative nepheline. Moreover, it also precludes valid interpretation of observation 5 above; as discussed by Presnall and Hoover (1984), analytical uncertainty alone can account for much of the variation in MORB variation. The remaining points are nevertheless valid and are consistent with evidence presented earlier, for example, for clinopyroxene involvement in petrogenesis (e.g. decreasing CaO/Al_2O_3 ratios, presence of resorbed megacryst pyroxene).

The subparallel trends in Figure 35 are therefore interpreted to represent trends of crystal fractionation at various pressures. Consequently, although little inference may be made regarding the nature of parental magmas (from other studies, possible parental magmas probably occupy a field or an array of compositions of differing normative silica; see, for example, Bryan et al, 1979), Figure 35

provides compelling evidence regarding polybaric fractionation of SWIR basalts. A fractionation scheme relating to high pressure crystallization is presented in the following section.

Another important issue is: does the most primitive lava (AG22-9-2) represent a primary magma? If this composition represents a primary liquid (i.e. is capable of being in equilibrium with its mantle source; Ito, 1974) then its position in Figure 35 places an upper limit on the pressure of melting (i.e. between 8 and 12 kb, or deeper).

Evidence accumulated from the literature suggests that partial melting of the sub-oceanic mantle in the aforesaid pressure range is a feasible mechanism for producing MORB (e.g. Presnall et al., 1979; Kushiro, 1980; Takahashi and Kushiro, 1983; Fujii and Bougalt, 1983; Fujii and Scarfe, 1985). Kushiro (1973) has demonstrated that primary magmas may be derived at relatively shallow depths (<25km).

In this regard, primary magmas (or direct mantle melts) should satisfy the following criteria: (a) they must have $Mg^{\#}$'s of between 68 and 73 (Green and Ringwood, 1967; Green, 1971; Kushiro, 1973) and (b) not have MgO and Ni contents below the apparent MORB upper limits of 9.0 wt% and 200 ppm respectively (e.g. Kay et al., 1970).

In this respect, the composition of AG22-9-2 could therefore represent a primary magma. It is perhaps important to note that this lava is even more primitive than primitive lavas dredged from the MAR near 22°N which Bryan et al. (1979) suggest may be primary melts produced at 9 kb pressure. By implication, sample AG22-7-1 and olivine basalts of Dredge 13 could similarly represent primary magmas. In this regard, the high Al_2O_3 contents of Dredge 13 olivine basalts and glasses could be important. More specifically, high alumina basalts are believed by some workers to be (near) primary melts (e.g. Kuo, 1960; see also Johnston, 1986 and references therein). These observations notwithstanding, the controversy regarding primary MORB liquids still stands; the hypothesis that primary MORB is generated at greater depths (e.g. O'Hara, 1968) has yet to be disproved.

The basalts in question therefore warrant further investigation since this aspect (the nature of primary magmas beneath this section of the SWIR) has important implications for the petrogenesis of the SWIR. Presently, the qualitative results outlined above are significant and provide important clues to the petrogenesis of the Agulhas 22 basalt suite. In the following section, results of quantitative modelling are presented in support of the petrogenetic model inferred from Figure 35.

6.2 Fractional Crystallization; Quantitative Modelling.

The hypothesis that geochemical variations may be a consequence of fractional crystallization can be tested quantitatively by a least squares approximation technique (Bryan et al., 1969) using proposed parent and daughter compositions and observed mineral chemistry. This technique involves mass balance calculation of an over-determined major element data matrix, defined by the parent and daughter compositions as well as the participating phases, relating the proposed end-members by the addition or subtraction of various mineral vectors (eg. see mineral vectors in Figure 28).

A number of models were tested on an HP1000 computer using a fortran program written by Prof. A.R. Duncan of the U.C.T Geochemistry Department. Data are first normalized to 100% on a volatile free basis, with all iron expressed as FeO. Final program output consists of the various independent vectors (the proposed daughter composition and participating phases), the calculated parental composition (the dependent vector) and the differences in oxide components between the calculated and observed parental composition (given as a residual component, positive or negative).

Criteria for a satisfactory model are as follows;

1. Differences should be as low as possible with no major discrepancy in any single oxide. Differences should at least not exceed limits of analytical tolerance.
2. The sum of squares of the differences (residual components) should not exceed 0.10 (eg. Wright and Doherty, 1971).
3. The proportions of independant vectors should sum close to 100 %. Moreover, they should represent geologically feasible proportions and preferably correspond with observed modes.

Initial mass balance calculations were determined with theoretical end-member mineral compositions (eg pure An, Ab, Fo, Fa) using Zr as an incompatible element to obtain a feasible degree of crystallization. This strategy was used in an attempt to identify initial solutions which potentially satisfied both major and trace element data. Refinement of selected models was performed using observed mineral chemistry and omitting Zr in the final calculation.

Trace element data were then used to independently evaluate the modelled fractionation schemes assuming that closed system fractionation was operable. For this procedure, Rayleigh Fractionation (Gast, 1968) is assumed by the equation;

$$(C^L)_i / (C^0)_i = F^{(D^*)_i - 1}$$

where $(C^L)_i$ is the observed concentration of element i in the daughter liquid, $(C^0)_i$ is the original concentration in the proposed parental liquid, F is the fraction of liquid remaining and $(D^*)_i$ is the bulk distribution coefficient of element i given by the mass balance equation:

$$(D^*)_i = \sum^{n} (D_i)^n . X^n$$

$(D_i)^n$ = distribution coefficient of element i in phase n.

X^n = weight fraction of phase n, as determined by the least squares solution model.

Distribution coefficients used (Table 20) were selected from the literature appropriate to basaltic compositions.

The assumption of Rayleigh fractionation, or surface fractionation, implies effective removal of the fractionate from the liquid, thereby precluding equilibration with the residual liquid. The presence of zoned crystals in the sample suite supports this assumption.

The models presented below were chosen to span the greatest compositional range observed at a given dredge site. The results are given in Tables 21 to 24 and are discussed individually below.

Table 20. Trace element distribution coefficients for basaltic liquid/mineral partitioning used in petrogenetic modelling (this study). Sources of literature as follows: (1) = Pearce and Norry (1979); (2) McCallum and Charete (1978); (3) le Roex (1980); (4) = Goodman (1972); (5) = Philpotts and Schnetzler (1970); (6) = McKay and Weill (1977); (7) = Dupuy and Coulon (1973); (8) = Griffen and Murthy (1969); (9) = Dale and Henderson (1972); (10) = Paster et al. (1974); (11) = Lindstrom (1976); (12) = Hart and Davis (1978); (13) = Bougalt and Hekinian (1974); (14) = Seward (1971); (15) = Nagasawa et al. (1976).

	OLIVINE	SOURCE	PLAGIOCLASE	SOURCE	CLINOPYROXENE	SOURCE
Zr	0.01	(1)	0.01	(1)	0.03 - 0.22	(2)
Nb	0.01	(1)	0.01	(1)	0.01 - 0.04	(2)
Y	0.01	(1)	0.013 - 0.031	(3)	0.5	(1)
Rb	0.008	(5)	0.05 - 0.12	(4)	0.004 - 0.08	(4)
Ba	0.005 ± 0.003	(6)	0.18 - 0.77	(7)	0.013 - 0.046	(5)
Sr	0.0012 - 0.072	(8)	1.27 - 2.84	(5)	0.11	(3)
Co	2.75 - 4.45	(9)	0.03	(10)	0.68 - 1.22	(9)
Cr	0.6 ± 0.2	(11)	0.05	(3)	4.72 - 11.43	(9)
Ni	(124/MgO) - 0.9	(12)	0.06	(13)	1.42 - 2.11	(9)
V	0.04 ± 0.02	(11)	0.04	(3)	0.74	(13)
Zn	0.86	(13)	0.13	(10)	0.5	(13)
	2.13	(3)				
Cu	0.11	(13)	0.44	(13)	1.5-2.4	(14)
Sc	0.13 - 0.22	(9)	0.01	(10)	2.38 - 3.23	(9)

	Cr - SPINEL	SOURCE
Sc	0.048 ± 0.001	(15)

Dredge 3

Table 21 gives the result of a least squares calculation relating the most primitive Dredge 3 basalt (AG22-3-4; $Mg^{\#}$= 62.6) to the most evolved lava (AG22-3-2; $Mg^{\#}$ = 58.5) by fractionation of 6.4 % plagioclase and 3.6 % olivine. The predicted and observed major element compositions are in excellent agreement and the mineral proportions are in accord with the observed modes.

Results of trace element modelling provide independent support for this fractionation scheme, with only Nb, Rb and Ba showing significant discrepancies. However, the poor precision of Nb measurements at such low concentrations precludes meaningful comparison of Nb contents. In addition, (as previously discussed) variations in Rb and Ba can be ascribed to sea-water exchange upon alteration. The Cr data have been omitted because of the presence of chrome spinel microphenocrysts in the lavas (ie. Cr is highly compatible in spinel). As little as 0.4 % fractionation of this phase can account for the the observed Cr variation, with a negligible effect on the major element results.

It is also noteworthy that lava AG22-3-2 has a lower Cu content than the predicted liquid, an observation which can be reconciled with the chalcophile behaviour of Cu and the fractionation of sulphide(s). In this respect, it is

Table 21. A mass balance calculation model relating the compositions of two lavas from Dredge 3. A satisfactory fit for a closed system fractional crystallization relationship between compositions of AG22-3-4 (parental) and AG22-3-2 (residual).

	Observed Residual Composition	Observed Parental Composition	Calculated Parental Composition	
wt %				Residuals
SiO_2	49.62	49.19	49.24	0.05
TiO_2	1.89	1.73	1.70	-0.03
Al_2O_3	15.07	15.43	15.46	0.03
FeO	10.49	9.94	9.98	0.04
MnO	0.18	0.18	0.17	-0.01
MgO	7.32	8.23	8.18	-0.05
CaO	10.48	10.49	10.30	-0.19
Na_2O	2.98	3.06	2.90	-0.16
K_2O	0.33	0.35	0.30	0.05
P_2O_5	0.20	0.19	0.18	-0.01
			R^2 =	0.08

Weight fractions :

89.65	%	Residual liquid
3.60	%	Olivine ($Fo_{81.9}$)
6.44	%	Plagioclase ($An_{66.4}$)
99.69	%	

	Observed Parental Composition	Observed Daughter Composition	Calculated Residual Composition	
ppm				Bulk D*
Zr	130	145	145	0.010
Nb	3.6	2.6	4.0	0.010
Y	35	41	39	0.012
Rb	3.9	5.0	4.3	0.035
Ba	14.9	13.3	16.6	0.007
Sr	164	154	159	1.280
Co	51	49	48	1.608
Ni	170	121	128	3.590
V	250	283	273	0.192
Zn	81	85	84	0.724
Cu	58	58	62	0.362
Sc	37	42	41	0.053

important to note that Bryan et al. (1979) have postulated the removal of ~ 0.1 % sulphide from FAMOUS basalts to account for analogous disrepancies (viz. low Cu and Ni contents in differentiates). The formation of immiscible sulphide droplets and sulphide-decorated vesicles could adequately account for such fractionation.

Dredge 5.

Least squares solution models for Dredge 5 lavas, particularly the 'less depleted' subset met with little success. This suggests that closed system fractional crystallization does not adequately explain geochemical variations within this dredge haul. However, a successful least squares solution (Table 22) was determined which can relate one of the most primitive Dredge 5 lavas (AG22-5-31; $Mg^{\#}$ = 63.9) to the most evolved Dredge 5 basalt (AG22-5-48; $Mg^{\#}$ = 59.4) by the removal of olivine (3.8 %) and plagioclase (2.9 %). The proportions of these phases are in agreement with observed modes.

The trace element abundances predicted on the basis of this least squares solution (Table 22) are in relatively close agreement with the presumed daughter composition. Higher Ba and Sr contents in lava AG22-5-48 relative to predicted values are interpreted to be due to alteration. Since chrome spinel is present in these lavas, Cr data have been omitted

Table 22. A mass balance calculation model to test for a relationship between Dredge 5 lavas. A satisfactory solution for a closed system fractional crystallization relationship between lavas AG22-5-31 (parental) and AG22-5-38 (residual).

	Observed Residual Composition	Observed Parental Composition	Calculated Parental Composition	
wt %				Residuals
SiO_2	49.33	49.53	49.59	0.02
TiO_2	1.77	1.67	1.67	0.00
Al_2O_3	15.37	15.45	15.50	0.05
FeO	10.02	9.91	9.91	0.00
MnO	0.17	0.16	0.17	0.01
MgO	7.24	8.68	8.67	-0.01
CaO	10.55	10.61	10.48	-0.13
Na_2O	3.19	3.04	3.07	0.03
K_2O	0.16	0.27	0.15	-0.12
P_2O_5	0.18	0.19	0.18	-0.01

R^2 = 0.08

Weight fractions : 94.54 % Residual liquid
3.72 % Olivine ($Fo_{85.6}$)
2.61 % Plagioclase ($An_{70.1}$)
100.87 %

	Observed Parental Composition	Observed Daughter Composition	Calculated Residual Composition	
ppm				Bulk D*
Zr	127	133	134	0.010
Nb	2.8	2.5	3.0	0.010
Y	34	38	36	0.011
Rb	2.7	3.1	2.9	0.025
Ba	14.4	8.0	15.2	0.005
Sr	168	151	169	0.859
Co	51	48	47	2.548
Ni	172	115	116	7.998
V	242	262	255	0.040
Zn	76	80	76	1.084
Cu	62	61	64	0.575
Sc	39	40	41	0.079

from the model (see argument above), but Cr variation can be satisfied by minor (< 0.5 %) Cr-spinel fractionation.

Dredge 8.

A least squares solution relating the compositions of the most primitive Dredge 8 basalt (AG22-8-1; $Mg^{\#}$ = 64.0) and the most evolved Dredge 8 basalt (AG22-8-2; $Mg^{\#}$ = 57.9) is given in Table 23. This model requires clinopyroxene in the fractionate. The phase proportions are; olivine = 2.6 %, plagioclase = 10.2 % and clinopyroxene = 2.9 %. Although pyroxene is not present as a phenocryst phase, the relative proportions of plagioclase and olivine are similar to observed modes. The fact that clinopyroxene is necessary to satisfy the observed variation where clinopyroxene is significantly absent, is a paradox faced by MORB petrologists worldwide (eg. Basaltic Volcanism Study Project, 1981). As previously noted, it is probable that clinopyroxene fractionation may occur at high pressures and, on account of the fact that the primary clinopyroxene stability field shrinks with decreasing pressure (eg. Presnall et al., 1978), consequent resorption - or crystal settling - might obliterate direct evidence for clinopyroxene crystallization. The pyroxene used in the model was the clinopyroxene megacryst core composition in lava AG22-12-1. This megacryst shows textural evidence for resorption and the core composition compares well with

Table 23. A mass balance calculation model testing a possible relationship between two Dredge 8 basalts by fractional crystallization. Parental composition is AG22-8-1 and residual composition is AG22-8-2.

	Observed Residual Composition	Observed Parental Composition	Calculated Parental Composition	
wt %				Residuals
SiO_2	49.81	50.26	50.32	0.06
TiO_2	2.14	1.76	1.85	0.09
Al_2O_3	15.48	16.24	16.17	-0.07
FeO	10.21	9.44	9.32	-0.12
MnO	0.17	0.16	0.16	0.00
MgO	6.95	7.57	7.57	0.00
CaO	10.31	10.75	10.65	-0.10
Na_2O	3.26	3.15	3.24	0.09
K_2O	0.47	0.25	0.40	0.15
P_2O_5	0.26	0.19	0.22	0.03

$R^2 = 0.07$

Weight fractions:
84.45 % Residual liquid
2.63 % Olivine ($Fo_{81.6}$)
10.16 % Plagioclase ($An_{61.1}$)
2.90 % Clinopyroxene ($Wo_{40.7}En_{48.7}Fs_{10.6}$)
100.14 %

	Observed Parental Composition	Observed Daughter Composition	Calculated Residual Composition	
ppm				Bulk D*
Zr	140	182	185	0.045
Nb	2.5	2.8	3.0	0.014
Y	38	47	44	0.103
Rb	1.3	5.8	1.5	0.035
Sr	161	156	153	1.316
Co	46	47	48	0.661
Ni	118	107	107	1.610
V	249	282	286	0.170
Zn	79	88	86	0.479
Cu	49	46	55	0.360
Sc	35	35	37	0.626

clinopyroxenes believed to be high pressure cognate megacrysts in FAMOUS lavas (Bence and Bender, 1978).

The predicted trace element abundances (Table 23) are comparable to the observed composition of basalt AG22-8-2, supporting a fractional crystallization relationship. Alteration is inferred as the agent responsible for discrepancies in Rb and Ba contents, while the lower Cu content of basalt AG22-8-2 relative to the predicted value is interpreted to be a consequence of sulphide fractionation.

The involvement of clinopyroxene in the postulated model is supported by the systematic variation in Ti/Zr ratios from basalt AG22-8-1 through porphyritic lavas (AG22-8-19, AG22-8-24) to basalt AG22-8-2. The partition coefficient for Ti and Zr (0.3 and 0.1 respectively in Ca-rich pyroxene; Pearce and Norry, 1979) suggests that clinopyroxene fractionation is responsible for this variation.

To satisfy Ni variation, an unreasonably low distribution coefficient is required (ie. Kd = 8). However, this discrepancy does not warrant rejection of the model since the remaining elements provide an acceptable solution. It is poosible that the magma accumulated olivine which would account for the elevated Ni content. There is, however, no direct evidence to support this contention since there is no

significant difference between the observed mean olivine composition ($Fo_{81.8}$) and the expected equilibrium olivine composition ($Fo_{82.0}$) determined on the basis of the Roeder and Emslie (1970) FeO/MgO partition equation (Kd = 0.3). Enrichment of equilibrium olivine in such a magma is a possible mechanism which may affect Ni contents but not fractionate the FeO/MgO ratio (eg. Filter pressing; Cox, 1979). Such a process may be relevant to this evolved lava since petrographic evidence suggests that it has an intrusive affinity.

Cr has been omitted from the model on account of the presence of chrome spinel (<< 1 % Cr-spinel fractionation could satisfy Cr variation with a negligible effect on the major element model).

Dredge 12

A calculated least squares solution model (Table 24) tests the validity of a fractional crystallization relationship among Dredge 12 lavas. Samples chosen to represent the most primitive and the most evolved Dredge 12 liquids are AG22-12-26 and AG22-12-23 respectively. The model indicates that these compositions may be related by 13.79 % crystallization, involving the removal of olivine (2.52 %), plagioclase (6.88 %) and clinopyroxene (4.62 %).

Table 24. A mass balance calculation to test for a relationship between two basalt compositions from Dredge 12 by fractional crystallization. The parental composition is AG22-12-26 and the residual composition is AG22-12-23.

wt %	Observed Residual Composition	Observed Parental Composition	Calculated Parental Composition	Residuals
SiO_2	49.54	49.76	49.77	0.01
TiO_2	1.67	1.43	1.48	0.05
Al_2O_3	16.91	16.71	16.69	-0.02
FeO	9.21	8.74	8.71	-0.03
MnO	0.15	0.15	0.15	0.00
MgO	7.14	8.04	8.04	0.00
CaO	10.82	11.10	11.09	-0.01
Na_2O	3.12	2.92	3.02	0.10
K_2O	0.25	0.18	0.22	0.04
P_2O_5	0.21	0.15	0.18	0.03
			R^2 =	0.02

Weight fractions:

86.21 %	Residual liquid
2.52 %	Olivine ($Fo_{81.0}$)
6.88 %	Plagioclase ($An_{59.8}$)
4.62 %	Ca-pyroxene ($Wo_{40.7}En_{48.7}Fs_{10.6}$)
100.24 %	

ppm	Observed Parental Composition	Observed Daughter Composition	Calculated Residual Composition	Bulk D*
Zr	108	132	124	0.073
Nb	1.4	1.3	1.6	0.017
Y	30	37	34	0.173
Ba	4.5	3.9	5.2	0.009
Sr	152	157	152	1.020
Co	45	43	44	1.217
Cr	336	262	293	1.930
Ni	151	121	125	2.267
V	218	237	243	0.271
Zn	70	74	75	0.553
Cu	52	47	56	0.515
Sc	35	34	35	1.094

The megacryst pyroxene core composition (AG22-12-1) was used to satisfy the major element mix. The least squares data indicate a satisfactory fit to the model.

The trace element abundances in the predicted residual liquid compare favourably with those observed in lava AG22-12-23, with analogous differences (eg. lower Rb and Sr and higher Cu contents are predicted) to models presented above. Nevertheless, differences are observed in incompatible element abundances (Zr and Y) that evidently refute this simple fractional crystallization model. These differences (eg. higher Zr and Y contents in observed liquids) are thus inferred to be the result of variable source region characteristics or slight differences in partial melting that produced Dredge 12 parental magmas.

In this respect, it is important to note that models attempting to relate the aphyric basalts of Dredge 12 to the sparsely porphyritic lavas were unsuccessful. More specifically, it was speculated that the aphyric lavas could be produced by the removal of plagioclase (predominantly) from a common parental magma (eg. that they could represent residual magma purged from a plagioclase-rich magma). This hypothesis implies that the aphyric lavas and the porphyritic lavas represent complimentary magmas. The unsatisfactory solutions do not refute this possibility; it

is concluded that phenocryst redistribution in porphyritic lavas is responsible for obscuring such a relationship.

High Zr and Ti contents in the aphyric lavas and correspondingly high $Mg^{\#}$'s could be qualitatively accounted for by a different degree of partial melting of the basalt source. If the latter explanation is relevant, it is consistent with the observation that the mantle beneath this section of the SWIR is heterogeneous at the scale of individual dredges. This within-dredge variation is analogous to, yet more subtle than, the variation observed among Dredge 5 and 13 lavas.

Conclusions

In summary, the models presented above provide quantitative support that; (i) fractional crystallization was an important process in the petrogenesis of the Agulhas 22 basalt suite and; (ii) that differences in incompatible element abundances at several dredge sites must be a consequence of partial melting and/or source region characteristics.

It is important to correlate these quantitative results with qualitative results illustrated by major element variation diagrams (eg. CaO/Al_2O_3 ratio versus $Mg^{\#}$; Figure 24, and

the system Di-Ol-Qz; Figure 35). The proportions of the phases in the inferred fractionates are;

(i) In model 1 (Dredge 3); ol:plag ~ 35:65.

(ii) In model 2 (Dredge 5); ol:plag ~ 60:40.

(iii) In model 3 (Dredge 8); ol:plag:cpx ~ 15:65:20

(iii) In model 4 (Dredge 12); ol:plag:cpx ~ 20:50:30.

The order in which these models is presented above corresponds to the sequence from the steepest negative slope in Figure 24 to the steepest positive slope. Despite the observation that model 4 does not adequately account for the geochemical variation among Dredge 12 lavas, it is interesting to compare (albeit speculative) the major element solution with that of model 3. Relative to model 3, clinopyroxene in model 4 apparently crystallizes at the expense of plagioclase (the proportion of olivine and the total amount of fractionate are compatible). This observation is consistent with crystallization at a somewhat higher pressure (eg O'Donnel and Presnall, 1981). In other words, compatible with the relative plotting positions of Dredge 8 and 12 lavas in the ternary system Di-Ol-Qz (see Figure 35;- Dredge 12 lavas plot slightly closer to the Ol apex than Dredge 8 lavas).

****

CHAPTER 7

DISCUSSION AND CONCLUSIONS

In this chapter, aspects of the Agulhas 22 mineralogical and chemical data are discussed in terms of their inferred petrogenesis and their tectonic setting.

7.1 Petrologic Processes at Slow Spreading Ridges

Seismic evidence (e.g. Nisbet and Fowler, 1978) and thermal budget considerations (e.g. Sleep, 1975; Kuznir and Bott, 1976; Kuznir, 1980) suggest that spreading rates should exceed a minimum of 0.45 to 0.9 cm/yr (half rate) for a steady state magma chamber (e.g. O'Hara, 1977; Bryan and Moore, 1977; Dungan and Rhodes, 1979) to be maintained. Consequently, magma chambers are believed to be ephemeral at slow spreading ridges, a hypothesis which predicts (a) the probability that more primitive basalts should reach the ocean floor (e.g. Stakes et al., 1984) and (b), that, in the absence of mixing, the chemical integrity of individual magma batches should be maintained (e.g. Batiza and Vanko, 1984). In simpler terms, the former point would be reflected by a relatively large range in basalt compositions and eruption temperatures and, by implication, evidence for polybaric crystallization.

Figure 36 represents a model of petrologic processes at a slow spreading ridge according to Flower (1980). This model predicts two or more stages of crystallization: (a) between 15 and 25 km depth and (b) less than 5 km depth. Based on the observation that plagioclase is evidently buoyant in basaltic magma (e.g. Flower, 1980; 1981; Elthon, 1984) and that this phenomenon is pressure dependent (e.g. Bottinga and Weill, 1970), Flower (1980) has suggested that the more widespread occurrence of plagioclase enriched basalt at slow spreading ridges (relative to fast spreading ridges) is to be expected. Fisk (1986) has noted that if the volume of crystals exceeds 30%, such magmas rarely erupt and Staudigel and Bryan (1981) have noted the importance of enrichment by mechanical redistribution upon eruption. Although this calls into question the relationship between sea floor spreading rate and plagioclase enrichment, the issue that a polybaric crystallization regime is likely to produce plagioclase enriched magmas is relevant here.

Flower (1980) suggests that complex plagioclase crystal morphologies and zoning patterns often found in MORB are explicable in terms of polybaric crystallization regime (i.e. the magma dynamics inferred from Figure 36). In contrast, Kuo and Kirkpatrick (1982) have concluded that plagioclase from DSDP Legs 45 and 46 MORB displays evidence for magma mixing, a contention supported by melt inclusion

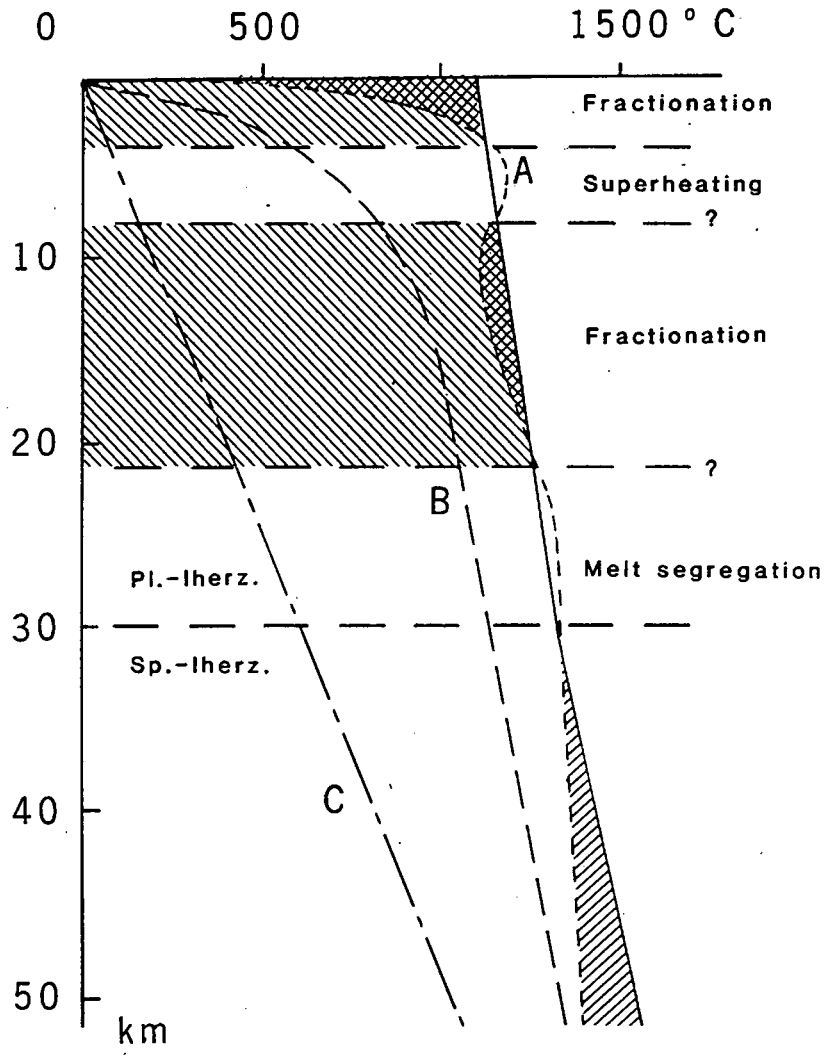

Figure 36: A model of magma dynamics at a slow spreading ridge (Flower, 1980) based on the theoretical geotherm (A) at the ridge axis. Curves B and C represent geotherms 30 km. from the ridge axis and average ocean crust respectively. (Geotherms after Sleep, 1975). The solid line represents the path of magma ascent. Depth intervals are schematic only. Pl-lherz = plagioclase lherzolite, sp-lherz = spinel lherzolite.

and geochemical evidence (Dungan and Rhodes, 1979; Rhodes et al., 1979). Despite this apparent contrast, zoning patterns in Agulhas 22 basalt plagioclase, although similar to other MORB plagioclase (e.g. Kuo and Kirkpatrick, 1982; Natland et al., 1983), are not identical. In the following section the basis for interpretation of zoning patterns and crystal morphology is outlined and a model of crystallization history is proposed.

7.2 Crystallization History

Plagioclase crystallization, as well as crystallization of other phases, probably accompanies magma movement because of cooling at the melt-country rock interface and effervescence of volatile constituents with decompression (Anderson, 1984). Consequently, it is reasonable to associate textural records of crystal growth with magma movement. For example, textural evidence (particularly plagioclase zoning patterns) has been presented to explain the crystallization processes in various igneous systems (e.g. Ewart, 1963; Pringle et al., 1974; Kuo and Kirkpatrick, 1982; Anderson, 1984). These studies have emphasized the genetic implications of magma movement on glomerocryst formation; turbulent flow may result in relative enrichment of parts of magmas in crystals (e.g. Wright and Fisk, 1971) to produce poikilitic glomerocrysts while crystals mutually attached along growth

zones (i.e. synneusis, Vance, 1969) may have "swum together" in the melt. These aspects are treated as evidence for magma dynamics in MORB genesis by Kuo and Kirkpatrick (1981). In this section, these relations are applied in an analogous fashion to the porphyritic lavas of Dredge 8 and 12 and loosely to the Agulhas 22 suite as a whole. The presence of calcic megacrysts in lavas of other dredges suggests a genetic link in the pre-eruption history of the suite in general.

The origin of oscillatory zoning in plagioclase is a complex and controversial issue (see Lofgren, 1974 for a good review). Models to explain oscillatory zoning are generally divided into two categories of behaviour (dynamical or static) according to whether the model implies movement of the plagioclase crystal in an absolute or relative sense to the surrounding melt (e.g. Anderson, 1984). In contrast to dynamic models referred to above, where external factors influence oscillatory zoning, a static model for oscillatory zoning has been developed by Loomis (1981,a & b). In this model, oscillatory zoning may arise by local convection of melt at the crystal-melt interface and the effect of water pressure on the equilibrium plagioclase composition.

It is recognized that interpretations of oscillatory zoning rely heavily on the coupling between interface kinetics and the diffusion of chemical species in the melt (e.g. Lasaga,

1981; 1982), and that the two types of behaviour outlined above may be seen as two end member models. In other words, it is not necessary to adopt either one or the other. Although the effect of water pressure is considered negligible on MORB plagioclase growth (e.g. Kuo and Kirkpatrick, 1982; based on low MORB water contents - Delaney et al., 1977), local convection at the crystal melt interface may itself be a function of external conditions (e.g. Allegre et al., 1984; Provost, 1985).

The model preferred here is that recently refined by the latter workers (Allegre et al., 1980; Provost, 1985) in which oscillatory zoning occurs at slow growth rates and is a function of changes in pressure, temperature and supersaturation. In view of the above, the crystallization history of the Agulhas 22 basalt suite is proposed below, combining evidence from previous chapters.

Stage 1 (Deep magma reservoir)

Nucleation and growth of type 1 plagioclase megacrysts occurred in primitive magma(s). Inclusion of high alumina spinel (sample AG22-8-16) suggests probable crystallization near the plagioclase/spinel lherzolite mantle boundary. Melt inclusions attest to trapped host magma possibly as a consequence of effervescence upon melt segregation.

Regrowth of slightly more calcic plagioclase rims and presence of poikilitic glomerocrysts suggests magma ascent (equilibrium plagioclase compositions become more calcic with decreasing pressure; Lindsley, 1966; Yoder, 1969) and turbulent behaviour. Primitive lava AG22-9-2 may represent a sample of such a magma erupted at the surface.

Stage 2 (Melt segregation and ascent)

Resorption of type 1 plagioclase megacrysts and nucleation of type 2 plagioclase megacrysts. Olivine also crystallized at this stage (indicated by its presence in glomerocrysts). Systematic morphologic and chemical variation from cores to rims of type 2 plagioclase megacrysts suggests initial rapid growth (presence of inclusions; patchy zoning indicates morphologic instability; Lasaga, 1981; Anderson, 1984) and consequent re-equilibration at slow growth rates (oscillatory zoning indicates slow growth and even periodic cessation of crystallization; Lasaga, 1982; Allegre et al., 1981). Overall reverse zoning is consistent with decreasing pressure (Yoder, 1969) and suggests that no significant heat loss occurred (for a contrary case, see Pringle et al., 1974). These observations are consistent with near adiabatic ascent (Figure 36) after initial rapid ascent (Provost, 1985). Variation of melt inclusion chemistry attests to differentiation during ascent and mineralogical

variations attest to polybaric re-equilibrium of the magmas and crystallization of clinopyroxene. Clinopyroxene megacryst in sample AG22-12-1 probably crystallized at this stage (or earlier) and presumably suffered resorption during ascent by reaction with host magma.

Stages 3 and 4 (Shallow level fractionation and eruption) Nucleation and growth of plagioclase phenocrysts and rims of similar composition on megacrysts, probably in a crustal magma chamber or sheeted dyke conduit system above a magma chamber (Pallister and Hopson, 1981). Porphyritic basalts may have been enriched in plagioclase by flow differentiation in such a process and/or upon eruption. It was probably at this stage (3) that the skeletal clinopyroxene rim grew upon the clinopyroxene megacryst of sample AG22-12-1. Ascent through the crust of porphyritic lavas was apparently accompanied by incorporation of olivine xenocrysts which show shock fabrics.

The nominal zoning of microphenocrysts in aphyric lavas in general indicates that chemical change of basalts within the crust was negligible (e.g. Fisk, 1986) and olivine microlites in several lavas attest to further cooling of 20°C or more after nucleation of microphenocrysts. In general, microphenocrysts and groundmass phases show textural evidence for high cooling rates prior to and upon extrusion.

Stage 5 (Post consolidation)

Secondary alteration effects occurred as a result of variable low temperature sea water alteration (palagonitization, formation of secondary chlorite, smectites and hydroxide phases).

7.3 Conclusions

Principle conclusions of this study are as follows:

(1) Basalts from the SWIR between 16 and 26 degrees east are olivine tholeiites with normal MORB characteristics. Aphyric (or microporphyritic) olivine-plagioclase basalt is the dominant lithology but several olivine basalts are also present. Porphyritic basalts (up to 20% plagioclase phenocrysts) comprise about 10% of the sample suite and are believed to be derived by accumulation of plagioclase and minor olivine. One such sample (AG22-12-1; $Mg^{\#}$ =64) is an olivine-plagioclase-clinopyroxene basalt with a single clinopyroxene megacryst which is partially resorbed. Clinopyroxene is absent as a phenocryst phase in more evolved lavas.

(2) Systematic ranges in mineral chemistry and the presence of distinct crystal populations in these lavas suggest an

origin due to polybaric crystal fractionation. The preferred mode of origin is given as:

(a) initial crystallization at depth of calcic bytownite (type 1 plagioclase) megacrysts and high-alumina spinel,

(b) nucleation and growth of reverse zoned sodic bytownite (type 2 plagioclase) megacrysts consequent to magma segregation and ascent, and

(c) crystallization within the oceanic crust prior to and upon eruption.

Melt inclusions in plagioclase megacrysts of Dredge 8 and 12 lavas provide evidence for initial entrapment upon decompression of a primitive magma with similar major element characteristics ($Mg^{\#}$=70; TiO_2=1.3 wt%; CaO/Al_2O_3 ratio=0.70) to most primitive lava AG22-9-2. Inclusions in more sodic, type 2 plagioclase megacrysts correspond to more evolved lava compositions and attest to differentiation of host liquids upon ascent or in a magma chamber. Resorption of type 1 plagioclase megacrysts (and the clinopyroxene megacryst in sample AG22-12-1) is explicable in terms of reaction with evolving magmas due to the effect of pressure on the phase relationships of basaltic magma(s).

(3) Projections of basalt and quench glass major element data in the pseudo-ternary system diopside-olivine-quartz (Walker et al., 1979) provide support for a polybaric crystallization history. Compositions plot within the low pressure olivine phase field, with only the most porphyritic lava having reached pyroxene saturation. Magnesian lavas (Mg≠≠ 66) plot close to the 10 kb pseudo-invariant point, consistent with liquids expected at pressures between 10 and 15kb (Stolper, 1980). Comparison of the clinopyroxene megacryst composition with MORB pyroxene believed to be of high pressure origin (Bender et al., 1978) indicates that this pyroxene could have a similar genesis. Trends in projected data are consistent with polybaric olivine, plagioclase and clinopyroxene fractionation and olivine ± plagioclase fractionation at low pressure.

(4) Quantitative modelling of crystal fractionation indicates that geochemical variations at certain dredge sites can for the most part be explained by crystallization of observed mineral phases. These variations are consistent with projections in the diopside-olivine-quartz pseudo-ternary.

(5) The overall chemical characteristics of the Agulhas 22 sample suite are within the range of normal, 'depleted' MORB from the SWIR, AAR and MAR in the vicinity of the Bouvet triple junction (le Roex et al., 1983; 1985; 1987) and variations in trace element abundances and inter-element

ratios indicate that at least 4 magma types are represented by the lavas, thereby precluding a relationship between all samples by simple crystal fractionation. A subset of least depleted basalts in Dredge 5 have an affinity to enriched Transitional type MORB from the SWIR between 0 and 11°E (le Roex et al., 1983) with comparatively low Zr/Nb (15-19), Zr/Y (3.7-3.9) and Y/Nb (4.1-4.5) ratios. Remaining Ridge A lavas have the following characteristics; Zr/Nb=26-56, Zr/Y=3.1-3.8 and Y/Nb=8-16. Ridge B basalts are the most depleted basalts with Zr/Nb=45-102, Zr/Y=3.0-3.9 and Y/Nb=12-34. The 'less depleted' Dredge 5 lavas and fine scale differences in inter-element ratios at individual dredge sites are believed to reflect local mantle heterogeneity, consistent with models of le Roex et al. (1983; 1985; 1987) for the suboceanic mantle in the Southern Ocean.

(6) While between ridge trace element variations provide compelling evidence for lateral mantle heterogeneity in the study area (eg. Zr/Nb, Zr/Y, Zr/Ba and Y/Nb ratios) certain variations are consistent with origins due to partial melting. Differences in partial melting may explain;

(a) between ridge variations in quench glass and whole rock compositions (Ridge A basalts have higher CaO/Al_2O_3 ratios, higher absolute MgO and FeO contents and lower normative plagioclase contents

than Ridge B basalts),

(b) higher nickel contents, at a given forsterite content, in olivine phenocrysts and micro-phenocrysts in Ridge A basalts relative to Ridge B basalt olivine, and

(c) higher Cu, Co and Sc contents, at a given Zr content, of Ridge A basalts relative to Ridge B basalts.

(7) The observation that Ridge A basalts are on average less depleted than Ridge B basalts is interpreted to be due to a relative increasing westward influence of an enriched MORB component. It is suggested that this is related to the waning eastward influence of the Bouvet mantle plume (eg. le Roex et al., 1983,1985) although this requires detailed isotopic analysis.

****

REFERENCES

Albee A.L. and Ray L. (1970) Correction factors for electron probe microanalysis of silicates, oxides, carbonates, phosphates and sulphates. Anal. Chem. 42(12), 1408-1414.

Alt J.C. and Honnorez J. (1984) Alteration of the upper oceanic crust, DSDP site 417: mineralogy and chemistry. Contrib. Mineral. Petrol. 87, 149-169.

Allegre C.J. and Minster J.F. (1978) Quantitative models of trace element behaviour in magmatic processes. Earth Planet. Sci. Lett. 38, 1-25.

Anderson A.T. (1976) Magma mixing: Petrologic process and volcanological tool. J. Volcan. Geotherm. Res. 1, 3-33.

Anderson A.T. (1984) Probable relations between plagioclase zoning and magma dynamics, Fuego Volcano, Guatemala. Amer. Mineral. 69, 660-676.

Anderson A.T. and Wright T.L. (1972) Phenocrysts and glass inclusions and their bearing on oxidation and mixing of basaltic magmas, Kilauea volcano, Hawaii. Amer. Mineral. 57, 188-216.

Aumento F., Loncarevic B.D. and Ross D.I. (1971) Hudson Geotraverse: Geology of the Mid Atlantic Ridge at 45°N. Phil. Trans. Roy. Soc. Lond. A268, 623-650.

Baird A.K. (1961) A pressed specimen die for the Norelco vacuum path x-ray spectograph. Norelco Rep. 8, 108.

Barth T.F.W. (1962) Theoretical Petrology, 2nd edition, New York, Wiley.

Ballard R.D., Holcomb R.T. and van Andel T.H. (1979) The Galapagos Rift at 86°W,3,Seet flows, collapse pits, and lava lakes of the rift valley. J. Geophys. Res. 84, 5407-5422.

Basaltic Volcanism Study Project (1981) Basaltic Volcanism on the Terrestrial Planets. Pergamon Press Inc. New York.

Bence A.E. and Albee A.L. (1968) Empirical correction factors for the electron microanalysis of silicates and oxides. J. Geol. 76, 382-403.

Bence A.E., Bayliss D.M., Bender J.F. and Grove T.L. (1979) Controls on the major and minor element chemistry of Mid-Ocean Ridge Basalts and Glasses. In: Deep Drilling

Results in the Atlantic Ocean: Ocean Crust (eds. Talwani M., Harrison C.G. and Hayes D.E.) American Geophysical Union, Washington. pp 331-341.

Bender J.F., Hodges F.N. and Bence A.E. (1978) Petrogenesis of basalts from the project FAMOUS area: experimental study from 0 to 15 kilobars. Earth Planet. Sci. Lett. 41, 277-302.

Bender J.F., Langmuir C.H. and Hanson G.N. (1984). Petrogenesis of Basalt Glasses from the Tamayo Region, East Pacific Rise. J. Petrol. 25, 213-254.

Best M.G. (1974) Contrasting types of chromium-spinel periodite xenoliths in basanitic lavas, Western Canyon, Arizona. Earth Planet. Sci. Lett. 23, 229-237.

Bideau D., Hekinian R. and Francheteau J. (1977) Orientation of ocean floor basaltic rocks at time of cooling: A general method. Contrib. Mineral. Petrol. 65, 19-28.

Bideau D and Hekinian R. (1984) Segregation Vesicles of Ocean Floor Basalts 1. Petrological Study of the Segregation Products. J. Geophys. Res. 89, 7903-7914.

Blanchard D.P., Rhodes J.M., Dungan M.A., Rodgers K.V.,

Donaldson C.H., Brannon J.C., Jacobs J.W. and Gibson E.K. (1976) The chemistry and petrology of basalts from Leg 37 of the Deep Sea Drilling Project. J Geophys. Res. 81, 4231-4246.

Bottinga Y. and Weill D.F. (1970) Densities of liquid silicate systems calculated from molar volumes of oxide components. Amer. J. Sci 269, 169-182.

Bougalt H. and Hekinian R (1974) Rift Valley in the Atlantic Ocean near 36°50'N : Petrology and Geochemistry of basaltic rocks. Earth Planet Sci. Lett. 24, 249-261.

Brandeis G., Jaupart C. and Allegre C. (1984) Nucleation, Crystal Growth and the Thermal Regime of Cooling Magmas. J. Geophys. Res. 89, 10161-10177.

Brooks C.K. (1976) The Fe_2O_3/FeO ratio of basalt analyses: an appeal for standardised procedure. Bull. Geol. Soc. Denmark 25, 117-119.

Bryan W.B. (1972) Morphology of Quench Crystals in Submarine Basalts. J. Geophys. Res. 77(29), 5812-5819.

Bryan W.B. (1974) Fe-Mg relationships in sector zoned

submarine basalt plagioclase. Earth. Planet. Sci. Lett. 24, 157-165.

Bryan W.B. (1979) Regional variation and petrogenesis of basalt glasses from the FAMOUS area, Mid-Atlantic Ridge J. Petrol. 20, 293-325.

Bryan W.B. (1983) Systematics of modal phenocryst assemblages in submarine basalts: petrologic implications. Contrib. Mineral. Petrol. 83, 62-74.

Bryan W.B. and Dick H.J.B. (1982) Contrasted abyssal basalt liquidus trends: evidence for mantle major element heterogeneity. Earth Planet. Sci. Lett. 58, 15-26.

Bryan W.B. and Moore J.G. (1977) Compositional variations of young basalts in the Mid-Atlantic Ridge rift valley near lat 36°49'N. Geol. Soc. Amer. Bull. 88, 556-570.

Bryan W.B., Thompson G., Frey F.A. and Dickey J.S. (1976) Inferred geologic settings and differentiation in basalts from the Deep Sea Drilling Project. J. Geophys. Res. 23, 4285-4304.

Bryan W.B., Thompson G and Ludden J.N. (1981) Compositional

variation in normal MORB from 22-25°N: Mid-Atlantic Ridge and Kane Fracture Zone. J. Geophys. Res. 86, B12, 11815-11836.

Buddington A.F. and Lindsley D.H. (1964) Iron-titanium oxide minerals and synthetic equivalents. J. Petrol. 5, 310-357.

Burns R.G. (1975) Crystal field effects in chromium and its partitioning in the mantle. Geochim. Cosmochim. Acta. 39, 857-864.

Carmichael I.S.E., Nicholls J. and Smith A.L. (1970) Silica activity in igneous rocks. Amer. Mineral. 55, 246-263.

Church S.E. and Tatsumoto M. (1975) Lead isotope relations in oceanic ridge basalts from the Juan de Fuca Ridge area, N.E. Pacific Ocean. Contrib. Mineral. Petrol. 53, 253-279.

Claque D.A. and Bunch T.E. (1976) Formation of ferrobasalt at East Pacific mid-ocean spreading centres. J. Geophys. Res. 81(3), 4247-4256.

Clocchiatti R. and Massare D. (1985) Experimental crystal growth in glass inclusions: the possibilites and limits of the method. Contrib. Mineral. Petrol. 89, 193-204.

Cox K.G. (1978) Komatiites and other high-magnesia lavas: some problems. Phil.Trans. Roy. Soc. Lond., A, 288, 599-609.

Cox K.G., Bell J.D. and Pankhurst R.J. (1979) The Interpretation of igneous rocks. Allen and Unwin, pp 151; 332-359.

Coish R.A. and Taylor L.A. (1979) The effects of cooling rate on texture and pyroxene chemistry in DSDP leg 34 basalts: A microprobe study. Earth Planet. Sci. Lett. 42, 389-398.

Camanske G.K. and Moore J.G. (1977) Composition and phase chemistry of sulphide globules in basalt from the Mid-Atlantic Ridge rift valley near 37°N lat. Geol. Soc. Amer. Bull., 88, 587-599.

Dale I.M. and Henderson P. (1972) The partitioning of transition elements in phenocryst bearing basalts and their implications about melt structure. Int. Geol. Congr. 24th, section 10: 105-111.

Davey S. (1984) A geochemical study of basalts dredged from a fracture zone north of the Bouvet Triple Junction. Unpublished honours project thesis. University of Cape

Town.

Deer W.A., Howie R.A. and Zussman J. (1978) Rock forming minerals volume 2A; Single chain silicates: Pyroxenes. Longman.

Delaney J.R., Muenow D., Ganguly J., Royce D. (1977) Anhydrous glass-vapour inclusions from phenocrysts in oceanic tholeiitic pillow basalts. EOS 58, 530.

Dick H.J.B. and Bullen T. (1984) Chromian spinel as a petrogenetic indicator in Abyssal and Alpine type peridotites and spatially associated lavas. Contrib. Mineral. Petrol. 86, 54-76.

Dickey J.S., Frey F.A., Hart S.R., Watson E.B. and Thompson G. (1977) Geochemistry and petrology of dredged basalts from the Bouvet Triple Junction, South Atlantic. Geochim. Cosmochim. Acta. 41, 1105-1118.

Dickey J.S. and Yoder H.S. (1972) Partitioning of chromium and aluminium between clinopyroxene and spinel. Carnegie Inst. Wash. Year Book 71, 384-392.

Dixon S. and Rutherford M.J. (1979) Plagiogranites as late-stage immiscible liquids in aphiolite and mid-ocean ridge suites: An experimental study. Earth Planet.

Sci. Lett. 45, 45-60.

Donaldson C.H. (1976) An experimental investigation of olivine morphology. Contrib. Mineral. Petrol. 57, 187-213.

Donaldson C.H. (1979) An experimental investigtion of the delay in nucleation of olivine in mafic magmas. Contrib. Mineral. Petrol. 69, 21-32.

Donaldson C.H. and Brown R.W. (1977) Refractory megacrysts and magnesium rich melt inclusions within spinel and oceanic tholeiites: indicators of magma mixing and parental magma composition. Earth Planet. Sci. Lett. 37, 81-89.

Duncan A.R., Erlank A.J. and Betton P.J. (1984) Appendix 1: analytical techniques and data base descriptions. Geol. Soc. S. Afr., Spec. Publ. 13, 389-395.

Dungan M.A. and Rhodes J.M. (1978) Residual glasses and melt inclusions in basalts from DSDP legs 45 and 46: Evidence for magma mixing. Contrib. Mineral. Petrol. 67, 417-431.

Dungan M.A., Rhodes J.M., Long P.E., Blanchard D.P., Brannon

J.C. and Rodgers K.V. (1979) The petrology and geochemistry of basalts from site 396, legs 45 and 46 of the Deep Sea Drilling Project. In: Init. Rep. Deep Sea Drill. Proj. 46, 89-113.

Dupuy C. and Coulon C. (1973) Li, Rb, Sr and Ba in Plagioclases of Andesite group from Logudaro and Bosano (Northeastern Sardinia). Cr. Ac. Sci. D., 277, 1593.

Eggler D.H. (1972) Water-saturated and undersaturated melting relations in a Paracutin andesite and an estimate of water content in the natural magma. Contrib. Mineral. Petrol. 34, 262-271.

Elthon D., Casey J. and Komor S. (1982) Mineral chemistry of ultramafic cumulates from the North Arm Mountain massif of the Bay of Islands ophiolite: evidence for high pressure crystal fractionation of oceanic basalts. J. Geophys. Res. 87, 8717-8734.

Elthon D. (1984) Plagioclase buoyancy in oceanic basalts: Chemical effects. Geochim. Cosmochim. Acta 48, 753-768.

Erlank A.J. and Kable E.J.D. (1976) The significance of incompatible elements in Mid-Atlantic Ridge basalts

from 45°N, with particular reference to Zr/Nb. Contrib. Mineral. Petrol. 54, 281-291.

Ewart A. (1963) Petrology and petrogenesis of the Quaternary pumice ash in the Taupo area, New Zealand. J. Petrol. 4, 392-431.

Fisher R.L. Jantz M.Z. and Comer R.L. (1982) GEBCO-SW-Indian Chart 9, 5th ed. Can. Hydrog. Surv., Ottowa, Ontario.

Fisk M.R. (1986) Mid-ocean ridge basalts from the Galapagos spreading center: Direct probes of magma chambers. Geology 14, no. 3, 204-207.

Fisk M.R. and Bence A.E. (1978) Experimental crystallization of chrome spinel in FAMOUS basalt 527-1-1. Earth Planet. Sci. Lett. 48, 111-123.

Fisk M.R., Bence A.E. and Schilling J.G. (1982) Major element chemistry of Galapagos Rift Zone magmas and their phenocrysts. Earth Planet. Sci. Lett. 61, 171-189.

Fisk M.R., Schilling J.-G. and Sigurdsson H. (1980) An experimental investigation of Iceland and Reykjanes

ridge tholeiites: I, Phase relations. Contrib. Mineral. Petrol. 74, 361-374.

Flower M.F.J. (1980) Accumulation of calcic plagioclase in ocean ridge tholeiite: an indication of spreading rate? Nature 287, 530-532.

Flower M.F.J. (1981) Thermal and kinetic control on ocean-ridge magma fractionation: contrasts between Atlantic and Pacific spreading axes. J. Geol. Soc. Lond. 138, 695-712.

Floyd P.A. and Tarney J. (1979) First order alteration chemistry of leg 49 basement rocks. Init. Rep. Deep Sea Drill. Proj. 49, 693-708.

Ford C.E., Russel D.G., Craven J.A. and Fisk M.R. (1983) Olivine-liquid equilibria: Temperature, pressure and composition dependence of the crystal/liquid cation partition coefficients for Mg, Fe^{2+}, Ca and Mn. J. Petrol. 24, 256-265.

Francis D. (1986) The pyroxene paradox in MORB glasses - a signature of picritic parental magmas? Nature 319, 586-589.

Frey F.A., Bryan W.B. and Thompson G. (1974) Atlantic Ocean Floor: Geochemistry and Petrology of Basalts From Legs 2 and 3 of the Deep Sea Drilling Project. J. Geophys. Res. 79, 35; 5505-5527.

Frey F.A., Dickey J.S., Thompson G., Bryan W.B. and Davies H.L. (1980) Evidence for heterogeneous primary MORB and mantle sources, NW Indian Ocean. Contrib. Mineral. Petrol. 74, 387-402.

Frey F.A. and Green D.H. (1974) The mineralogy, geochemistry and origin of iherzolite inclusions in Victorian basanites. Geochim. Cosmochim. Acta 38, 1023-1059.

Fujii T. and Kushiro T. (1977) Melting relations and viscocity of an abyssal tholeiite. Carnegie Inst. Washington. Yearbook 76, 461-465.

Fujii T. and Bougalt H. (1983) Melting relations of a magnesian abyssal tholeiite and the origin of MORBs. Earth Planet. Sci. Lett. 62, 283-295.

Fujii T. and Scarfe C.M. (1985) Compositions of liquids coexisting with spinel iherzolite at 10kbar and the genesis of MORBs. Contrib. Mineral. Petrol. 90, 18-28.

Gast P.W. (1968) Trace-element fractionation and the origin of tholeiitic and alkaline magma types. Geochim. Cosmochim. Acta, 32, 1057-1086.

Gibb F.G.F. (1974) Supercooling and the crystallization of plagioclase from a basaltic magma. Miner. Mag. 39, 641-653.

Goodman R.J. (1972) The distribution of Ga and Rb in coexisting groundmass and phenocryst phases of some basic volcanic rocks. Geochim. Cosmochim. Acta, 36, 303-317.

Graham A.L., Symes R.F., Bevan J.C. and Din V.K. (1978) Chromium-Bearing spinels in some rocks of Leg 45: Phase chemistry, zoning and relation to host basalt chemistry. In; Init. Repts. DSDP 45, 581-586.

Green D.H. (1971) Compositions of basaltic magmas as indicators of conditions of origin: Application to oceanic volcanism. Philos. Trans. R. Soc. Lond. Ser. A 268, 707-725.

Green D.H., Hibberson W.O. and Jacques A.L. (1979) In: The Earth: Its origin, structure and evolution, M.W. McElhinney, ed. (Academic Press, New York), p 265.

Green D.H. and Ringwood A.E. (1967) The genesis of basaltic magmas. Contrib. Mineral. Petrol. 15, 103-190.

Green D.H., Ringwood A.E., Ware N.G. and Hibberson W.O. (1972) Experimental petrology and petrogenesis of Apollo 14 basalts. Proc. Lunar Sci. Conf. 3, 197-206.

Griffen W.L. and Murthy V.R. (1969) Distribution of K, Rb Sr and Ba in some minerals relevant to basalt genesis. Geochim. Cosmochim. Acta, 33, 1389-1414.

Grove T.L. and Bence A.E. (1977) Experimental study of pyroxene-liquid interaction in quartz normative basalt 15597. Proc. Lunar Sci. Conf. 8th, pp 1549-1579.

Grove T.L. and Bryan W.B. (1983) Fractionation of pyroxene-phyric MORB at low pressure: an experimenal study. Contrib. Mineral. Petrol. 84, 293-309.

Haggerty S.E. (1976) Opaque minerals in terrestrial igneous rocks. In : Oxide Minerals, Chapter 8. (Ed.) D. Rumble III, Southern Printing Company.

Hanson G.N. and Langmuir C.H. (1978) Modelling of major elements in mantle-melt systems using trace element approaches. Geochim. Cosmochim. Acta 42, 725-741.

Hart S.R. (1969) K, Rb, Cs contents and K/Rb and K/Cs ratios of fresh and altered submarine basalts. Earth Planet. Sci. Lett. 6, 295-303.

Hart S.R. (1970) Chemical exchange between seawater and deep ocean basalts. Earth Planet. Sci. Lett. 9, 269-279.

Hart S.R. and Davis K.E. (1978) Nickel partitioning between olivine and silicate melt. Earth Planet. Sci. Lett 40, 203-219.

Hart S.R., Erlank A.J. and Kable E.J.D. (1974) Sea floor basalt alteration: some chemical and Sr isotope effects. Contrib. Mineral. Petrol. 44, 219-230.

Hekinian R., Moore J.G. and Bryan W.B. (1976) Volcanic rocks and processes of the Mid Atlantic Ridge rift valley near 36°49'N. Contrib. Mineral. Petrol. 57, 145-162.

Humphris S.E., Morrison M.A. and Thompson R.N. (1978) Influence of rock crystallization history upon subsequent lanthanide mobility during hydrothermal alteration of basalts. Chem. Geol. 23, 125-137.

Irvine T.N. (1965) Chrome spinel as a petrogenetic indicator, 1, Theory. Can. J. Earth Sci. 2, 648-672.

Irvine T.N. (1967) Chromian spinel as a petrogenetic indicator, 2. Petrologic applications. Can. J. Earth Sci. 4, 71-103.

Ito K. (1973) Analytical approach to estimating source rock of basaltic magmas: Major elements. J. Geophys. Res. 78(2), 412-431.

Jackson E.D. (1969) Chemical variation in coexisting chromite and olivine in chromite zones of the Stillwater Complex. Econ. Geol. Mon. 4, 41-71.

Jacques A.L. and Green D.H. (1980) Determination of liquid compositions in high pressure melting of peridotite. Am. Mineral. 64, 1312-1321.

Jaeger J.C. (1967) Cooling and solidification of igneous rocks. In: Hess H.H. and Poldervaart A. (eds) Basalts. New York, Wiley, pp 503-506.

Jones J.G. (1969) Pillow lavas as depth indicators. Amer. J. Sci. 267, 181-195.

Kable E.J.D. (1972) Some aspects of the geochemistry of selected elements in basalts and associated lavas. Unpublished PhD thesis, University of Cape Town.

Kay R., Hubbard N. and Gast P.W. (1970) Chemical characteristics of oceanic ridge volcanic rocks. J. Geophys. Res. 75, 1585-1613.

Kirkpatrick R.J. (1974) Kinetics of crystal growth in the system $CaMgSi_2O_6$ - $CaAl_2SiO_6$. Am. J. Sci. 274, 215-242.

Kirkpatrick R.J. (1977) Nucleation and growth of plagioclase, Makaoputii and Alae lava lakes, Kilauea Volcano, Hawaii. Geol. Sci. Amer. Bull. 88, 78-84.

Kirkpatrick R.J. (1979) Processes of Crystallization in Pillow Basalts, Hole 396B, Leg 46. Init. Rep. Deep Sea Drill. Proj. 46, 259-269.

Kirkpatrick R.J. (1983) Theory of nucleation in silicate melts. Am. Mineral. 68, 66-77.

Kudo A.M. and Weill D.F. (1970) An igneous plagioclase thermometer. Contrib. Mineral. Petrol. 25, 52-65.

Kuno H. (1960) High Alumina basalts. J. Petrol. 1, 121-145.

Kuo L-C. and Kirkpatrick (1982) Pre-eruption history of phyric basalts from DSDP and zoning patterns in plagioclase. Contrib. Mineral. Petrol. 79, 13-27.

Kushiro I. (1973) Origin of some magmas in oceanic and circum-oceanic regions. Tectonophysics 17, 211-222.

Kushiro I. (1980) Changes with pressure of degree of partial melting and K_2O content of liquids in the system Mg_2SiO_4 - $KAlSiO_4$ - SiO_2. Carnegie Inst. Wash. Year Book 79, 267-271.

Langmuir C.H. and Bender J. (1984) The geochemistry of oceanic basalts in the vicinity of transform faults: observations and implications. Earth Planet. Sci. Lett. 69, 107-127.

Langmuir C.H., Bender J.F., Bence A.E., Hanson G.N. and Taylor S.R. (1977) Petrogenesis of basalts from the FAMOUS area: Mid-Atlantic Ridge. Earth Planet. Sci. Lett. 36, 133-156.

Langmuir C.H. and Hanson G.N. (1980) An evolution of major element heterogeneity in the mantle sources of basalts. Phil. Trans. Roy. Soc. Lond. A297, 383-407.

Lasaga A.C. (1981) Implications of a concentration-dependent growth rate on the boundary layer crystal-melt model. Earth Planet. Sci. Lett. 56, 429-434.

Lasaga A.C. (1982) Toward a master equation in crystal growth. Amer. J. Sci. 282, 1264-1288.

Leeman W.P. and Scheidegger K.F. (1977) Olivine/liquid distribution coefficients and a test for crystal liquid equilibrium. Earth Planet. Sci. Lett. 35, 247-257.

Le Bas M.J. (1962) The role of aluminium in igneous clinopyroxenes with relation to their parentage. Amer. J. Sci. 260, 267-288.

Le Maitre R.W. (1984) A proposal by the I.U.G.S. Subcommission on the systematics of igneous rocks for a chemical classification of volcanic-rocks based on the Total Alkoli Silica (TAS) Diagram. Aust. J. Earth Sci. 31(2), 243-255.

le Roex A.P. (1980) Geochemisry and mineralogy of selected Atlantic Ocean Basalts. Unpublished PhD thesis, University of Cape Town.

le Roex A.P. (1985) Geochemistry, mineralogy and magmatic evolution of the basaltic and trachytic lavas from Gough Island, South Atlantic. J. Petrol. 26(1), 149-186.

le Roex A.P. and Dick H.J.B. (1981) Petrography and geochemistry of basaltic rocks from the Conrad fracture zone on the America-Antarctic Ridge. Earth Planet. Sci. Lett. 54, 117-138.

le Roex A.P., Dick H.J.B., Erlank A.J., Reid A.M., Frey F. and Hart S.R. (1983) Geochemistry, mineralogy and petrogenesis of lavas erupted along the Southwest Indian Ridge between the Bouvet triple junction and 11 degrees east. J. Petrol. 24, 267-318.

le Roex A.P., Dick H.J.B., Gulen L., Reid A.M. and Erlark A.J. (1987) Local and regional heterogeneity in MORB from the Mid-Atlantic Ridge between 54.5°S and 51°S: Evidence for geochemical enrichment. Geochim. Cosmochim. Acta 51, 541-555.

le Roex A.P., Dick H.J.B., Reid A.M. and Erlank A.J. (1981) Ferrobasalts from the Spiess Ridge segment of the Southwest Indian Ridge. Earth Planet. Sci. Lett. 60, 437-451.

le Roex A.P., Dick H.J.B., Reid A.M., Frey F.A., Erlark A.J. and Hart S.R. (1985) Petrology and geochemistry of basalts from the American-Antarctic Ridge, Southern Ocean: implications for the westward influence of the Bouvet mantle plume. Contrib. Mineral. Petrol. 90, 367-380.

le Roex A.P. and Erlank A.J. (1982) Quantitative evaluation of fractional crystallization in Bouvet Island lavas. J. Volcanol. Geotherm. Res. 13, 309-338.

le Roex A.P., Erlank A.J. and Needham H.D. (1981) Geochemical and mineralogical evidence for the occurrence of at least three distinct magma types in the "FAMOUS" region. Contrib. Mineral. Petrol. 77, 24-37.

Leung I.S. (1974) Sector zoned titanaugites: Morphology, Crystal Chemistry and Growth. Amer. Mineral. 59, 127-138.

Lindsley D.H. (1966) Melting relations of plagioclase of high pressures. Carnegie Inst. Washington Year Book 65, 204.

Lindstrom D.J. (1976) Experimental Study of the Partitioning of the Transition Metals between Clinopyroxene and Coexisting Silicate Liquids. Unpubl. Ph.D. Thesis, Univ. of Oregon, Oregon.

Lofgren G.E. (1974) An experimental study of plagioclase crystal morpholgy: iscothermal crystallization. Am. J. Sci. 274, 243-273.

Lofgren G.E. (1980) Experimental studies on the dynamic crystallization of silicate melts. In: Hargraves R.B. (ed) Physics of Magmatic Processes. Princeton. Princeton Univ. Press, pp 487-551.

Longhi J., Walker D. and Hays J.F. (1978) The distribution of Mg and Fe between olivine and lunar basaltic liquids. Geochim. Cosmochim. Acta 42, 1545-1558.

Loomis T.P. (1981a) An investigation of disequilibrium growth processes of plagioclase in the system anorthite-albite-water by methods of numerical simulation. Contrib. Mineral. Petrol. 76, 196-205.

Loomis T.P. (1981b) Numerical simulations of crystallization processes of plagioclase in complex melts: the origin of major and oscillatory zoning in plagioclase. Contrib. Mineral. Petrol. 81, 219-229.

MacKenzie W.S., Donaldson C.H. and Guilford C. (1982) Atlas of igneous rocks and their textures. Longman Group Limited.

Mathez E.A. (1973) Refinement of the Kudo-Weill plagioclase thermometer and its application to basaltic rocks. Contrib. Mineral. Petrol. 41, 61-72.

McBirney A.R. and Noyes R.M. (1979) Crystallization and layering of the Skaergaard Intrusion. J. Petrol. 20, 487-554.

McKay G.A. and Weill D.F. (1976) Petrogenesis of KREEP. Proc. Seventh Lunar Sci. Conf., 2427-2447.

Melson W.G., Vallier T.L., Wright T.L., Byerly G. and Nelen J. (1976) Chemical diversity of abyssal volcanic glass erupted along Pacific, Atlantic and Indian Ocean seafloor spreading centres. In: The Geophysics of the Pacific Ocean Basin Margin. A.G.U. Monograph Series 19, 351-368.

Miura Y. (1984) Computer Simulation of Anomalous Composition of Mg-Fe Plagioclase in meteorites. Proc. 9th Symposium on Antarctic Meteorites. (Ed) T. Nagata. Memoirs Nat. Inst. Polar Research. Special issue 35, 226-242.

Miyashiro A., Shido F. and Ewing M. (1970) Crystallization and differentiation in abyssal tholeiites and gabbros from mid ocean ridges. Earth Planet. Sci. Lett. 7, 361-365.

Muir I.D. and Tilley C.E. (1964) Iron enrichment and pyroxene fractionation in tholeiites. Geol. J. 4, 143-156.

Muir I.D. and Tilley C.E. (1966) Basalts from the northern part of the Mid Atlantic Ridge, II, The Atlantis Collection near 30°N. J. Petrol. 7, 193-201.

Mysen B.O. and Kushiro I. (1979) Pressure dependence of nickel partitioning between forsterite and aluminous silicate melts. Earth Planet. Sci. Lett. 42, 383-388.

Nabalek P.I. and Langmuir C.H. (1986) The significance of unusual zoning in olivines from FAMOUS area basalt 527-1-1. Contrib. Mineral. Petrol. 93, 1-8.

Nagasawa H., Schreiber H.D. and Blanchard D.P. (1976) Partition coefficients of REE and Sc in perovskite and melilite and their implications for Allende inclusions. (Abs.) - Lunar Sci. 8, 588-590.

Nathan H.D. and van Kirk (1978) A model of Magmatic Crystallization. J. Petrol. 19, 66-76.

Natland J.H. (1978) Crystal morphologies in basalts from DSDP site 395, 23°N, 46°W, Mid Atlantic Ridge. Init. Rep. Deep Sea Drill. Proj. 45, 423-445.

Natland J.H. (1980) Crystal morphologies in basalts dredged and drilled from the East Pacific Rise near 9° and the Siqueiros Fracture Zone. Init. Rep. Deep Sea Drill. Proj. 54, 605-632.

Natland J.H., Adamson A.C., La Verne C., Melson W.G. and O'Hearn T. (1983). A compositionally nearly steady-state magma chamber of the Costa Rica Rift: evidence from basalt glass and mineral data. Init. Rep. Deep Sea Drill. Proj. 69, 811.

Natland J.H. and Melson W.G. (1980) Compositions of basaltic glasses from the East Pacific Rise, and

Siqueiros Fracture Zone, near 9°N. Init. Rep. Deep Sea Drill. Proj. 54, 705-723.

Nisbet E.G. and Fowler C.M.R. (1978) The Mid-Atlantic Ridge at 37 and 45°N: some geophysical and petrological constraints. Geophys. J. Res. Astron. Soc. 54, 631-660.

Norrish K. and Hutton J.T. (1969) An accurate x-ray spectrographic method for the analysis of a wide range of geologic samples. Geochim. et. Cosmochim. Acta 33, 431-453.

Norton I.O. (1976) The present relative motion between Africa and Antarctica. Earth Planet. Sci. Lett. 33, 219-230.

O'Donnell T.H. and Presnall D.C. (1980) Chemical variations of the glass and mineral phases in basalts dredged from 25-35°N along the Mid-Atlantic Ridge. Amer. J. Sci. 280A, 845-868.

O'Hara M.J. (1977) Geochemical evolution during fractional crystallization of a periodically refilled magma chamber. Nature 266, 503-507.

Osborne E.F. and Tait D.B. (1952) The system diopside-forsterite-anorthite. Am. J. Sci. (Bowen Volume), 413-433.

Padden F.J. (Jr.) and Keith H.D. (1973) Mechanism for lamellar branching in isotactic polypropylene. J. Appl. Phys., 44 (No. 3), 1217-1223.

Pallister J.S. and Hopson C.A. (1981) Samail ophiolite plutonic suite: Field relations, phase variation, cryptic variation and layering, and a model of a spreading ridge magma chamber. J. Geophys. Res 86, 2593-2644.

Papike J.J., Cameron K.L. and Baldwin K. 91974) Amphiboles and pyroxenes: characterisation of *other* than quadrilateral components and estimates of ferric ion from microprobe data (abstract). *Abstracts with Program*, Geol. Soc. Amer. 6, 1053-1054.

Paster T.P., Schauwecker D.S. and Haskin L.A. (1974) The behaviour of some trace elements during solidification of the Skaegaard layered series. Geochim. Cosmochim. Acta., 38, 1549-1577.

Pearce J.A. and Norry M.J. (1979) Petrogenetic implications of Ti, Zr, Y and Nb variations in volcanic rocks. Contrib. Mineral. Petrol. 69, 33-47.

Powell R. and Powell M. (1977) Geothermometry and oxygen barometry using co-existing iron-titanium oxides: a reappraisal. Min. Mag. 41, 257-263.

Presnall D.C., Dixon S.A., Dixon J.R., O'Donnell T.H., Brenner N.L., Shrock R.L., Dyons D.W. (1978) Liquidus phase relations on the join diopside-forsterite-anorthite from 1atm. to 20kbar: their bearing on the generation and crystallization of basaltic magma. Contrib. Mineral. Petrol. 66, 203-220.

Presnall D.C., Dixon J.R., O'Donnell T.H. and Dixon S.A. (1979) Generation of mid ocean ridge tholeiites. J. Petrol. 20, 3-35.

Presnall D.C. and Hoover J.D. (1984) Composition and depth of origin of primary mid-ocean ridge basalts. Contrib. Mineral. Petrol. 87, 170-178.

Price R.C., Kennedy A.K., Riggs-Sneeringer M. and Frey F.A. (1986) Geochemistry of basalts from the Indian Ocean triple junction: implications for the generation and evolution of Indian Ocean ridge basalts. Earth Planet. Sci. Lett 78, 379-396.

Pringle G.J., Trembath L.T., Parjari G.E. jr (1974) Crystallization history of a zoned plagioclase. Mineral. Mag. 39, 867-877.

Provost A. (1985) Oscillatory zoning in plagioclase: A logical issue after rapid magma ascent. Terra Cognita volume 5, abstract V18, p 330.

Rhodes J.M., Dungan M.A., Blanchard D.P. and Long P.E. (1979) Magma mixing at mid ocean ridges: evidence from basalts drilled near 22°N on the mid-Atlantic ridge. Tectonophysics 55, 35-61.

Robie R.A. and Waldbaum D.R. (1968) Thermodynamic properties of minerals and related substances at 298.15K and one atm. pressure and at higher temperatures. Bull. U.S. Geol. Survey 1259.

Roedder E. (1976) Petrologic data from experimental studies on crystallized silicate melt and other inclusions in lunar and Hawaiian olivine. Amer. Mineral. 61, 684-690.

Roeder P.L. (1974) Activity of iron and olivine solubility in basaltic liquids. Earth Planet. Sci. Lett. 23, 397-410.

Roeder P.L. and Emslie R.F. (1970) Olivine-liquid equilibrium. Contrib. Mineral. Petrol. 19, 275-289.

Sato H. (1977) Nickel content of basaltic magma: identification of primary magmas and a measure of the degree of olivine fractionation. Lithos 10, 113-120.

Sato H. (1978) Segregation vesicles and immiscible liquid droplets in ocean floor basalt of hole 396B, IPOD/DSDP Leg 46, Init. Rep. Deep Sea Drill. Proj. 46, 283-286.

Schiffman P. and Lofgren G. (1982) Dynamic crystallization studies on the Grande Ronde Pillow Basalts, Central Washington. J. Geol. 90, 49-78.

Schilling J.-G. (1973) Iceland Mantle Plume: Geochemical study of Reykjanes Ridge. Nature 242, 565.

Schilling J.-G. (1975) Azores Mantle Blob: rare earth evidence. Nature 242, 2-5.

Schilling J.-G., Zajac M., Evans R., Johnston T., White W., Devine J.O. and Kingsley R. (1983). Petrologic and geochemical variations along the mid-Atlantic Ridge from 29°N to 73°N. Am J. Sci. 283, 510.

Sclater J.G., Bowin C., Hay R., Haskins H., Purie J., Phillips J. and Tapscott C. (1976). The Bouvet Triple Junction. J. Geophys. Res. 81, 1857-1869.

Scott R.B. and Hajash A. jr (1976) Initial submarine alteration of basaltic pillow lavas: A microprobe study. Am J. Sci. 276, 480-501.

Seward T.M. (1971) Distribution of transition elements in the system $CaMgSi_2O_6$-$Na_2Si_2O_5$-H_2O at 1000 bars pressure. Chem. Geol. 7.

Shibata T., De Long S.E. and Walker D. (1979) Abyssal tholeiites from the Oceanographe Fractue Zone I. Petrology and Fractionation. Contrib. Mineral. Petrol. 70, 89-102.

Sigurdsson H. (1977) Spinels in Leg 37 basalts and peridotites: phase chemistry and zoning. In: Init. Rep. Deep Sea Drill. Proj. 37.

Sigurdsson H. and Schilling J.-G. (1976) Spinels in Mid-Atlantic Ridge basalts: chemistry and occurrence. Earth Planet. Sci. Lett. 29, 7-20.

Simkin T. and Smith J.V. (1970) Minor element distribution in olivine. J. Geol 78, 304-325.

Sleep N.H. and Rosendahl B.R. (1979) Topography and tectonics of mid-ocean ridge axes. J. Geophys. Res. 84, 6831-6839.

Smith D. and Lindsley D.H. (1971) Stable and metastable augite crystallization trends in a single basalt flow. Am. Mineral. 56, 225-233.

Smith R.E. (1967) Segregation vesicles in basaltic lava. Amer. J. Sci. 265, 696-713.

Staudigel H. and Bryan W.B. (1981) Contrasted Glass-Whole Rock Compositions and Phenocryst Re-Distribution, IPOD sites 417 and 418. Contrib. Mineral. Petrol. 78, 255-262.

Staudigel H., Hart S.R. and Richardson S.H. (1981) Alteration of the oceanic crust: processes and timing. Earth Planet. Sci. Lett. 52, 311-327.

Stakes D.S., Shervais J.W. and Hopson C.A. (1984) The Volcanic-Tectonic Cycle of the FAMOUS and AMAR valleys, Mid Atlantic Ridge (36°47'N): Evidence from basalt glass and phenocryst compositional variations for a steady state magma chamber beneath the valley

midsections, AMAR 3. J. Geophys. Res. 89(B8), 6995-7028.

Stolper E. (1980) A phase diagram for Mid-Ocean Ridge Basalts: Preliminary results and implications for petrogenesis. Contrib. Mineral. Petrol. 74, 13-27.

Sun S.S., Nesbitt R.W. and Sharaskin A.Ya. (1979) Geochemical characteristics of mid-ocean ridge basalts. Earth Planet. Sci. Lett. 44, 119-138.

Takahashi E. and Kushiro I. (1983) Melting of a dry peridotite at high pressures and basalt magma genesis. Am. Mineral. 68, 859-879.

Tarney J., Wood D.A., Varet J., Saunders A.D. and Cann J.R. (1979) Nature of Mantle Heterogeneity in the North Atlantic: Evidence from Leg 49 Basalts. In: Deep Drilling Results in the Atlantic Ocean: Ocean Crust (eds. Talwani M., Harrison C.G. and Hayes D.E.), American Geophysical Union, pp 285-301.

Thompson G., Bryan W.B. and Melson W.G. (1980) Geological and geophysical investigation of the Mid-Cayman Rise Spreading Centre: Geochemical variation and petrogenesis of basalt glasses. J. Geol. 88, 41-55.

Thornber C.R. and Huebner J.S. (1985) Dissolution of olivine in basaltic liquids: experimental observations and applications. Am. Mineral. 70, 934-945.

Thy P. (1983) Spinel minerals in transitional and alkali basaltic glasses. Contrib. Mineral. Petrol. 83, 141-149.

Tiller W.A. (1977) On the Cross-Pollenation of Crystallization Ideas between Metallurgy and Geology. Phys. Chem. Minerals 2, 125-151.

Walker D., De Long S.E. and Shibata T. (1980) Crystal-ring microstructures in oceanographer fracture zone basalts. Contrib. Mineral. Petrol. 74, 1-6.

Walker D., Shibata T. and De Long S.E. (1979) Abyssal tholeiites from the oceanographer fracture zone II: Phase equilibria and mixing. Contrib. Mineral. Petrol. 70, 111-125.

Watson E.B. (1976) Glass inclusions as samples of early magmatic liquid: determinative method and application to a South Atlantic basalt. J. Volcan. Geotherm. Res. 1, 73-84.

White W.M. and Schilling J.-G. (1978) The nature and origin of geochemical variation in Mid-Atlantic Ridge basalts from the Central North Atlantic. Geochim. Cosmochim. Acta 42, 1501-1516.

Yoder H.S. and Tilley C.E. (1962) Origin of basalt magmas: an experimental study of natural and synthetic rock systems. J. Petrol. 3, 342-352.

Yoder H.S. jr (1969) Experimental studies bearing on the origin of anorthosite. In: Y.W. Isachen (ed) Origin of anorthosite and related rocks. New York State Mus. Sci. Serv. Mem. 18, 13-22.

****

APPENDIX 1: ANALYTICAL PROCEDURE

A-1.1 Whole rock analysis

The analytical procedure has been discussed in some detail in Section 1.4. In Table A-1, estimates of analytical tolerance, detection limits and accuracy of the method are given based on counting statistics (from le Roex, 1980).

A-1.2 Electron probe microanalysis

Counting staistics based on microprobe analyses are presented in Table A-2 and A-3. Details of natural and synthetic standards used are given in Table A-4. In Table A-3, the standard deviation of the mean of replicate analyses of the same basaltic glass is given for comparison with the theoretical precision based on counting statistics. For glass data of this study, an average of at least three glass analyses per sample proved to be adequate. Provided analyses were not taken immediately adjacent to microphenocrysts or phenocrysts (ie. avoiding possible chemical gradients), the glasses are relatively homogeneous with respect to microprobe precision.

Homogeneity at the micron scale is a problem in evaluating the absolute accuracy of this analytical technique. Nevertheless, Reid (1977) has noted that by using abundance data obtained by another method (eg. XRF), analysing one standard against another achieves good agreement. In this respect, details of standards used (eg. Table A-4) are presented including their compositions for reference.

A full analysis directory is given on microfiche (see sleeve on inside back cover).

Table A-1. Estimates of detection limits (lower limit of detection, or LLD), precision and accuracy (ie. absolute error) based on counting statistics and calibration curves for XRF analysis. Major elements expressed in weight %, trace elements in ppm.. Detection limits at the 99 % confidence level and counting errors at the 95 % confidence level (Data from le Roex, 1980).

Oxide/ element	wt %/ ppm.	Precision	Accuracy	LLD
SiO_2	50.0	0.140	0.264	0.036
TiO_2	1.0	0.008	0.008	0.005
Al_2O_3	15.0	0.080	0.079	0.022
Fe_2O_3	9.0	0.038	0.064	0.014
MnO	0.15	0.008	0.003	0.008
MgO	8.0	0.148	0.086	0.072
CaO	12.0	0.028	0.030	0.008
Na_2O	2.5	0.032	0.067	0.080
K_2O	0.2	0.002	0.022	0.002
P_2O_5	0.2	0.012	0.018	0.010
Zr	40 - 400	0.94 - 1.4		1.4
Nb	4 - 150	1.0 - 1.2		1.8
Y	20 - 40	0.8 - 1.0		1.3
Rb	2.5 - 90	0.8 - 1.1		1.5
Ba	10 - 800	2.1 - 6.0		6.7
Sr	80 - 800	1.0 - 1.7		1.5
Co	18 - 100	1.9 - 2.5		4.5
Cr	25 - 350	1.5 - 2.1		2.2
Ni	10 - 208	2.5 - 3.7		4.0
V	50 - 350	2.4 - 3.7		5.5
Zn	8 - 150	0.9 - 1.7		1.4
Cu	5 - 90	1.0 - 1.2		2.9
Sc	25 - 40	1.0 - 1.2		1.2

Table A-2. The counting statistics for phase compositions determined to be closest to the grand averages analysed by the Cameca Camebax Microprobe (this study). All data based on counting times of ten seconds. Figures in parentheses are Ni data for a counting time of 50 seconds.

	Glass		Pyroxene		Olivine	
	LLD	2 σ	LLD	2 σ	LLD	2 σ
SiO_2	0.06	0.36	0.05	0.28	0.05	0.26
TiO_2	0.06	0.09	0.05	0.05	0.04	0.03
Al_2O_3	0.05	0.27	0.03	0.08	0.04	0.03
Cr_2O_3	0.09	0.05	0.05	0.05	0.05	0.04
FeO	0.12	0.37	0.09	0.24	0.09	0.32
MnO	0.08	0.10	0.07	0.06	0.07	0.06
MgO	0.04	0.17	0.03	0.16	0.04	0.27
CaO	0.04	0.20	0.04	0.20	0.03	0.03
Na_2O	0.04	0.11	0.03	0.04	-	-
K_2O	0.03	0.04	0.03	0.02	-	-
NiO	-	-	-	-	0.12 (0.06)	0.07 (0.05)

Plagioclase		Oxides	
LLD	2 σ	LLD	2 σ
0.09	0.38	0.04	0.03
-	-	0.04	0.05
0.07	0.26	0.04	0.20
-	-	0.05	0.25
0.14	0.10	0.08	0.37
-	-	0.08	0.07
0.05	0.03	0.04	0.15
0.06	0.22	0.03	0.03
0.06	0.11	-	-
0.04	0.03	-	-
-	-	-	-

Table A-3. Glass analyses (Dredge 1) illustrating the precision and homogeneity by microprobe.

	1.		2.		3.	
	wt %	2 σ	wt %	2 σ	wt %	2 σ
SiO_2	50.26	0.36	50.18	0.29	50.26	0.27
TiO_2	1.67	0.09	1.58	0.06	1.58	0.06
Al_2O_3	15.81	0.27	15.88	0.10	15.92	0.10
FeO	9.43	0.37	9.44	0.19	9.33	0.22
MnO	0.17	0.10	0.16	0.01	0.16	0.02
MgO	8.10	0.17	8.03	0.04	8.00	0.06
CaO	11.39	0.20	11.39	0.06	11.45	0.10
Na_2O	3.15	0.11	3.11	0.03	3.09	0.04
K_2O	0.13	0.04	0.12	0.01	0.12	0.01

	4.		5.		6.	
	wt %	2 σ	wt %	2 σ	wt %	2 σ
SiO_2	50.20	0.40	49.84	0.38	49.86	0.31
TiO_2	1.55	0.07	1.48	0.04	1.50	0.05
Al_2O_3	15.80	0.12	15.81	0.05	15.94	0.19
FeO	9.03	0.19	9.19	0.09	9.30	0.17
MnO	0.17	0.04	0.17	0.02	0.15	0.03
MgO	8.61	0.06	8.61	0.05	8.64	0.06
CaO	11.33	0.19	11.52	0.12	11.57	0.13
Na_2O	2.83	0.35	3.10	0.05	3.13	0.07
K_2O	0.04	0.05	0.10	0.01	0.10	0.02

Analyses 1 to 3 : AG22-1-13

1. Single analysis; 2 σ as per counting statistics.
2. Mean of 4 analyses & standard deviation of the mean.
3. Mean of 10 analyses & standard deviation of the mean.

Analyses 4 to 6 : AG22-1-1

4. Mean of 10 replicate analyses on a single spot.
5. Mean of 4 analyses & standard deviation of the mean.
6. Mean of 6 analyses & standard deviation of the mean.

Table A-4. Standards used for the analysis of major elements in individual phases. Abbreviations and compositions are given below.

	Ol.	Plag.	Cpx.	Oxide/ spinel	Glass
Si	M-Ol	NUNI	DIOP	K-P	DIOP
Ti	K-P	-	RUT	RUT	RUT
Al	-	NUNI	K-H	CHRO	K-H
Cr	CHRO	-	CHRO	CHRO	CHRO
Fe	M-OL	K-H	K-H	ILMT	K-H
Mn	RHOD	-	RHOD	RHOD	RHOD
Mg	M-OL	K-H	K-H	CHRO	K-H
Ca	DIOP	LACO	DIOP	K-P	DIOP
Na	-	NUNI	K-H	-	K-H
K	-	OR-1	K-H	-	K-H
Ni	NISI	-	-	-	-

STANDARD	NAME	SiO_2	TiO_2	Al_2O_3	Cr_2O_3	FeO	MnO	MgO	CaO	Na_2O	K_2O	NiO
M-OL	Marjalahti Olivine	40.24	-	-	-	11.53	-	48.08	-	-	-	-
K-P	Kakanui Pyrope	41.46	0.47	23.73	-	10.68	0.28	18.51	5.17	-	-	-
CHRO*	Synthetic Chromite	-	0.47	19.41	44.50	22.10	0.21	12.30	-	-	-	0.14
RHOD	Synthetic Rhodonite	46.70	0.03	0.17	-	3.73	40.76	0.56	7.82	0.05	-	-
DIOP	Synthetic Diopside	55.47	-	-	-	-	-	18.62	25.90	-	-	-
NISI	Synthetic Ni Silicate	28.69	-	-	-	-	-	-	-	-	-	71.32
NUNI	Nunivac Plagioclase	66.10	-	19.90	-	0.06	-	0.05	0.98	8.40	3.30	-
K-H**	Kakanui Hornblende	40.37	4.72	14.90	-	7.95	0.09	12.80	10.30	2.60	2.05	-
LACO	Lake County Plagioclase	51.55	-	30.99	-	0.41	-	-	13.24	3.63	0.13	-
OR - 1	Orthoclase, Val Switzerland	64.39	-	18.57	-	0.03	-	-	-	1.15	14.92	-
RUT	Synthetic Rutile	-	100.00	-	-	-	-	-	-	-	-	-
ILMT***	Synthetic Ilmenite	-	45.70	-	-	36.10	4.77	0.31	-	-	-	-

Composition of standards used for microprobe analysis of minerals

* CHRO : Contains 0.25% V_2O_5.

** K-H : Contains 3.30% Fe_2O_3, 7.95% FeO and 0.94% H_2O.

*** ILMT : Contains 11.60% Fe_2O_3, 0.92% Nb_2O_5.

****

APPENDIX 2: PHASE EQUILIBRIA/THERMOMETRY

A-2.1 Olivine

The determination of olivine crystallization temperatures is strongly dependent upon critical assessment of equilibrium FeO/MgO partitioning. As discussed in Section 3.2., the following assumptions are important and relevant to the procedure:

(i) The application of an FeO/MgO partition coefficient, or Kd, of 0.3 $\pm$ 0.03 (Roeder and Emslie, 1970).

(i) Adoption of an Fe_2O_3/FeO ratio of 0.15 for host liquids (eg. Brooks, 1976).

In Table A-5, a complete listing of olivine equilibria is given; eg. olivine composition, the Kd calculated between olivine and the proposed co-existing liquid and the calculated temperature of crystallization. Temperatures of quenching (assuming equilibration of the most iron-rich olivine rims and quench glass) and of crystallization of the most Mg-rich olivines (olivine-whole rock equilibria; ie. intratelluric crystallization) are presented. For comparison, predicted liquidus temperatures (according to Roeder and Emslies equation [1970]) are given in Table A-6.

A-2.2 Plagioclase

In Table A-6, plagioclase liquidus temperatures as determined by the method of Nathan and Van Kirk (1978) are given for comparison with olivine liquidus temperatures. Except in the case of porphyritic lavas (eg. AG22-8-19,-24 and AG22-12-3,-11,-13,-27), olivine liquidus temperatures are on average 32 degrees higher than plagioclase liquidus temperatures.

Temperatures of quenching as determined by the Mathez (1974) equation (equation 7, this text) are presented in Table A-7. The apparent discrepancy in plagioclase and olivine quench temperatures has been discussed in the text and the similarity between (plagioclase) eruption and liquidus temperatures noted. From this it is inferred that these sodic microphenocrysts are low-pressure liquidus phases. Moreover, it is evident that plagioclase nucleation is not as sensitive to small drops in temperature as is olivine (eg. Donaldson, 1976).

Hence, if these quench temperatures are believed to be real, the implication is that the bulk of the lavas have been

erupted at temperatures higher than would be expected if magma chambers were continually operable beneath the SWIR between 16 and 26° E (see text for details). A corollary to this statement is that the operation of magma chambers and consequent continued crystallization within the crust, would be expected to produce lavas more evolved than the average Agulhas 22 basalt.

A worked example using Mathez's (1974) geothermometer is presented below and the procedure outlined. The quench glass and the most sodic plagioclase microphenocryst composition of sample AG22-1-1 are used.

The Mathez geothermometer: A worked example.

AG22-1-1.

(1) Calculate the molecular proportions of relevant oxides; ie. divide wt. % oxide by oxide molecular weight and convert to cation mole values. Normalize to 1.

eg. Si = 0.592
Al = 0.127
Ca = 0.225
Na = 0.055

(2) Determine the input data as per equation 7, taking into account the activity correction factor for plagioclase (ie. taken from Figure 3 of Mathez, 1974).

eg. λ = 1.154
Φ = -0.297
σ = 0.503 (@ 67.4 mole % An.)

(3) Rearranging Mathez's equation gives a quadratic function with;

$a = 1$
$b = (-19.01 - \ln \lambda/\sigma)/0.01176$
$c = (-1.29*10^{-3}*\Phi)/0.01176$

Substituting data from step 2 gives;

b = 1687
c = 325791

and T = 1192 °C. (the positive root minus 273 K)

Table A-5. Olivine equilibria data for the Agulhas 22 basalt suite. The first three columns pertain to the FeO/MgO exchange between the most Fe-rich olivine microphenocryst rims and quench glasses (ie. quenching). The last three columns pertain to equilibratiion of most Mg-rich olivine cores and whole rock compositions. Dashes indicate absence of glass or whole rock data. Temperatures based on the MgO thermometer of Roeder (1974).

SAMPLE NUMBER	OLIVINE/LIQUID EQUILIBRIA					
	Quench glass/olivine			Whole rock/olivine		
	Fo %	Kd.	T /°C	Fo %	Kd.	T /°C
AG22-1-1	86.1	0.305	1166	86.7	0.297	1171
AG22-1-4	84.9	0.333	1158	-	-	-
AG22-1-13	85.3	0.288	1144	-	-	-
AG22-3-2	81.9	0.307	1141	83.7	0.273	1119
AG22-3-4	82.8	0.306	1128	84.8	0.296	1153
AG22-3-8	82.5	0.305	1143	-	-	-
AG22-5-8	84.5	0.311	1145	-	-	-
AG22-5-9	81.2	0.293	1103	-	-	-
AG22-5-10	84.9	0.290	1158	-	-	-
AG22-5-14	82.4	0.285	1136	84.2	0.271	1124
AG22-7-1	85.9	0.273	1131	86.9	0.311	1181
AG22-8-2	-	-	-	82.2	0.300	1119
AG22-8-9	82.9	0.283	1125	83.7	0.292	1123
AG22-8-16	81.2	0.318	1135	-	-	-
AG22-8-24	81.6	0.289	1123	83.4	0.281	1091
AG22-9-1	87.1	0.275	1139	88.7	0.305	1186
AG22-12-1	84.7	0.317	1142	-	-	-
AG22-12-4	81.2	0.299	1118	-	-	-
AG22-12-20	85.7	0.300	1148	-	-	-
AG22-12-35	85.1	0.285	1147	85.9	0.266	1145
AG22-13-1	86.4	0.289	1151	87.3	0.309	1150
AG22-13-14	81.3	0.297	1161	85.6	0.303	1147
AG22-13-25	86.6	0.279	1154	87.3	0.290	1155
AG22-13-32	86.4	0.268	1151	-	-	-

Table A-6. Olivine and plagioclase liquidus temperatures and compositions as determined on whole rock data by the method of Nathan and Van Kirk (1978). Olivine data based on FeO/MgO equilibria (eg. Roeder and Emslie, 1970).

SAMPLE	OLIVINE		PLAGIOCLASE	
	T /°C	Fo %	T /°C	An %
AG22-1-1	1237	86.9	1195	75.9
AG22-3-2	1205	82.7	1179	71.9
AG22-3-4	1222	85.0	1181	72.1
AG22-3-20	1213	84.3	1177	71.2
AG22-3-23	1217	83.4	1176	71.3
AG22-3-29	1209	82.9	1179	71.7
AG22-3-34	1211	83.8	1183	71.2
AG22-5-2	1224	86.0	1189	73.0
AG22-5-7	1221	85.6	1190	73.3
AG22-5-14	1207	82.9	1175	70.5
AG22-5-15	1220	84.9	1189	73.0
AG22-5-18	1221	85.6	1190	73.6
AG22-5-31	1228	85.7	1182	72.3
AG22-5-38	1228	85.9	1177	71.7
AG22-5-46	1228	85.9	1197	73.7
AG22-5-48	1205	83.2	1185	71.2
AG22-5-51	1219	84.8	1186	72.3
AG22-5-59	1233	86.5	1187	72.0
AG22-5-65	1210	84.0	1180	70.1
AG22-5-66	1203	82.9	1172	69.4
AG22-5-68	1230	86.2	1181	72.4
AG22-7-1	1239	87.9	1192	74.0
AG22-8-1	1211	84.5	1193	72.4
AG22-8-2	1198	82.4	1177	70.2
AG22-8-9	1207	83.8	1193	72.9
AG22-8-11	1205	83.6	1195	72.4
AG22-8-15	1210	84.2	1197	73.6
AG22-8-19	1194	82.3	1213	75.1
AG22-8-24	1195	82.7	1225	77.0
AG22-9-2	1251	88.9	1199	76.2
AG22-12-3	1196	84.6	1245	78.8
AG22-12-11	1193	83.6	1225	74.7
AG22-12-13	1194	86.0	1284	82.7
AG22-12-23	1208	84.2	1205	73.9
AG22-12-24	1213	85.0	1209	75.3
AG22-12-26	1223	86.3	1207	75.4
AG22-12-27	1198	84.5	1223	76.3
AG22-12-31	1208	84.2	1200	73.3

continued over page ...

Table A-6 continued.

AG22-12-35	1218	85.0	1188	72.6
AG22-12-42	1210	84.1	1197	73.9
AG22-12-63	1214	85.0	1181	69.5
AG22-13-1	1228	87.6	1204	74.2
AG22-13-14	1223	86.1	1197	74.5
AG22-13-24	1229	87.3	1205	74.7
AG22-13-25	1229	87.5	1207	75.0

Table A-7. Eruption temperatures based on equilibration of quench glasses and most sodic microphenocrysts. Temperatures calculated using the Kudo and Weill (1972) geothermometer as modified by Mathez (1974).

Sample	Temperature /°C
AG22-1-1	1192
AG22-1-4	1191
AG22-1-13	1187
AG22-3-2	1181
AG22-3-4	1191
AG22-5-8	1198
AG22-5-14	1206
AG22-7-1	1197
AG22-8-9	1203
AG22-8-16	1186
AG22-8-24	1179
AG22-9-1	1187
AG22-12-1	1203
AG22-12-4	1201
AG22-12-20	1185
AG22-12-35	1187
AG22-13-1	1188
AG22-13-14	1192
AG22-13-25	1197
AG22-13-32	1185

****

- 8 MAR 1989